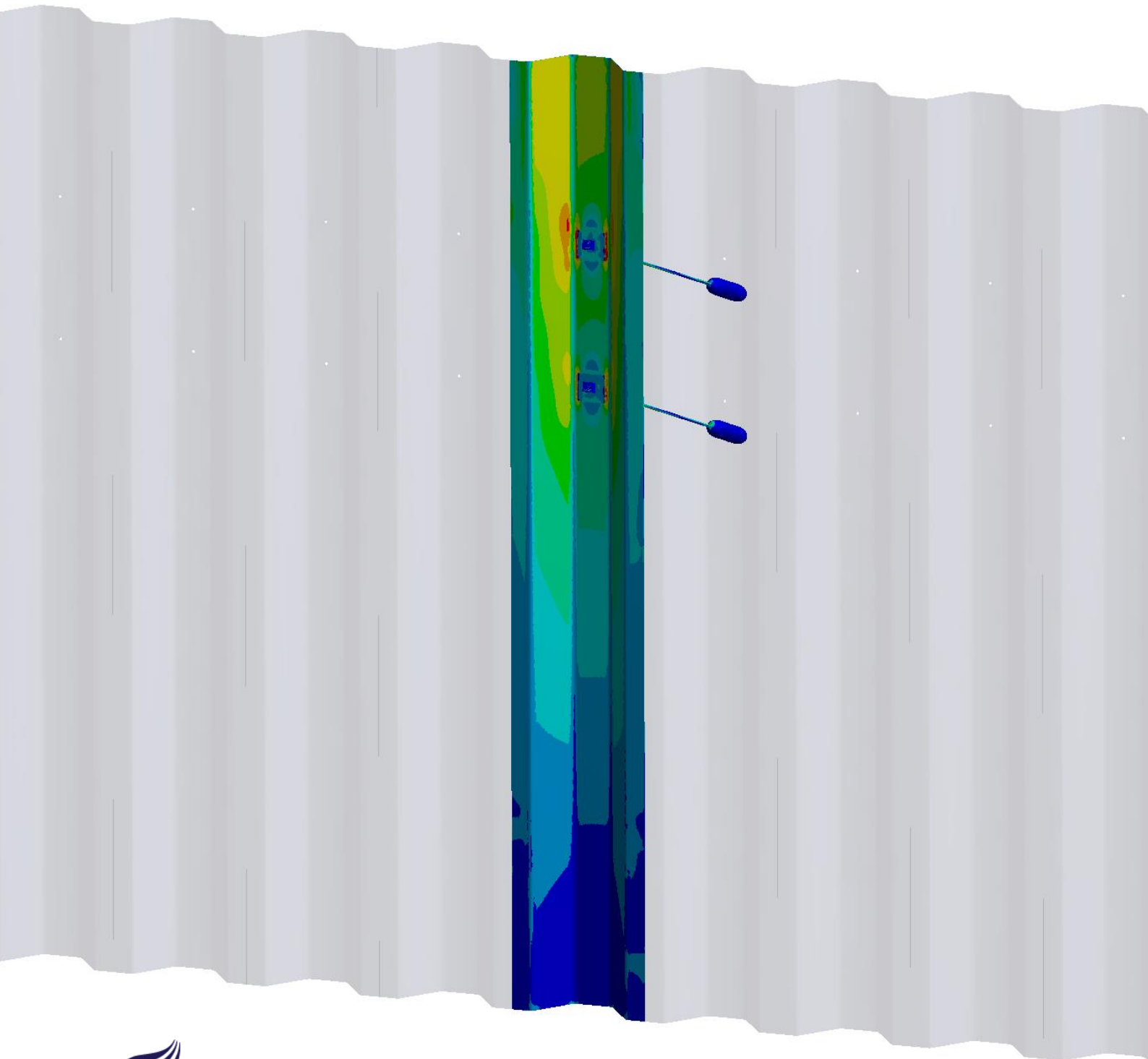


Numerical Analyses of the Behaviour of a Sheet Pile Wall

Master's Thesis



AALBORG UNIVERSITY
STUDENT REPORT

Erik Gammeljord & Mathias Sundahl Grønholdt
Structural and Civil Engineering
Aalborg University Esbjerg



Project Title

Numerical Analyses of the
Behaviour of a Sheet Pile Wall

Field of Study

Structural and Civil Engineering

Project Period

Master's Thesis

September 2016 – June 2017

Date for Submission of Assignment

June 8th 2017

Group Number

BM4-2

Students

Erik Gammeljord

Mathias Sundahl Grønholdt

Supervisors

Lars Damkilde

Sven Krabbenhøft

Printed Editions: 1

Number of Pages

Project: 101

Appendix: 148

Synopsis

This thesis deals with detailed numerical analyses of the behaviour of a sheet pile wall. The project contains three main parts, each investigating a subject of a sheet pile wall.

The first part concerns the design of a retaining wall, as multiple theories applicable to the design of the wall exist. A handful of analytical methods are chosen and compared to a numerical approach.

The second part investigates the load transferal between the anchor and the sheet pile considering the ULS case. The design of the load bearing plate and the dimensions of the sheet pile wall are analysed. Furthermore, focus will be on the optimisation process of the numerical analyses in order to reduce computational time.

The last part deals with deformations of a sheet pile wall. A study of the geotechnical parameters is performed to investigate the influence of the parameters on the deformations of the wall. Additionally, a field example is compared to an optimised numerical model focusing on fitting the model to make a proper approximation of the behaviour of the wall.

Group members

Erik Gammeljord

Mathias Sundahl Grønholdt

Preface

This project deals with ‘Numerical Analyses of the Behaviour of a Sheet Pile Wall’ and is written by the two M.Sc. students Erik Gammeljord and Mathias Sundahl Grønholdt in the period 01-09-2016 to 08-06-2017 at the Department of Civil Engineering at Aalborg University Esbjerg.

The focus of the project concerns analyses of the influences of soils on a sheet pile wall. The analyses include finite element(FE) calculations concerning both the soil and the structural components. The fundamental theory forming the basis for the analyses has been introduced throughout the report. It is presumed that the reader has a basic understanding and knowledge of both soil related and structural FEM. The report is primarily intended for the project supervisors and the examiners due to it being a learning based project. However, it may also be used as inspiration for future work.

Every chapter is led by a description of what is covered by the chapter end then succeeded by the subchapters. Equations are indicated by numbers in the form of $(xx.yy)$. xx describes the number of the chapter and yy the equation number in that respective chapter. Figures and tables will be numbered likewise apart from figures and tables located in appendix which are in the form of $(A.yy)$. Sources are referenced by $[zz]$, with zz being the respective number in the reference list located in the end of the report. Calculations have been kept from the main report. Any relevant calculations, numerical analyses and results are located in the belonging appendix report and supplied appendix A.21. References to the appendix have been made when necessary. A list of the used relevant software is given in appendix A.1.

Special gratitude is addressed to following for input and guidance during the project period:

- Lars Damkilde, Lic. Techn., Professor - Department of Civil Engineering at Aalborg University
- Sven Krabbenhøft, Extern Lecturer - Department of Civil Engineering at Aalborg University
- Morten Schouboe Rasmussen, Senior Design Engineer - Züblin A/S
- Ole Møller, Design Manager - Per Aarsleff A/S

Contents

| | | |
|----------|---|-----------|
| 1 | Introduction | 1 |
| 1.1 | Retaining Walls | 2 |
| 1.2 | Scope of Project | 8 |
| 2 | Problem Statements Concerning a Sheet Pile Wall | 9 |
| 2.1 | Description of Issues Related to a Sheet Pile Wall | 9 |
| 2.2 | Investigation of Issues Related to a Sheet Pile Wall | 15 |
| 3 | Fundamental Theory Concerning Geotechnical Structures | 17 |
| 3.1 | Soil Material Theory | 17 |
| 3.2 | Theory of Plasticity in Soils and Steel | 24 |
| 3.3 | Failure Theory in Soils | 33 |
| 3.4 | Yield Lines in Steel Plates | 34 |
| 3.5 | Membrane Effect in a Plate | 36 |
| 4 | Applied Analytical Theory of Sheet Pile Wall Calculations | 37 |
| 4.1 | Calculation of a Sheet Pile Wall in Denmark | 37 |
| 4.2 | Calculation of a Sheet Pile Wall in Germany | 40 |
| 4.3 | Calculation of a Sheet Pile Wall by KSP | 42 |
| 4.4 | Calculation of a Sheet Pile Wall by Finite Element Method | 46 |
| 4.5 | Comparison of Sheet Pile Wall Calculation Methods | 49 |

| | | |
|----------|--|-----------|
| 5 | Anchor Force in Thin Walled Sheet Pile | 57 |
| 5.1 | Preconditions of the Numerical Model of the Sheet Pile | 57 |
| 5.2 | Study of the Plate Designed According to the Eurocode | 64 |
| 5.3 | Parameter Study Concerning Anchor Attachment Detail | 65 |
| 5.4 | Collapse Analysis of the Sheet Pile | 71 |
| 5.5 | Study of the Influence of Membrane Effect | 74 |
| 6 | Deformations of a Sheet Pile Wall | 75 |
| 6.1 | Study of the Numerical Model Using OptumG2 | 76 |
| 6.2 | Numerical Model Based on Field Example | 77 |
| 6.3 | Geotechnical Parameters Used in the Deformation Analyses | 82 |
| 6.4 | Sensitivity Analyses of Geotechnical Parameters | 83 |
| 6.5 | Optimisation of the Numerical Model | 88 |
| 7 | Discussion | 93 |
| 8 | Conclusion | 97 |
| | Bibliography | 99 |
| A | Appendix | |

Introduction

During the past years, an increasing need for denser settlement in urban areas has caused an equivalent increase in the use of retaining walls. Retaining walls are necessary solutions, as the space required for a sloped construction is not always available. The primary use of a retaining wall is to restrain the soil in two distinct elevations making it an essential part of an excavation site. However, a retaining wall is an expensive solution compared to a soil slope which has no need of artificial structural walls stabilising the surrounding soil. Figure 1.1 illustrates an excavation site located in San Francisco where dense population makes a soil slope highly unfavorable.



Figure 1.1: In land construction pit ensuring stability in a dens urban area.[1]

Retaining walls are also widely used in ports where this construction method provides easy and safe berthing for ships and offshore equipment. A typical sheet pile quay is shown in figure 1.2.



Figure 1.2: A quay constructed as a retaining wall in the harbour of Esbjerg.[2]

Various diverse types of retaining walls exist that each fulfill unique design criteria such as space requirements, soil and ground water issues and other geotechnical configurations. The most commonly known and used retaining walls count:

- Sheet pile walls
- Secant pile walls
- Soldier pile walls

Even though retaining walls are well-known constructions and the design and dimensions are based on solid theory which rarely results in failures, a variety of theories related to soil mechanics are still in discussion. With the increasing need for further validation designing a construction, geotechnicians face new challenges and an increasing need for more detailed investigations.

1.1 Retaining Walls

A retaining wall may seem like a simple structure with the main purpose of retaining the soil on its backside. However, when dealing with soil it often gets complicated. In this chapter the mechanics of a retaining wall will be discussed and the most important components of a retaining wall will be elaborated.

1.1.1 Stability of a Retaining Wall

The purpose of a retaining wall is to keep soil in place during or after an excavation where a slope is inappropriate. As the angle of the slope increases, problems regarding the stability may occur, if the properties of the soil are insufficient. The stability issue of a slope is illustrated in figure 1.3, where a sand slope has an incline greater than the capability of the material, resulting

in failure of the slope. The definition of failure is that the coloured domain will separate from the base of the slope and rush down, thus the slope is said to fail. In the figure a failure mode has been predicted numerically and the colours indicate the magnitude of movements. The failure line depends on the steepness of the slope, as well as the properties of the material forming the slope.

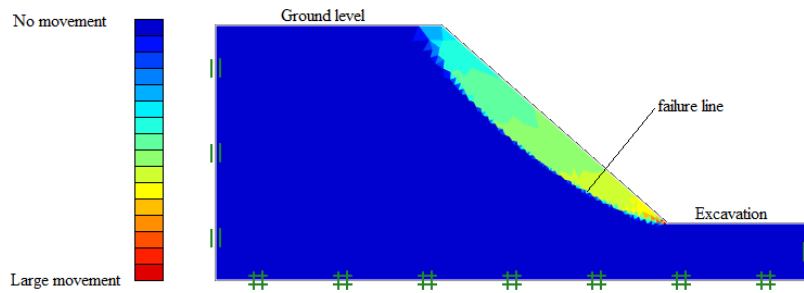


Figure 1.3: Numerical model of an insufficient slope consisting of sand in failure mode.

In such cases where surroundings do not allow for enlargement of the slope in order to lower the inclination, a retaining wall may be considered. A retaining wall also has stability issues for insufficient design, which is shown for an arbitrary case in figure 1.4.

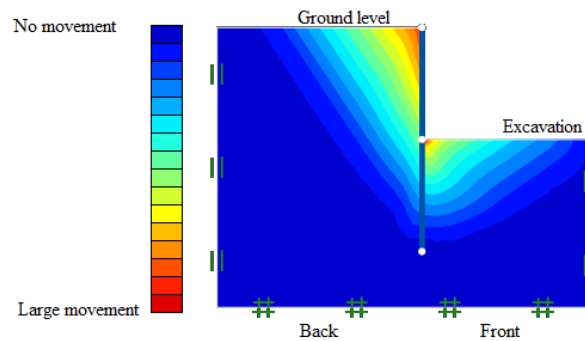


Figure 1.4: Numerical model of an insufficient cantilever sheet pile wall situated in sand in failure mode.

As shown in figure 1.4 the embedment depth is deep in the soil. This is related to the earth pressure from the backside of the wall, as the soil will try to overthrow the wall. If the earth pressure is of a greater magnitude, a deeper footing is needed, as this will act as a resistance and ensure stability of the wall. The magnitude and distribution of the earth pressure on a wall is a debated topic and highly depends on choice of theory. Before the FEM was introduced in soil mechanics, hand calculations were the norm, but now intelligent software is on the rise. In chapter 4 a study of different earth pressure theories are presented.

A retaining wall can be considered as a cantilever beam with a differential load (earth pressure) and a fixed footing. The dimensions of the wall or type is important, as it needs to be able to withstand the moment introduced by the earth pressure. However, by adding a fixed point

in the upper part of the wall in form of an anchor the influence of the earth pressure may be reduced, which will be further elaborated in section 1.1.3.

1.1.2 Sheet Pile Wall

A sheet pile wall is the most common type of retaining wall. The installation is relatively cheap and can be performed in many different ways depending on the surroundings. A typical installed sheet pile wall is shown in figure 1.5.



Figure 1.5: Typical installed sheet pile wall with an outside waling level.[3]

The sheet piles consist of folded steel plates which are driven into the soil prior excavation by either driving, vibration or pressing. The steel elements are usually folded in Z- or U-segments, as illustrated in figure 1.6. The sheet piles are locked together by interlocks which create a tight connection. The connection can also be waterproofed by gaskets, if high water table is an issue. Due to the unique form of the sheet profiles, the resistance is relatively high for the profiles compared to the amount of material, which makes it possible to use the profiles for deep excavations. This makes the sheet piles comprehensive diverse in its use. Furthermore, the addition of one or multiple anchor levels will increase the resistance greatly, if the active soil pressure is significant.

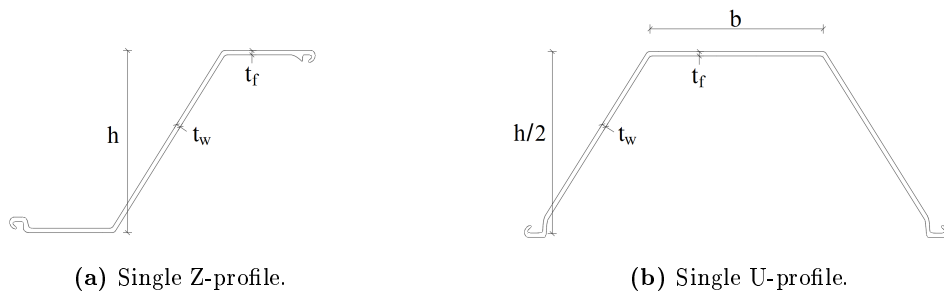


Figure 1.6: Cross sections of different sheet pile sections.

Issues may arise if the soil domain consists of either dense sand or fat clay, which may be countered by the installation method called *staggered* walls. This method reduces the amount

of material as well as the probability for interlock slip-off during driving of the sheet piles. Commonly every other sheet pile has reduced embedment depth, which is allowed, if the stability is sufficient. This is possible, when the full section modulus of the sheet piles is not needed.

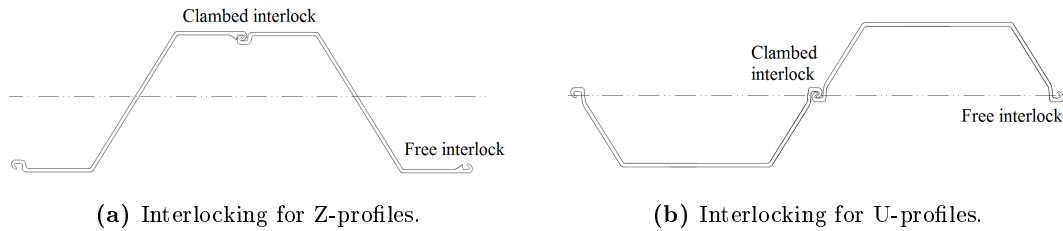


Figure 1.7: Interlocking for the two sheet pile types. Note that the free interlocks cannot be clamped once being driven into the soil.

It is often desired to reduce the number of drivings, and a simple solution is clamping of the interlocks between profiles and then driving two piles in the earth at a time. However, since there is no possibility of clamping the interlocks after installation, it is important to account for the behaviour of the wall as the strength of the complete wall is reduced by clamping only every other interlock. This issue is further elaborated in section 2.1.1.

In the last 20 years the U-profile has seen changes in its dimensions. E.g. the width of a AU18 profile has increased from 600 *mm* to 750 *mm*, while the thickness has decreased by 1 *mm*. The mass per meter has also decreased making each sheet pile more cost efficient compared to the strength, since there has been no reduction in the elastic section modulus. In fact, the only property for a standard profile which has not changed is the sectional modulus per meter. A complete data sheet for an AU18-profile is apparent in appendix A.2.[4]

The secant pile and soldier pile solutions will not be covered in this project, thus the need for a in depth elaboration is not relevant. However, presentations including installation, mechanics and advantages are found in appendix A.3 for further interest.

1.1.3 Anchoring of a Retaining Wall

In order to prevent failure or inappropriate design of the wall due to excessive earth pressure acting on the sheet pile, an anchor may be introduced which provides the desired stability. Anchors are installed in levels which means there are multiple anchors in the same height along the wall. For deep excavations the application of multiple anchor levels may be necessary.

The size and length of the components of an anchor depend on the properties of the soil and the size of the retaining wall. The stability of the wall is greatly improved by the appliance of the anchor block, as the soil in front of the block acts in favour of the stability. This is a result of the shear forces appearing, as it tries to displace the body of soil as illustrated in figure 1.8. The failure zone is a result of the assumed failure theory which is important to consider designing

the installation of the anchor, as the anchor must be placed outside of the failure zone of the wall.

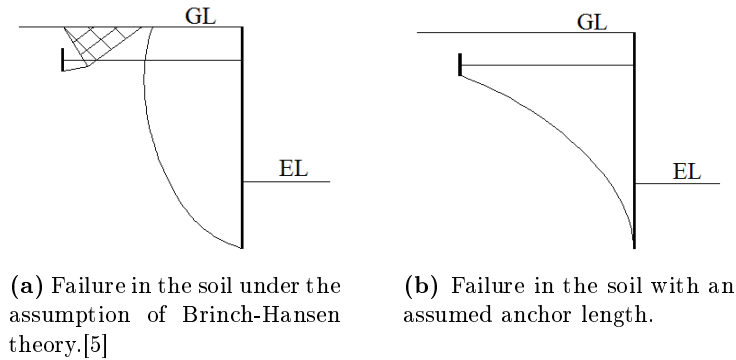


Figure 1.8: Failure of a plate anchor showing the soil body acting in favour of the retaining wall. The failure lines are caused by different assumptions elaborated in chapter 4.

The surroundings directly determine which kind of anchor installation is possible. Because of this, there are different types of anchors and anchor components which suit the respective installation method. In general, anchors are distinguished in two types, the grout anchor and the plate anchor.

The most traditional anchor is the plate anchor. The anchor tendon is attached to the retaining wall at a specific level, and the attachment is called the anchor head, which is pictured in figure 1.9a. The design of the load bearing plate is significant, as the plate transfers the anchor force to the retaining wall. If the plate is designed insufficiently, the force could possibly lead to collapse of the wall caused by inappropriate load transferal.

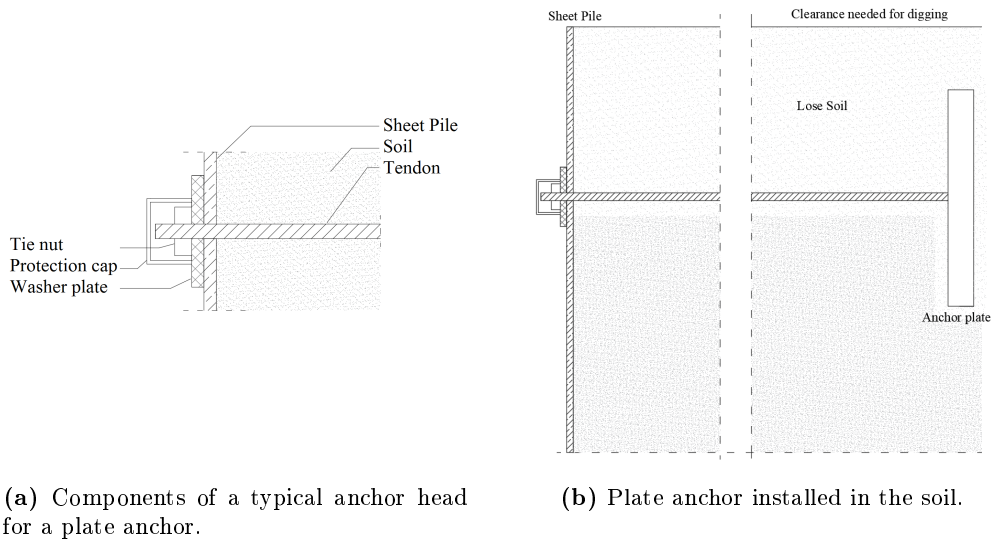


Figure 1.9: Components of a plate anchor.

The tendon is buried horizontally on the backside of the retaining wall, and at the end a block is attached typically consisting of a concrete or steel, acting as a resistance. This type of anchor is easy to install by excavation on the backside, but the method requires that digging of the backside is allowed, as the tendon and resistance block is buried in the soil. This is illustrated in figure 1.9b.

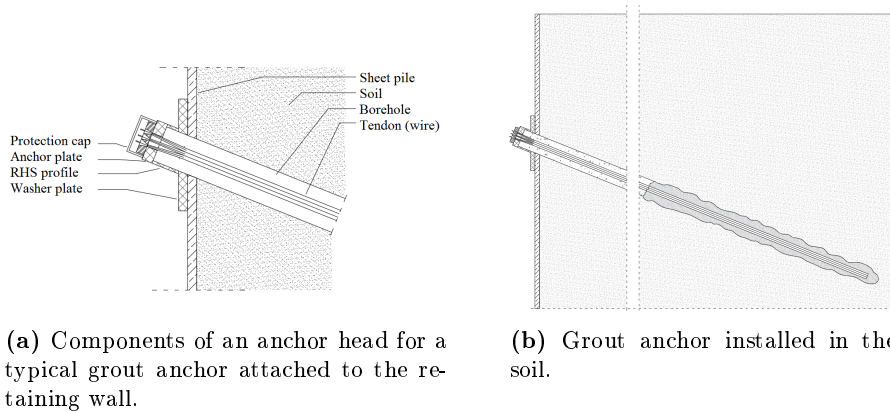


Figure 1.10: Components of a grout anchor.

If digging of the backside is not allowed, a grout anchor can be installed instead. The grout anchor is typically attached differently to the retaining wall, which is shown in figure 1.10a. The anchor tendon is installed with an inclination inside the soil. This is useful, as it allows for e.g. placement of the anchor block beneath the foundation of an existing house. The installation of the grout anchor is initiated by boring of a borehole starting from the retaining wall. As the sufficient length is reached, a concrete mass is pumped through the drilling pipe and fills the bottom of the hole. The concrete then forms a fixed longitudinal block which utilises the shear force acting between the soil and concrete. The tendon is attached in the wet concrete and the drill is removed gradually.

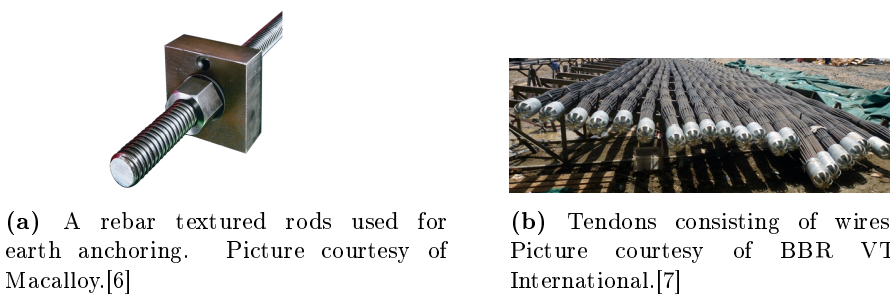


Figure 1.11: Types of tendons for anchoring.

The tendon consists of either wires or a rebar textured rod, which may be used for both configurations. In figures 1.11a and 1.11b the rod and wires are illustrated respectively. After the wall has been installed, the soil on the excavation side is removed gradually. As an excavation level just below the anchor level is reached, the anchor is installed. At this stage only a small part of the full earth pressure is established. The anchor is then pretensioned to avoid slacking

of the tendon, which prevents outwards deformations of the retaining wall caused by the earth pressure. Pretensioning will be performed just before the remaining excavation happens.

The anchor can be attached to the wall directly or by a waling level, which is elaborated in appendix A.4 for further interest.

1.2 Scope of Project

The project consists of studies of issues concerning an anchored sheet pile wall. The studies include Ultimate Limit State (ULS) analyses performed using the numerical software, ANSYS Workbench and OptumG2, and Serviceability Limit State (SLS) analyses performed using OptumG2.

In order to achieve this a total of three parts have been formulated in the project. In the first part the foundation will be laid in form of the fundamental theory concerning the material, properties and behaviour of the soil. This will lead to an explanation of four different calculation methods for determination of the earth pressure. Those methods are then compared and discussed considering the design of a sheet pile wall.

The second part consists of failure analyses of an anchored sheet pile wall. The analyses concern the issues regarding an anchored wall using a load bearing plate for transferal of forces introduced by the anchoring to the sheet pile. An in depth study of the influence of the different parameters has been performed.

The last part consists of a study of the deformations, which is an expanded SLS analysis. A study of the influence which the relevant parameters have on the deformations of the wall, will be established. This leads to a comparison between numerically generated deformations and experimental data.

Problem Statements Concerning a Sheet Pile Wall

Retaining walls have been used for several decades, but still to this day, different kinds of issues concerning the design and functionality exist. The design is getting more sophisticated continuously, but this also raises new issues. A variety of these issues will be addressed in this chapter to illustrate some of the challenges the industry faces today regarding the design and the mechanics of retaining walls. The issues count both ULS and SLS cases which must be considered during the design of retaining wall structures. Some issues concern actual failure of a wall and are referred to as ULS. SLS concerns both the aesthetics and the use of the wall, where for example deformations are considered. Too large deformations of a wall may seem unsafe, and it may complicate the use of the area in front of the wall e.g. in limited excavation sites or in the railway industry. However, where the aesthetics are without significance, large deformations of a retaining wall may cause unwanted or critical displacements elsewhere.

In section 2.2 some of the discussed issues will be selected, and this will lead to the initiating problem for the work of the project.

2.1 Description of Issues Related to a Sheet Pile Wall

In the following sections the different possible issues related to retaining walls are addressed and discussed. The sections will act informatively and not investigative.

The issues of consideration count:

- Attachment of anchors in a thin walled sheet pile
- Vertical bearing capacity
- Oblique bending of coupled sheet piles
- Off-centering of an anchor

2. PROBLEM STATEMENTS CONCERNING A SHEET PILE WALL

- Pretensioning of an anchor
- Strain compatibility in an anchor tendon
- Numerical modeling of deformations in a retaining wall

The list may be split into the two categories mentioned in section 2 - ULS and SLS.

2.1.1 ULS Related Cases

Attachment of Anchors in a Thin Walled Sheet Pile

When an anchor level is installed in a sheet pile, a load bearing plate may be attached to the sheet pile to transfer the loads from the tendon to the sheet pile. This anchor load may cause yielding or local failure in the sheet pile as the profile is thin walled. Figure 2.1 illustrates the possible issue occurring for insufficient design of the load bearing plate. It is known that high stresses occur in the flanges having a small plate. Enlarging the plate will transfer more of the load to the webs of the profile leading to a redistribution of the high stresses. It is of interest to generate a relationship between the different dimensions of the plate and the resulting stress distributions. Note, this issue is only related to anchors without a waling level.

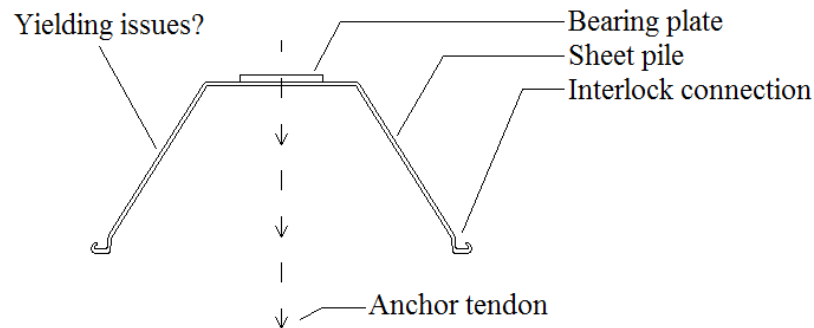


Figure 2.1: Anchor attached to a U-shaped sheet pile by a load bearing plate. Possible issue in the cross section concerning yielding or failure caused by a too great anchor force.

Vertical Bearing Capacity of a Sheet Pile

The vertical bearing capacity of a sheet pile wall is a discussed topic, due to the base resistance area of a sheet pile being indeterminate. When designing a retaining wall the vertical bearing capacity needs to be checked to secure stability of the wall and here the effective area is of interest. As figure 2.2 reveals different considerations of this area exist. The fact that the area is indeterminate, is because of the effect of the soil sticking to the sheet pile during installation, thus acting as a plug increasing the vertical bearing capacity.

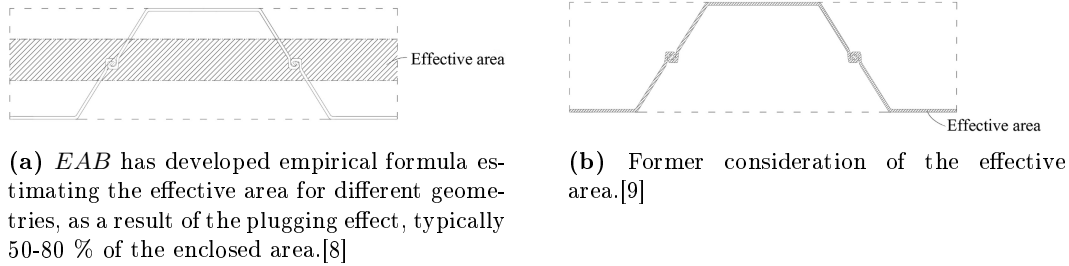


Figure 2.2: Different considerations of the base resistance area of a sheet pile wall.

Figure 2.2 reveals great difference between the considerations of the effective area. Several unknowns are associated with the determining of the vertical bearing capacity of a sheet pile, which is expressed by the figure. It is however evident that the actual capacity must be determined based on 0-100 % of the enclosed area. Through empirical data the studies of *EAB*¹ reveal that the effective area is around 50 % of the enclosed area or greater. Due to the insecurity of the actual value, a study of the parameter is of interest.[8]

Oblique Bending of Coupled Sheet Piles

When sheet piles are driven into the soil, the coupling of the profiles is not insignificant. It is possible to drive sheet piles into the soil both as a single profile or paired. Pairing of the sheet piles reduces the number of driving actions during installation reducing the overall cost. However, to ensure the paired piles are driven down simultaneously, the connecting interlock is clamped illustrated in figure 2.3. This fixity of the interlocks causes several issues.

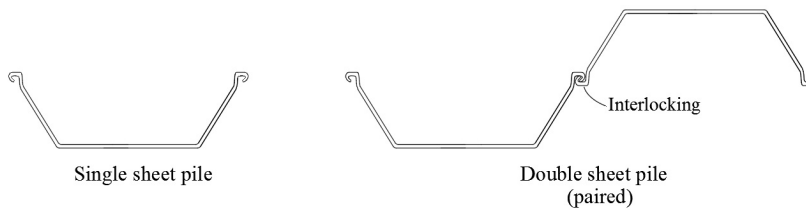


Figure 2.3: Single and paired U-shape sheet piles.

In beam theory, the *neutral axis* is defined as the axis with no axial strain and where bending evolves around. The neutral axis is shown for a U-shaped sheet pile in figure 2.4.

As a load, e.g. the earth pressure, is perpendicular to the plane of the walls, the neutral axis coincides with the minor principal axis of inertia. For a paired U-shaped sheet pile the neutral axis is rotated as illustrated in figure 2.4, meaning the effective height of the paired piles is decreased. The effective height is the distance from the neutral axis to the remote pile point. This results in a loss of strength and stiffness due to the moment of inertia being reduced, which

¹Recommendations on Excavations: EAB made by the German Geotechnical Society.

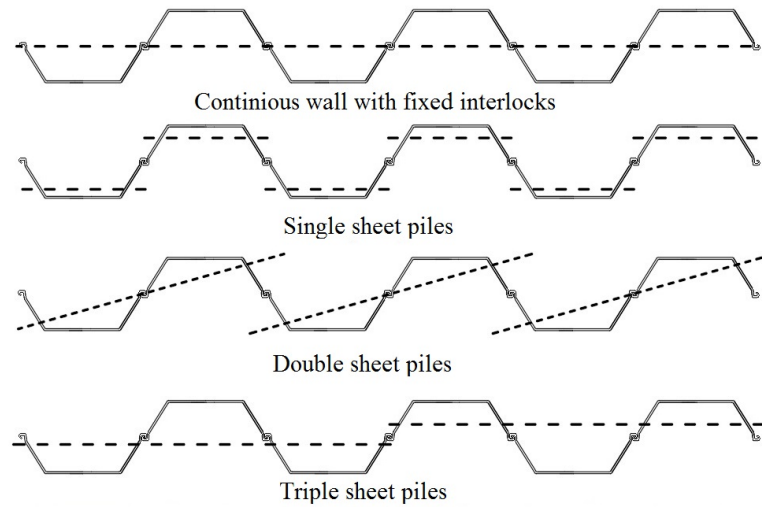


Figure 2.4: Neutral axes for a single and paired U-shape sheet pile with and without fixed interlocks.

must be accounted for. A guideline for inclusion of the factor is available, but the procedure needs optimisation, as it generates highly conservative values.[10]

Off-centering of an Anchor

As mentioned, the most commonly used steel sheet piles are the U- and Z-types illustrated in figure 1.6. The interlocks (seen in figure 1.7) at the ends of the profiles ensure shear transmission between the sheets and increase the overall strength of the retaining wall construction. For Z-shaped sheets an issue regarding the installation of anchors is apparent. The issue concerns the interlocks being placed in the center of the coupled flanges coinciding the position of the anchors. The location of the interlocks causes issues, as a part of the interlocking needs to be removed to allow for the load bearing plate to be attached. It is possible to solve this issue by off-centering the anchor from the interlock, as illustrated in figure 2.5. However, this leads to the possibility of new issues forming affecting the stability of the wall. A waling could solve this, but cases where a waling is not an option due to space requirements etc., exist.

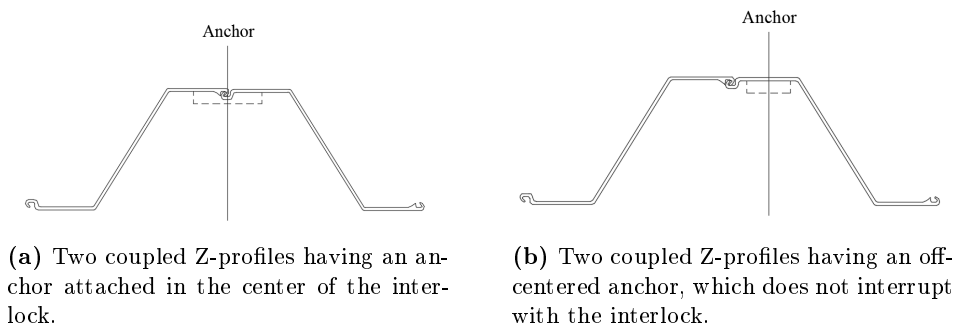


Figure 2.5: Off-centering of anchors.

2.1.2 SLS Related Cases

Pretensioning of an Anchor

In section 1.1.3 two types of anchors are presented. For both configurations an anchor tendon may be used to connect the sheet pile to an anchor block in the soil. The purpose of the anchor is to enhance the resistance of the wall further against the earth pressure. As the earth pressure affects the wall, great tension in the tendon appears as the wall is pushed forward. This tension may cause large deformations in the tendon which could prove to be critical.

A tendon is typically made of high quality steel, thus elongations are large before reaching yielding and further plastic elongation, which is normally not allowed. As the anchor is installed, it gets pretensioned in order to prevent slacking of the tendon. However, there are no specific design rules concerning the magnitude of the pretension, which is typically determined as a result of a qualified guess. If the magnitude of the pretension is too great the wall could be pushed into the soil, and if the magnitude is too low the wall could be pushed outwards until the anchor *activates*. The effects of pretensioning are illustrated in figure 2.6.[11]

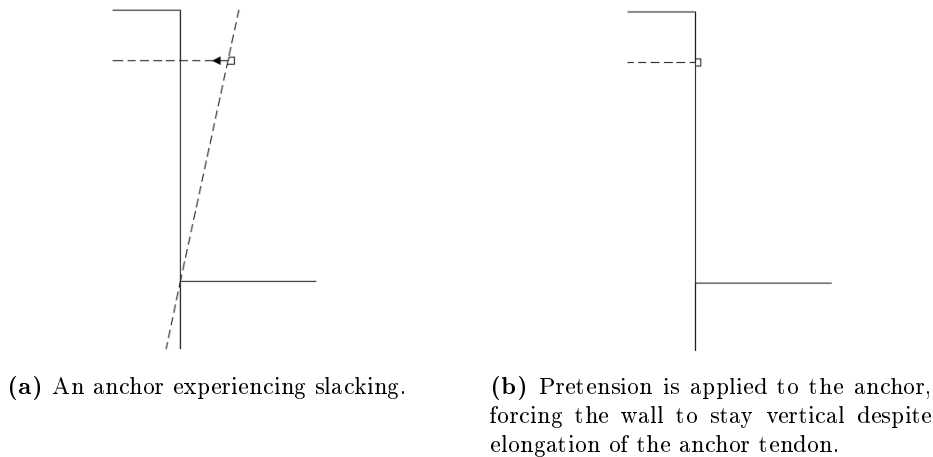
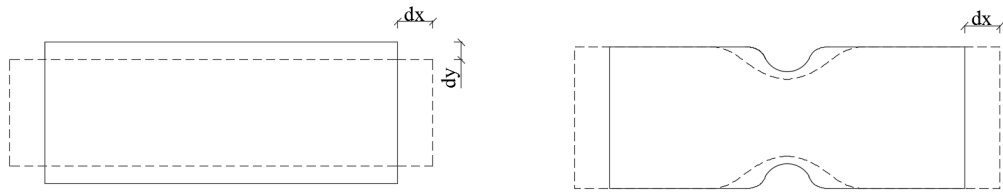


Figure 2.6: Effects of pretension of an anchor.

Strain Compatibility in an Anchor Tendon

As a retaining wall is installed and the excavation is happening, the earth pressure gets established and the applied anchors will activate. Steel has the same Young's Modulus independent of the quality, and thus high quality steel allows for larger elongations within the elastic zone. Thus a load of great magnitude leads to a large elongation of a tendon, and this effect is important to consider. In case of a weak spot in the tendon caused by e.g. fabrication imperfections, the stress level could intensify at the weak spot. This could result in failure because of the appearance of failing strains in the anchor tendon due to the full elongation happening locally. The effect is illustrated in figure 2.7.



(a) Deformations of a perfect modeled plate caused entirely by tension. Strains and deformations are evenly distributed throughout the entire length of the plate.

(b) Deformations of a plate by inclusion of an imperfection caused by tension. Strains are intensifying in the area of the imperfection leading to a critical state.

Figure 2.7: Influence of the inclusion of imperfections in a plate.

Numerical Modeling of Deformations in a Retaining Wall

Experience shows that experimental deformations of a retaining wall are difficult to replicate numerically, as numerically generated deformations result in an overestimation of up to 200 %, as illustrated in figure 2.8. This highly conservative estimations of the deformations, this issue is of great interest.

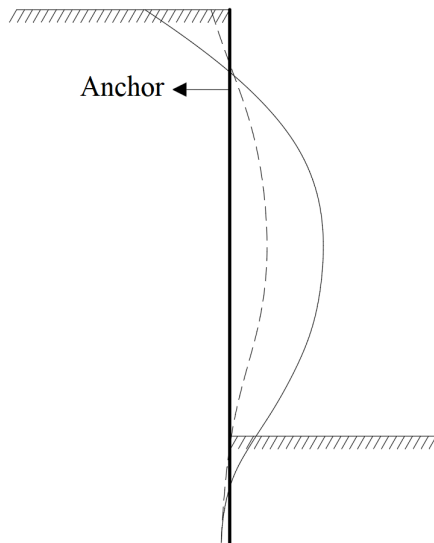


Figure 2.8: Typical numerical overestimation of deformations in a retaining wall.

Large deformations could prove to cause issues for other components of the retaining wall. These may influence the elongation of the anchor tendon and change how the earth pressure affect the wall. The overestimation may be caused by various reasons such as insufficient or conservative determination of the soil and structural related parameters. The soil domain may be inaccurately determined or it could be a result of the numerical calculation method.

2.2 Investigation of Issues Related to a Sheet Pile Wall

In section 2.1 issues related to the installation and use of a retaining wall are presented and addressed. This leads to the problem statement for the project work which will be processed and attempted to be fulfilled:

"How are the actions on a sheet pile wall determined, and how do these affect the sheet pile in regards to the ULS and SLS cases?"

This initiating problem is solved through the following chapters including both analytical and numerical analyses of ULS and SLS cases. Due to the time frame of the project period, it has not been possible to cover all of the addressed issues and a only a few have been investigated. As it appears in the following, oblique bending, vertical bearing capacity and off-centering of an anchor have all been excluded from the project, as a result of time shortage and availability of experimental data generation.

The following studies will be performed:

- Anchor force on a thin walled sheet pile
- Pretensioning of an anchor
- Numerical modeling of deformations in a retaining wall

The investigation of these studies is primarily based on the use of the FEM. Besides solving the initiating problem, optimisation will also be in focus in order to illustrate the strength of the different methods and reduce computational time in the analyses. Initially an investigation of the design of a sheet pile is performed in chapter 4. The purpose of this chapter is to illustrate the strength of the FEM and to introduce some of the fundamentals in soil mechanics combined with structural analyses.

Fundamental Theory Concerning Geotechnical Structures

This chapter explains some of the fundamental theory in the project concerning soil mechanics, material modeling and calculation of a retaining wall. This will act as the fundamental knowledge to proceed with the investigations throughout this project. Since there are several distinguished studies in this project, it is not the goal of this chapter to cover all theories but merely to cover the most essentials.

Earth pressure and the strength of the soil are significant factors, as a retaining wall is designed. These effects are examined in section 3.1.

3.1 Soil Material Theory

In soil mechanics tension and compression are not normal terms, instead shear resistance is used. Normal and shear stresses appear along a line, as soil is slipping, when failure occurs. This line is a so-called *failure line* which will be elaborated in section 3.3. The normal stresses are pressures along the failure line and are usually split into the effective failure stress and the pore pressure denoted σ'_f and u respectively. This yields:

$$\sigma_f = \sigma'_f + u \quad (3.1)$$

Different experiments show that the failure shear stress, τ_f , depends on two contributions:

- Friction
- Cohesion

This connection was found by Coulomb and later formulated by Mohr. A Mohr-Coulomb material is a material behaving by this failure criterion which usually include clay and sand that

comply to the criterion. The primary failure function for cohesionless soils like sand is written as:

$$\tau_f = \sigma'_f \cdot \tan\varphi \quad (3.2)$$

Where φ is the angle of friction for the material. σ'_f is the pressure of the soil with the water pressure subtracted. The angle of friction is a measure of the maximum angle of which a slope of the given material has in order to ensure stability of the slope. It is distinguished by two states, the peak friction angle, φ_p , and the critical state angle of friction, $\varphi_{cv/crit}$. Figure 3.1 illustrates the correlation between the normal and shear stress, when a sand specimen is subjected to shear stress in a Direct Shear Test for different packing states of sand. Direct Shear Test is explained in appendix A.6.1.

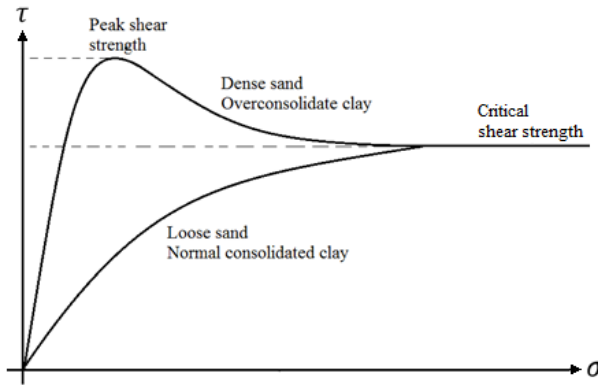


Figure 3.1: Normal and shear stress relation for dense and loose sands.

For dense sand the interlocking between the soil particles generates a high amount of shear strength, and as the limit strength is exceeded, the particles will start to slide and roll over one another. This causes an expansion in the soil volume called dilation, which reduces the strength of the soil. The strength reduces until reaching a new equilibrium state, called the critical state. For loose sand, the shearing process will cause the soil particles to rearrange and reach a denser configuration. The soil will dislocate and gain strength until the specimen reaches a peak value, which is equal to the critical state for dense sands. As figure 3.1 reveals, dense packed sand has two different shear strengths. The friction angle is found by developing a Mohr-Coulomb diagram for different test configuration respectively.

Clay and sand have different properties which means that the formula of τ_f has different appearances for the different materials. As sand is a frictional material meaning the friction of the sand is crucial to its strength, equation 3.2 is valid. However, clay is a cohesive material and therefore the cohesion between the particles is a factor which yields an expansion of the equation:

$$\tau'_f = c' + \sigma'_f \cdot \tan\varphi' \quad (3.3)$$

Where c' is the effective cohesion. Equation 3.3 is valid for drained cohesive materials where friction is included. In case of undrained clay only cohesion contributes to the strength of the material, and therefore a constant shear resistance is apparent:

$$\tau_f = c_u \quad (3.4)$$

Where c_u is the undrained cohesion. Figure 3.2 shows the properties of the different materials. The strength parameters can be quantified by field tests which are often extensive and therefore expensive to perform. For minor constructions known values may be used, if field tests are not required. However, the tests are necessary for major projects to ensure that the properties of the soil used in calculations are reliable. In appendix A.5 empirical values are given.

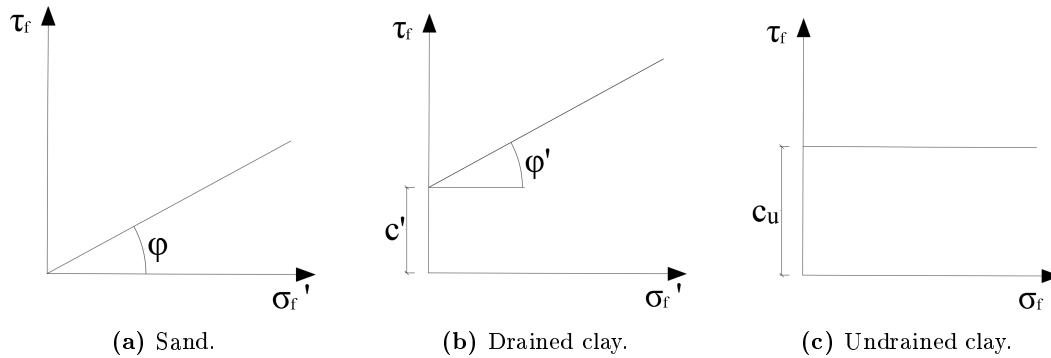


Figure 3.2: Failure surfaces for different Mohr-Coulomb materials.

As the stresses are known these can be used to draw Mohr's circle which is used to illustrate the failure condition of a material. A circle within the failure surfaces yields stability, which is illustrated in figure 3.3.

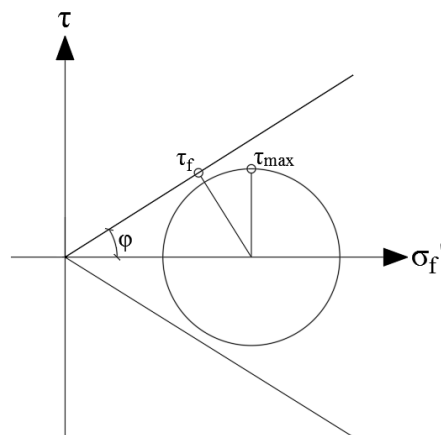


Figure 3.3: Mohr's circle drawn for a sand material. The circle lies within the failure surfaces which means that yielding of the material is not apparent. Furthermore, this tells that the angle of the slope is less than the angle of friction of the material.

Clay is considered undrained when a load is applied to the material in short term time scope, as a long term load would lead to drainage of the clay. In order to determine whether a material is in short term or long term equation 3.5 may be used as an approximation:

$$T = \frac{k \cdot C_c}{\gamma_w \cdot H^2} t \quad (3.5)$$

Where T is the time factor, k is the hydraulic conductivity of the material, C_c is the consolidation modulus, H is the distance of drainage, γ_w is the unit weight of the water and t is the time of the drainage of the material. As the function is logistical distributed the material will never be completely drained. Common practice states that drained condition and thereby long term is apparent for $T \geq 4$. Experience reveals that this number may be reduced to 2.[12]

3.1.1 Earth Pressure on a Retaining Wall

The distribution of the earth pressure acting on a wall depends on a series of variables:

- Depth
- Angle of the wall and ground levels
- Stress condition
- Density of soil
- Strength of soil
- Drainage conditions
- Assumption of movement

All variables influence the magnitude of the earth pressure and its distribution. However, an essential variable is the assumption of the movement of the construction. If a construction is said to not move, a *resting earth pressure* is present. The resting earth pressure is determined by the following:

$$\sigma_y = \gamma \cdot d + p \quad (3.6)$$

Where σ_y is the vertical principal stress component, γ is the soil density, d is the depth and p is the load on the ground surface. For an infinite soil element with a load the assumption is made, that the horizontal stress component is proportional to the vertical stress component for a resting earth pressure. Thus the following is obtained:

$$e_0 = \sigma_x = \sigma_y K_0 = (\gamma \cdot d + p) K_0 \quad (3.7)$$

Where K_0 is called the resting/initial earth pressure coefficient. The K coefficient is the ratio between the horizontal stress and the vertical stress and is a dimensionless empirical coefficient. An estimate for K_0 may be obtained from equation 3.8:

$$K_0 = 1 - \sin(\varphi) \tag{3.8}$$

For a retaining wall the assumption that no movement appears, is invalid. A retaining wall is assumed to move at failure and by this assumption the earth pressure is calculated. The goal is then to achieve stability of the construction in the assumed failure state.

The movement will redistribute the earth pressure and depending on the direction, active and passive sides are formulated for the wall which is given in figure 3.4a. A parallel movement of the wall will not cause redistribution of the vertical stress component, but it will change the horizontal. If the movement is away from the soil the horizontal stress component will decrease until a failure state is obtained in the soil. This is called an active earth pressure. An opposite movement yields the appearance of passive earth pressure which was first stated by Rankine in 1857. In figure 3.4b an illustration of the magnitude of an active and passive earth pressure is presented according to the wall displacement, u .

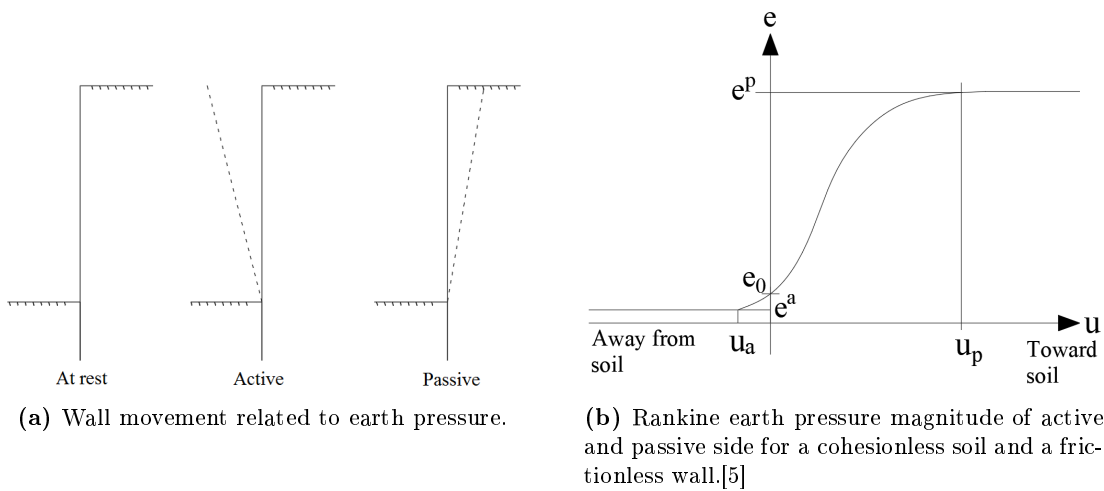


Figure 3.4: Earth pressure in active and passive state.

In chapter 4 it appears how the Rankine earth pressures were further evolved and utilised in later theories. The final earth pressure formula takes the aforementioned variables into account and may be compressed to one equation for the earth pressure:

$$e = e_\gamma + e_p + e_c = \gamma' d K_\gamma + p K_p + c K_c \tag{3.9}$$

Equation 3.9 is a result of three contributions that are illustrated in figure 3.5:[5]

- e_γ - Earth pressure as a result of the density of the soil
- e_p - Earth pressure as a result of surface load
- e_c - Earth pressure as a result of cohesion

Usually more of the contributions are apparent at once, as an excavation site is often designed having surface loads. The contributions are added together by superposition, and result in a non exact solution. The formula however, produces conservative values which are desired.

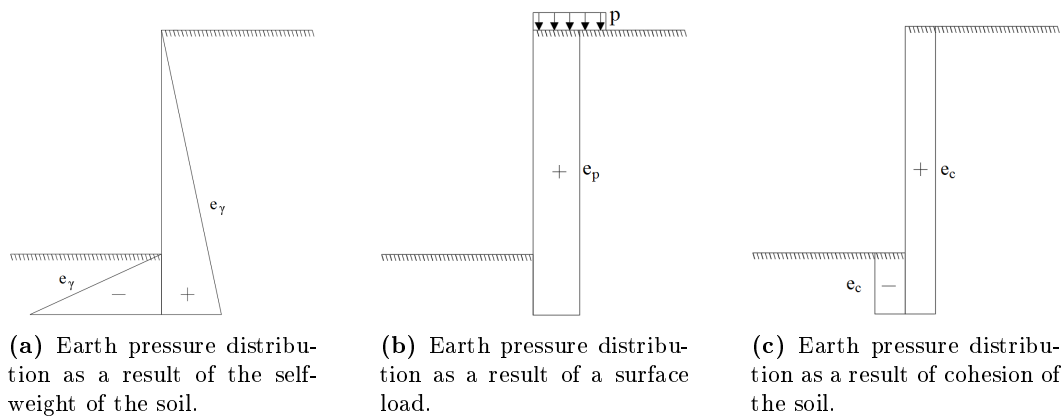


Figure 3.5: Distributions of the different earth pressure contributions.

3.1.2 Wall Friction

If the soil moves either upwards or downwards along a wall, a shear stress is apparent producing what is called wall friction which is denoted as follows:

$$\tau_w = e \cdot \tan(\delta) + a_w \quad (3.10)$$

Where τ_w is the shear component, δ is the wall friction angle and a_w is the adhesion along the wall. The wall friction angle is an important parameter when determining the magnitude of the earth pressure, as it influences the direction of the resulting earth pressure. Additionally, the wall friction is impacted by the strength of the soil, the friction properties between the wall and soil, the direction of the wall movement and the ability of the wall to obtain vertical loads. The general influence of the wall friction on the earth pressure will be further elaborated in chapter 4.

If the surface of a wall is considered *rough* - which is common for a wall surrounded by frictional soils - the wall friction angle is estimated equal to the friction angle of the soil, thus full transfer of forces between the soil and wall is apparent. However, a wall may also be considered *smooth*,

which refers to a wall situated in cohesive soils where $\delta = 0$. This is solely applicable in theory, as a wall is never completely smooth.[5][13]

3.1.3 Soil Stiffness

Stiffness of soil is a parameter which is difficult to quantify both by field- and laboratory tests. In order to test the soil, a test specimen has to be abducted for experimental purpose which introduces disturbances to the specimen that are inevitable. This leads to underestimation of the actual stiffness of a given domain.

Stiffness values are possible to determine by experiments, but often experience is the determining factor when decided on a specific stiffness. An easy, however expensive, method is the Triaxial Test which is elaborated in appendix A.6.2. In this test the modulus of elasticity can be derived directly by the use of local strain gauges.

For cohesive soils an estimate of the stiffness is given from C_c . This method allows for the use of a Field Vane Test which is a cheaper in situ solution for undrained cases. The method is presented in appendix A.6.5. The modulus of consolidation for cohesive soils is estimated from equation 3.11:

$$C_c \approx \frac{4000c_v}{w} \quad (3.11)$$

Where c_v is the vane shear stress, and w is the water content. As C_c is determined, the modulus of elasticity is estimated from:

$$C_c = \frac{E(1 - \nu)}{(1 + \nu)(1 - 2\nu)} \quad (3.12)$$

Where ν is Poisson's ration, and E is the modulus of elasticity for pressure tests.[14]

A third method is the Cone Penetration Test (CPT) which is similar to the Standard Penetration Test (SPT) which are elaborated in appendices A.6.3 and A.6.4 respectively. In a CPT the sleeve and tip resistance, by penetrating the soil, are found from which it is possible to derive the stiffness. This method is applicable for both cohesionless and cohesive soils.[15]

Experience shows that the stiffness in the soil tends to increase with increasing stress level for real soil behaviour.

3.2 Theory of Plasticity in Soils and Steel

In soil mechanics an idealisation of soil as a continuum is performed, meaning a soil element is subdivided indefinitely without altering its characteristics. This is necessary due to soil being a mixture of particles of varying content with pore spaces between these particles. By idealising a soil element as a continuum, this mixture is neglected, and approximations for further mathematical treatment of soil materials are possible.

When a soil element is exposed to a load of magnitude below its critical load, the soil is often said to be represented as an elastic material. This is, as mentioned, an approximation, thus a linear static analysis can be performed where Hooke's law is assumed valid, and the stress-strain relation can be found. However, when the soil is exposed to a load of higher magnitude, this linearity will vanish and a nonlinearity of the relation will occur. Typical stress-strain relations are seen in figure 3.6.

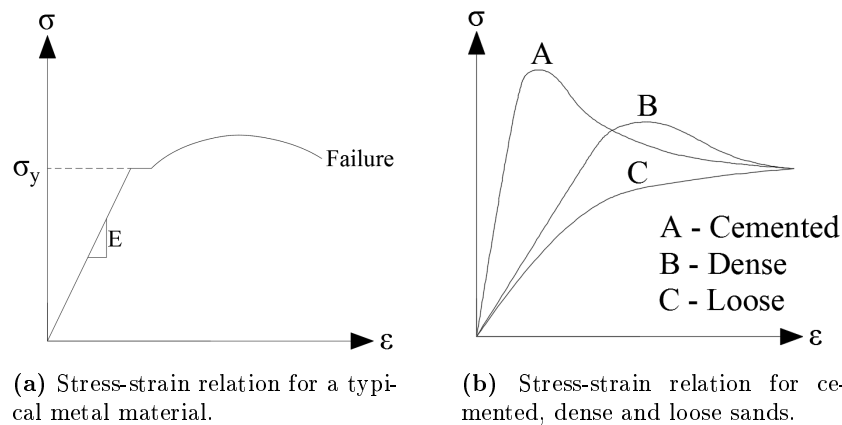


Figure 3.6: Stress-strain relation for steel and soil materials with various properties. Proportions of the relations are not comparable.

As the relations enter the nonlinearity, it is said to enter the plastic region, which means the strains will be irreversible and loading and unloading will cause a phenomenon called hardening. This is valid for metallic materials, but not for soils due to its complexity.[16]

3.2.1 Yield Criteria

A yield criterion is a set of mathematical conditions which describes the yielding behaviour for a given material. Each material behaves differently being exposed to a load, thus different criteria have been developed throughout time. In this section the different yield criteria will be elaborated which is used later in the analyses.

A yield criterion can be visualised as a function f equal to the components of stresses, as given in equation 3.13.

$$f(\sigma_{xx}, \sigma_{yy}, \sigma_{zz}, \tau_{xy}, \tau_{yx}, \tau_{zx}) = k \quad (3.13)$$

Where k is a constant. If the stress components are known, the yield surface can be visualised in the principal stress space, e.g. as shown in figure 3.7 for the Mohr-Coulomb yield criterion.

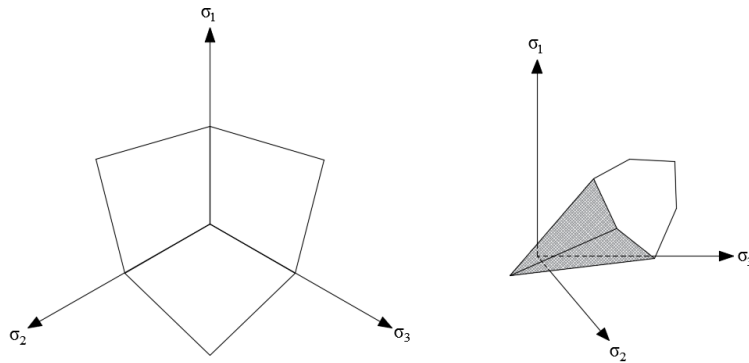


Figure 3.7: Mohr-Coulomb yield criterion in the deviatoric plane and principal stress space respectively.

A point in the principal stress space represents the state of the stress in the element called a stress point. If the stress state changes, the stress point will also change position. The line represent the yield surface, meaning if the stress point is inside the surfaces, the stress state is said to be in the elastic region. If the stress point is at the surface the stress state is in the plastic region and if outside, failure of the material has been reached, and the yield theory cannot be utilised further. The yield surface is described by the function $f = k$.

Mohr-Coulomb Yield Criterion

Figure 3.7 represents the Mohr-Coulomb yield criterion in the deviatoric plane and in the principal stress state respectively. The criterion could also be visualised in the meridian plane, as illustrated in figure 3.8. The Mohr-Coulomb failure criterion is given as:

$$\tau = c + \sigma \tan \varphi \quad (3.14)$$

The Mohr-Coulomb yield criterion is a modification of the Coulomb criterion which is given as:

$$\sigma = \sigma_0 + \tau \cdot \tan \varphi \quad (3.15)$$

Where σ_0 is the normal stress after failure, and φ is the friction angle of failing. The Mohr-Coulomb criterion is well fitted for sandy or drained clayey materials.

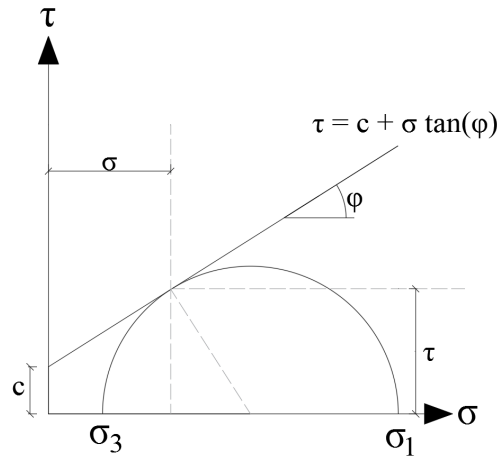


Figure 3.8: A representation of the Mohr-Coulomb yield criterion in the meridian plane.

Tresca Yield Criterion

In soils, undrained clay is quite a special case. It is possible to apply the Mohr-Coulomb failure criterion on this material, but the behaviour is better described using Tresca, where shearing is the critical state for the material. The Tresca criterion is given in equation 3.16:

$$\tau \geq \frac{1}{2}(\sigma_1 - \sigma_3) \quad (3.16)$$

For $\sigma_1 > \sigma_2 > \sigma_3$ where σ_i are the principal stresses. The failure surface encloses an infinite hexagon shaped cylinder, which is illustrated in figure 3.9.

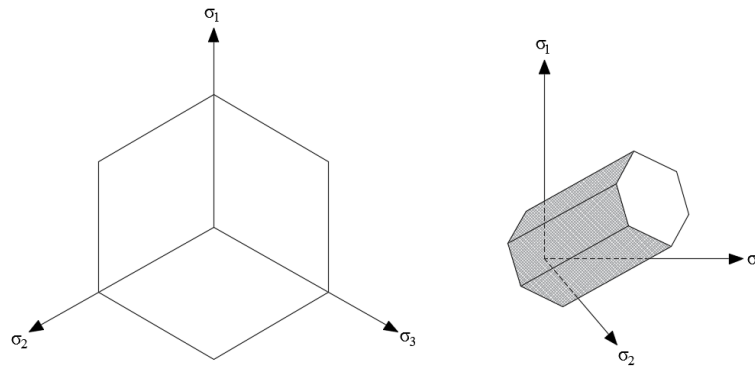


Figure 3.9: The Tresca yield criterion in the deviatoric plane and principal stress space respectively.

Tresca describes the undrained state of clay also called the short term state. In this state the strength of the clay is said to be equal in both tension and compression. An approximation of undrained clay is no change in the volume of the material due to a load, corresponding to incompressible state and $\nu = 0.5$.

The Tresca criterion is applicable in some cases for steel, as it states that a material has equal strength in tension and compression. However, experience reveals that von Mises criterion is a better approximation, due to the shear strength being less than the tension and compression strength for Tresca.

Von Mises Yield Criterion

The von Mises yield criterion is suitable for steel. In principal, the von Mises yield criterion could be applied to soil materials, but would result in significant deviations in comparison to experimental results. However, when applied to steel the theory and results are in agreement. The criterion is defined, as given in equation 3.17:

$$\sigma_v = \sqrt{\frac{1}{2} \left((\sigma_1 - \sigma_2)^2 + (\sigma_2 - \sigma_3)^2 + (\sigma_3 - \sigma_1)^2 \right)} \quad (3.17)$$

The failure surface is illustrated in figure 3.10, which reveals great similarities to the Tresca criterion. In fact the only difference between the criteria is von Mises representing a circle in the deviatoric plane where Tresca represents a hexagon. Thus the shear strength according to von Mises criterion being equal to the tension/compression strength, which is not the case for Tresca as mentioned.

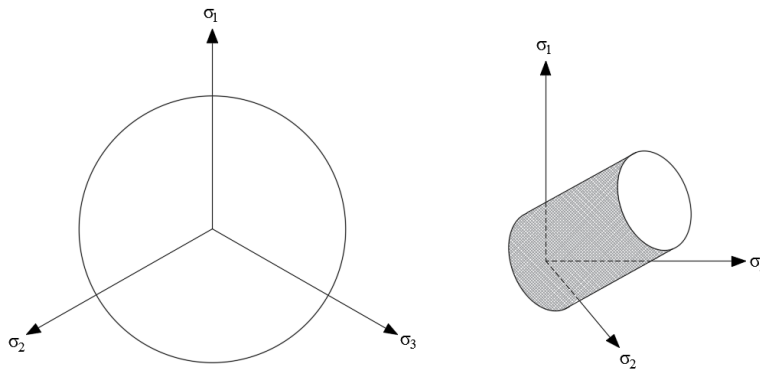


Figure 3.10: Von Mises yield criterion in the deviatoric plane and principal stress space respectively.

3.2.2 Flow Rules

The term *plastic flow* refers to the deformation following yielding, thus *flow rule* refers to the general concept of the behaviour of a material as an element being exposed to a load. Plastic flow then only concerns the plastic region and is valid when the deformations are irreversible. When describing plastic flow the constitutive relationship (stress-strain) is derived linking the *plastic strain rate* to the stress state. In soil materials there is an unknown amount of plastic deformation already locked inside the material, thus the constitutive relationship may lead to inaccurate results caused by a lack of knowledge concerning the load history. Therefore the

plastic strain rate is used instead to avoid the issue of irreversibility. Further, knowledge about what happens as a stress point reaches the yield surface is also of interest.[17]

Normality

Examining figure 3.11 the term normality can be explained. The yield surface will expand, if the stress point is exceeding the yield point in the direction of the vector, \mathbf{v} . \mathbf{v} is normal to the yield surface, and this idea of 'normality' is quite important. The normality condition is defined by an *associated flow rule* which is given in equation 3.18. Associated flow rule describes the behaviour of isotropic materials beyond yielding.

$$d\boldsymbol{\varepsilon}^p = \lambda \frac{\partial f}{\partial \boldsymbol{\sigma}} \quad (3.18)$$

Where f denotes the yield condition and λ is a positive multiplier. The word *associated* refers to the fact that the plastic strains are associated to the yield surface, and equation 3.18 ensures that the plastic strains will be normal to the yield surface, f . Due to λ being a multiplier the magnitude of the plastic strain rates are not directly specified, unless more information is given.

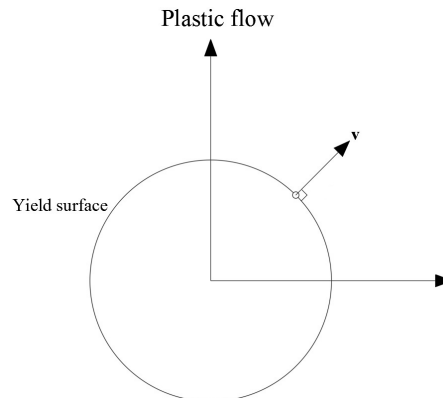


Figure 3.11: Example of normality for a yield surface.

Soil materials usually do not behave as stated by the associated flow rule. In contrary, the plastic flow will always be dilational which will be explained in section 3.2.3. For non-associated flow the normality conditions are not valid.

Non-associated flow

Experiments considering soil materials have shown that smaller values for the rate of dilation are obtained from experiments compared to the theory. This is a result of several factors depending on the type of soil. During shearing some types of soil experience compaction rather than dilation, some types have no volumetric strain and for dilating soils, the rate of dilation is

usually not as large, as given by the associated flow theory. The non-associated flow is defined in equation 3.19 and has similarities to the mathematical formula for associated flow:

$$d\boldsymbol{\varepsilon}^p = \lambda \frac{\partial g}{\partial \boldsymbol{\sigma}} \quad (3.19)$$

The yield function, f , is replaced by *plastic potential* function, g . If $g = f$, the associated flow rule is obtained, but for $f \neq g$ non-associated flow occurs. This means the plastic strain rates will not be normal to the yield surface as shown in figure 3.12.

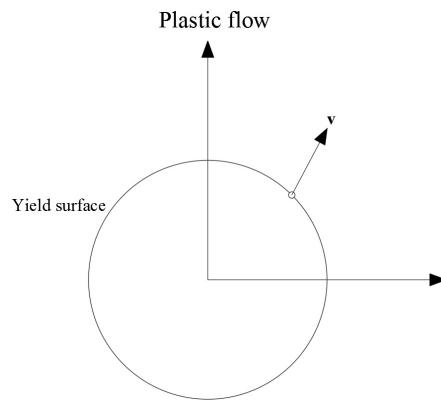


Figure 3.12: Non-associated flow not being normal to the yield surface.

Non-associated flow has more disadvantages in regards to applications, but the issue concerning dilation can be rectified. Often a non-associated material is 'converted' into an associated material in order to simplify calculations. This type of conversion does not take the dilation into account, but it appears that the dilation has influence, which will be briefly discussed in section 3.2.3.[17]

3.2.3 Angle of Dilation

Dilation is the indication of the rate which an elements volume is changing during shearing. For positive dilation the element lid is moving upward, thus the element is increasing in volume (dilating). If the dilation is negative the lid is moving downward, thus the volume of the element is reduced (compression or contracting). The dilation angle, ψ , is illustrated in figure 3.13.

When a material is increasing in volume subjected to a load, the shear strength of the material will weaken as the density of the element will decrease, as soil is a particular material. In equilibrium the particle mixtures have a specific arrangement of packing. When exposed to shearing, denser packing may happen before steady shearing occurs. This phenomenon is illustrated in figure 3.14.

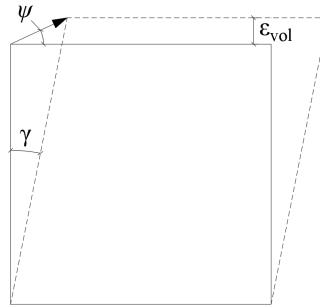


Figure 3.13: Angle of dilation.

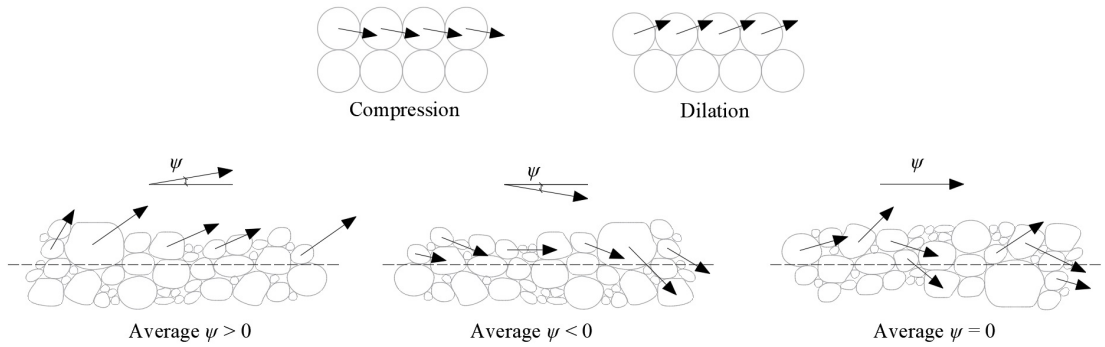


Figure 3.14: Arrangement of particles subjected to volume change.[18]

As shown in figure 3.14 dilation is described by an *angle of dilation*. The angle is assumed to be constant during plastic straining. The angle of dilation is given in equation 3.20:

$$\psi = \tan^{-1} \left(\frac{dy}{dx} \right) \quad (3.20)$$

By considering the change in strain, equation 3.20 may be rewritten:

$$\tan(\psi) = \frac{d\varepsilon_{vol}}{d\gamma} \quad (3.21)$$

Equation 3.21 is only an approximation which is given in figure 3.15.

Each granular material has a characteristic angle of dilation. Several 'rules of thumb' exist for the angle of dilation. If the angle is equal to zero, it corresponds to the volume not changing being exposed to shearing. This is characteristic for clay materials which either has a very low angle or none. For cohesionless materials, like sand and gravel, where the frictional angle is greater than 30°, the dilation angle is estimated by the equation 3.22:

$$\psi = \varphi - 30^\circ \quad (3.22)$$

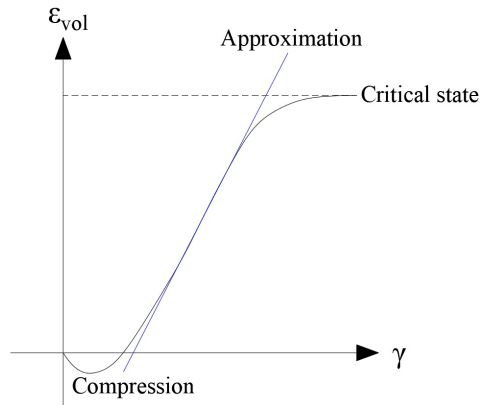


Figure 3.15: Dilation caption.

It is important to note, that equation 3.22 only produces approximate values which is in agreement with experimental results. As mentioned in section 3.2.2, non-associated plasticity theory may be difficult to apply in a model, thus a conversion to the associated region may be of interest. A modified frictional angle obeying the associated plasticity theory can be found by using equation 3.23:

$$\tan(\varphi_{reduced}) = \frac{\sin(\varphi)\cos(\psi)}{1 - \sin(\varphi)\sin(\psi)} \quad (3.23)$$

Equation 3.23 is an approximation and it appears that $\psi \geq 0$ at all times. The modified frictional angle is dependent on the angle of dilation and the non-associated frictional angle. The modified angle of friction is reduced which is shown in figure 3.16.

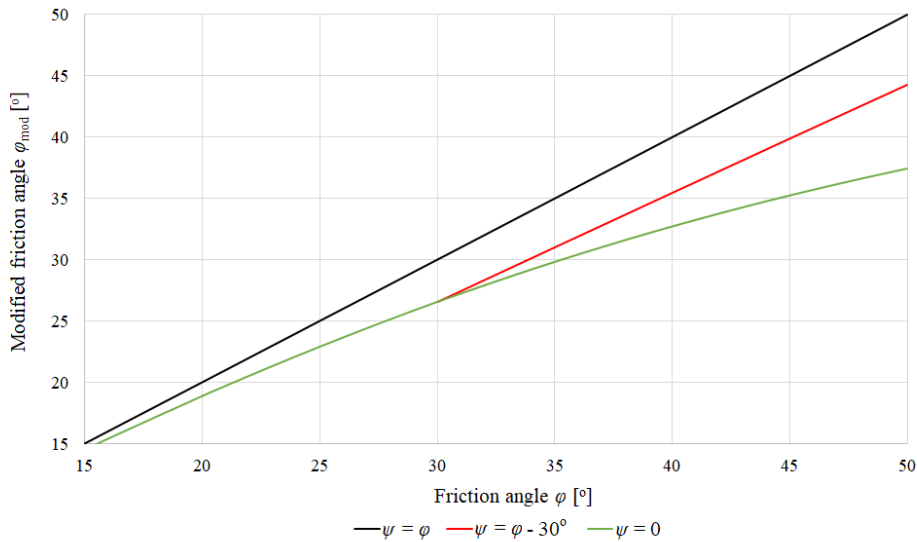


Figure 3.16: Dependency between the friction angle and the angle of dilation.[19]

Three different examples are illustrated in figure 3.16 showing the approximated values. It appears that for the modified frictional angle, the angle of dilation is above zero and is less than the unmodified version. Thus a dependency is valid between the frictional angle and the dilation angle.[18][20]

3.2.4 Lower and Upper Bound Theorems

The theory of plasticity may be applied to predict approximate values for the collapse load in an extensive range of applications. This is utilised in the two theorems of lower and upper bound, where the usage is often referred to as a limit analysis. The collapse load theorems must not be confused with the yielding theorems, as they are not concerning elastic strains or plastic flow, but related to the collapse load. However, in some cases they will be the same thus yielding will immediately lead to collapse. In other cases, yielding will occur before any sign of collapse will happen. Application of both bound theorems has restrictions, as they do not comply to non-associated flow rules. However, they can be used for soils, but in a restricted form.

Lower Bound Theorem

"Collapse will not occur if any state of stress can be found that satisfies the equation of equilibrium and the traction boundary conditions and is everywhere 'below yield'."

(e.g. R.O. Davis & A.P.S. Selvadurai, Plasticity and Geomechanics, 2002, pp. 111)

Upper Bound Theorem

"Collapse must occur if, for any compatible plastic deformation, the rate of working of the external forces on the body equals or exceeds the rate of internal energy dissipation."

(e.g. R.O. Davis & A.P.S. Selvadurai, Plasticity and Geomechanics, 2002, pp. 111)

A lower bound solution will in general provide a value lower than the *exact* value. In contrary an upper bound will provide a higher value. If both theorems are applied, the exact solution will be in the interval of the lower and upper bound solutions.[17]

The theorems are also applicable to the calculations of plates consisting of steel or isotropic reinforced concrete which will be investigated further in section 3.4, where the theory of yield lines is evaluated. The theory of lower and upper bounds has been further elaborated in appendix A.7.1.

3.3 Failure Theory in Soils

As stated in section 3.1 most soil materials comply to the Mohr-Coulomb yield criterion, which is shown in figure 3.2. This theory will estimate when the materials will yield and thereby fail, but not how the soil domain will fail.

In the following, failure of a retaining wall will be evaluated in order to construct a base for chapter 4 concerning the different earth pressure calculation methods. Regarding the stability of the wall, two conditions appear, which have to be fulfilled:

- Static conditions
- Kinematic conditions

In order to fulfill the static conditions the failure criteria must be met in any point of the failure surface. The procedure is to determine the stress state in the failure surface by equilibrium and the failure criteria. Any boundary conditions including friction and earth pressure must be evaluated likewise. A solution based on the static conditions is a lower bound solution.

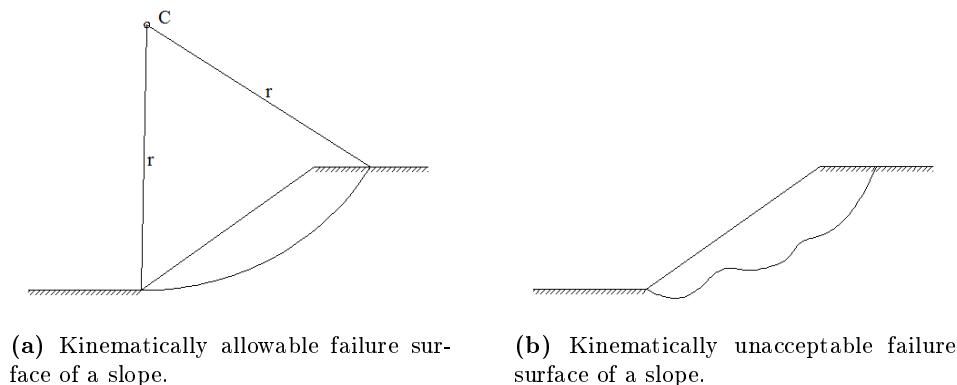


Figure 3.17: Failure surfaces.

The kinematic conditions are fulfilled, if the failure of the wall comply to the governing equations, as a kinematic allowable solution cannot be obtained from equilibrium. Failure fulfilling the conditions often follows a single failure surface, as shown in figure 3.17a. These are only fulfilled if the surface of the body in failure is continuous and follows a specific geometry. This means that the surfaces of the failure body and the soil not in failure must touch at any point and not contain interruptions such as bulges or dents which is the case in figure 3.17b.

The failure surface may take on different forms. In this context it is relevant to consider the flow rules of plasticity, mentioned in section 3.2. The failure surface complying to associated flow rule only has the opportunity of following a straight line or a circle as shown in figure 3.18.

An alternative to the circle failure is the logarithmic spiral failure that during empirical results is shown to be a more realistic representation of the actual failure for non-associated materials.

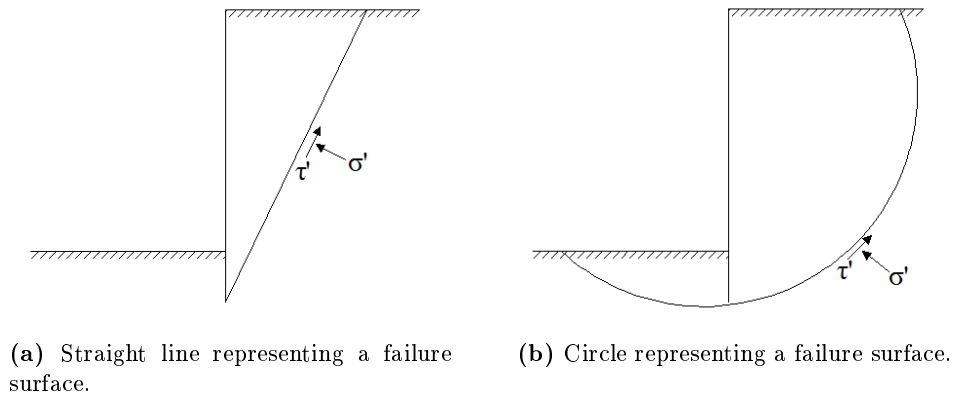


Figure 3.18: Kinematically allowable failure surfaces following associated flow rule.

This failure surface however, is only kinematically allowable for $\psi \neq 0$, if the body of soil in failure is enlarged equivalent to the requirements for the logarithmic spiral. In practice the expansion does not meet the requirements, but is still considered a proper approximation for a kinematically allowable failure surface. An example is shown in figure 3.19.[5]

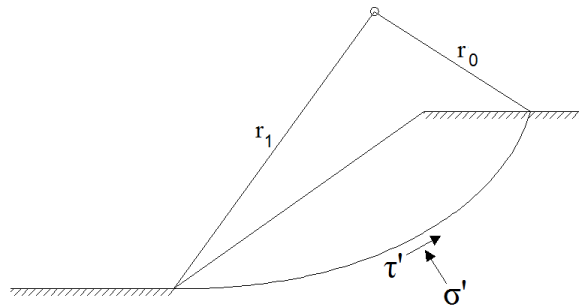


Figure 3.19: Logarithmic spiral failure.

A solution based on the kinematic conditions produces an upper bound solution.

Any of the illustrations in this section represent slip line failures where a failure surface separates two stiff bodies of soil. The soil may also be assumed to fail in zones where the whole separated body of soil will experience deformations.

3.4 Yield Lines in Steel Plates

For most numerical failure analyses a threshold value is usually set which marks either yielding or collapse if exceeded. For linear elastic analyses the threshold will usually be equal to the yield strength. For nonlinear analyses the threshold may be an more or less indefinite parameter to determine. It is clear that for a material subjected to a dynamic repeating load the appearance of fractures may cause failure of the material, given that the fracture is growing towards a critical

state. In these fatigue limit state analyses (FLS), stresses exceeding the tensile strength are critical, even in the outer fibers of the cross section. However as ULS analyses are performed, the formation of cracks may not be fatal e.g. for a sheet pile, as the ultimate load is only applied once and not repeated.

In such cases the theory of yield lines may be applied in order to determine, if an excess of the tensile stress is fatal. Yield line theory will therefore be applied to the failure analyses of the sheet pile configuration in this project, which will be discussed in section 5.4.

3.4.1 Yield Line Theory

Especially for reinforced concrete beams and plates, the statement of the appearance of fractures not being fatal is logical, as fractures form due to tension, but typically wont lead to failure. In these cases yield line theory is used to determine the bending capacity of the elements.

The theory relies on the formation of yielding hinges that will also be used in section 4.1, which is a result of the rearrangement of stresses in a yielding cross section.

In the theory of plasticity the yielding hinge is idealised to a point or line connecting two non deforming stiff segments not considering elastic deformations. The deformations regarding yielding may approach infinity which does not make any logical sense considering the physics. The rotational capacity is therefore introduced which is a measure of the allowable deformations of a yielding hinge before the introduction of failing strains.[21]

The lower bound and upper bound theorems are applicable to the calculations of the load capacity of a plate or beam by the use of the yield line theory. The exact value for the yielding force will be in the span of these two values. In practice an infinite amount of yielding mechanism exists and theoretically any must be evaluated in order to determine the strength of an element. However, it is possible due to experience to reduce this to a few cases. The precision of the estimated mechanism is insignificant being close to the worst case, as changes in moment capacity are relatively small near this case.

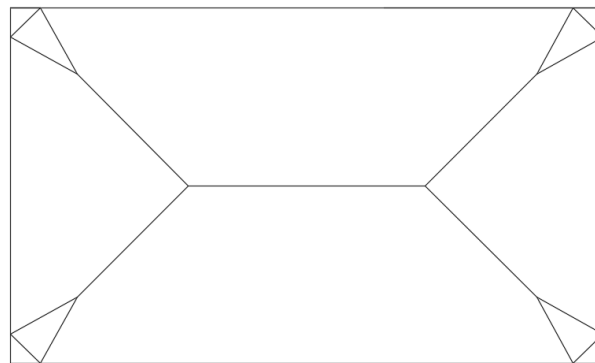


Figure 3.20: A yielding mechanism of a plate having corner levers.

It is known that the inclusion of corner effect and corner levers in a yielding mechanism, pictured in figure 3.20, will lead to a reduced capacity of a plate. Corner levers may occur, if the anchoring of the corners is inappropriate. The development of corner levers can be predicted from the boundary conditions of the plate. Due to the complexity of the analytical approach the corner effect is usually not included in the determination of the failure mechanism. However, a calculation including this will be performed in appendix A.7.3 in order to illustrate the error occurring by exclusion.

3.5 Membrane Effect in a Plate

Applying yield line theory as the capacity of beams or plates are determined, changes in the geometry until the development of the yielding mechanism are neglected for stiff plastic materials, which is assumed in section 3.4. However for plates, considerable deformations occur due to stresses even beneath the yielding capacity. In practice these deformations are significant to the bending capacity, and the phenomenon is called *catenary actions* for beams and *tensile membrane actions* for plates.[21]

For small deflections compressive membrane effect or the so-called dome effect is dominant, and for large deflections the tensile membrane effect dominates. The configuration of the boundaries is essential to the scale of the effect. The elements must be fixed against displacements in its longitudinal direction in order for the actions to appear, as additional tension will increase the capacity.[22]

For plates the total capacity can be written, as in equation 3.24 by inclusion of the tensile membrane actions:

$$p = p_j + p_m \tag{3.24}$$

Where p_j is the capacity obtained from K.W. Johansen's yield line theory, and p_m is the contribution of the tensile membrane actions.

Section 5.5 will include a study of the scale of the effect when the capacity of a sheet pile is determined numerically.

Applied Analytical Theory of Sheet Pile Wall Calculations

In this chapter an introduction to the calculation of sheet piles is apparent. It will appear that in Denmark Brinch Hansens theory is commonly used and this procedure differs to other methods used around the world. A small variety of these analytical approaches is investigated and compared to a numerical method.

4.1 Calculation of a Sheet Pile Wall in Denmark

In Denmark the most commonly recognised method for designing a sheet pile wall is by application of the Brinch Hansen earth pressure theory, as this is a relatively simple method. The theory is approximated such that the failure will follow a realistic pattern. In this method the height of the wall is found which yields a necessary anchor force and a plate moment ensuring stability.

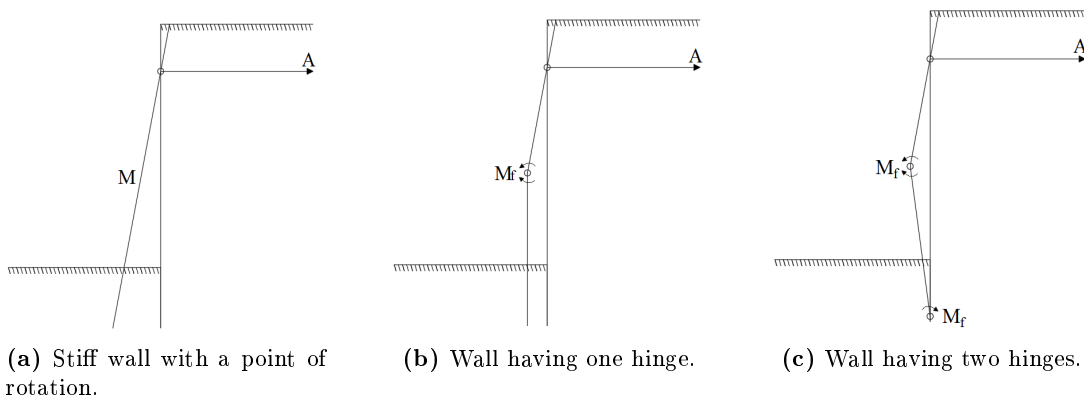


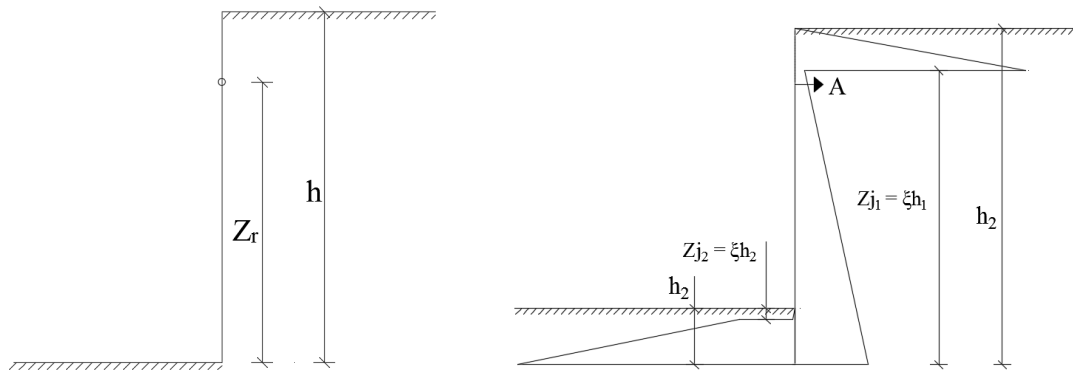
Figure 4.1: Possible failure modes of an anchored sheet pile wall, as claimed by Brinch Hansen.[5]

The wall is able to fail by different modes according to the theory, which is illustrated in figure 4.1. If the wall is properly designed to fail following one of the modes, it will always fail by this mode. Which mode is most favourable to estimate depends on the possibilities regarding installation depth, choice of anchor and choice of profile. Where all these factors are not predetermined all the modes may be evaluated in order to minimise costs in the specific case.

The theory relies on an initially estimated total height of the wall which is then calibrated. The height is used to establish the relative point of rotation, ρ :

$$\rho_i = \frac{z_r}{h_i} \tag{4.1}$$

Where z_r defines the distance from the foot of the wall to the attachment point of the anchor, as shown in figure 4.2a. As ρ is found, the earth pressure coefficients, K , presented in section 3.1.1 are determined as well as, ξ , which may be read from related diagrams based on experiments. The physical meaning of ξ is pictured in figure 4.2b.



(a) Position of the point of rotation.

(b) Example of an earth pressure distribution as claimed by Brinch Hansen having a point of rotation in the level of the anchor and no yielding hinges. Pressure changes appear both on the active and passive side.[5]

Figure 4.2: Necessary parameters in the calculation of the earth pressure using Brinch Hansens theory.

When determining the earth pressure coefficients, the roughness of the surface of the wall has great influence. The theory only handles an absolutely smooth or rough wall. From ξ , the height of the pressure change, Z_j , is determined in equation 4.2:[5]

$$Z_j = \xi \cdot h \tag{4.2}$$

The earth pressures are calculated by:

$$e^x = \gamma' d K_\gamma^x + p K_p^x + c K_c^x \quad (4.3)$$

$$e^y = \gamma' d K_\gamma^y + p K_p^y + c K_c^y \quad (4.4)$$

Where e^x is the pressure beyond the pressure change and e^y is the pressure below. The scale of the earth pressure coefficients, K , are defined by the rotation of the wall which yields either passive or active earth pressure.

Evaluation of moment equilibrium will determine the stability of the chosen wall height. Calibration formulas are applied in order to calibrate the height to ensure stability. When a retaining wall is placed in soil consisting of different strata, additional pressure changes appears, as the properties of the soil changes.

The method relies on associated flow rule theory, as the failure surfaces do not allow for dilation and therefore are not kinematically allowable in case of frictional soils. This seems to be in contrast to the fact that the failure surface is approximated to reflect a real failure. A failure following Brinch Hansen is shown in figure 4.3. As illustrated the failure surface has not the appearance of a straight line or circle. However Brinch Hansen formulated the failure surface as a combined failure consisting of multiple circles resulting in a rather characteristic development.

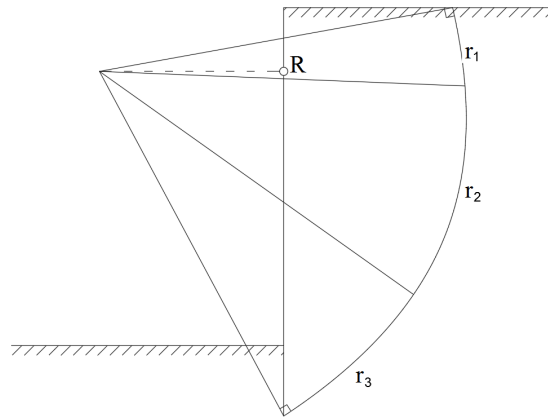


Figure 4.3: A failure surface composed of multiple circle fragments each having unique radii, r_i . R defines the point of rotation which in this case is placed high. In case of a relative low placement of the point of rotation, the failure will be a combined failure consisting of a failure surface as well as a zone failure.

The method has a series of limitations. Equilibrium has to be fulfilled horizontally, but the theory does not require vertically equilibrium. The vertical forces are neglected from the calculations, which may lead to improper design.

Another drawback of the method is the modeling of the soil strata in the back side. The issue rises, as a stratum of low strength has a overlying stratum having greater strength properties. The failure line of the soil may cross the stratum boundaries and the theory claims that the

properties utilised inside the failure zone are the properties corresponding to the overlying stratum. As this stratum has greater strength, this yields a non-conservative consideration of the actual behaviour. The issue is illustrated in figure 4.4. The theory does not handle skew strata either, which may lead to inappropriate approximations.

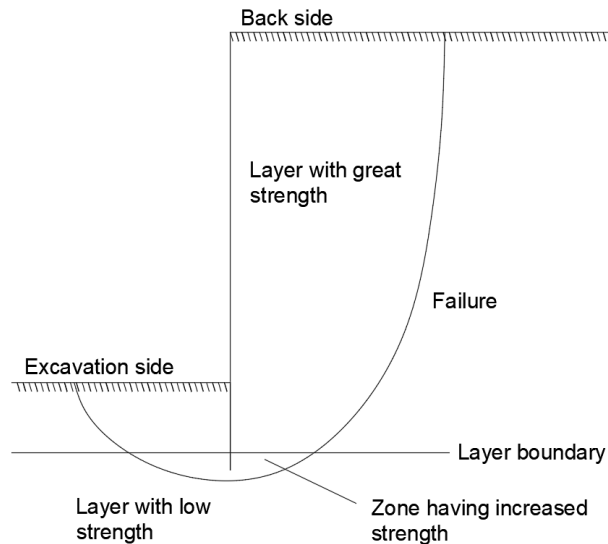


Figure 4.4: Non-conservative issue regarding modeling of strata. A stratum having less strength than the overlying will lead to increased strength compared to the actual case.

4.2 Calculation of a Sheet Pile Wall in Germany

The German standard for calculation of a sheet pile wall is well recognised. The standards of consideration are DIN 1054 and DIN 4085.

According to the German standard the earth pressure can be calculated directly from the effective density of the soil, surface loads and cohesion, as Brinch Hansen prescribed using earth pressure coefficients. The classically earth pressure from the self-weight of the soil is shown in figure 4.5. However, when an anchor is installed, the resulting change in pressure is given differently.[8]

According to recommendations based on numerous field tests, the pressure may be redistributed, if the retaining wall is either propped or anchored. The redistribution of the earth pressure may be performed as illustrated in figure 4.6. This will lead to a more favourable distribution of the pressure, which may then lead to smaller profiles.[23]

The calculations of the retaining wall is initiated by estimating an embedment depth. The required depth is found by moment equilibrium about the anchor. This is performed by iteration as for the theory of Brinch Hansen.

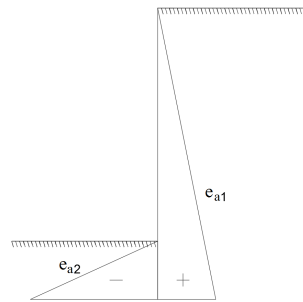


Figure 4.5: Classically earth pressure on a retaining wall, where only the self-weight contribution is apparent.

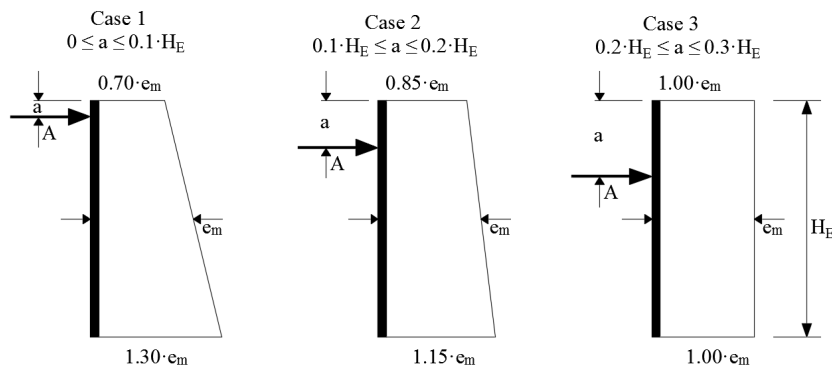


Figure 4.6: Redistribution of earth pressure according to recommendations. e_m is taken as the mean value of the earth pressure on the back side of the wall from the top point to the level of excavation.[23]

The wall according to German standards has to fulfill equilibrium - both horizontally and vertically. The anchor force for anchored retaining walls is a result of P_G and P_Q , which are obtained from the actions on the retaining wall by equilibrium. G corresponds to the self-weight of the soil and Q is the reaction force in the lower failure slip surface. The reaction force depends on the frictional angle of the soil and the angle of the anchor, as shown in figure 4.7. The anchor force which the soil allows, R_A , is found by equilibrium.[23]

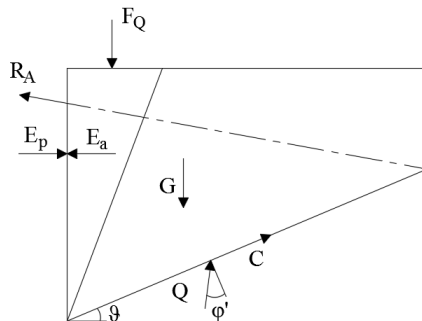


Figure 4.7: Force diagram of forces acting on the slip body used to determined the allowable anchor reaction.[24]

In figure 4.7 a number of forces appear:

- G is the self-weight of the soil, as mentioned
- F_Q is the surface load
- E_a and E_p are the active and passive earth pressure respectively
- C is the the cohesive force which is calculated as:

$$C = c' \cdot L \tag{4.5}$$

Where c' is the effective cohesion, and L is the slip surface length which depends on the angle of planar slip, ϑ

- Q is the reaction force, as mentioned
- R_A is the allowable anchor force

It has been found that the procedure is identical to the method described in the British standards. However the definition of the roughness of the wall differs. The wall can not be considered as completely rough in the German standards which in contrary is possible according to British Standard, BS 8002.

4.3 Calculation of a Sheet Pile Wall by KSP

Brinch Hansens earth pressure theory was published in 1953. Since then it has been used despite having flaws regarding distribution of earth pressure and neglecting vertical equilibrium of the wall. In 1992 the method of KSP (Kinematically and Statically Plausible calculations) was formulated which is the foundation of an alternative method.

The theory is called plausible, as a number of conditions which must be fulfilled are not completely fulfilled:

- Equilibrium
- Compatibility
- Stress-strain relation must be known and fulfill the chosen physical conditions

As the conditions are not completely fulfilled the calculations are only considered kinematically and statically plausible and therefore not allowable. The method relies on the theory of logarithmic spiral failure. The minimum and maximum plausible earth pressures are obtained from the classically earth pressure calculation and the movement of the wall.[25]

In order to calculate the earth pressure according to KSP some assumptions have to be made:

- All materials obey the Mohr-Coulomb yield criterion
- Every stratum boundary are known
- The parameters are constant within every stratum
- The soil is considered as a continuum
- Tension in the soil is allowed

In theory KSP require an infinite amount of calculations, as the wall is partitioned into pieces, and infinite different spirals can be drawn for each point separating the elements. However, due to experience a great number of these may be excluded from the calculations. The variation of the resulting earth pressure acting on an element is then either assumed constant over this element or the variation is found for each element. For every element a maximum and minimum value is found. A plausible earth pressure is then e if $e_{max} \geq e \geq e_{min}$, as equilibrium is fulfilled for any spiral. e_{max} and e_{min} correspond to the classically passive and active soil pressure respectively.

The calculation of the earth pressure distribution is partitioned in three phases:

- Phase 1 - Unit earth pressures are determined corresponding to classically slip failure
- Phase 2 - Unit earth pressures are determined corresponding to a simply supported anchored wall
- Phase 3 - Unit earth pressures are determined corresponding to a fully fixed wall

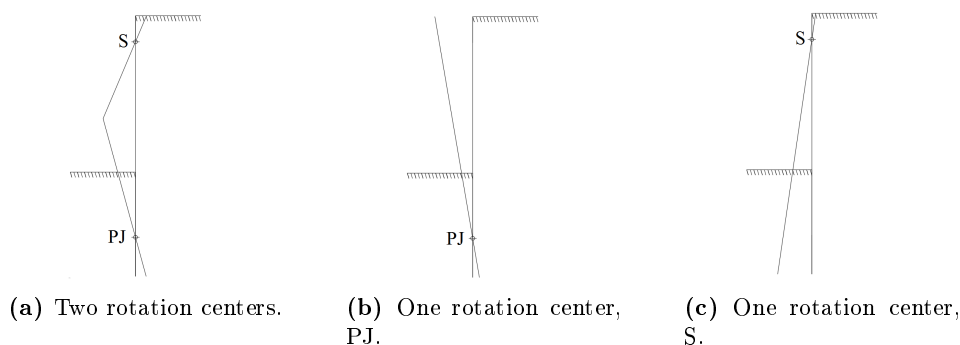


Figure 4.8: Failure with one or two rotation centers, S and PJ. Picture courtesy of DGF.[25]

The movement of the retaining wall and thereby the failure is determined from the assumptions made regarding the rotation of the wall which is based on the supports of the wall. In general 3 different failures of the retaining wall are allowed in the calculations of KSP which are shown in figure 4.8. From the figure it yields that:

- If PJ is placed below the embedment depth, the wall is considered simply supported
- If PJ is placed above the embedment depth, the wall is considered fully fixed

The placement of the points, S and PJ , has great influence on the determining of the earth pressure distribution, as these will lead to changes in pressure in the distribution. Above S the earth pressure is considered passive on the back side of the wall and below PJ the earth pressure is considered active on the excavation side of the wall.

The unit earth pressures, e , have to be calculated corresponding to a completely rough and smooth wall, as formulated in equation 4.6:

$$e = e_s + A(e_r - e_s) \quad (4.6)$$

Where e_r and e_s are the earth pressure in a given point corresponding to completely rough and smooth wall respectively. A is an interpolation factor for the friction which is a result of roughness factors. However, above S and below PJ the wall must always be considered as completely smooth.[25]

As only a simply supported retaining wall is considered, only phases 1 and 2 will be evaluated. A redistribution of the earth pressures is apparent according to figure 4.9, where the γ -case is considered.

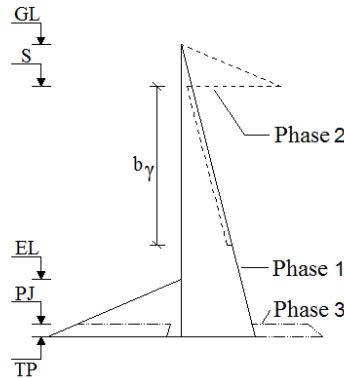


Figure 4.9: Earth pressure distribution corresponding to the three mentioned phases for the γ -case.

From figure 4.9 it is apparent that b_γ describes the distance from the point of rotation to the depth of redistributed earth pressure. The variable is found as:

$$\frac{a + b_\gamma}{a} = 10 \tan(\varphi) \quad (4.7)$$

Where a is the distance between the surface of the back side and the point of rotation, S . The pressure reduction corresponds to Δe_γ which is apparent along the distance b_γ . Δe_γ is found in the level of the rotation center, S , and is given in equation 4.8:

$$\Delta e_\gamma = 0.2\sigma_a \quad (4.8)$$

Where:

$$\sigma_a = \gamma'z \quad (4.9)$$

According to KSP calculations pressure reduction will only be applied, if S is positioned under the surface of the back side, and if a weak stratum is placed above a stronger. In theory, KSP is a better alternative to the method of Brinch Hansen, but is still not complete, as pressure reduction is not corrected for weak strata laying below a stronger as mentioned.

Design

The design of the wall is initiated by estimating a vertical anchor force from the resulting unit earth pressures in the toe of the wall, TP , which is used to estimate the embedment depth by vertical equilibrium. In order to determine the horizontal anchor force component, A_h , moment equilibrium must be evaluated about the toe of the wall, as equation 4.10 states:

$$A_h = \frac{M_{TP}}{zA - TP} \quad (4.10)$$

Where zA is the distance between the level of the anchor and the excavation level, M_{TP} is the moment about the toe of the wall and TP is the embedment depth.

The final embedment depth is found iterative by calculating the reaction force in the toe point which is needed to fulfill horizontal equilibrium by equation 4.11. As the embedment depth is the only changeable variable, this is modified until the reaction is equal to 0:

$$R = \frac{M_{TP}}{zA - TP} - Q_{TP} \quad (4.11)$$

Where Q_{TP} is the resultant of the horizontal forces acting on the wall.

4.4 Calculation of a Sheet Pile Wall by Finite Element Method

As the design of the sheet pile wall is performed according to the FEM, OptumG2 is used. OptumG2 is a numerical geotechnical software used for analyses of stability and deformation issues. The calculations in the software are performed under the assumption of plain strain, as OptumG2 is a 2D software. The numerical calculations in this section are used for comparative reasons.

It is possible to perform a wide range of analyses in OptumG2. For the analyses in this chapter Strength Reduction analysis will be utilised. The strength reduction analysis relies on reduction of certain parameters of either the soil or the structural elements for a given setup until the optimal magnitude is obtained. A reduction factor (RF) is found which is the maximal reduction required to ensure stability. A reduction factor greater than 1 yields a stable configuration and below 1 yields an unstable configuration.

It is not possible by this type of analysis to evaluate both the soil and structural components simultaneously. As the reduction of the soil parameters is determined, the parameters of the structural elements are fixed and likewise when the reduction of the structural components are determined. The soil parameters reduced for Mohr-Coulomb materials are c and $\tan\varphi$. Reduction of the structural parameters only counts the plastic yield moment of the wall for the retaining walls. The reductions are given in equations 4.12 and 4.13 respectively:[19]

$$RF_{soil} = \frac{c}{c_{red}} = \frac{\tan\varphi}{\tan\varphi_{red}} \quad (4.12)$$

$$RF_{structural} = \frac{m_p}{m_{p,red}} \quad (4.13)$$

Where m_p is the plastic yield moment which is an important factor for excavations supported a sheet pile wall.

The analysis does not lead to an absolute solution, but relies on the principles of lower and upper bounds given in section 3.2.4. The span of the interval depends on the appearance and refinement of the mesh. A narrow difference between the values corresponding to the bounds, yields a sufficient representation. Regarding the type of flow rule the strength reduction analysis is strictly limited to associated flow rule.[19]

The elements used by OptumG2 in the bounds analyses are given in figure 4.10.

In numerical analyses the mesh is essential to the results obtained. It is clear that a finer mesh leads to better results. This is illustrated in figure 4.11, where the results from the lower and upper bound analyses are given. The refinement of the mesh is the only changeable variable.

4.4. Calculation of a Sheet Pile Wall by Finite Element Method

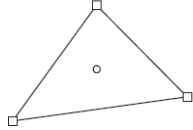
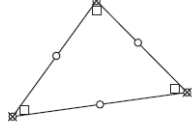
| | |
|---|--|
|  | <p>Lower</p> <p>Linear interpolation of stresses. Statically admissible stress discontinuities are included between elements.</p> <p>Notes: This element produces rigorous lower bounds on the collapse load. The displacements are constant within each element.</p> |
|  | <p>Upper</p> <p>Quadratic interpolation of displacements and linear interpolation of stresses. The B matrix is integrated using the triangle vertices.</p> <p>Notes: This element produces rigorous upper bounds on the collapse load. The displacements are continuous between elements.</p> |

Figure 4.10: Type of elements used estimating the lower and upper bounds.[26]

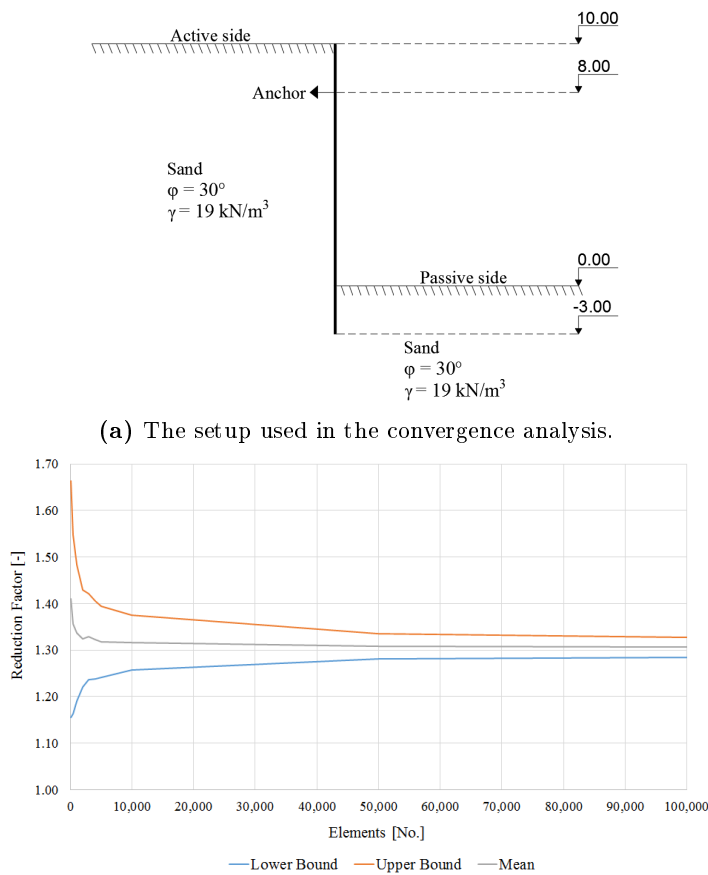


Figure 4.11: Convergence analysis. A completely uniform mesh used throughout the analysis.

As figure 4.11 reveals an inappropriate fine mesh is needed in order to obtain converging results. However, the possibility of incorporating adaptive mesh is apparent in OptumG2. This feature rearranges the mesh in order generate a fine mesh in areas of interest and a coarse mesh where

the refinement is insignificant. By the use of adaptive mesh, precise results are obtained using relative few elements, as given in table 4.1 which leads to a decrease in computational time.

Table 4.1: Bounds using a uniform mesh with a large number of elements and a adaptive mesh having few elements. 3 adaptive iterations are used.

| Mesh | No. elements | RF - Lower bound | RF - Upper bound |
|----------|--------------|------------------|------------------|
| Uniform | 100,000 | 1.285 | 1.328 |
| Adaptive | 5,000 | 1.288 | 1.310 |

Calculations

The calculations of the sheet pile wall using the FEM is carried out by initially fixing the strength parameters of the retaining wall and determining the embedment depth by iteration. The controlling parameter is the RF which must be equal to 1 in a lower bound analysis in order to ensure the optimal embedment depth which has been found to correspond to the embedment depth of Brinch Hansen. This configuration results in a moment distribution and a corresponding anchor force. In the calculation of the earth pressure only the soil parameters are considered assuming a rigid plate. It is possible to optimise the structural design parameters which has been performed in section 4.5.2 where the procedure is described.

The analyses are carried out using the setup given in section 4.5, and a series of numerical parameters are listed below:

- No. elements: 5,000
- Adaptive mesh iterations: 3
- The mesh has been refined along the wall, with a size of 0.05
- Yield criterion: Mohr-Coulomb

The mesh as a result of 3 iterations is given in figure 4.12.

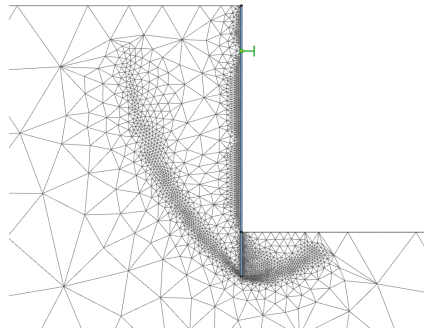


Figure 4.12: Mesh used in further analyses. The mesh is rearranged through 3 adaptive iterations where shear dissipation is the controlling parameter.

4.5 Comparison of Sheet Pile Wall Calculation Methods

In the following sections comparison of the different calculation methods appear. Not only will the results be evaluated, but also a comparison of the different components in the respective theories will be performed.

In section 4.5.2 the results will be evaluated. A relatively simple example is chosen which possibly will show the differences between the theories. The example is given in figure 4.13.

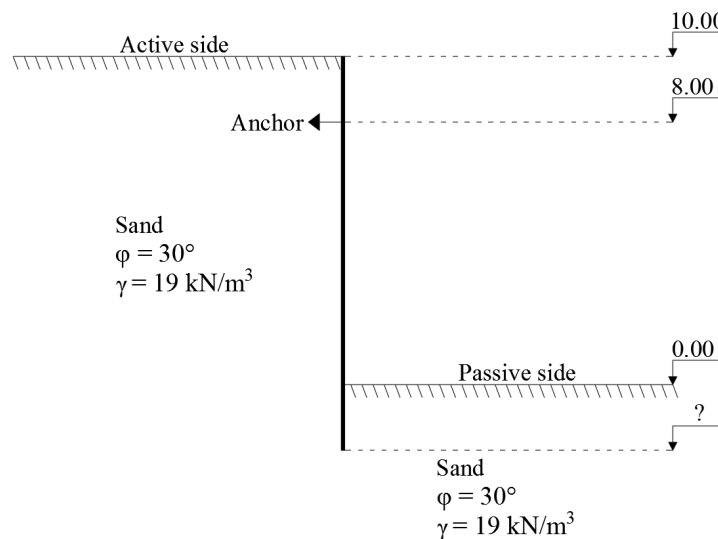


Figure 4.13: Chosen configuration with the chosen parameters.

4.5.1 Theoretically Comparison of Sheet Pile Wall Calculation Methods

In this section the theoretically differences between the different methods are evaluated.

Equilibrium of a Sheet Pile

Brinch Hansens method for determining earth pressure distributions has flaws regarding equilibrium. The method does not require vertical equilibrium at all which may result in insufficient design. Therefore KSP was formulated as an alternative for which vertical, horizontal and moment equilibrium are required, as mentioned in section 4.3.

The German standard and the numerical approach both rely on equilibrium, and for the FEM especially this fact leads to a distinctive earth pressure distribution which is illustrated in figure 4.15d.

Evaluating vertical equilibrium the vertical bearing capacity has great influence. The methods have different perspectives on this phenomenon. The method of Brinch Hansen does not include

any vertical bearing capacity. KSP states that the capacity is equal to 0, as the wall friction and the vertical component of the anchor force only must ensure vertical equilibrium.

Roughness of Wall

The roughness of the wall is significant to the calculations of the earth pressure. Apart from the method according to the German standard any evaluated method only has the opportunity of operating with completely rough or completely smooth walls corresponding to $\delta = \varphi$ and $\delta = 0^\circ$ respectively, where δ is the walls angle of friction.

In the German standard it is not possible to obtain a completely rough wall, and it is recommended that a completely smooth wall is not used, as it is not realistic. However calculations can be made in order to use realistic values of δ .

For the FEM it is possible to define the roughness. It is chosen to define a completely rough wall that corresponds to the theory of Brinch Hansen which ensures a basis for comparison.

Earth Pressure Coefficients

Earth pressure coefficients are essential to the calculation of the magnitude of the earth pressure. Every evaluated analytical method utilises earth pressure coefficients which differ and are given in table 4.2. It applies to any of the methods that the earth pressure coefficients are determined based on the roughness of the wall.

Table 4.2: Earth pressure coefficients used in the comparison. PC is short for change in pressure.

| Method | Active side | | Passive side | |
|-----------------|-----------------|-----------------|-----------------|-----------------|
| Brinch Hansen | Above PC: 5.800 | Below PC: 0.230 | Above PC: 0.270 | Below PC: 5.300 |
| KSP | Rough: 0.273 | Smooth: 0.333 | Rough: 5.804 | Smooth: 3.000 |
| German standard | 0.280 | | 5.000 | |

The theory of Brinch Hansen states that pressure changes occur which affects the earth pressure coefficients. This appears in table 4.2 where different coefficients must be used above and below the changes on both the active and the passive side of the wall. The KSP method has similarities to this method, as it appears in figure 4.15. The placement of the change in pressure is different from the two methods, thus leading to small deviations in the earth pressure distributions. KSP states that the level is equal to the rotation center as mentioned in section 4.3. Brinch Hansen however, states that the change in pressure is above the rotation center and below the ground level of the passive side. The calculations of the placements are found in appendix A.21, where relevant calculation scripts are located. The German standard states no change in pressure and only one coefficient is applied to each side.

The earth pressure distribution stated in OptumG2 is obtained through the FEM. The initial stress state is chosen by the user as the initial stress coefficient, K_0 . The final distribution then appears as equilibrium is obtained.

Redistribution of Earth Pressure

It is possible to redistribute the earth pressure for anchored retaining walls according to KSP and the German standard, as this represents more realistic distributions. The redistribution of the earth pressure in the KSP method is controlled by the support level of the retaining wall. This appears in figure 4.9.

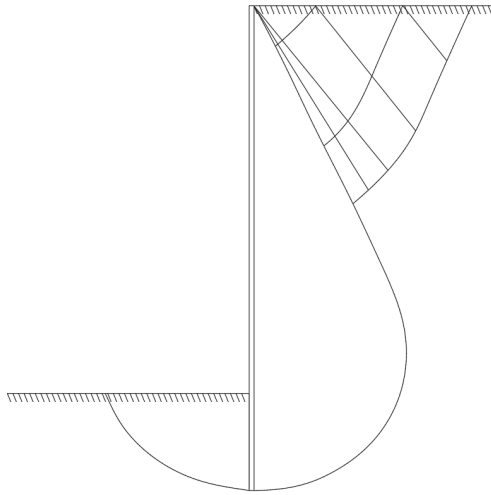
As stated in figure 4.6 the redistribution is a result of the height of the anchor relative to the height of the excavation according to German standard.

Failure of the Wall

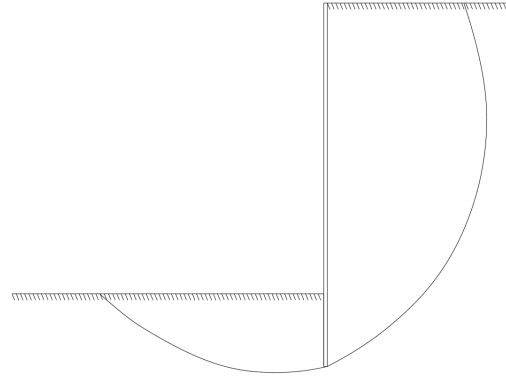
The different methods assume different failures of the soil, where the different failure conditions influence the determination of the earth pressure coefficients. Brinch Hansens method assumes the wall to fail as a combined failure, with both slip surface and break zones.

In contrary both KSP and the German standard are assumed not to fail by combined failure. In the KSP method the failure body will break in zones following a logarithmic spiral as shown in figure 4.14b. When the soil breaks in zones, it means the soil body will not act as a stiff body which is the case in a slip failure. According to the recommendations in the German standard slip surface is used and for active failure the surface is represented by a straight line. An example is given in figure 4.14c.[23]

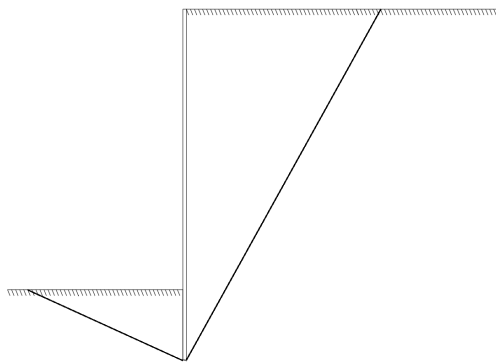
Numerically the failure of the soil is a result of the stresses. Figure 4.14d shows the failure of the evaluated retaining wall.



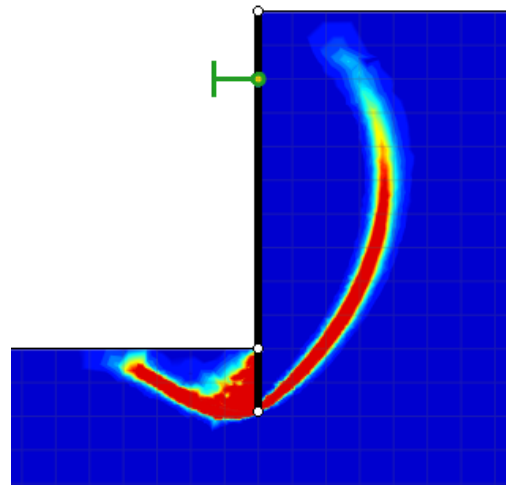
(a) Example of combined failure assumed by Brinch Hansen. The failure body contained by the slip line is assumed to be a stiff body.



(b) Example of a logarithmic zone failure assumed in the KSP method.



(c) Example of an active slip surface failure assumed in the German standard.



(d) Example of failure using numerical software.

Figure 4.14: Examples of active failure of a retaining wall for the different methods.

4.5.2 Comparison of Results of Sheet Pile Calculations

In the following section the results will be presented, and illustrations of the sheet pile wall with the fitting earth pressure distribution are given.

Table 4.3: Comparison of results for the calculation of sheet pile walls for different calculation methods in the ULS case. The numerical results are the basis for the comparison. The wall has been calculated as a rigid plate in all cases using characteristic values.

| Comparison | Anchor Force | Dev. | Maximum Plate Moment | Dev. | Sheet Pile Length | Dev. |
|------------------------|--------------|-------|----------------------|-------|-------------------|------|
| | [kN/m] | [%] | [kNm/m] | [%] | [m] | [%] |
| OptumG2 | 249.7 | 0.0 | 359.8 | 0.0 | 11.93 | 0.0 |
| KSP | 228.9 | -9.1 | 333.4 | -10.5 | 12.01 | 0.7 |
| German standard | 180.8 | -30.1 | 304.3 | -22.2 | 12.09 | 1.3 |
| Brinch Hansen | 228.8 | -9.2 | 250.0 | -43.9 | 11.93 | 0.0 |

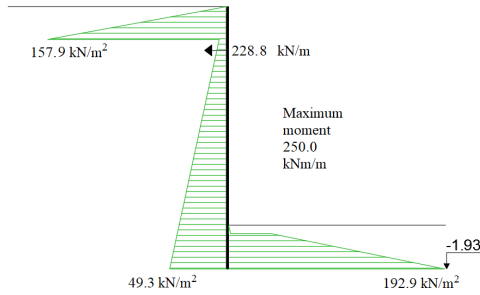
The KSP method was proposed as a better alternative opposed to the method by Brinch Hansen, but never gained much recognition in the industry. This is related to the fact, that sheet pile walls designed by using the Brinch Hansen method has been used in the field for decades having few failures even though the KSP method indicates a higher maximum wall moment. The KSP moment is around 30 % greater than the moment stated by Brinch Hansens method, which is in agreement with the theory of KSP, as mentioned in section 4.3. In this case the KSP method would result in a more expensive retaining wall, thus making the Brinch Hansen method more favourable. It is important to notice that the method of KSP is rather difficult to apply, as the calculations are extensive and require great effort.

The anchor force obtained in the Brinch Hansen method is only for the horizontal force without taking the vertical force into account. However, the vertical equilibrium could be accounted for by calculations afterward, thus designing a grout anchor having both horizontal and vertical force components. The German method has similar conditions where only the horizontal anchor force is found. Still the KSP method is different, as the method is designed with an inclined anchor making the total anchor force greater than what is shown in table 4.3. Only the horizontal force components for the anchor force are compared.

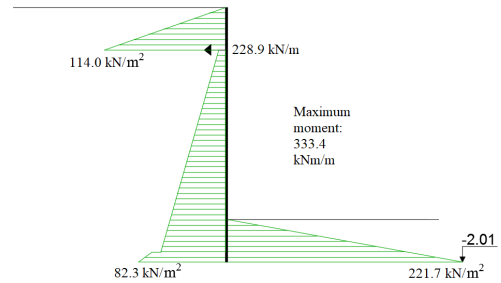
The embedment depth is nearly identical for all methods. Only minor deviations are found and would be insignificant when installing the wall.

An interesting and important observation concerns the results obtained numerically. The results for both the anchor and the plate moment are significantly larger than the other methods. However, for comparative reasons the retaining wall is considered a rigid structure and is therefore not optimised. Both lower and upper bound solutions have been determined numerically and the mean value is used in this example.

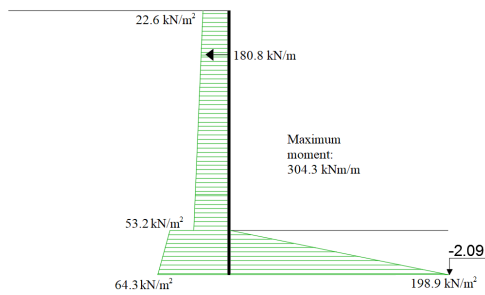
The numerical calculations are distinguished from the other methods in many aspects. The type and quality of the sheet pile wall must be chosen in the initial phase of the calculations. Using the analytical methods the type of sheet pile is chosen as the last step by choosing the sheet pile according to the obtained necessary sectional modulus. The configuration of the environment



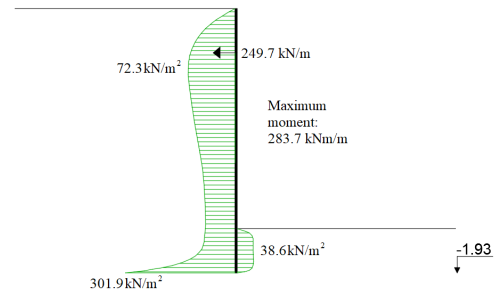
(a) Earth pressure distribution according to Brinch Hansens theory.



(b) Earth pressure distribution according to KSP theory.



(c) Earth pressure distribution according to German practice.



(d) Earth pressure distribution according to OptumG2, associated flow rule.

Figure 4.15: Earth pressure distributions altering the method used.

is equal in the different methods, but the numerical calculations prove the reliability of the structure. Creating the model the strength, type of profile, anchor level and the length of the profile are all important factors. By utilising OptumG2 and its functions, the ratio between the anchor force and plate moment may be illustrated as shown in figure 4.16.

The procedure is initiated by determining the extreme ratios by modeling the wall as a rigid plate having a fixed end anchor with a given finite yield strength, thus the minimum plate moment related to the maximum anchor force is found. If the fixed anchor is modeled as a fixed rigid support and a finite yield moment strength is applied to the wall, the minimum anchor force related to the maximum plate moment is determined. Afterwards the relationship is tracked by reducing the anchor force and vice versa.

Figure 4.16 is computed applying the same type of profile having the same steel quality. There are three curves having unique embedment depths illustrating the influence. A longer profile will result in a smaller force and corresponding plate moment. However, there is a minimum

4.5. Comparison of Sheet Pile Wall Calculation Methods

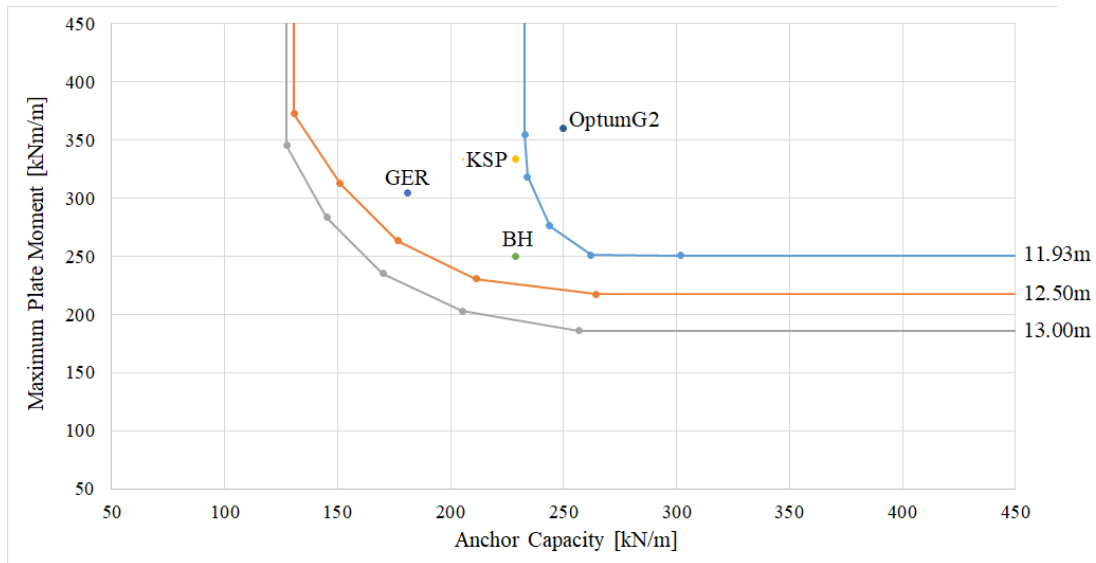


Figure 4.16: Safety design for the correlation between the anchor capacity and the plate moment for sheet pile walls with different lengths. Analytical results are included for reference.

limit to the length of the profile in order to prevent collapse. Different lengths have been used to illustrate the importance.

This design study clearly shows a decrease in the plate moment and anchor force if compared to the values of table 4.3. Using engineering judgment the desired design can be established.

Anchor Force in Thin Walled Sheet Pile

In this chapter numerical analyses of how the forces are transferred between the different components of a sheet pile wall are investigated.

Initially the preconditions and configurations of the numerical model will be presented in section 5.1. The numerical model and related submodel used for time reduction will be presented in sections 5.1.1 and 5.1.2 respectively. This is followed by an explanation of the conditions and considerations regarding the elastoplastic model in section 5.1.3.

The actual studies of the load bearing plate will be initiated by calculations considering a plate according to the Eurocode DS/EN 1993-5 in section 5.2, which then are followed by different related investigations by altering the relevant design variables. The dimensions obtained from the calculations will be used as a reference in the parameter study performed in section 5.3. The calculations and design according to the Eurocode appears in appendix A.8.

Deformations are not considered in any analysis in this chapter. Deformations of a sheet pile will however be investigated and evaluated in chapter 6.

5.1 Preconditions of the Numerical Model of the Sheet Pile

In order to initiate the analyses of the investigation it is necessary to obtain a basis for the design of the sheet pile and the corresponding load bearing plate. The analyses have been carried out using the ArcelorMittal Sheet Pile called AU18 having a length of 10 *m*. The technical specifications of the AU18-profile are given in appendix A.9.[27]

The detail of the attachment of the anchor will include a load bearing plate and a projecting block attached to the thin walled sheet pile having an inclination allowing the anchor to act in a corresponding angle. The detail is illustrated in figure 5.1. The three components have been perforated at the center with a skew hole allowing for an anchor tendon of a diameter of 30 *mm* to be attached. The tendon has been excluded from the analyses in order to elude possible assembling issues which might rise during modeling of the skew hole and to reduce computational time. The omission of the anchor tendon do not lead to possible errors, but instead only contribute to lightened the complexity of the structure. The anchor force will be

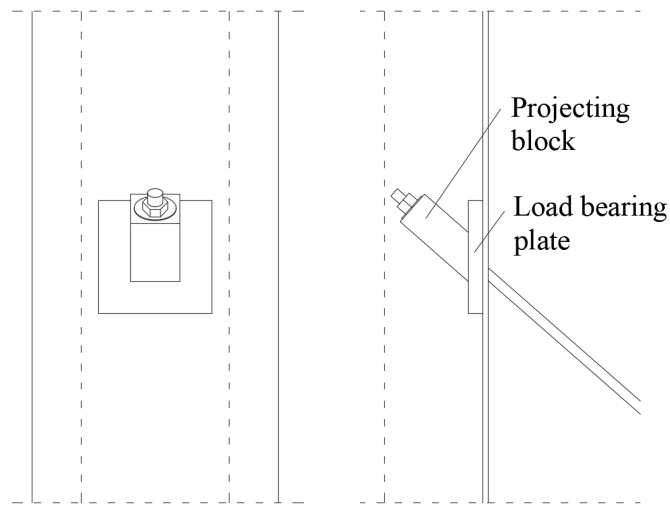


Figure 5.1: Attachment of the anchor in the sheet pile with a load bearing plate.

applied on the skew face of the projecting block in order to simulate the pull of the anchor. The force is not given a specific value, as it varies throughout the different investigations.

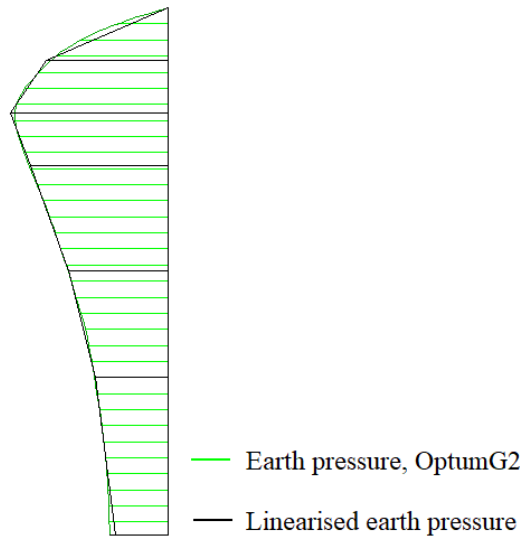


Figure 5.2: Linearisation of the earth pressure distribution obtained numerically in section 4.5.2.

The earth pressure is applied to the sheet pile model. The earth pressure distribution applied to the model corresponds to the resulting distribution computed numerically given in section 4.5.2. As ANSYS Workbench requires a linear varying load, the distribution is linearised, as illustrated in figure 5.2. The linearisation is considered a valid approximation, as the resulting earth pressure is somewhat equivalent to the original earth pressure in OptumG2. The pressure is applied to act normal to the surface of the sheet pile, as ANSYS Workbench does not give the opportunity of application of a linear varying pressure in a specific direction.

5.1.1 Setup of the Numerical Model

As the sheet pile is modeled, a number of assumptions have been made concerning the boundary conditions which will be explained in this section. The model is constructed entirely of solid elements. The specific model in ANSYS Workbench is illustrated in figure 5.3.

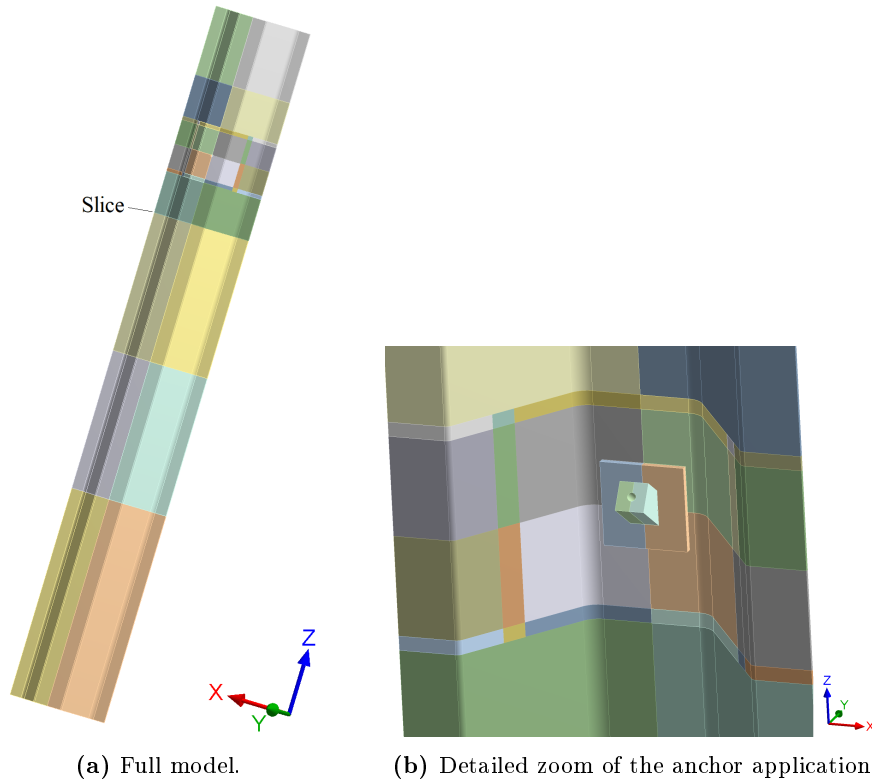


Figure 5.3: Numerical model of the sheet pile analysed in ANSYS Workbench. In section 5.1.2 implementation of a submodel of the area of interest is described.

The bottom section of the sheet pile is constrained from movements in the y - and z -direction, but all directional rotations are allowed. This is done to model the effect of having soil on both sides of the wall as a constraint. Because of this, the sheet pile model has a reduced height of 10 m as the embedment depth is not taking into account. The sides are allowed to move in the z - and y -direction, but not in the x -direction in order to simulate symmetry of the section. The top surface of the sheet pile is considered completely free and movements in any direction are allowed which ensures a realistic model of the wall. The boundary conditions are illustrated in figure 5.4.

Another assumption is the idealisation of the interlocks between the sheet pile sections. As the modeled sheet pile wall is a result of two half U-sections enclosing one full section, two interlocks are apparent. The interlocks are considered both stress and moment transferring. This is however only the case for preprocessed paired sheet pile sections where the interlocks are clamped, welded or elsehow fixed together. The idealisation is given in figure 5.5, where

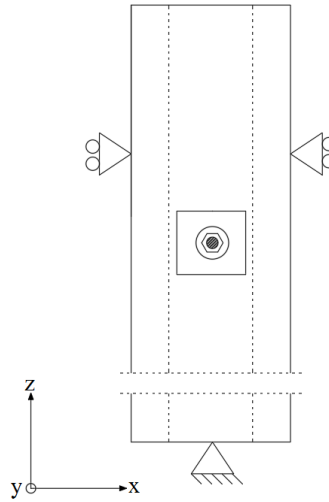
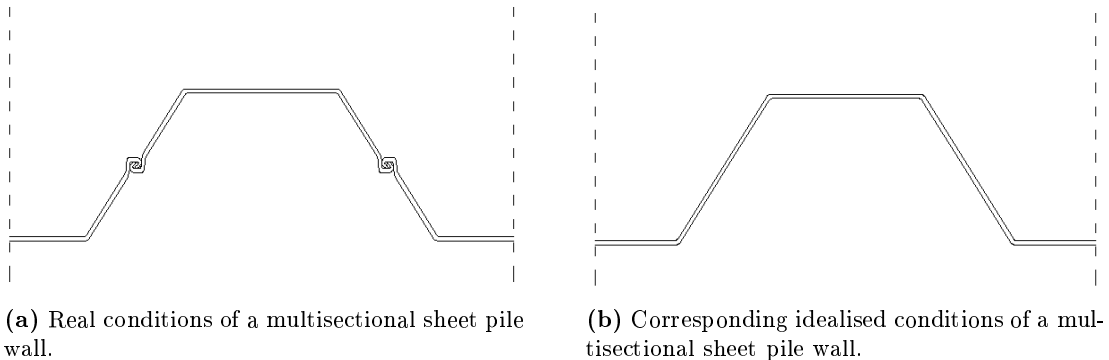


Figure 5.4: Boundary conditions for the modeled sheet pile in ANSYS Workbench.

the interlocks are removed and the webs of the profiles are assumed fully aligned. This however is an approximation as this differs to reality. It is chosen to neglect this fact in the analyses concerning this specific issue, as it does not interfere with the results in the area of interest.



(a) Real conditions of a multisectional sheet pile wall.

(b) Corresponding idealised conditions of a multisectional sheet pile wall.

Figure 5.5: Idealisation of the interlocks in the analyses of the thin walled sheet pile.

The model is sliced as illustrated in figure 5.3a to allow for application of pressures of different magnitudes along the height of the sheet pile wall and in order to construct an appropriate mesh. The slices are then bonded together in parts which ensures consistency in the model. The projecting block and the load bearing plate are bonded together as well, and the plate is then bonded to the sheet pile. This is an approximation, as friction may appear between the different parts. However this friction is neglected, as it leads to insignificant differences.

The mesh of the model appears in figure 5.6. It is clear that a fine mesh must be used in the area of the contact between the load bearing plate and the sheet pile. This has been implemented as a well defined stress distribution is of interest in this area. In the rest of the sheet pile a coarse mesh is implemented in order to minimise computational calculation time. The refinement of the

elements in the area of interest is a result of a study of convergence, which appears in appendix A.10.1.

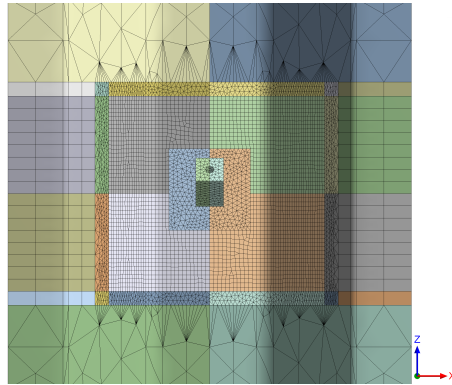


Figure 5.6: Mesh of the model. Only the area, around the anchor point having a fine mesh, is shown.

5.1.2 Setup of the Numerical Submodel

Computational time is an important aspect, as numerical calculations are executed. A fine mesh is often necessary in order to obtain convergence and for large models a refined mesh may cause inappropriate calculation time. To reduce computational time a method to only model a part of the large model is therefore of interest. In these analyses a rather large model is used having a fine mesh around the area of interest illustrated in figure 5.3b, thus a submodel for the area of interest will be used.

Implementing a submodel, an initial calculation of the large model is needed, as the deformations from the full structure are applied at the cut boundaries of the submodel. It is important that any outer forces acting on the full model are replicated in the submodel. This feature gives the opportunity of changing the mesh or reconstructing the model creating fillets or chambers for welding etc. Figure 5.7 illustrates the submodel.

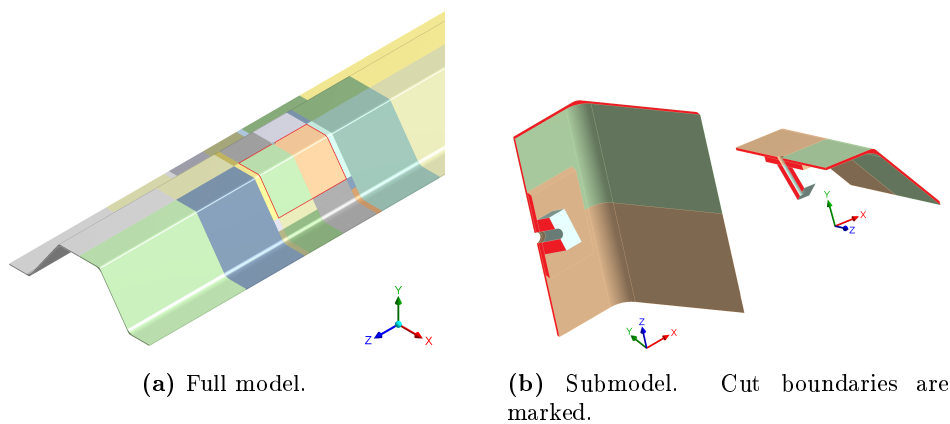


Figure 5.7: Submodel principal for a sheet pile.

The submodeling feature in ANSYS Workbench is built on the principles of St. Venant which states that '*The difference between the effects of two different but statically equivalent loads becomes petite at sufficiently large distances to the load.*' The principles are considered valid if the stresses are insignificant in the cut boundary, and if the forces are applied in great distance to the cut which then does not affect the mechanical behaviour.[28]

Appendix A.10.3 includes a study of the implementation of the submodel. A validation of the feature appears together with a study of the possibility of creating a half model as the sheet pile is assumed symmetrical about the axis through the anchor tendon. It is found that a submodel of a half sheet pile is applicable as the stresses in the models are equal. The symmetry of the plate has been proven in appendix A.10.2.

In order to obtain reliable results the anchor force will be applied to the model in steps, in a way that allows the stresses to distribute properly compared to a case where the full load is applied at once and then released. Besides, this procedure reduces the computational time compared to the same amount of separate analyses as the solver converges at a higher rate using an Elastoplastic model which is described in section 5.1.3. In appendix A.10.4 it is validated that it is possible to convert the results from each time step from the full model to the right steps in the submodel.

Another method for reducing the computational time is the implementation of shell elements, which are less time consuming. The implementation has been performed in appendix A.10.6, where the procedure has been validated as well. Due to the complexity of the sheet pile, it has been found that the reduction in the computational time does not outweigh the time spend on creating the shell elements in the numerical model, thus this type of element has not been included further.

5.1.3 Setup of the Numerical Elastoplastic Model

As default ANSYS Workbench calculates structures using a linear elastic solver. In this model the stress distribution appearing is a result of the load bearing plate distributing the anchor force onto the sheet pile. In order to capture the most realistic transmission of the stresses, a nonlinear elastoplastic behaviour is implemented.

In a nonlinear calculation the cross section of the structure is utilised more efficiently, as the stresses are redistributed by iterations during the calculation. This type of analysis is more advanced than a typical linear analysis and yields extensive computational time. By using the submodel configuration as described in section 5.1.2, acceptable calculation time is maintained, still having a sufficient mesh in order to represent the stress state in the model.

The plastic part of the solver can be described by two different hardening models which and used, as true hardening differs from the engineering hardening illustrated in figure 5.8:

- Bilinear
- Multilinear

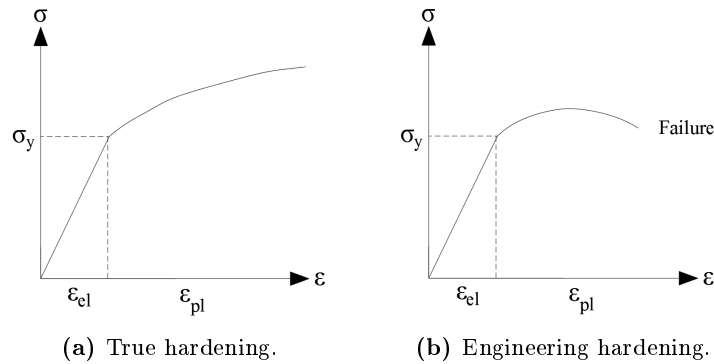


Figure 5.8: Engineering hardening differs to true hardening. In the nonlinear analyses the true hardening is approximated.

Bilinear hardening has only two variables, as strains exceed the elastic part, namely the yield stress and the tangential modulus. In contrary the multilinear model has multiple tangential modules, as the strains grow. This setup is a more realistic representation of true hardening, but is correspondingly more time consuming to calculate. In these analyses the realistic multilinear model given in figure 5.9 is preferred, as this model represents the actual behaviour more accurate than the bilinear model as stated. A yield strength of 355 MPa is chosen.

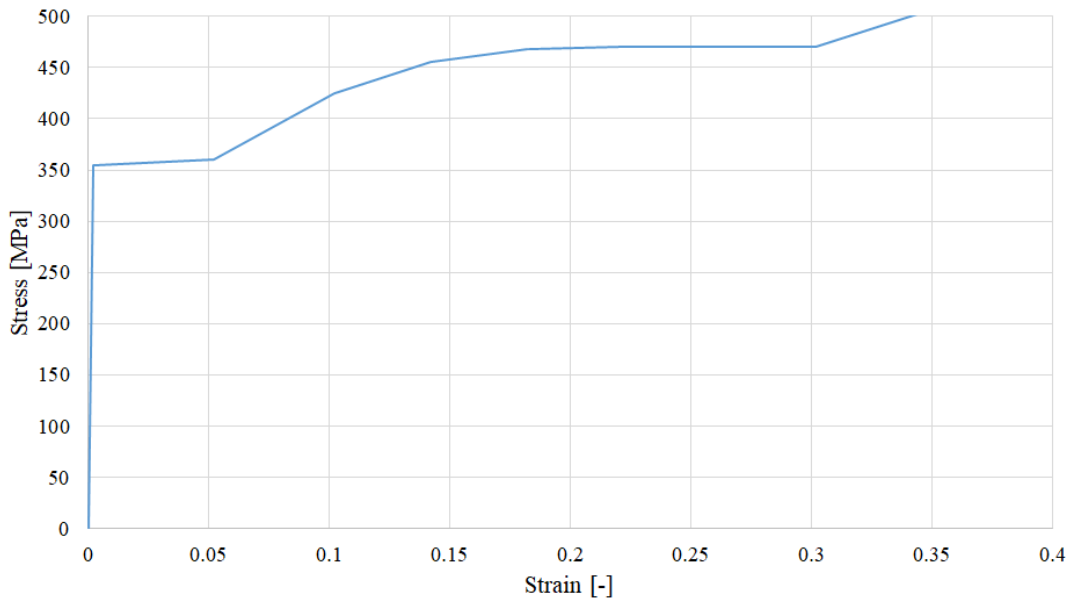


Figure 5.9: Realistic multilinear model applied to the numerical model. The peak after a strain of 0.3 is implemented in order to ensure a stable solution. The plastic model has been proven applicable in appendix A.10.5.

5.2 Study of the Plate Designed According to the Eurocode

A study of the recommendations given in the Eurocode DS-EN 1993-5-2007 has been carried out for the load bearing plate. This study is performed in order to verify that the calculations using the procedure of the Eurocode yields allowable results for the case of ULS by the use of a numerical method.

The study includes determination of the minimum allowable dimensions of the load bearing plate by the application of a fixed horizontal anchor force of 350 kN and a corresponding vertical force of 200.75 kN , which is a result of the inclined anchor of 35° . Additionally, a study will be performed to investigate the collapse load of an anchor force having the recommended dimensions of the load bearing plate. The investigations are presented in the following.

The dimensions recommended by the Eurocode have been determined in appendix A.8 and are given in table 5.1.

Table 5.1: Minimum and maximum allowable dimensions of the load bearing plate according to the Eurocode.

| Parameter | Minimum Dimension | Maximum Dimension |
|-----------|-------------------|-------------------|
| | [mm] | [mm] |
| Width | 292.8 | 336.0 |
| Length | 292.8 | 504.0 |
| Thickness | 21.0 | - |

Study of the Dimensions of the Plate

The minimum and maximum dimensions given in table 5.1 are used as a basis for the numerical dimension study. The width and length are altered equally as the thickness of the plate is fixed, ensuring the plate being quadratic.

In order to ensure stability the equivalent von Mises stress must be below 470 MPa which is the tension capacity of steel having a yield strength of 355 MPa . At a stress level of 470 MPa , cracks will appear in the area of high stresses which may lead to collapse of the sheet pile. It is chosen to allow for some yielding in the cross section, as a member has some strength beyond yielding, which therefore may not be fatal.

The analyses are constructed as explained in the previous sections. The resulting stress distributions are established and are given in appendix A.11.1. Evaluating a plate having the dimensions of $250\times 250\text{ mm}$ both the flanges and web of the sheet pile are yielding in the outermost fibers of the cross section. It appears from the stress and strain distributions that failure occurs in the cross section having these dimensions. By increasing the dimensions of the load bearing plate, the stress level fades slightly. However, at $275\times 275\text{ mm}$ the stresses are redistributed from the flange to the web of the sheet pile. The tendency develops with increasing dimensions and at the dimensions of $330\times 330\text{ mm}$ no yielding occur. Thus, the stresses will decrease with increasing sizes of the plate.

Study of the Anchor Force Acting on the Sheet Pile

The minimum dimensions of the load bearing plate revealed by the Eurocode are used in this analysis. The anchor force is gradually increased from 200 *kN* horizontally to 450 *kN*, and the vertical component of the force is altered correspondingly. 200 *kN* has been chosen as the initial force, as smaller loads will lead to collapse near the excavation level caused by the earth pressure acting on the retaining wall. This will cause the calculations to supply unreliable results, as the deformations are substantial.

In appendix A.11.2 the corresponding developing stress distributions for the increasing force are illustrated. In figure A.60 the stress levels at different magnitudes of the force are given. As the anchor force reaches around 400 *kN*, failing stresses are initiated in the sheet pile. However, as the force experiences further increase the stresses redistributes causing the maximum stress to fall beneath failure. If cracks have appeared, a possible collapse of the sheet pile is real, thus the maximum anchor force is around 400 *kN* for a AU18 sheet pile being exposed to the earth pressure calculated in section 4.4. Cracks may not be fatal, as the sheet pile will only experience the ULS load in one cycle, meaning the crack growth may not be critical, which has been explained in section 3.4.

By considering the stress distributions in the figures A.61 to A.71 located in appendix A.11.2, it is apparent that around 300 *kN*, the stresses reach the yielding strength which develops in the web of the sheet pile. Around the load bearing plate yielding occurs at all anchor force magnitudes, and at 425 *kN* failure occurs in the web of the sheet pile.

5.3 Parameter Study Concerning Anchor Attachment Detail

In section 5.2 the allowable dimensions and forces have been investigated by the use of the regulations prescribed in the Eurocode regarding a sheet pile wall and its components. In the following the different dimension parameters have been altered in order to reveal the influence of the parameters, as stress distributions and failure are considered. Common for any of the analyses is the anchor force ranging from 200 *kN* to 450 *kN*, and the inclination of the anchor being 35°, apart from a study considering the angle of the anchor tendon.

The following parameters will be investigated:

- Thickness of the load bearing plate
- Width of the load bearing plate
- Length of the load bearing plate
- Angle of the anchor tendon
- Thickness of the sheet pile

5.3.1 Thickness of the Load Bearing Plate

The influence of change in the thickness of the load bearing plate has been studied. In appendix A.12.1 the resulting stress distributions have been given for the different size configurations. The development in the stresses in the area of interest have been illustrated which yield interesting results. Having a thin load bearing plate of 15 mm , the submodel experiences high stresses throughout the most of the model. As the thickness increases the extent of this area will decrease as well as the scale of the stresses. An interesting development however arises, as the plate becomes relatively thick. This is illustrated by the formation of plastic strains in the sheet pile, which is given in figure 5.10. It is of interest to minimise plastic strains, as these causes permanent deformations.

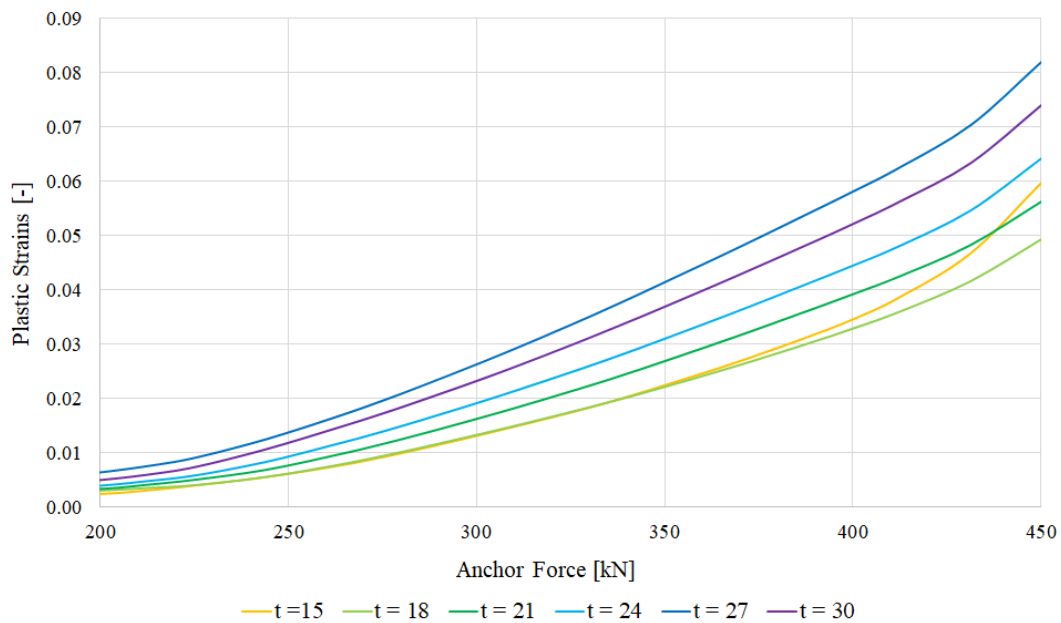


Figure 5.10: Development of the maximum plastic strains in the sheet pile for different thickness configurations of the load bearing plate.

It appears that there is an optimal thickness of the load bearing plate. This may be as a result of the change in stiffness of the plate, as the thickness increases. A thin plate will be able to bend at a curvature corresponding to the behaviour of the sheet pile. In comparison a thick plate is stiff compared to the sheet pile resulting in creation of an unfavourable push on the sheet pile. That said the thickness must be at a certain size, as it appears in figure A.78 for a plate with 15 mm thickness that the tensile strength of the sheet pile is exceeded.

The study reveals that a thickness of around 18 mm is optimal for this configuration examining only the developed plastic strains. However, considering the stress levels, these nearly reaches the tensile strength which is risky.

5.3.2 Width of the Load Bearing Plate

The study concerning the width of the plate has been performed, and the results are given in appendix A.12.2. The study reveals that by increasing the width of the plate the load bearing capacity of the sheet pile will increase correspondingly. The maximum width of the load bearing plate is limited by the inner width of the sheet pile. However, it is possible to find a minimum dimension, which is around 275 mm based on the study performed illustrated in figure A.86. For a width of 250 mm a clear collapse of the sheet pile is apparent which is shown in figure A.85, as the level of the plastic strains trails towards an asymptote.

5.3.3 Length of the Load Bearing Plate

As it appear in section 5.3.2 the load bearing capacity increases, as the width increases. The same development is true, as the length of the load bearing plate is prolonged, which is shown in appendix A.12.3. A length of 275 mm causes failure of the sheet pile, and it has been established in section 5.2 a length of 292 mm is sufficient. The tensile strength is exceeded for configurations having a length of 350 mm , but as figure 5.11 reveals, no critical plastic strains are developed, and therefore failure is not assumed beyond a length of 292 mm .

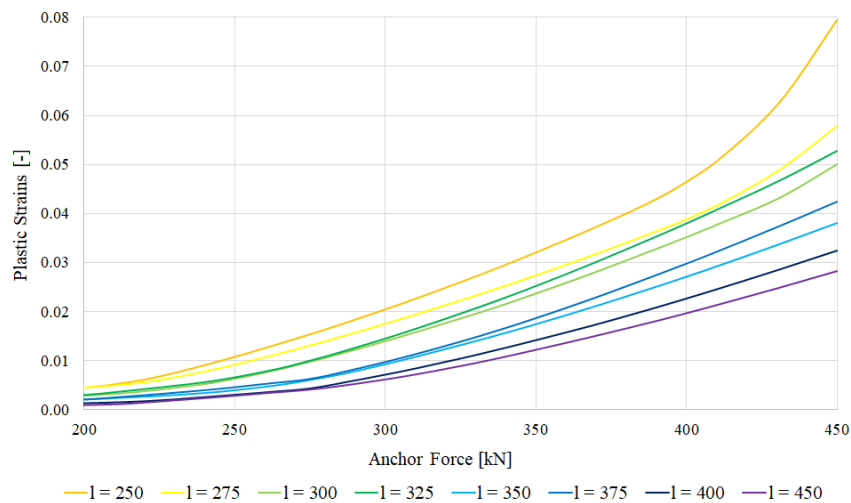


Figure 5.11: Development of the maximum plastic strains in the sheet pile for different length configurations of the load bearing plate.

5.3.4 Angle of the Anchor Tendon

The anchor inclination has been investigated, and the results are located in appendix A.12.4. Evaluating the results the development is interesting, as the angle of the tendon is increased. The stress distributions only reveal insignificant changes, as the angle is altered. As the angle reaches 40° the stresses starts to increase, and at 50° the stresses reaches 99 % of the tensile strength, which may indicate that failure of the sheet pile is imminent. However, as figure A.126

shows no critical strains are reached for any of the angle configurations. Also revealed by the figure is that there seems to be an optimal angle, which is around 20° . This may be as a result of the shear forces introduced in the load bearing plate causing the stresses to redistribute in favour of the sheet pile.

5.3.5 Thickness of the Sheet Pile

The influence of the thickness of the sheet pile has been investigated in this section, and the results are given in appendix A.12.5. In order to perform a realistic analysis the prescriptions regarding corrosion of a sheet pile according to the Eurocode DS/EN 1993-5 are used.

In Eurocode DS/EN 1993-5 different corrosion rates are prescribed, which differs according to the respective environment of operation. In table 5.2 rates for common soil environments are given according to the Eurocode. The excavation side of the sheet pile is exposed to corrosion as well, however the rate is different and depends on the outer exposure. The Eurocode states that the rate for a sheet pile located in a normal atmosphere will corrode at a rate of 0.01 mm per year and 0.02 mm for sheet piles located where marine conditions may affect the structure. The higher rate of the two is a conservative consideration and will be used.

Table 5.2: Recommended values for thickness reduction due to corrosion for a sheet pile situated in soil. Values corresponding to Non-compacted and non-aggressive environment are used in this project.

| Required Design Working Life | 5 Years | 25 Years | 50 Years | 75 Years | 100 Years |
|--|---------|----------|----------|----------|-----------|
| Undisturbed natural soils (sand, silt, clay, schist, ...) | 0.00 | 0.30 | 0.60 | 0.90 | 1.20 |
| Polluted natural soils and industrial sites | 0.15 | 0.75 | 1.50 | 2.25 | 3.0 |
| Aggressive natural soils (swamp, marsh, peat, ...) | 0.20 | 1.00 | 1.75 | 2.50 | 3.25 |
| Non-compacted and non-aggressive fills (clay, schist, sand, silt, ...) | 0.18 | 0.70 | 1.20 | 1.70 | 2.20 |
| Non-compacted and aggressive fills (ashes, slag, ...) | 0.50 | 2.00 | 3.25 | 4.50 | 5.75 |

The different thickness configurations are a result of the years of exposure. Table 5.3 shows the reduced thickness of the sheet pile corresponding to the years of exposure.

Table 5.3: Reduced thickness of the sheet pile for the corresponding years of exposure.

| Years of Exposure | Reduced Thickness of Flange | Reduced Thickness of Web |
|-------------------|-----------------------------|--------------------------|
| [Years] | [mm] | [mm] |
| 0.00 | 10.50 | 9.10 |
| 6.25 | 10.16 | 8.78 |
| 12.50 | 9.88 | 8.50 |
| 25.00 | 9.30 | 7.92 |
| 50.00 | 8.30 | 6.92 |

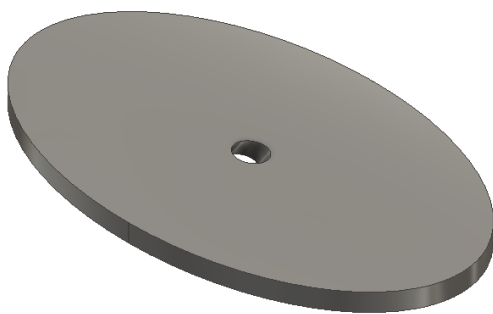
The analysis reveals that for 12.5 years of exposure the critical stresses are captured. However, the development of plastic strains shows that the stresses are not fatal. As the thickness is further reduced failure occur, and the maximum allowable force is reduced similar to the reduction of the cross sectional area which is revealed by table 5.4.

Table 5.4: Maximum force as a result of reduction in thickness of the sheet pile. The different configurations have not been tested beyond a force of 450 kN .

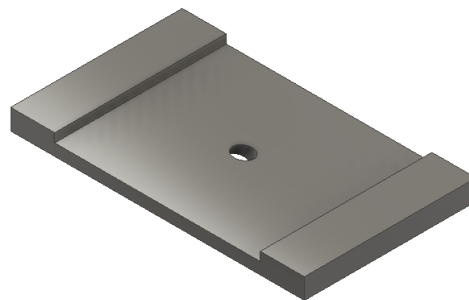
| Years of Expossure | Maximum Anchor Force |
|--------------------|-----------------------|
| | [kN] |
| 0.00 | > 450 |
| 6.25 | > 450 |
| 12.50 | > 450 |
| 25.00 | 415 |
| 50.00 | 335 |
| 100.00 | Failure for any force |

5.3.6 Shape of the Load Bearing Plate

Beside these parameters also a study of unconventional shapes has been performed. The considered shapes are illustrated in figure 5.12. An elliptical shape has been chosen as this may lead to a copacetic transferal of the forces, and therefore excess material could possibly be saved. The length of the greater axis of the ellipse is fixed, and the minor axis is then altered in the range of 200 mm to 292 mm . The study is performed in appendix A.12.6 and reveals allowable stress and strain states at a minimum length of the minor axis of 225 mm . In table 5.5 it is stated that the required material volume for an ellipse plate of this configuration, corresponds to a quadratic plate having the dimensions 297.25x297.25 mm . Other dimensions are shown in the table for comparative reasons.



(a) Elliptical shape. The great axis is fixed and the minor axis, b , is altered.



(b) Rectangular shape with extra material added to both ends of the plate. The plate has been placed with the 'feet' pointing both upwards and downwards. The height of added material has been altered.

Figure 5.12: Different unconventional shapes considered for the load bearing plate.

5. ANCHOR FORCE IN THIN WALLED SHEET PILE

Table 5.5: Material used creating the elliptical plates. The corresponding quadratic area has been given for comparison.

| Length b | Area of Elliptical Plate | Corresponding Lengths of Quadratic Plate |
|------------|--------------------------|--|
| $[mm]$ | $10^3 [mm^2]$ | $[mm]$ |
| 200.00 | 78.54 | 280.25 |
| 225.00 | 88.36 | 297.25 |
| 250.00 | 98.17 | 313.33 |

Another shape considered is a rectangular plate with added 'feet', which is illustrated in figure 5.12b. Investigating the load transferal, this shape is optimal as the loads are distributed away from the point of application of the tendon. The study of the influence of the application of these 'feet' is carried out in appendix A.12.7 where the feet are pointing both upwards and towards the sheet pile.

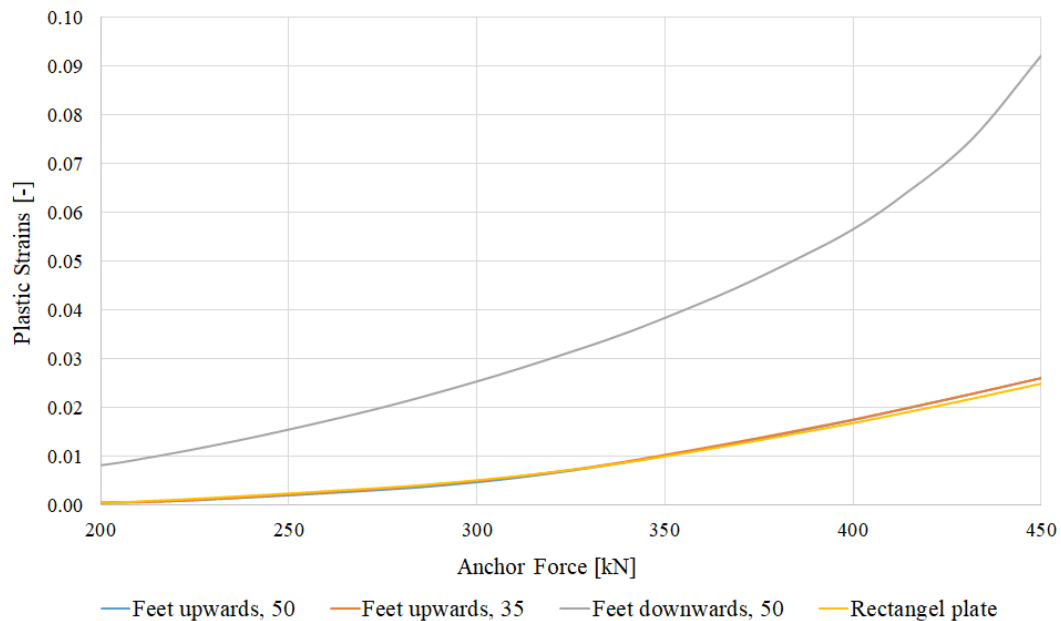


Figure 5.13: Development of the maximum plastic strains in the sheet pile obtained from the study regarding the application of additional material on the load bearing plate.

Evaluating the results it is evident that the appearance of the applied feet are without significance when these are pointed upwards. In figure 5.13 the maximum plastic strains are plotted as a function of the force applied, where the results are compared to a rectangular plate without 'feet' representing a threshold. As stated the figure reveals that the strains are almost identical for different sizes of the feet, which is confirmed by the stress distributions given in appendix A.12.7. Facing the 'feet' downwards will in comparison decrease the load bearing capacity of the sheet pile significantly.

5.3.7 Summarisation of Parameter Study Concerning the Anchor Attachment Detail

The study reveals a series of minimum and maximum or optimal dimensions of the load bearing plate for a sheet pile configuration exposed to an inclined anchor force. Some of the investigations have led to interesting results such as the thickness of the load bearing plate for which a thin plate causes high stresses in a large area and a thick plate causes high stresses in a rather limited area.

Evaluating the results given in appendices A.12.1 to A.12.7 where the relevant references are found in the respective sections, it is seen that the stresses are subjected to increases and decreases as the force grows. This is caused by the redistribution of stresses which a nonlinear analysis provides.

As the angle of the anchor does not change the load bearing capacity significantly, a parameter of relatively great importance is the width of the plate. Small percentage changes lead to significant deviations in the capacity that are greater than e.g. the importance of the length, which is supported by the development of plastic strains in the sheet pile.

Also unconventional shaped load bearing plates have been analysed. The purpose of creating unconventional shapes is to reduce the sufficient amount of material and still prevent failure. However, as it is evident in section 5.3.6, the application of material in the ends has insignificant importance to the load bearing capacity. Also elliptical shapes have been investigated, for which it is possible to reduce the width, but this fact will not compensate for the material used. This is true as the sufficient elliptical plate corresponds to a quadratic plate of 297.25 mm which is larger than the minimum quadratic dimensions of 275 mm proven in section 5.2.

5.4 Collapse Analysis of the Sheet Pile

In this section the yield mechanism in the area of the anchoring in the sheet pile have been captured through a collapse analysis. The plastic model evaluated in section 5.4.1 has been implemented in the numerical model for this analysis.

The useability of this model has been validated in appendix A.7.2. The results of this validation reveal that the collapse mechanism obtained numerically in general coincides with the relevant theory.

The results of the implementation on the sheet pile are available in section 5.4.2.

5.4.1 Plastic Model for Capturing Yield Lines Numerically

In order to create a realistic plastic model numerically which captures the development of yielding hinges and yield lines, some examples are executed. In figure 5.14 a plastic model is given which allows for large strains as yielding is reached. In appendix A.7.2 the appliance of the plastic

model is validated. The model is held up against an analytical approach for determining the critical yielding mechanism.

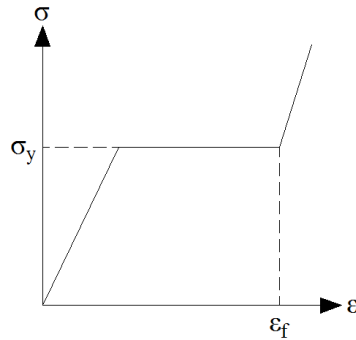


Figure 5.14: Plastic model which illustrate realistic formation of yield lines numerically.

The intention of this plastic model is, that the strain enlargement beyond yielding will ensure the redistribution of the stresses up to the occurrence of failing strains. Large plastic strains mark the lines of yielding.

5.4.2 Results of Collapse Analysis

Only the submodel of the sheet pile has been investigated, as only this area is of interest. The scale of the collapse load is mainly controlled by the yielding stress for the plastic model which is chosen to 400 MPa. The intention is not to find a collapse load, but solely to investigate the formation of the yielding mechanism.

The colour scheme in the figures 5.15 and 5.16 are chosen such that the failing strains of 19 % and beyond will be yellow and towards a red color for increased visibility.

Figure 5.15 reveals the contours of the yielding mechanism. It is apparent that the area around the edges of the anchoring will develop a yielding hinge, as large strains appear. Additionally, the zone in the web after the bend of the sheet pile will develop a yielding hinge according to the numerical results. A yield line between the ends of the yielding hinges may form, but in order to conclude that this line represents an actual hinge, the distribution of plastic strains in the cross section of the sheet pile must be considered, which is possible by investigating figure 5.16.

Evaluating figure 5.16 the appearance of the yielding hinges in the flange of the sheet pile around the anchoring and in the web are correct, as figure 5.16a reveal full development of plastic strains in the whole cross section. Figure 5.16b shows that the line between the yielding hinges is in fact not a yield line, as failing strains are not fully developed. However, the formation of the line is most likely a part of the collapse mechanism.

The results of the analysis reveal that the areas containing stresses beyond yielding or failure in sections 5.2 and 5.3 are coinciding with the resulting yield line pattern captured in this section.

Stresses of such scale in these areas may in fact be fatal as these could possibly result in the development of a yielding hinge and not just be formed as a result of singularities.

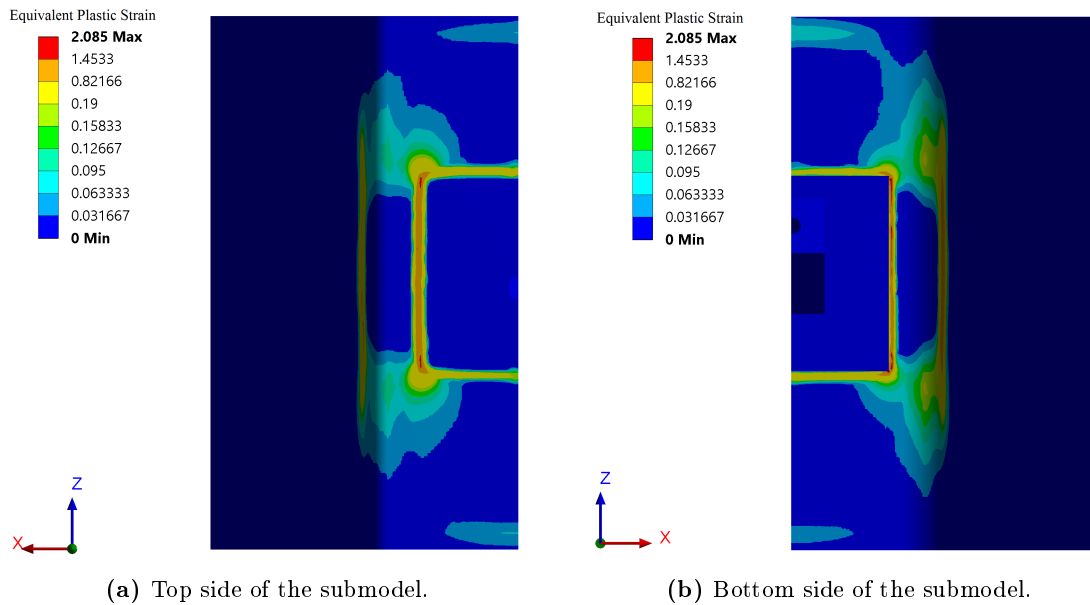


Figure 5.15: Plastic strain contours on different sides of the sheet pile. Large strains marks the appearance of yielding hinges.

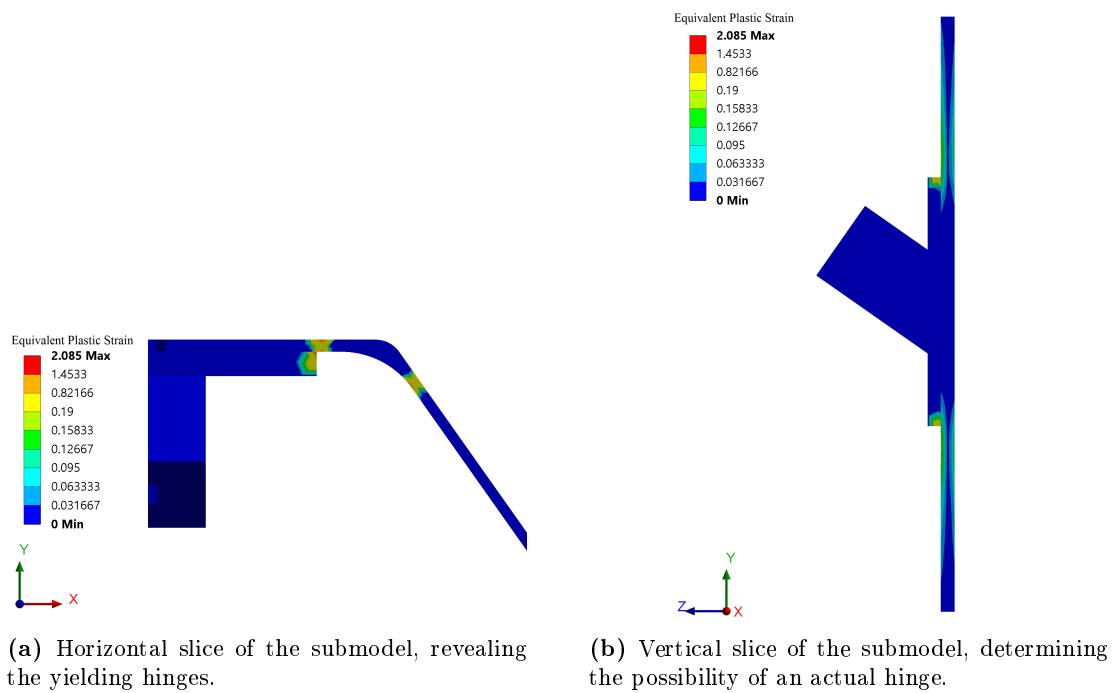


Figure 5.16: Slices of the submodel. These figures are used for determination of actual hinges.

5.5 Study of the Influence of Membrane Effect

The membrane effect has great influence on the capacity of plate. The membrane effect occurs, as strains form in the middle surface of a plate due to bending, that results in normal forces in a cross section.

Appendix A.13 contains a study of the membrane effect occurring in a simple plate, which shows that membrane effects appear by altering the boundary conditions of the considered plate. The load carrying capacity is greatly influenced by the inclusion of membrane effects, as an inclusion results in a relatively higher collapse load than determined through the yield line theory. This is because the theory of yield lines is a relatively simple method which does not include the changes in geometry.

The shape of the sheet pile provides the perfect conditions for the membrane forces to occur. Tensile and compressive membrane forces will form in sheets depending on the movement. The separate sheets are restricted from horizontal movement along the soil as a result of the interlocking. The scale of the effect has not been investigated.

Deformations of a Sheet Pile Wall

Deformations of a retaining wall are of interest in the SLS case where large deformations could result in various issues related to aesthetics, space requirements in an excavation site and soil movement. In this chapter a thorough investigation of computational modeling of the deformations of a sheet pile wall will be executed. The study will be performed by the use of OptumG2 which is used to determine the deformations for a numerical model based on an existing project where several measurements have been taken throughout the different installation phases. However, prior the comparison a sensitivity study of the settings in OptumG2 is performed to enhance the precision of the approximated model. Additionally a sensitivity analysis of the geotechnical parameters will be performed in order to determine the influence of each parameter on the deformations.

As the actual comparison is carried out, initially a simplified model is produced. This is followed by a model based on the two sensitivity analyses in which the values and settings have been optimised considering the given data from the site. This model is compared to the experimental deformation measurements. Finally the parameters and conditions in the model have been altered to illustrate what has to be estimated in order to replicate the actual movements of the sheet pile wall. The process of this study has been illustrated in figure 6.1.

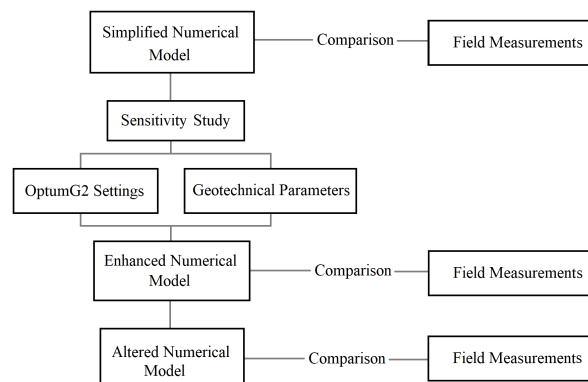


Figure 6.1: Illustration of the different processes when fitting a numerical model to measurement data from the field.

6.1 Study of the Numerical Model Using OptumG2

In the following sections a sensitivity analysis of the settings in OptumG2 will be examined in regards to the deformations. This is done in order to ensure a reliable approximation.

6.1.1 Elastoplastic Analysis Concerning the Deformations of a Sheet Pile Wall

Deformations are captured utilising an Elastoplastic Analysis. This type of analysis in OptumG2 involves several coupled stages representing the realistic construction scenario, e.g. gradually excavation of a construction pit using a sheet pile wall, which has a significant influence on the deformations obtained. This makes it a suitable analysis, determining the deformations of a sheet pile wall having several excavation stages.

As mentioned, the elastoplastic analysis consists of several stages. The first stage is the initial stress stage which computes the initial stress distribution in the soil which is characterised by the initial earth pressure coefficient, K_0 . In this stage the sheet pile wall has been installed, but no excavation has been performed. In the following stages the excavation level is lowered gradually. As the anchor level is excavated, an anchor may be applied and pretensioned if necessary. Each stage is then computed, and any result is carried to the next stage, which means the results captured by the final stage has accounted for every previous stages. It is possible to capture the deformations of each stage.

An elastoplastic analysis has several configurations whose influences on the deformations are investigated. In the following section several initial settings in OptumG2 will be investigated before the simplified numerical model will be compared to the measurements.

6.1.2 Determination of the Initial Settings

This section is initiated by a study of influence, concerning the mesh and the required number of elements ensuring convergence of the deformation results. For this analysis lower bound elements are chosen, as this type provides conservative results. The elements surrounding the sheet pile wall have been refined to ensure that the deformations of the wall are captured sufficient. The example used in these studies is identical to the model used in section 4.5.

In appendix A.14.1 a study of convergence concerning the mesh using elastoplastic analyses is performed and the results are given. From this it has been chosen to use an appropriate number of 2000 elements in the future validations. The appearance is given in figure 6.2. Since the mesh is generated from scratch each time an analysis is performed, the newly created mesh may contain minor variations, as the generation is random. This may affect the results, thus a study is performed to investigate the influence of these variations. By performing identical analyses multiple times and comparing the results, the deviations are found. In appendix A.14.2 this study is given. Since the deformations of the sheet pile wall have a maximum of around 40 mm and the found variations are equal to 2 %, the deviations are found to be of insignificant

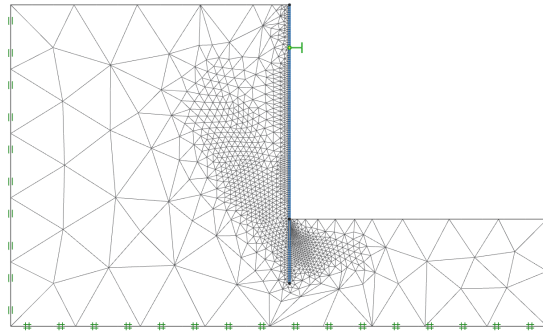


Figure 6.2: The used OptumG2 model with appropriated mesh used in the studies.

influence and are neglected in the comparisons. However, in the following sensitivity studies are computed three times each, and a mean value is determined.

Another study is performed concerning the size of the soil domain. When modeling the sheet pile wall the size of the soil domain is specified entirely by the user. However, it must be of sufficient size not to interfere with the more essential domains near the sheet pile wall given by the failure zones. There is no upper limit in the scale of the computed soil domain, however it is of interest to keep the size as small as possible to prevent inappropriate computational time. The influence of the size of the soil domain is therefore investigated. In appendix A.14.3 the results are given and explained, and the results reveal that the size of the soil domain has an influence, but the coherence in the results is rather vague. The greatest deviation is approximately 5 % by increasing the overall size of the soil domain by a factor of 2.5. However, this leads to increased computational time, and according to the results greater accuracy is not ensured. It has been chosen not to specify the required size of the soil domain further.

The final determination of initial settings is performed by investigating the appropriate number of stages in the elastoplastic analyses which is required to obtain convergence. The results are presented in appendix A.14.4, which reveal that 5 stages are sufficient for this example. The optimal settings determined in the studies of this section will be implemented in the following sections.

6.2 Numerical Model Based on Field Example

To test the reliability of a numerical model, deformation data is compared to in situ field measurements. A numerical model will always be an approximation, as the field conditions are often very complex and nearly impossible to replicate, thus it is important to create the numerical model by lowering the complexity of the real case while still being as comparable as possible. Using different theories to describe a given behaviour it is important that the best approximation is chosen or altered accordingly. The goal of this section is to use a simple numerical model to describe the deforming behaviour of a sheet pile wall and compare the resulting deformations to in situ measurements. Parameters used in this comparison are captured from the design report for the given project.

In the following sections, inclinometer measurements from a project called *Dokk1* will be elaborated, followed by a short description of the project from which the field measurements are given. Finally the numerical model will be presented, and the related approximations will be given which will end up in an examination of any deviation.

6.2.1 Data Measurements in the Field

Inclinometers are used to measure the deformations of a sheet pile wall. The procedure is described in appendix A.15 and results in a series of inclinations, which by integration will lead to the determination of the deformations of the sheet pile. This integration is possible, when at least one exact location of the wall is known, which is commonly chosen to be the embedded tip, as the tip is assumed to be fully fixed in the ground. However, the method does not include considerations concerning parallel shift of the wall.

As the inclinometer casing is welded to the web of the sheet pile, the measuring directions *A* and *B* differs to the anticipated direction of movement. These directions are used, converting the direct data into deformations normal and tangential to the direction of wall, *N*- and *T*-directions respectively which are illustrated in figure 6.3.

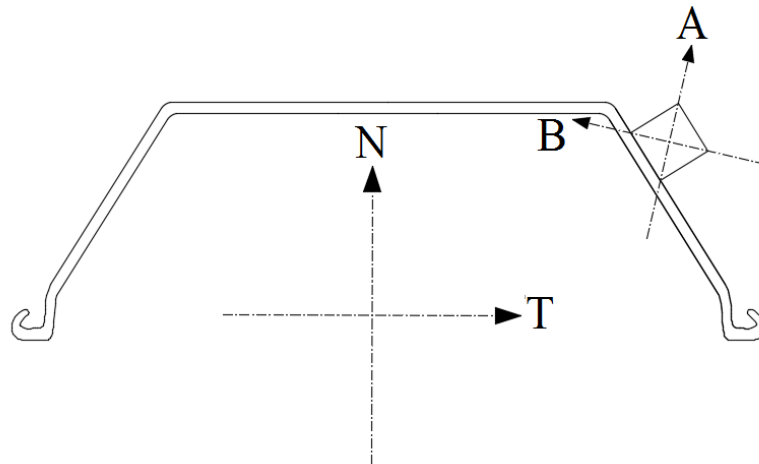


Figure 6.3: Direction of measurements compared to the direction of anticipated movement of the wall.

The inclinometer casing is permanently welded to the wall. This provides the opportunity of measuring the deformations over time. This is useful as excavation and installation of anchors happens gradually, thus it is possible to evaluate the stages individually.

6.2.2 Description of the Dokk1 Project

The inclinometer measurements are performed during the construction of *Dokk1* in Aarhus. The measurements were performed between 2011 and 2013 which accounts for the various phases related to the construction of the retaining walls.

The considered retaining wall was performed as a sheet pile wall with an excavation level of approximately 10 m and an embedment depth of up to 14 m. Four levels of inclined grout anchors were installed in the wall, as the soil primarily consisted of fat clay having a high plasticity index which is typical for the soil under Aarhus. It has been chosen to examine the data of inclinometer *iV32* which is located in the western side of the excavation site. This inclinometer is chosen due to the availability of geotechnical examinations and measurements being well documented for that specific area. In figure 6.4 the excavation site is pictured which marks the locations of the inclinometer casings and the geotechnical examinations.

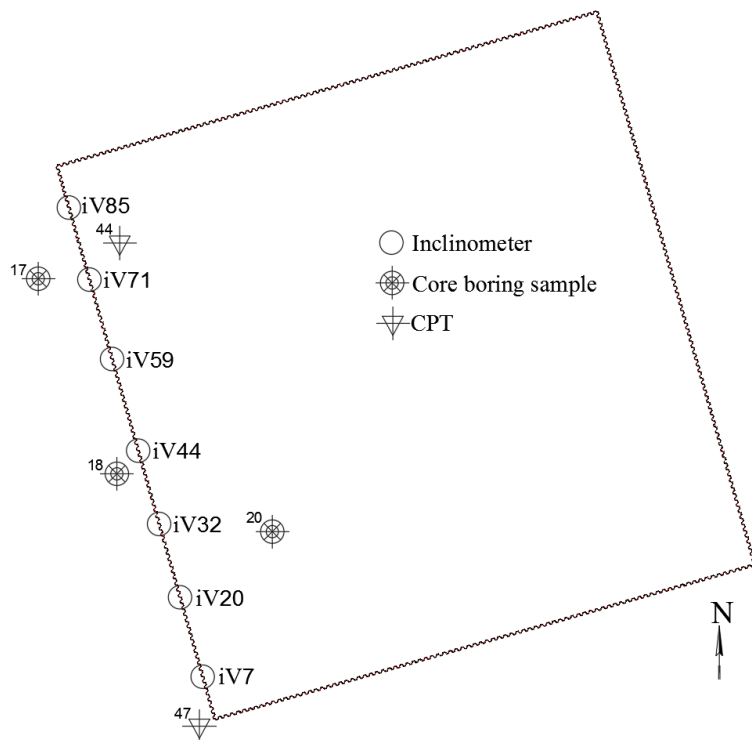


Figure 6.4: Construction site of *Dokk1* with related inclinometer casing placements and available geotechnical examinations.

The composition of the soil strata for *iV32* has been extracted and replicated from core boring sample 18, which is given in appendix A.16. Furthermore *CPT44*, which is given in appendix A.17, is also chosen for additional determination of soil parameters used in the later sections.

The sheet pile wall consists of PU32 sheets and is installed as a staggered wall, which is mentioned in section 1.1.2. From the geotechnical reports, the following information is extracted and given in table 6.1.

Søvind Marl has unique properties. It separates itself from other clayey materials by having a high plasticity index, high content of limestone and the behaviour of the clay is highly depending of the water content. The plasticity index is defined as the difference between the liquid limit and the plastic limit where Søvind Marl clay usually has an index of 50 % to 200 %. The

6. DEFORMATIONS OF A SHEET PILE WALL

Table 6.1: Extracted information from the geotechnical report for the *Dokk1* project. The information is inserted in the numerical model.

| Soil | Description | Level | $\gamma_{dry}/\gamma_{sat}$ | φ | c |
|-------------------|-------------|----------------|-----------------------------|-----------|-----------|
| | | [m] | [kN/m^3] | [°] | [kPa] |
| Sand, fill | Coarse | +1.90 to -0.85 | 18.00/20.00 | 35.00 | 0.00 |
| Clay, fill | Fat | -0.85 to -4.35 | 17.00/17.00 | 15.00 | 4.00 |
| Sand, fill | Fine | -4.35 to -6.75 | 18.00/20.00 | 35.00 | 0.00 |
| Clay, fill | Fat | -6.75 to -7.60 | 17.00/17.00 | 15.00 | 4.00 |
| Clay, Søvind Marl | Very Fat | -7.60 to ? | 17.50/17.50 | 15.00 | 20.00 |

properties of this clay material varies over short distances which also makes it difficult to model. In the initial simplified numerical model this stratum will be based on approximations.

Information concerning anchors are given in table 6.2.

Table 6.2: Information regarding grout anchors used in the project *Dokk1*.

| Grout Anchors | Level | Angle | Diameter, Tendon | Length, Tendon | Pretention | Yield Strength | Young's Modulus |
|---------------|-------|-------|------------------|----------------|------------|----------------|-----------------|
| | [m] | [°] | [mm] | [m] | [MPa] | [MPa] | [MPa] |
| Anchor 1 | -0.3 | 24.0 | 36.0 | 29.7 | -260.0 | 950.0 | 210,000 |
| Anchor 2 | -3.6 | 22.0 | 36.0 | 29.7 | -260.0 | 950.0 | 210,000 |
| Anchor 3 | -4.3 | 25.0 | 36.0 | 29.7 | -260.0 | 950.0 | 210,000 |
| Anchor 4 | -6.2 | 25.0 | 36.0 | 29.7 | -260.0 | 950.0 | 210,000 |

Stages in the analyses have been created in order to simulate the installation of the anchors. Excavation is performed to the levels of the separate anchors which is followed by the installation and pretensioning of the anchors. Since anchors *A2* and *A3* have close proximity, these are approximated to be installed in the same level of excavation. An overview of the various stages is presented in appendix A.18.

6.2.3 Numerical Model based on the Dokk1 Project

Utilising the different stages, it is possible to extract deformation distributions for each stage which are comparable to the measurements in the field. It is important to note that deformations of the wall do not appear instantly, but will develop over time until an equilibrium is found. Measurements in the field were performed at different times, and it is not apparent whether the wall has reached equilibrium or not. In figure 6.5 the generated mesh and specific levels are shown.

From core boring sample 18, the levels were extracted and the parameters were given in the geotechnical report and the mentioned *CPT44*. The uncertainties concerning the determination of the geotechnical parameters are typically high, thus the parameters are usually conservative. In the advanced numerical model the parameters can be altered to account for this uncertainty, but this is not the case for the first comparison.

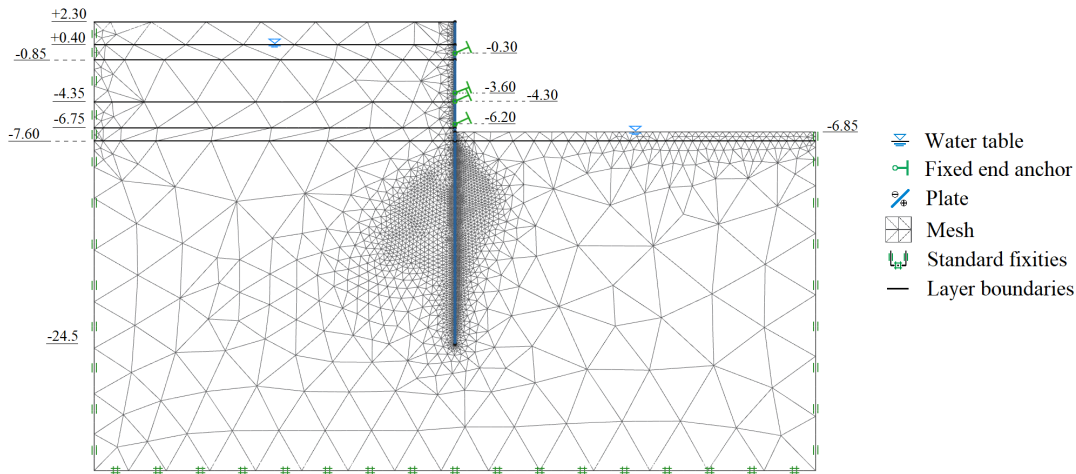


Figure 6.5: The numerical model and its features.

It has been chosen, to use the Mohr-Coulomb yield criterion for the fill strata consisting of sand and clay and Tresca yield criterion for the stratum consisting of Søvind Marl. This corresponds to the exclusion of the long term effect where the soil stratum is considered drained. As stated in section 3.2.1 the undrained condition of clay is well described using Tresca. The non-associated flow rule is chosen for the sand with a dilation angle determined according to section 3.2.2. For clay the associated flow rule has been chosen.

The simplified numerical model consists of four stages each accounting for the application of an anchor. Each time an anchor is installed the appropriated magnitude of the pretension has been applied. Figure 6.6 reveals the results from the initial numerical model which are compared to the in situ measurements.

From figure 6.6 it is evident that the numerical model is not appropriate approximation. The shape of the generated curve is significantly different and reveals a parallel drift of the lower part of the wall, which is caused by a rotation of the soil domain, possibly as a result of the assumed soil behaviour. However, the magnitudes of the local maxima of the deformation curves are rather similar, but do not appear in the same locations.

Several opportunities are available for optimisation of the model, as numerous parameters have not yet been altered and standard parameters and conditions have been used. In section 6.3 the influence on the deformations of several geotechnical parameters will be examined which will be used to create the optimised numerical model. The stages will also undergo a refinement in order to provide an equivalent fit to the different phases of the actual scenario.

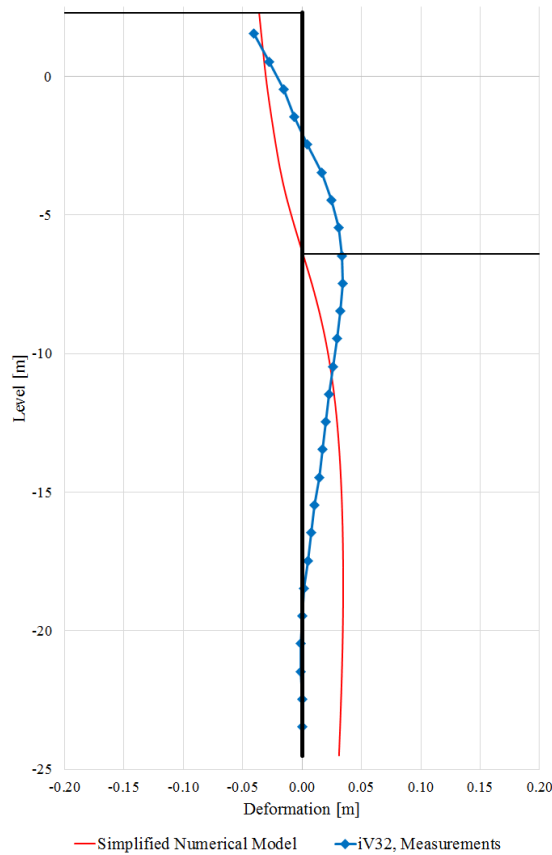


Figure 6.6: Comparison between the simplified numerical model and the in situ measurements.

6.3 Geotechnical Parameters Used in the Deformation Analyses

In general, geotechnical engineering has a long history of modeling based on empirical data, even though geotechnicians has a great theoretical and analytical understanding of the behaviour of the soil. This may be caused by long standing traditions and the safety of the past. Usually, as specific soil parameters are determined, empirical models are applied with correlation coefficients. These coefficients are based on experience and fitted to the location of the test. Thus a characteristic design parameter is obtained and can be used further in the design process.

Strength parameters, such as the friction angle and cohesion are all part of the important geotechnical parameters used in the design phase of geotechnical structures. Uncertainties may be related to the test methods for determination of these parameters, as mentioned. In the following, an introduction to the most common geotechnical tests, determining the parameters is given.

6.3.1 Determination of Geotechnical Soil Parameters

Technology is getting ever more advanced, which leads to new test methods being developed. However, new technology is usually expensive, thus simple test methods to determine geotechnical parameters are still used in the industry. This is the case for the field vane test that is used to determine the undrained cohesion of clayey soil materials. In appendix A.6.5 the concept of the field vane test is explained.

Among other in situ tests the newer methods CPT and SPT are used that are explained in appendices A.6.3 and A.6.4 respectively. These tests require heavier and far more expensive machinery than the field vane test, but are capable of determining several other parameters besides cohesion by extensive use of empirical formulas. The correlation is largely based on geographic location and engineering judgment which questions the uncertainties of these tests. Besides the in situ tests, there are laboratory tests such as the direct shear test and triaxial tests that are explained in appendices A.6.1 and A.6.2 respectively. These tests require an undisturbed soil sample from the site for testing purpose, and the laboratory equipments used are rather expensive.

As it appears, several test methods to determine the geotechnical soil parameters exist. A reasonably well developed soil model based on well described test methods increases the efficiency and precision of the numerical model. However, the accuracy of the tests is arguable since the tests may yield different results for soils located at the same site. Investigating the precision of the tests can be a everlasting task and instead the focus in section 6.4 will be on the influence of each parameter on the deformations of a sheet pile wall.

6.4 Sensitivity Analyses of Geotechnical Parameters

In section 6.1.2 the optimal settings for an elastoplastic analysis in OptumG2 were found. These settings will be utilised in the following sections, as the influence of various parameters is investigated. Only one parameter or setting must be altered separately in order to achieve results as accurate as possible for comparative purposes. Investigating a new parameter, the previous parameter will be reset to its standard value. For the purpose of higher precision each calculation will be run in a total of three times according to section 6.1.2. For this study a numerical model is used, referred to as the *reference example*.

Initially the numerical preconditions of the reference example will be elaborated, which is then followed by the results of the sensitivity studies. The sensitivity study deals with both the soil parameters and the anchor properties. Since the properties of the sheet pile are well known entities, the wall will not be studied.

6.4.1 Preconditions of the Reference Example

The reference example consists of the parameters given in table 6.3 that are equal to the parameter settings in the example in section 4.5. Only the embedment depth is different, which has been prolonged to three meters and the assumption of a full rigid sheet pile wall and anchor is removed. In figure 6.7 the reference example is illustrated with the relevant levels.

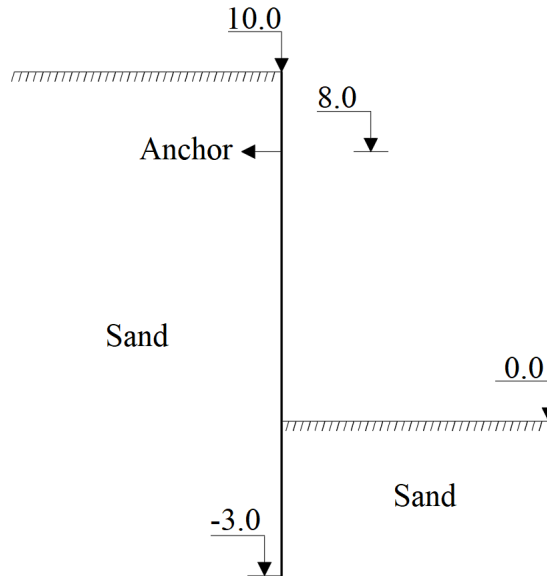


Figure 6.7: Reference example used in the sensitivity analyses.

Table 6.3: Soil parameters and conditions used in the reference example.

| Soil Parameters and Conditions | |
|------------------------------------|----------------------------|
| Material | Loose Sand |
| Friction Angle | 30° |
| Cohesion | 0 <i>kPa</i> |
| Flow Rule | Associated |
| Unit Weight | 19 <i>kN/m³</i> |
| Stiffness | 20 <i>MPa</i> |
| Poisson's Ratio | 0.2 |
| Initial Earth Pressure Coefficient | 1 |
| Wall/Soil Friction | 1 |

The bending moment and anchor force have been determined for the reference example which yields sufficient design of the sheet pile wall and anchor. The properties for the appropriate sheet pile and anchor are given in tables 6.4 and 6.5 respectively which will be used as input in the analyses.

The sheet pile wall consists of AU14 profiles which is possible to choose as a setting under Arcelor-Mittal products in OptumG2. The dimensions of the sheet pile are sufficient, as this size having a yield strength of 355 *MPa* is able to resist a bending moment of 235 *kNm/m*

Table 6.4: Properties of the appropriate sheet pile - AU14.

| Sheet Pile Wall <i>Moment = 235 [kNm/m]</i> | AU14 |
|---|----------------|
| Sectional Area | 132 cm^2/m |
| Plastic Section Modulus | 1163 cm^3/m |
| Moment of Inertia | 28680 cm^4/m |
| Young's Modulus | 210000 MPa |
| Yield Strength | 355 MPa |

Table 6.5: Properties of the appropriate anchor - C355.

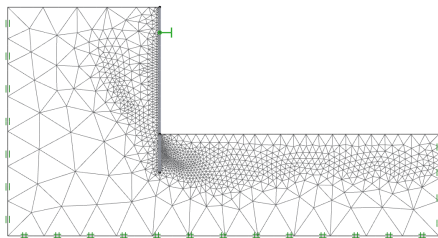
| Anchor <i>F_{anchor} = 170 [kN/m]</i> | C355 |
|---|--------------|
| Sectional Area | 5 cm^2 |
| Young's Modulus | 210000 MPa |
| Yield Strength | 355 MPa |
| Spacing | 1 m |

which is the design value. The design of the anchor has been performed in the same manner, thus both the sheet pile and anchor are capable of withstanding the different exposures, but not act as rigid structures, which is preferable.

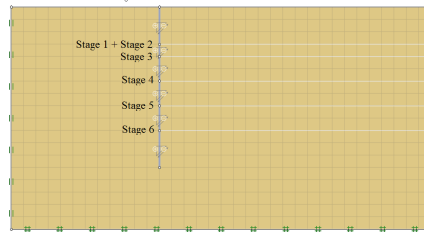
The mesh settings, as a result of section 6.1 are shown in table 6.6 and a generated mesh based on these settings is illustrated in figure 6.8a.

Table 6.6: Mesh settings for the reference example.

| Mesh Settings | |
|------------------------------|-------------------|
| Element Type | Lower |
| No. Of Elements | 2000 |
| Mesh Adaptivity | Shear dissipative |
| Adaptive Iterations | 3 |
| Maximum mesh size along wall | 0.1 m |



(a) A generated mesh for the reference example based on the mesh settings listed in table 6.6. The size of the soil domain magnitude is apparent as well.



(b) Gradually excavation levels of the different stages used in the reference example.

Figure 6.8: OptumG2 initial settings for the sensitivity analyses.

A total of six stages has been chosen in agreement with section 6.1.2. The anchor has been applied to the sheet pile wall in stage 2 and the excavation level is gradually lowered in the rest of the stages, as it appears in figure 6.8b. The size of the soil domain has been chosen so the boundaries do not interfere with the failure zone.

6.4.2 Sensitivity of Parameters

By altering the parameters separately, deformations along the full course of the sheet pile wall are extracted for comparison purposes. In figure 6.9a a deformation plot from OptumG2 is shown which has been converted in figure 6.9b.

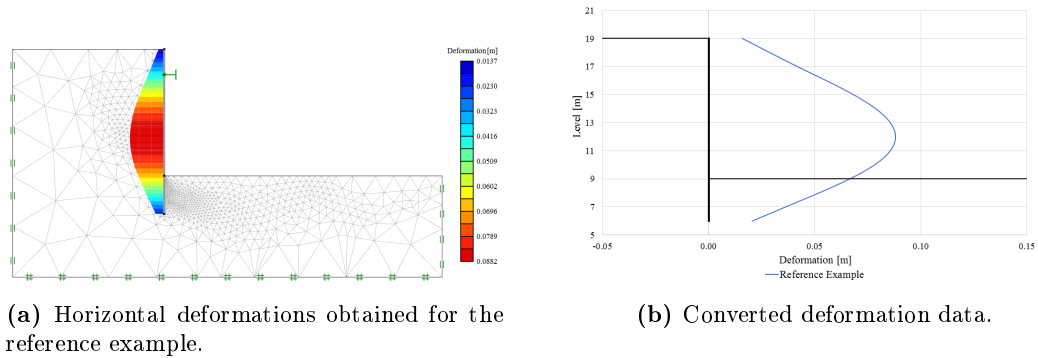


Figure 6.9: Deformation results for the reference example.

The deformation curves given in figure 6.9 are of opposite sign, which is as a result of how the sheet pile wall is modeled in OptumG2. The real behaviour is illustrated in figure 6.9b. The results of the sensitivity study for the parameters are given in appendix A.17.1, where a plot is illustrating the influence for each parameter alteration.

In figure 6.10 the influence of each parameter on the horizontal deformations is illustrated. The figure illustrates the relative percentage deviation from the reference example, as a function of the percentage change of the values. The altered values are given in table 6.3.

It is evident from figure 6.10 that the influence is nonlinear for each parameter. However, some of the parameters reveal a linear curve, but this is due to the amount of data points captured. It is important to note, that only one stratum represent the full soil domain. This is, as mentioned not the case for the numerical model in the *Dokk1* project.

The strength parameters such as the friction angle, cohesion and the unit weight shows significant influences on the deformations. This is both apparent in figure 6.10 and in appendix A.17.1. Other parameters such as the wall friction, modulus of elasticity and the initial condition have less significant influences, but still significant enough requiring alternation in the enhanced numerical model.

A study of the anchor settings has also been done and the results are given in appendix A.17.2. The inclination angle of the anchor has a great influence. As the anchor is inclined the resistance

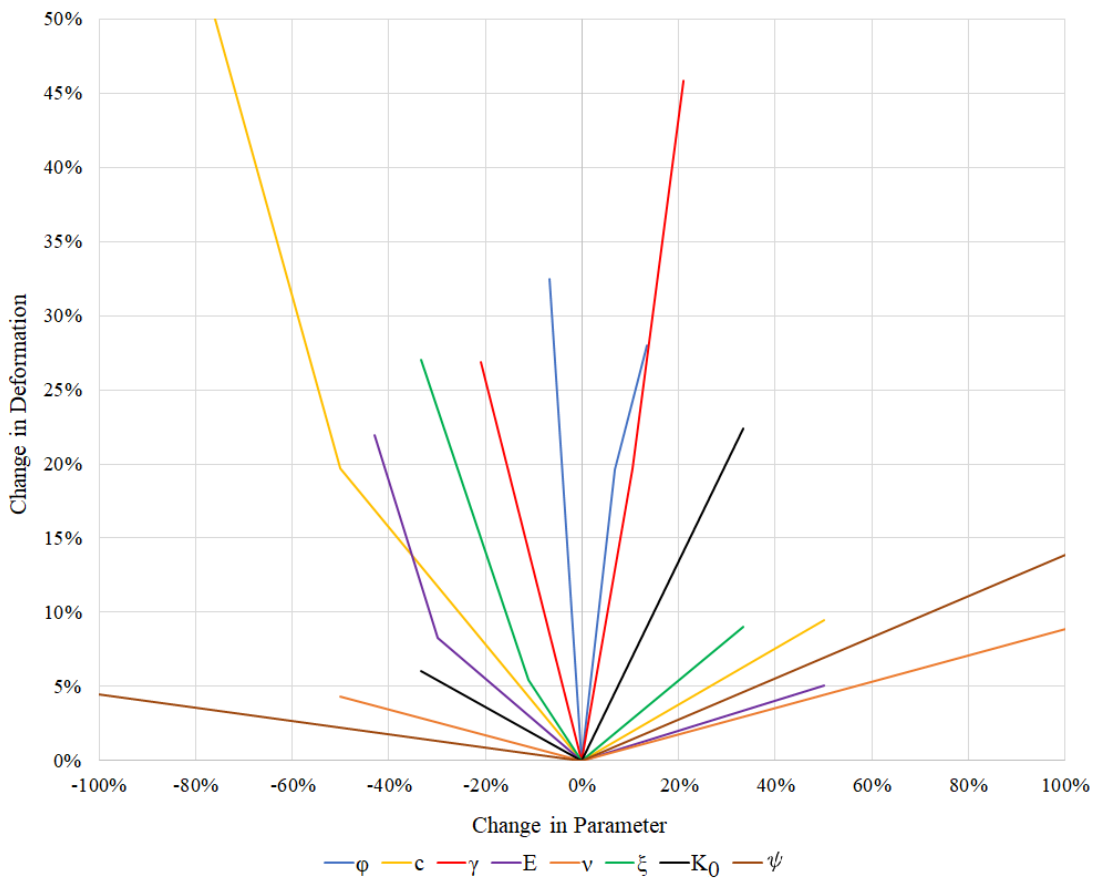


Figure 6.10: Influence of the different parameters. A steep curve yields relatively great influence, meaning a small change in the parameter has a great influence on the deformations of the sheet pile wall and vice versa.

will decrease and larger deformations appear. This is due to the the horizontal component of the resistance of the anchor decreasing and as the earth pressure acts horizontally at any time.

Another interesting result is the anchor level in figure A.188 which reveals that the positioning of the anchor is not without influence. It must not be placed to high on the wall, otherwise the maximum deformation will increase at the middle of the wall. However, the anchor position could actually be optimised in the reference example by lowering the position which is evident in the figure.

The quality of the numerical results are equal to the quality of the numerical approximation. Knowing which parameters has the greatest influence, it is also known which approximation will have to be as accurate as possible, e.g. the unit weight of the soil is important, thus the soil stratum must be determined accurately. Judging from this study no parameter is without any significant influence. In the following an enhanced numerical model based on the simplified will be created by optimising the parameters and conditions.

6.5 Optimisation of the Numerical Model

In comparison to the simplified model investigated in section 6.2, any parameter included in the calculations will be altered in order to fit the soil profile for the *Dokk1* project which is required when creating the enhanced numerical model. By using the information obtained from the CPT together with the equations stated in section 3.1, the values for the respective strata are determined. The values are given in table 6.7.

Table 6.7: Calculated parameters for the respective soil strata used in the enhanced numerical model.

| Soil | E | ν | K_0 | δ |
|-----------------------|-------|-------|-------|---------------|
| | [MPa] | [-] | [-] | [°] |
| Sand, fill | 40.0 | 0.20 | 0.80 | $2/3 \varphi$ |
| Clay, fill | 2.5 | 0.25 | 0.30 | $1/3 \varphi$ |
| Sand, fill | 10.0 | 0.20 | 0.67 | $2/3 \varphi$ |
| Clay, fill | 2.5 | 0.25 | 0.30 | $1/3 \varphi$ |
| Clay, Søvind Marl[29] | 50.0 | 0.10 | 0.73 | $1/3 \varphi$ |

For the determination of ν known values have been used. As it appears from table 6.7, Søvind Marl clay has a relatively low value of ν which is related to the properties of the clay mentioned in section 6.2.2. Furthermore, the Søvind Marl stratum is partitioned in four different strata in order to capture the change in the properties, as the depth increases. Through the four strata the cohesion is ranging from 15 - 20 *kPa* increasing downwards. Besides the change of the parameters, the stages have been optimised to fit the different phases of the *Dokk1* project. The stages are apparent in appendix A.18.

The Søvind Marl clay behaviour has been modeled according to the Mohr-Coulomb yield criterion. This is due to the resulting deformations of the sheet pile wall being apparent in the long term case, thus the soil strata are considered drained. In contrary, clay strata in short term are considered undrained which corresponds to the Tresca criterion. This case is seen in appendix A.19. Applying the Tresca criterion, Poisson's ratio is equal to 0.5 which corresponds to an incompressible material. This leads to a parallel shift of the wall situated in the respective stratum.

Besides the yield criterion, the enhanced numerical model is also accounting for the installation of staggered wall. The stiffness of the wall has been reduced and is considered permeable beneath level -8.5 where the staggering appears. As OptumG2 is only capable of handling 2D cases, it is not possible to model the staggered wall directly. However, a staggering of the wall would influence the strength negatively as some piles would have a significantly shorter embedment depth. A reduction of the stiffness of 1/3 is implemented, as a third of the wall is staggered. In appendix A.19 the inclusion of the staggering has been studied and compared to a identical wall not considering staggering.

The results obtained using the enhanced numerical model are given in figure 6.11 where also the measured deformations are given.

Compared to figure 6.6 in section 6.2.3, the enhanced model reveals a clear improvement of the results. The development of the deformations follows the shape of the experimental results and

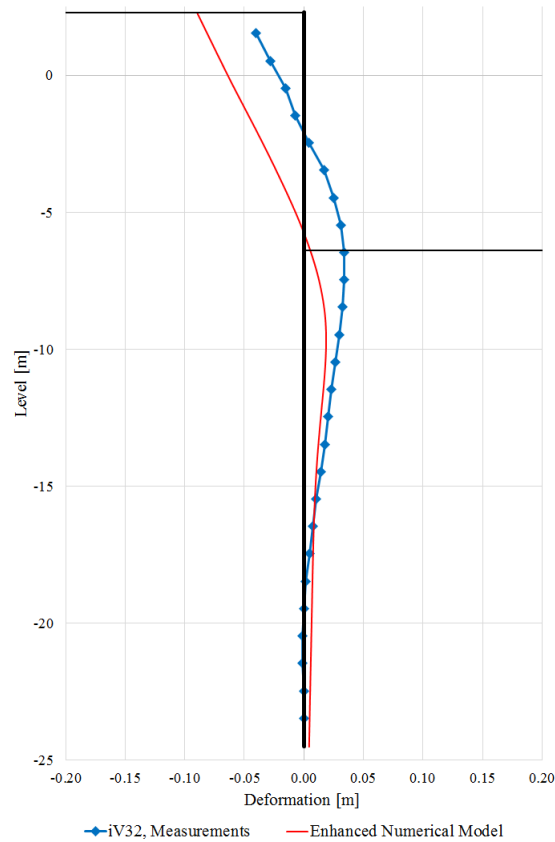


Figure 6.11: Enhanced numerical model compared to the measurement in the field.

the parallel shift has almost disappeared. The small parallel shift still appearing, is caused by the Poisson's ratio for the strata causing a characteristic movement of the wall. As stated in section 6.2.1, the parallel shift cannot be measured through the used method of inclinometers, as the tip of the wall must be considered completely fixed which may be the reason for the small deviations at the bottom of the wall in figure 6.11.

6.5.1 Alteration of the Numerical Model

The deformations at the top of the wall for the enhanced model indicate large deviations compared to the simplified numerical wall. The top deformations are caused by the pretension of the anchors that pull the wall towards the soil. Considering the deformations, the pretension appears to have a stronger pull in the enhanced model than the simplified which is not the case. This is as a result of the change in the parameters such as the wall friction and the initial stress conditions. The deformations obtained are approximately twice the size of the measurements which may be explained by several factors as follows:

- The geotechnical parameters are determined conservatively
- Stages and ground levels diverge from the phases in the actual scenario
- The actual pretension of the anchors does not correspond to the stated

The determination of geotechnical parameters is still a highly debated subject, as the variation of these parameters over a rather small area may be significant and this effect may cause conservatively determination to account for this uncertainty. Increasing the unfavourable parameters in the numerical model, the deformations would increase correspondingly. The unit weight of the soil is of significantly importance as it influence the magnitude of the earth pressure directly, thus conservative or inappropriate determination of the boundaries of the strata yields great influence. Easing these parameters is solely based on guesses, as no further information is provided for a better estimate. The same applies to the modeling of the stages and the corresponding excavation levels, as the numerical model has been carefully modeled according to the information provided.

The deviations may also be caused by the magnitude of the pretension in the four anchors as stated. Since the upper anchor levels have significant influence on the deformations in the top of the wall, deviations between the designed pretension and the modeled could interfere with the results. Thus an altered numerical model is investigated by changing the magnitude of the pretension for the four anchors to fit the deformation curve for the measurements in the field.

The magnitude of the pretension is 260 *MPa* according to the designed values for all four anchor levels. In table 6.8 the fitted magnitudes of the pretensions are given. The resulting deformations are illustrated in figure 6.12.

Table 6.8: Altered magnitudes of the pretensions resulting in fit of the measured deformations.

| | Designed Pretension | Fitted Pretension | Percentage of Designed Magnitude |
|----------|--------------------------------|------------------------------|---|
| | [<i>MPa</i>] | [<i>MPa</i>] | [%] |
| Anchor 1 | 260 | 195 | 75 |
| Anchor 2 | 260 | 45 | 17 |
| Anchor 3 | 260 | 90 | 35 |
| Anchor 4 | 260 | 350 | 135 |

A near perfect fit is achieved by altering the pretension of the anchors. However, the new values are far from the designed values, thus it may be concluded that the source of the deviations in the enhanced model are not entirely related to the magnitude of the pretension.

An issue related to the SLS case concerning strain compatibility may rise, as great elongations will appear before reaching yielding using high strength anchor tendons. The issue has been investigated for an anchor situated in the *Dokk1* project and is presented in appendix A.20. The study reveals that for the given properties of the anchor, failure will not be an issue reaching the calculated deformations. However, as the test load is introduced, yielding occur in small scale which is not desired. The results appear in appendix A.20 as well.

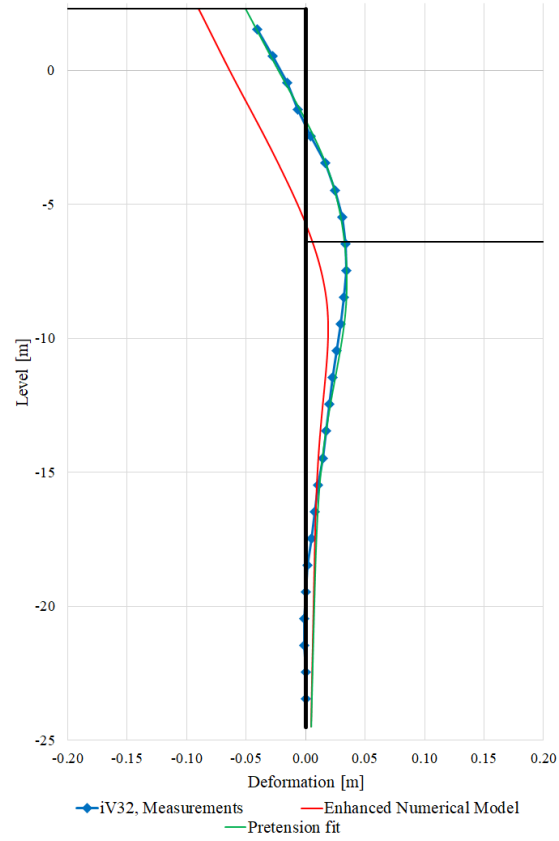


Figure 6.12: Altered numerical model with fitted pretension of anchors.

Discussion

The project is partitioned in three parts. A discussion on top of the investigations of each part will appear.

In Denmark the earth pressure theory of Brinch Hansen is highly praised, as it is applied for the design of retaining walls determining the earth pressure. The theory has proven reliable since it was proposed several decades ago, as failure of walls designed according to this theory is rare. This is despite the theory having flaws and being immoderate in some aspects. Apart from the theory of Brinch Hansen other methods exist when designing a retaining wall analytically. A small selection of these theories has been presented in chapter 4 and the differences are evaluated in section 4.5.

As the use of numerical modeling in geotechnics have become commonly accepted, the analytical methods have been compared to a numerical approach which utilises the stress conditions in an FE representation of the soil. The results for the analytical methods deviate both in the anchor force and plate moment where the German standard yields the lowest anchor force and the theory of Brinch Hansen gives the lowest plate moment. This deviation is due to several factors in the calculations, as all of the theories states that equilibrium must be fulfilled to secure stability of the wall. The earth pressure is the essential factor in the design of retaining walls and considering the determined earth pressure distributions given in figure 4.15, great differences are apparent. These differences are found in the relevant assumptions and earth pressure coefficients. The method of Brinch Hansen and the KSP method reveal great similarities compared to the results of the German standard which differs notable regarding the earth pressure distributions. This leads to the significant deviations in the design parameters given in table 4.3. When comparing the analytical methods to the numerical approach, great deviations are found. These deviations may be caused by the assumption that the sheet pile is a full rigid plate in the numerical model and this leads to an overestimation of the design parameters. Using optimisation techniques both the anchor force and the plate moment may be lowered accordingly as the sheet pile profiles are utilised to its fullest potential, revealed by figure 4.16. Through optimisation, values are obtained in the same region as the analytical methods, which supports the validity of the analytical results. However, optimisation of the results is rather limited for the analytical methods. The theory of Brinch Hansens gives opportunities to optimise the design by introducing hinges in the calculations. The KSP method gives the same opportunity, but this is not possible according to

the German standard. Common for any of the approaches including the numerical, the placement of the anchor can be altered resulting in optimised earth pressure distribution considering the design of the wall. The relevant standards do not dictate one approach above another, as long as both horizontal and vertical capacity are proven, thus the least expensive solution and most accessible method is desirable.

The approaches evaluated in chapter 4 all produces characteristic design parameters for the use of ULS calculations. Considering the ULS case a study of the influence of the load bearing plate in a direct anchored sheet pile has been investigated. Yielding or collapse can be an issue when designing the load bearing plate according to the Eurocode and thus different dimensions have been examined. To make the examination, numerical modeling is utilised with different assumptions required to reduce the complexity of the model. It has been chosen to model the earth pressure on the sheet pile as a linear varying pressure. However, this inclusion makes the calculations more complicated, as the anchor force has to be of a certain magnitude otherwise the sheet pile will fail due to the earth pressure. The results of the parameter study performed for the load bearing plate are revealed in section 5.3. The study shows quite interesting results in some cases. Not surprisingly larger dimensions of the plate yield greater capacity of the sheet pile. However, this is not the case considering the thickness of the plate and the inclination of the anchor, where optimal values exist. The results of the thickness study have been discussed in section 5.3.1. The optimal value of the thickness more or less corresponds to the value determined using the Eurocode DS/EN-1993-5. According to the calculations the thickness does not completely decide the capacity. In contrary, the relationship between the thicknesses of the sheet pile and the load bearing plate is more essential, as the bending of the load bearing plate has to be able to follow the curvature of the sheet pile. The inclination of the anchor has influence on the capacity of the sheet pile, however the influence is insignificant compared to some of the other parameters. The optimal angle is around 20° according to the study. Using this angle, it is possible to save material and therefore lower the expenses using this inclination where possible. The idea of application of unconventional shapes is to utilise the amount of material to its fullest potential, as the cost of production may be increased compared to a rectangular or quadratic plate. As it is examined in section 5.3.6, an elliptical shape does increase the capacity of sheet pile. However, considering the material consumed it is evident that for equal mass the quadratic setup results in a greater capacity. The inclusion of additional material in the ends of a rectangular shaped plate has proven to be of insignificance. This conflicts with the expectations of the influence of the redistribution of the stresses caused by the supplementary material.

As multiple analyses - each including different settings and configurations - were necessary, it has been of interest to decrease the time consumption of the analyses. This includes both calculation time and time consumption during the modeling phase. As the model consists of a thin walled profile, the implementation of shell elements is an obvious possibility. Using shell elements a drastic reduction in the calculation time appears. However, considering the modeling phase of shell elements, these elements have been ignored, as the time consumed during modeling more than doubled, as it appears in appendix A.10.6. Ultimately, the implementation of a submodel of the structure has been chosen. Compared to shell elements the calculation time has doubled using submodeling, but the modeling phase has been halved correspondingly. If only one numerical model of the load bearing plate was needed for the analyses, e.g. the shape was kept at all time, the implementation of shell elements would be worthwhile.

Concerning the SLS case of the sheet pile wall, deformations have been considered. As for the numerical model examined in chapter 5, it is important to reflect on results obtained in the analyses of the deformations, as the models are based on approximations of the actual conditions. Often the parameters are determined conservatively and therefore calculated deformations are typically greater than what has been measured. The project deals with this issue and investigates the influence of the parameters on the deformations along with the validity of the model.

The simplified model in figure 6.6 clearly indicates that the model is not a good approximation. The behaviour of the wall is different in shape and shows a parallel shift at the bottom of the wall. By investigating the important features of the numerical software and recognising the influential geotechnical parameters the enhanced numerical model has been created. The wall curvature is captured approximately, but the magnitude does not correspond to the measurements, despite all the correct values have been used according to the geotechnical reports and examinations. The parallel shift has also almost disappeared for the enhanced model and it has been found that modeling the behaviour of the Søvind Marl clay according to Trescas yield criterion, results in the soil surrounding the wall moving as a solid body. By decreasing the value of Poisson's ratio the parallel shift decreases accordingly. This effect is not revealed in the sensitivity study of the geotechnical parameters. The parallel shift may be true, as a parallel movement of the wall is not possible to capture by the measurement method using inclinometers. By altering some of the parameters such as the pretension, it is possible to reach the exact curve of the wall. However, this altering is based solely on guesses. The pretension is a rather uncontrollable size, and it has been proven that the magnitudes have to be lowered compared to the provided data in order to fit the deformations. This may be a result of slacking of prior tensioned anchors as a lower level of anchors are installed and pretensioned. However, the magnitude of the pretension for each anchor is highly unlikely to be the sole reason of the deviation for the deformation results. The real deviation is probably found in a mixture of conservative parameters, soil and water strata, and anchor and wall parameters. Changing any of these values or settings would be based on an estimated guess, nullifying the quality of the comparison. The geotechnical examinations are also done in a rather large proximity to the iV32 inclinometer casing. This may result in the soil strata, at the casing, varying from the core boring sample 18 which is utilised in the numerical model.

Setting up the numerical model can be a challenging task based on this knowledge from the deformation study. The ultimate goal is to represent the real model as close as possible by making various approximations based on valid assumptions. The real model is often highly complex and requires an immense amount of information to describe in detail. However, by reducing the complexity of the model while still keeping the key elements, a valid approximation of the model can be obtained. Thus, recognising which element is important for the model, is a vital process when making the numerical model. However, this require a heavy amount of information which is clearly shown from this study. The information needed to design the wall for ULS cases is rather small, compared to making a well fitted estimate of the deformations. Thus, the industry faces great challenges when it comes to describing the soil.

Conclusion

Sheet piling is a useful tool for retaining soil in excavation sites where surroundings do not allow for establishment of slopes. The earth pressure acting on the wall defines the design criteria of the wall, which is caused by the properties of the soil as well as outer surface loads.

The initiating problem stated in section 2.2 has been investigated, which this project is a result of. The problem statement is rather broad and due to the time frame it has not been possible to examine every single aspect. The project deals with determining of the actions on the sheet pile wall, which are used in the design phase including ULS and SLS cases. In SLS the deformations of the wall are considered and proven acceptable. For ULS only a small selection of topics have been examined.

Through the study of the calculation methods for designing a retaining wall, it can be concluded that the analytical approaches have limited optimisation opportunities. Using numerical tools, optimised results can be obtained without greater complications leading to a cheaper configuration of the wall.

On top of the ULS study of the load bearing plate it is found that design proposed by the Eurocode is sufficient. Through optimisation of the parameters a more appropriate design can be obtained. Furthermore it is concluded that the implementation of time reducing initiatives has succeeded, as the computational time as well as the modeling phase have been reduced remarkably.

The numerical model concerning the behaviour of the wall has proven to be a proper approximation, as the deformations results are in agreement with the measurements provided from field tests. It has been found through the study that the precision of the determination of the soil parameters and soil behaviour models are significant. The structural properties such as the resistance of the wall and the pretensioning of the anchors are also important. However, these are determined with higher accuracy. On top of this and the discussed topics it must be concluded that by the proper precautions the deformations of a sheet pile wall can be calculated with great accuracy.

Bibliography

- [1] Ditte Møller. Picture: Transbay transit center, 25-03-2015. Photographed.
- [2] Erik Gammeljord. Picture: Esbjerg harbour, 11-05-2017. Photographed.
- [3] Sheet-piling.ru. Picture: Sports stadium warszawa, polen, 09-05-2017.
URL: <http://www.sheet-piling.ru/upfiles/201408455678731.jpg>.
- [4] ArcelorMittal. Sheet pile catalogues, 04-11-2016. Mail correspondence with ArcelorMittal providing old sheet pile catalogues dating from 1986 to 2016.
- [5] N.K. Ovesen, L.D. Fuglsang, G. Bagge, and A. Krogsbøll. *Lærebog i Geoteknik*. Polyteknisk forlag, 2012.
- [6] Macalloy. Macalloy 1030 and s1030 post tensioning bar, 07-06-2017.
URL: <http://www.macalloy.com/products-and-services/macalloy-1030-and-s1030-post-tensioning-bar.html>.
- [7] A Global Network Of Experts. Bbr ground anchors, 16-01-2017.
URL: <http://www.bbrnetwork.com/technologies/ground-anchors.html>.
- [8] The German Geotechnical Society. *Recommendations on Excavations EAB*. Wilhelm Ernst & Sohn, 2014.
- [9] S. Gundorph. Spidsbæreevne af indfatningsvægge - baseret på litteratursøgning, 27-09-2016.
URL: <http://www.danskgeotekniskforening.dk/sites/default/files/pdf/pdf2010/Powerpoint.Spidsb%C3%A6reevne.080210.pdf>.
- [10] Prof.dr.ir. A. Verruijt Prof.ir. A.F. van Tol. *Steel Sheet Pile Walls In Soft Soil*. DUP Science, 2002.
- [11] INOXLIN Connecting Design. Anchor tendons for sheet pile systems, 04-01-2017.
URL: <http://www.inoxline.dk/Macalloy%20Ankerstang.html>.
- [12] J. Bjerre, N.S. Hansen, D. Høybye, and C. Milling. *Find formelen Geoteknik*. Polyteknisk Forlag, 2014.

- [13] S. Hilary B. John, C. Tim and B. Michael. *ICE Manuals of Geotechnical Engineering, Volume 1*. Institution of Civil Engineers, 2012.
- [14] Ramboll Danmark A/S. *Ballasttal - Sundolitt*. Ramboll, 2005.
- [15] National Cooperative Highway Research Program. *NCHRP - Synthesis 368 - Cone Penetration Testing*. Transportation Research Board, Washington 2007.
- [16] K. Krabbenhøft. *Basic Computational Plasticity*. Department of Civil Engineering, Technical University of Denmark, 2002.
- [17] A.P.S. Selvadurai R.O. Davis. *Plasticity and Geomechanics*. Cambridge University Press, New York, 2002.
- [18] W. Powrie. *Soil Mechanics, Concepts and Applications, 2nd Edition*. Taylor & Francis Group, LLC, 2014.
- [19] K. Krabbenhøft, AV. Lymain, and J. Krabbenhøft. *OptumG2 - Theory*. Optum Computational Engineering, 2016.
- [20] R. de Borst P. A. Vermeer. *Non-associated Plasticity for Soils, Concrete and Rock*. Delft University of Technology, 1984.
- [21] B.C. Jensen and B. Bonnerup. *Plasticitetsteori*. Nyt Teknisk Forlag, 2014.
- [22] M.P. Nielsen. *Limit Analysis and Concrete Plasticity*. Department of Structural Engineering and Materials, Technical University of Denmark, 1999.
- [23] ThyssenKrupp GfT Bautechnik. *Sheet Piling Handbook Design*. ThyssenKrupp GfT Bautechnik, 2008.
- [24] E. Kranz. *Über die Verankerung von Spundwänden*. Ernst & Sohn, 1953.
- [25] N. Mortensen and W.P. Lund. *KSP-beregning af Jordtryk på Spunsvægge - dgf-Bulletin 13*. Dansk Geoteknisk Forening, 2012.
- [26] K. Krabbenhøft, AV. Lymain, and J. Krabbenhøft. *OptumG2 - Analysis*. Optum Computational Engineering, 2016.
- [27] ArcelorMittal. Sheet piling products, 02-11-2016.
URL: <http://sheetpiling.arcelormittal.com/section/more/id/13/referer/usections/name/usections>.
- [28] B. de Saint-Venant. *Memoire sur la torsion des prismes*. S.l., 1853.
- [29] Geo. 89800 ny baneforbindelse vejle fjord, 17-03-2017.
URL: http://www.vejdirektoratet.dk/DA/vejprojekter/vejlefjord/Dokumenter/Documents/Sk%C3%B8n%20af%20jordparametre%20for%20tunnel_linje%20D_med%20bilag.pdf.
- [30] Nidal Khoury. Picture: Secant piled wall with iconic emirates towers as a backdrop, 09-05-2017.
URL: https://upload.wikimedia.org/wikipedia/commons/d/d3/Dubai_construction_1.jpg.

-
- [31] pkomarpdbgi. Picture: Soldier pile, 09-05-2017.
URL: <https://www.flickr.com/photos/128359845\spacefactor\@m{}N04/15437607466/in/photolist-pwaLRY-7x9maZ-8N4WkY-dWF5Yg-q1yguh-q2jbj1-pLeyw6-p6EeRS-78aGKf-nqez7k->
- [32] Geotech. Geotechnical data for cohesion, 27-09-2016.
URL: <http://www.geotechdata.info/parameter/cohesion.html>.
- [33] Yeung & Kitch Coduto. Ce 326 mod 12 9a direct shear test, 09-02-2015.
URL: <https://www.youtube.com/watch?v=Iqw00Z4eCT0>.
- [34] Bishop and Bjerrum. Triaxial test device diagram, 18-05-2017.
URL: <https://zh.wikipedia.org/wiki/File:Paper4g.jpg>.
- [35] Yeung & Kitch Coduto. Ce 326 mod 12.9b triaxial shear test, 09-02-2015.
URL: <https://www.youtube.com/watch?v=hq4U1Lm8oIs>.
- [36] P. K. Robertson and K. L. Cabal. *Guide to Cone Penetration Testing for Geotechnical Engineering, 6th Edition*. Gregg Drilling & Testing, Inc., 2015.
- [37] Lusilier. Cone penetrometer, 18-06-2013.
URL: https://commons.wikimedia.org/wiki/File:Cone_penetrometer.svg.
- [38] Geotechnical and Foundation Engineering. 2.4.3 standard penetration test astm d1586-11, 16-02-2017.
URL: <http://foundationeng.blogspot.dk/2015/07/243-standard-penetration-test-astm-d1586.html>.
- [39] J. E. Bowles. *Foundation Analysis and Design, 5th Edition*. The McGraw-Hill Companies, Inc., 1996.
- [40] geotechdata.info. Standard penetration test, 16-02-2017.
URL: <http://www.geotechdata.info/geotest/standard-penetration-test.html>.
- [41] Dansk Geoteknisk Forenings Feltkomité. Referenceblad for vingeforsøg, August 1999, 3rd Edition.
URL: http://www.danskgeotekniskforening.dk/sites/default/files/pdf/referenceblade/Referenceblad_201-Vingeforsoeg.pdf.
- [42] K.W. Johansen. *Beregning af Krydsarmerede Jernbetonpladers Brudmoment*. Dansk Byggeskik, 1931.
- [43] Autodesk Help. Examples of contact, 15-03-2017.
URL: <http://help.autodesk.com/view/ASMECH/2014/ENU/?guid=GUID-BFD9750D-ADD3-4C57-BA5A-3413C8AA5454>.
- [44] CAE Associates. Why use mpc based contact for bonded connections, 15-03-2017.
URL: <https://caeai.com/blog/why-use-mpc-based-contact-bonded-connections>.
- [45] Ekrem Canli. Vertical inclinometer for measuring horizontal subsurface deformation in a borehole, 09-05-2017.
URL: https://upload.wikimedia.org/wikipedia/commons/e/e8/Vertical_inclinometert1.jpg.

Numerical Analyses of the Behaviour of a Sheet Pile Wall

Master's Thesis

Appendix



Group members

Erik Gammeljord

Mathias Sundahl Grønholdt

A. Appendix

Contents:

| | | |
|-------------------|--|---------|
| · Appendix A.1 | Relevant used Software | I |
| · Appendix A.2 | U-profile Change in History | II |
| · Appendix A.3 | Alternatives to a Sheet Pile Wall | III |
| · Appendix A.4 | Alternative to Direct Anchoring | VI |
| · Appendix A.5 | Parameters | VIII |
| · Appendix A.6.1 | Direct Shear Test | IX |
| · Appendix A.6.2 | Triaxial Test | XI |
| · Appendix A.6.3 | Cone Penetration Test (CPT) | XIV |
| · Appendix A.6.4 | Standard Penetration Test (SPT) | XVI |
| · Appendix A.6.5 | Field Vane Test | XVIII |
| · Appendix A.7.1 | Theorems for Yield Line Calculations | XIX |
| · Appendix A.7.2 | Analytical Validation of Yield Line Calculations | XXIII |
| · Appendix A.7.3 | Yield Line Calculation by Inclusion of Corner Effect | XXVIII |
| · Appendix A.8 | Calculation of the Load Bearing Plate, DS/EN 1993-5 | XXXIII |
| · Appendix A.9 | Arcelor Sheet Pile Catalogue | XXXIV |
| · Appendix A.10.1 | Study of Convergence | XXXV |
| · Appendix A.10.2 | Validation of Symmetry of Model | XXXVIII |
| · Appendix A.10.3 | Validation of Submodel | XL |
| · Appendix A.10.4 | Validation of Load Step Application | XLII |

A. APPENDIX

| | | |
|-------------------|--|---------|
| · Appendix A.10.5 | Validation of Multilinear Model | XLIV |
| · Appendix A.10.6 | Implementation of Shell Elements | XLVI |
| · Appendix A.11.1 | Dimension Study | LIII |
| · Appendix A.11.2 | Force Study | LVI |
| · Appendix A.12.1 | Appendix - Thickness Study of the Load Bearing Plate | LXII |
| · Appendix A.12.2 | Width Study | LXIX |
| · Appendix A.12.3 | Length Study | LXXV |
| · Appendix A.12.4 | Angle Study | LXXXIV |
| · Appendix A.12.5 | Thickness Study of Sheet Pile | XCII |
| · Appendix A.12.6 | Ellipse Study | XCVIII |
| · Appendix A.12.7 | 'Foot' Study | CV |
| · Appendix A.13 | Membrane Actions | CXI |
| · Appendix A.14.1 | Mesh Influence Study | CXVI |
| · Appendix A.14.2 | Influence of Repeatable Identical Analyses | CXVII |
| · Appendix A.14.3 | Soil Domain Influence Study | CXIX |
| · Appendix A.14.4 | Stage Influence Study | CXXII |
| · Appendix A.15 | Inclinometer Measurements | CXXIII |
| · Appendix A.16 | Core Boring Sample | CXXIV |
| · Appendix A.17 | CPT Sample | CXXIX |
| · Appendix A.17.1 | Parameter Influence Results | CXXXII |
| · Appendix A.17.2 | Anchor Parameter Influence Results | CXXXVII |
| · Appendix A.18 | Stages in the Deformation Analysis | CXL |
| · Appendix A.19 | Enhanced Numerical Model Study | CXLII |
| · Appendix A.20 | Deformations in Anchor Tendon | CXLIV |
| · Appendix A.21 | Dropbox Link | CXLVIII |

A.1 Relevant used Software

Listed below is the relevant software with version number used in this project.

| Software | Version |
|-----------------|-------------------|
| ANSYS Workbench | 17.1 |
| AutoCAD | 2017 |
| Inventor | Professional 2016 |
| OptumG2 | 2017.03.30 |
| MATLAB | 2016b |
| WINSPOOKS | 1.12 |

A.2 U-profile Change in History

In the past 20 years, the standard U-profile has seen different changes in its dimension. However, the sectional modulus per meter has not changed. In the following, data from catalogues in the last 20 years will be shown. In figure A.1 a outline of a U-profile with relevant notations is shown.

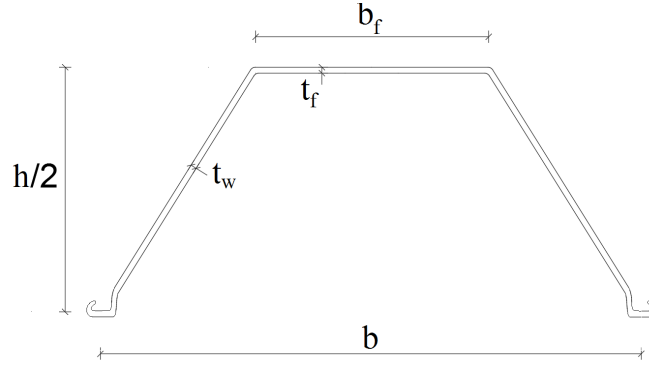


Figure A.1: Related U-profile for table A.1.

Table A.1: U-profile data from sheet pile catalogues through the last 20 years. Catalogue data provided by ArcelorMittal.

| Year | t_w | t_f | b | b_f | $h/2$ | Mass | | Modulus | |
|------|-------|-------|-------|-------|-------|----------|-----------|--------------------|----------------------|
| | | | | | | per pile | per meter | per pile | per meter |
| | | | | | | [kg] | [kg/m] | [cm ³] | [cm ³ /m] |
| 1986 | 10.0 | 13.0 | 600.0 | 335.0 | 200.0 | 187.0 | 146.0 | 514.0 | 2000.0 |
| 1987 | 9.7 | 12.4 | 600.0 | - | 200.0 | 180.0 | 141.0 | - | 2000.0 |
| 1990 | 9.7 | 12.4 | 600.0 | 365.0 | 200.0 | 180.0 | 141.0 | 480.0 | 2000.0 |
| 1995 | 10.0 | 12.4 | 600.0 | 307.0 | 215.0 | 180.0 | 141.0 | 529.0 | 2000.0 |
| 1997 | 10.0 | 12.4 | 600.0 | 307.0 | 215.0 | 179.0 | 140.0 | 529.0 | 2000.0 |
| 1999 | 10.0 | 12.4 | 600.0 | 307.0 | 215.0 | 179.0 | 140.0 | 529.0 | 2000.0 |
| 2001 | 10.0 | 12.4 | 600.0 | 307.0 | 215.0 | 179.0 | 140.0 | 529.0 | 2000.0 |
| 2006 | 10.0 | 12.0 | 750.0 | 336.0 | 222.0 | 164.6 | 129.2 | 579.0 | 2000.0 |
| 2012 | 10.0 | 12.0 | 750.0 | 336.0 | 222.0 | 164.6 | 129.2 | 579.0 | 2000.0 |
| 2016 | 10.0 | 12.0 | 750.0 | 336.0 | 222.0 | 164.6 | 129.2 | 579.0 | 2000.0 |

A.3 Alternatives to a Sheet Pile Wall

Secant Pile Walls

The secant pile wall is an alternative to the sheet pile wall and is preferred, when the installation is critical concerning the impact on the surroundings. This type of retaining wall is performed by drilling holes of wide diameters which is reinforced by either steel profiles or cage reinforcement and then filled with concrete. The drilling has a minimum of excitation of the surrounding, thus making it a prime example of a retaining wall used in denser settlements. The installation method can be rather complex, as every other drilling hole is performed initially and filled. Afterwards, the holes in between are drilled in half-hardened concrete which is necessary, as intersections are needed in order to waterproofen the wall and to make it coherent. Only every second pile is reinforced. If anchor levels are needed, the anchors are typically attached to the unreinforced piles. An example of a secant pile wall is shown in figure A.2.



Figure A.2: Typical secant pile wall with one anchor level besides a soldier pile wall.[30]

Other advantages are the working depth of the wall because of the strength and the waterproofing abilities. Also impulses are not apparent during installation which is preferred, if the surroundings are vibration sensitive. However, the installation of the piles is both expensive and risky compared to other types of retaining walls. The risk lies in the reinforcement of the piles. As the drilling shafts are often deep, it is difficult to place the steel profiles or cages and still obtaining the required cover layer. A general concern is cracks in the cover of the concrete pile that may result in corrosion of the reinforcement. Because of the economical aspects contractors usually select other types of walls if possible.

Another issue may be present where anchoring of the secant piles are needed. For installation purpose, a recess is created in the concrete pile to secure space for the anchor head. This recess is shown in figure A.3.

The angle of the recess varies depending on the inclination of the installed anchor, thus the width of the recess increases correspondingly. For anchors having great inclinations a deep recess has

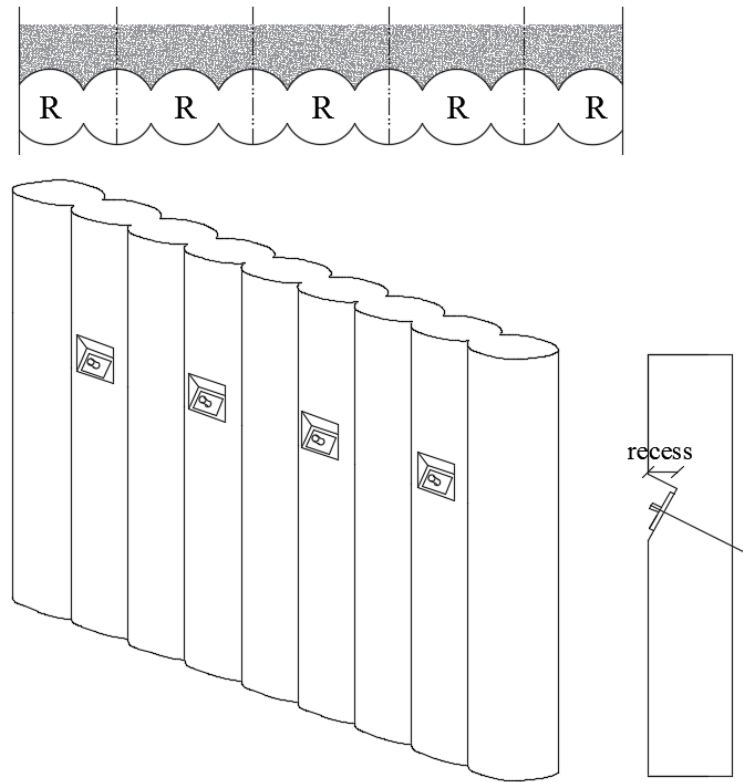


Figure A.3: Recess cut into a secant pile wall. *R* refers to reinforcement

to be cut in order to fit the anchor head in the pile which in some cases decreases the cross section significantly and thus the resistance of the secant pile wall. Currently no guideline is available for the maximum width of the recess corresponding to a given anchor force.

Soldier Pile Wall

Compared to other types of retaining walls the soldier pile wall is a cheap solution, as this type is usually built from what material is available. The method is often used for temporary setups which also means that the aesthetics of the wall are often insignificant. A typical soldier pile wall is pictured in figure A.4.



Figure A.4: Typical soldier pile wall.[31]

The wall is constructed by placing open steel profiles - such as IPE or HE beams - by driving, vibrating or boring¹. If drilling is preferred, the space between the soil and the profiles is filled with sand or gravel to prevent collapse of the drilling shaft and to stabilise the steel profile.

While excavation is performed, planks of wood or concrete are slotted in between the steel profile acting as stabilisers and preventing the soil from entering the excavation area. By the end of the excavation a full retaining wall is formed.

Other advantages of this type of wall are easy installation of the wall and that driving or vibration is not necessary which means that the method can be applied close to shock sensitive surroundings. However there are also disadvantages. The soldier pile wall is a temporary configuration, but may also be used as a permanent structure, if the aesthetics of the wall is acceptable. This type also has both limited resistance and working depth compared to other methods. It is however possible to apply anchors to increase the resistance, but this require application of a waling level, as anchors cannot be attached directly to the wall.

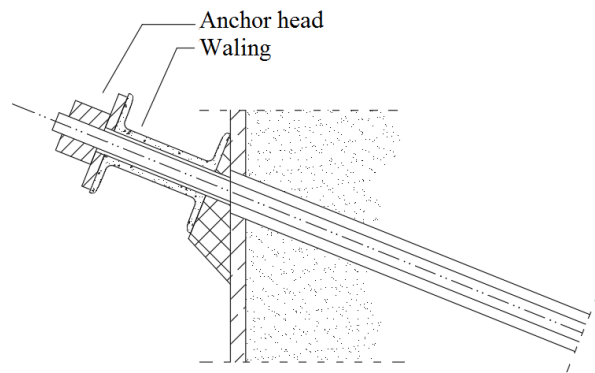
¹Boring: Pre-drilling.

A.4 Alternative to Direct Anchoring

A waling can be designed in different ways depending on the given situation. For example an outer waling level can consist of two U-shaped steel profiles both attached to a load transfer block. Between the two profiles there is a gap allowing the anchor tendon to be attached, as shown in figure A.5b. This kind of waling is visible and usually only used in short-term situations for the construction pit. A possible issue could be space requirements in the pit where the waling could cause concerns, as the combined extra width could be approximately 50-80 *cm*, which may not be allowed regarding the use of the pit. An example of an outer waling level is shown in figure A.5a.



(a) Outer waling level attached on a soldier pile wall in a construction pit in Copenhagen.



(b) Components of a waling.

Figure A.5: Outer waling level.

If the retaining wall is a permanent structure, another kind of waling is often used. This kind of waling is installed inside the back side to prevent space issues and to protect the anchor head construction. For example in a harbor a waling level may be challenging regarding berthing ships, thus a permanent waling level inside the back side is preferable. An illustration of an permanent waling level is pictured in figure A.6.

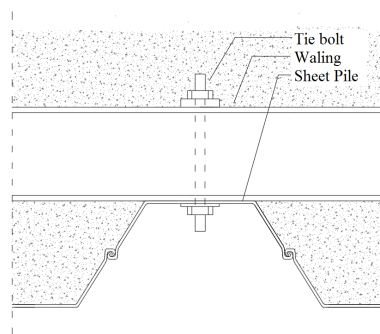


Figure A.6: Permanent waling installed on the back side.

The purpose of a waling level is to distribute the individual anchor load to the retaining wall, thus instead of having a point load, the load is distributed over a line. This means the whole wall will resist the load instead of a single sheet pile.

A.5 Parameters

In this section typical values for the parameters mentioned in section 3.1 will appear. The strength parameters can be quantified by field tests which are often extensive and therefore expensive to perform. However, the tests are necessary to ensure that the properties of the soil used in calculations are reliable.

The compression of sand has great influence on the angle of friction and thereby the strength of the soil. In table A.2 estimated values for the parameter are found.

Table A.2: Estimated values for the angle of friction in sand.[5]

| Grain Distribution | Friction angle, φ | | |
|--------------------|---------------------------|-------------------|------------------|
| | Loose compaction | Medium compaction | Dense compaction |
| | [°] | [°] | [°] |
| Even distributed | 27 | 32 | 37 |
| Medium distributed | 29 | 35 | 41 |
| Uneven distributed | 30 | 37 | 44 |

Furthermore the angle has to be reduced if the grains are rounded or sphere shaped and can be increased if the grain size corresponds to gravel.

The same applies to cohesion. In table A.3 typical values are given which can be used for minor structures.

Table A.3: Typical values for cohesion of different normally consolidated materials.[32]

| Definition | Undrained Cohesion, c_u |
|-----------------------------|---------------------------|
| | [kPa] |
| Clayey sandy gravel | 20 |
| Clayey sand | 5 |
| Silty sand | 22 |
| Sandy clay loam (saturated) | Min. 10 |

A.6 Test specifications for Soil Parameter Determination

A.6.1 Direct Shear Test

A Direct Shear Test is used to determine the friction angle for a soil sample. The experimental setup is shown in figure A.7 where a soil sample is subjected to both a normal force and a shear force simultaneously. The box is split into an upper and lower part which moves separately by applying a horizontal pressure to the upper part which gradually increases in magnitude. The horizontal pressure will then generate a shear stress in the soil sample while the vertical pressure is kept constant.

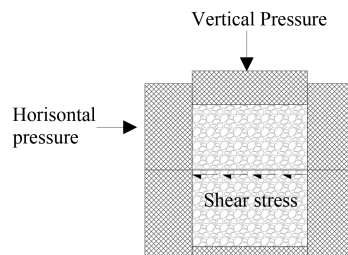


Figure A.7: Experimental setup for a Direct Shear Test.

A pair of strain gauges will record the horizontal movement in the soil sample, and the relation between the shear stress and the strains is obtained as shown in figure A.8.

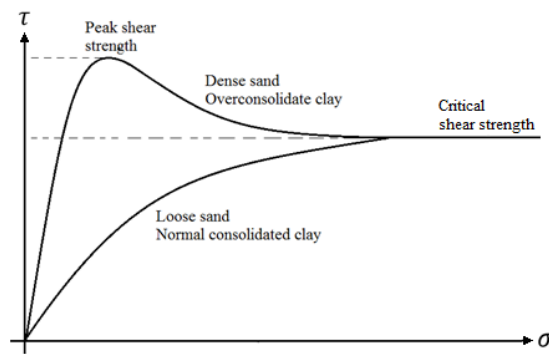


Figure A.8: Shear stress and strain relation illustrated for both a dense and a loose sand sample.[33]

As shown in figure A.8 the critical shear strength is obtained from the experiment. This strength parameter may be used to determine the friction angle by orchestrating a series of test altering the vertical force subjected to the soil sample, thus leading to new shear stresses for each magnitude interval. By developing a Mohr-Coulomb plot of the normal- and shear stress relation, the friction angle can be determined relatively easy. However, only one failure plane is developed for the Mohr-Coulomb plot due to the nature of the experiment. In figure A.9 the friction angle is obtained by plotting a direct line between the measured points. For dense sand a peak shear strength is also obtained because of how the particles is packed. As this peak strength is exceeded, the particles will begin to slide and roll which causes expansion or dilation of the

soil, reducing the strength of the soil. The strength will eventually level out and reach a new equilibrium.

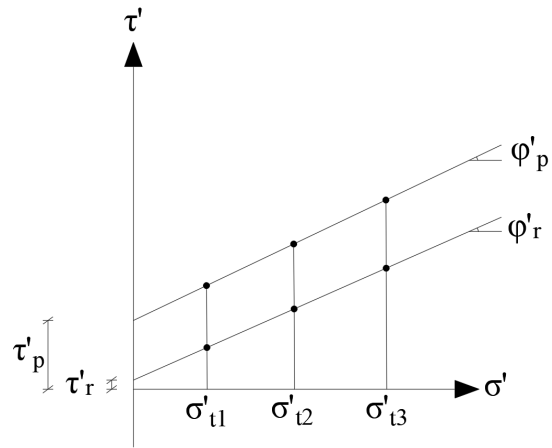


Figure A.9: Determination of the friction angle by the use of a shear box and its related measurements.[33]

A.6.2 Triaxial Test

The triaxial test consists of a soil sample installed in a pressure cell as shown in figure A.10. It is possible to pressurise the cell by a vertical and horizontal stress σ_1 and σ_3 respectively. Several pore and dial gauges are attached which measure the pressure and the vertical displacements. An essential part of the setup is the connection for drainage, which controls the fluid flow in the sample.

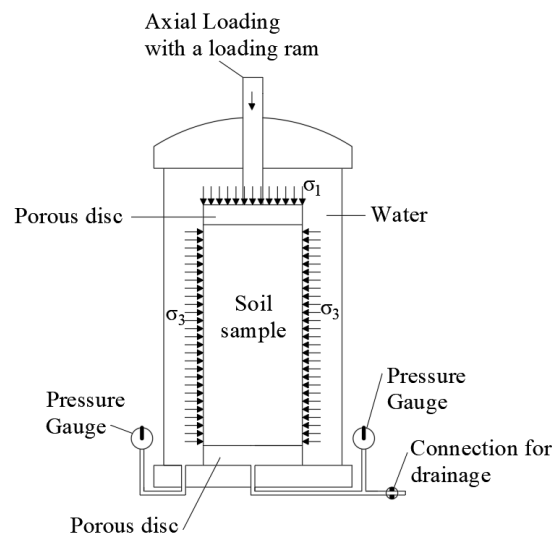


Figure A.10: Triaxial test and its experimental set up.[34]

The test consists of two phases:

- Phase 1: Consolidation phase. The cell pressure is increased which provides a uniform confining stress around the soil specimen equal to the principal stress σ_3 . Depending on the type of test the soil specimen may be allowed to consolidate or not.
- Phase 2: Shearing phase. A load is applied to the top of the cell and since there is no shear stresses on either the top or the sides of the cell these are principal planes. Thus the stress applied on the top is a principal stress equal to σ_1 . This stress is then gradually increased until the soil specimen fails.

The test can be distinguished into four different types by the drainage conditions which is governed by the fluid connection. These four types are explained briefly in the following.

Unconsolidated-Undrained (*UU*)

In both phases the valve is closed, thus it is assumed the soil volume does not change and an excess pore pressure is generated. This is a rather quick test to perform, as there is no wait time for consolidation or drainage of the sample. The purpose of this test is to measure the undrained shear strength, τ_u . The horizontal stress σ_3 is kept at a constant level in phase 1, and in phase 2 the vertical stress σ_1 is gradually increased until failure occurs. The normal and shear stress relation is illustrated by drawing a Mohrs Circle for each test with a specific magnitude of σ_3 . However, since the valve is closed no consolidation occurs and thus the soil cannot gain any strength in a time interval. This means the Mohrs Circles sphere will stay constant as shown in figure A.11. If a line is drawn between all the test circles φ is obtained which is equal to zero for this type of test.

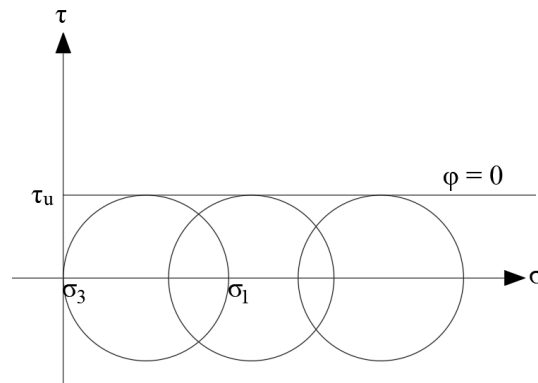


Figure A.11: Experimental setup and results plotted in a normal and shear stress diagram for a *UU* Triaxial test.[35]

Consolidated-Drained (*CD*)

In both phases the valve is open. During the consolidation phase σ'_3 will move from the origin on the normal stress axis to a point of the consolidation stress. It is actually the effective consolidation stress, as no pore pressure appears (the test is assumed to be performed over long time which secures no generation of pore pressure), and the soil will consolidate and correspondingly increase in strength. In phase 2, σ'_1 is gradually increased until failure occurs. Similar to the *UU* test, it is possible to draw a Mohr's Circle for each test. Since the soil is allowed to consolidate and thereby increase its strength, the magnitude of σ'_3 will be influenced. In figure A.12 three different Mohr's Circles are illustrated, along with the determination of the friction angle.

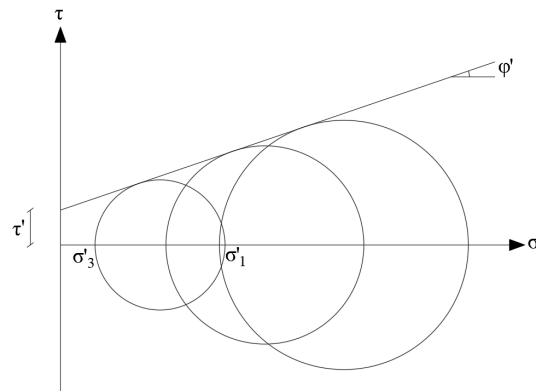


Figure A.12: Experimental setup and results plotted in a normal and shear stress diagram for a *UC* Triaxial test.[35]

Consolidated-Undrained (*CU*)

In this type of test the valve is open in phase 1 and closed in phase 2. During the shearing phase the excess pore pressure, Δu , is measured, which can be used to compute both the effective and total stresses during shearing. This is illustrated in figure A.13.

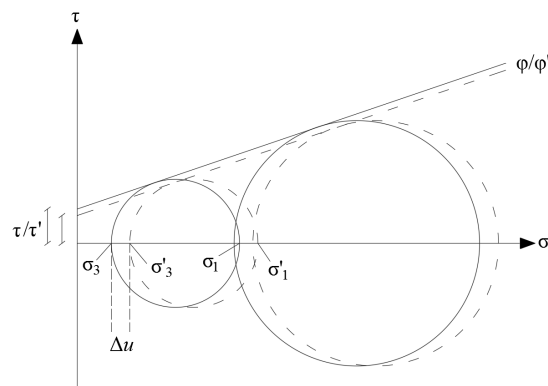


Figure A.13: Experimental setup and results plotted in a normal and shear stress diagram for a *CU* Triaxial test.[35]

Unconsolidated-Drained (*UC*)

For a *UC* test the valve is closed in phase 1 and open in phase 2. This type is only used for cohesive soils, and is similar to the *UU* test.[35]

A.6.3 Cone Penetration Test (CPT)

The CPT is ideally performed initially for a projected area, as this is a good way of mapping the layout of the underground of the site. It is then possible to reduce the frequency of more expensive drilling and sampling of soil tests, as these can be aimed for the most interesting areas. The data from the CPT can also be used to determine various soil parameters by the use of correlation formulas. In table A.4 the soil parameters are shown with a ranking of the precision of the correlation.

Table A.4: Soil parameters which can be determined by correlation formulas using data obtained from CPT.[36]

| Soil Parameter | CPT, Applicability |
|----------------------------|--------------------|
| Static Pore Pressure | High |
| Overconsolidation Ratio | Medium |
| Relative Density | High |
| Friction Angle | Medium |
| Undrained Shear Strength | High |
| Initial Shear Modulus | Medium |
| Stress-strain relationship | Low |

The CPT system is installed in a truck. The truck is then placed above the targeted location, and the weight of the truck is used as a reaction mass to push down a rod in the ground. The test then consists of pushing the instrumental rod into the ground and measuring the forces subjected to the rod by the soil. In figure A.14 the different parts of the rod are illustrated.

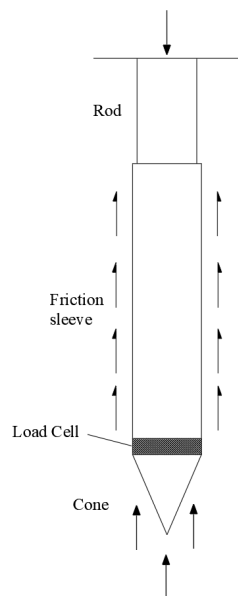


Figure A.14: Cone penetration rod.[37]

In figure A.14 a Piezocone rod is illustrated which is the most common equipment used in CPTs. The rod consists of three different parts. The cone which measure the bearing resistance to penetration, the friction sleeve which measures the side friction and the load cell which also measure the pore pressure. There is several load cells inside the friction sleeve. The lower load cells measures the vertical load from the tip only. The upper load cells measures both the vertical load from the tip and the sides, thus each resistance is found from each load cell by subtraction. The tip resistance, q_c , is given as:

$$q_c = \frac{F_c}{A_c} \quad (\text{A.1})$$

Where F_c is the load from the tip, and A_c is the cross sectional area of the cone. The side friction, f_{sc} , is given by:

$$f_{sc} = \frac{F_s}{A_s} \quad (\text{A.2})$$

Where F_s is the side friction force, and A_s is the outside area of the friction sleeve. The friction is often presented by the friction ratio, R_f , which is given as:

$$R_f = \frac{f_{sc}}{q_c} 100\% \quad (\text{A.3})$$

Besides the above parameters the pore pressure is also measured. As the tip of the rod is forced through the soil, measurements of q_c , R_f and u are taken alongside. Considering the magnitude of each parameter and their mutual relation, the soil strata may be determined. For clay the cone resistance is low but the side friction is high, which is opposite for sand. See Robertson et al., 1986. for further information concerning a chart describing the behaviour of the soil based on the CPT.[36]

A.6.4 Standard Penetration Test (SPT)

The standard penetration test, first developed around 1927, is used to determine subsurface soil properties such as the modulus of elasticity for soil, density and the friction angle. This type of test is applicable for all types of soils, but is most commonly used for cohesionless soil types. The test is rather simple and consists of the following steps:

- A rod is driven 460 mm into the soil material at the bottom of a borehole.
- The rod is then driven down 150 mm two times, and the adequate number of poundings for the rod to reach the depth is recorded. To drive down the rod, a hammer is attached with a standard mass and a falling distance. The initial 150 mm is to ensure that the soil is undisturbed. The sum of poundings for the next 150 mm is recorded and used as the penetration count, N . The penetration count provides an indication of the relative density of the soil and is used as an empirical geotechnical correlation to determine the approximate value of the soil strength properties.

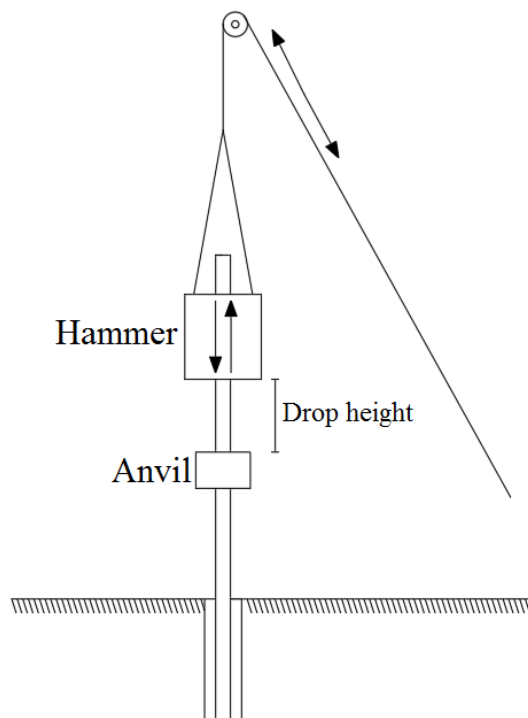


Figure A.15: Standard penetration test.[38]

From the penetration count N the modulus of elasticity may be estimated using different empirical formulas. However, it is important to include local experience of the soil to obtain the best fit for a specific locality. In table A.5 equations for the modulus of elasticity as a result of N are given, and the friction angle as a result of N is given in table A.6.

A.6. Test specifications for Soil Parameter Determination

Table A.5: Examples of equations for an approximate value of E for cohesionless soils.[39]

| Soil Type | Classification | Standard Penetration Test |
|--------------|---------------------|---------------------------|
| | | [kPa] |
| Sand | Normal Consolidated | $E = 500(N + 15)$ |
| | Over Consolidated | $E = 40000 + 1050N$ |
| | Saturated | $E = 250(N + 15)$ |
| | Gravelly | $E = 1200(N + 6)$ |
| | Clayey | $E = 320(N + 15)$ |
| Clay or Sand | Silts | $E = 300(N + 6)$ |

Table A.6: Approximately correlation between penetration count, N , and soil properties.[40]

| Penetration Count N | Packing | Relative Density | Friction Angle |
|-----------------------|------------|------------------|----------------|
| [N] | | [%] | [$^\circ$] |
| < 4 | Very Loose | < 20 | < 30 |
| 4-10 | Loose | 20 - 40 | 30 - 35 |
| 10-30 | Compact | 40 - 60 | 35 - 40 |
| 30-50 | Dense | 60 - 80 | 40 - 45 |
| > 50 | Very Dense | > 80 | > 45 |

A.6.5 Field Vane Test

The in situ field vane test is a relatively fast and cheap method to measure the undrained cohesion in a fully saturated clayey soil. The test consists of a four-bladed vane attached to a rod being driven into the soil. The rod will then slowly be rotated and the required torque is measured until the vane rotates rapidly. At this point, the soil fails around the vane and any further measurements are invalid. The measurements are used to determine the undrained shear strength using the following equation:

$$c_v = \frac{F \cdot a}{M} \quad (\text{A.4})$$

Where c_v is the vane strength, F is the force, which is the weight measured in the test multiplied by the gravitation, and a is the distance from the vane to the end of the rod (at the rotation point). M is the static moment of the surface of the vane.[41] There are different types of vanes which makes the static moment specific to each vane. The vane strength is then correlated to the undrained cohesion:[5]

$$0.5 \cdot c_v = c_u \quad (\text{A.5})$$

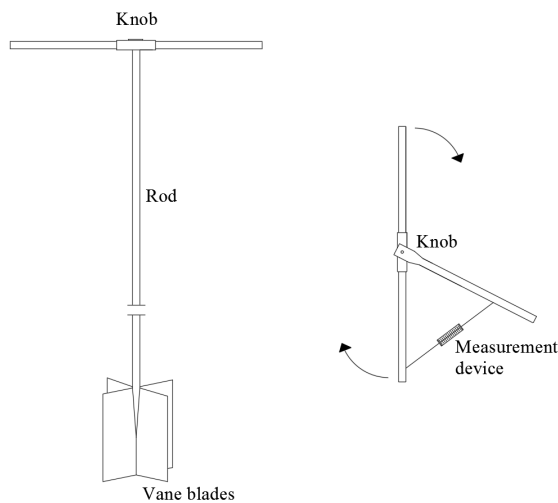


Figure A.16: Equipment used in a field vane test.

A.7 Yield Lines

A.7.1 Theorems for Yield Line Calculations

Especially for reinforced concrete beams and plates the statement of the appearance of fractures not being fatal is logical, as fractures form due to tension, but typically won't lead to failure. In these cases yield line theory is used to determine the bending capacity of the elements.

The theory relies on the formation of yielding hinges that is also mentioned in section 4.1, which is a result of the rearrangement of stresses in a yielding cross section. Figure A.17 illustrates a rectangular cross section in which yielding is initiated as the surface is exposed to yielding stresses. As the load is increased, the area of yielding expands, and when the whole cross section is yielding, a yielding hinge is developed.[21]

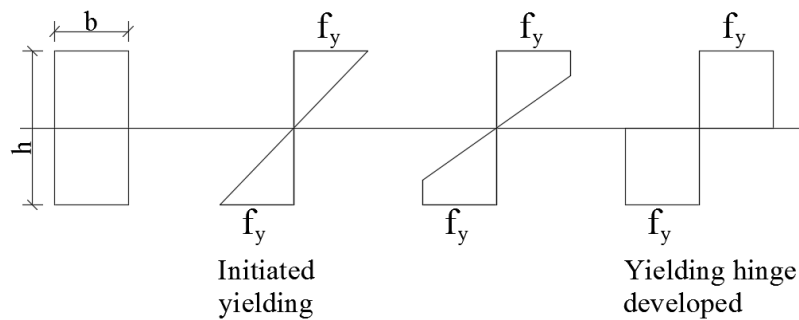


Figure A.17: The formation of an yielding hinge from initiating yielding to yielding of the whole cross section.

In the theory of plasticity the yielding hinge is idealised to a point or line connecting two non-deforming stiff segments not considering elastic deformations. The deformations regarding yielding may approach infinity which does not make any logical sense considering the physics. The rotational capacity is therefore introduced which is a measure of the deformations of a yielding hinge before the introduction of breaking strains.[21]

Lower bound value

A lower bound value in the theory of yield lines may be found by evaluating equilibrium of an infinitesimal plate element which is illustrated in figure A.18 having the lengths dx and dy and being exposed to a distributed load p .

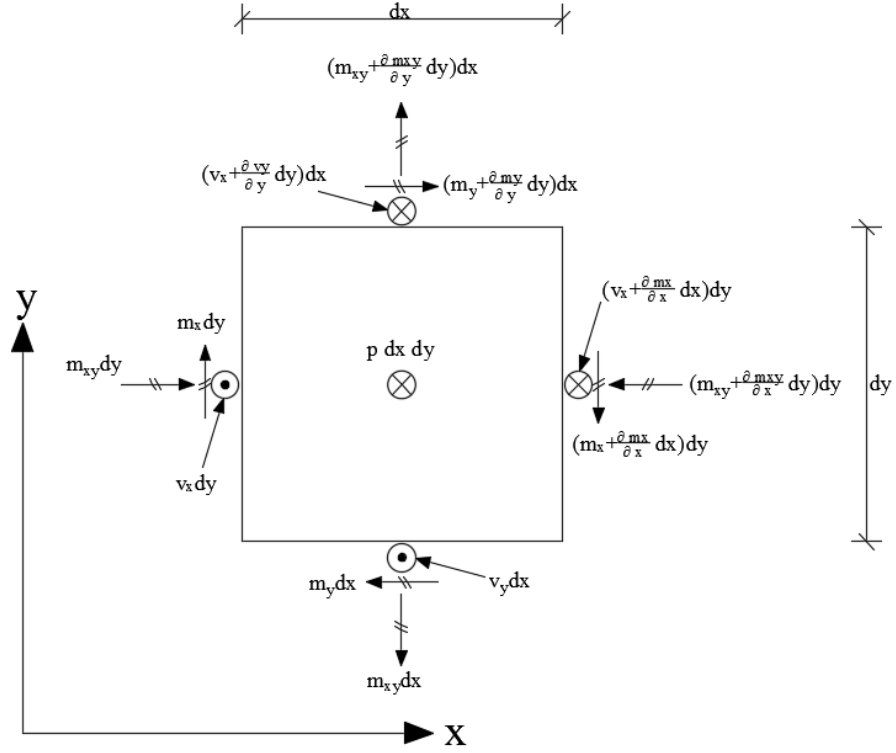


Figure A.18: Infinitesimal plate element.

For the element vertical equilibrium yields:

$$\begin{aligned}
 p dx dy + \frac{\partial v_x}{\partial x} dx dy + \frac{\partial v_y}{\partial y} dx dy &\Rightarrow \\
 p + \frac{\partial v_x}{\partial x} + \frac{\partial v_y}{\partial y} &= 0
 \end{aligned} \tag{A.6}$$

Moment equilibrium is evaluated about a line through the center of the element parallel to the y-axis in equation A.7:

$$v_x dy dx + \frac{\partial v_x}{\partial x} dx dy \frac{dx}{2} - \frac{\partial m_x}{\partial x} dx dy + \frac{\partial m_{xy}}{\partial y} dy dx = 0 \tag{A.7}$$

It is seen that the second part of equation A.7:

$$\frac{\partial v_x}{\partial x} dx dy \frac{dx}{2} \tag{A.8}$$

is of insignificant magnitude in comparison to the other parts.

This yield - after shortening - expressions for v_x and v_y correspondingly:

$$v_x = \frac{\partial m_x}{\partial x} - \frac{\partial m_{xy}}{y} \quad (\text{A.9})$$

$$v_y = \frac{\partial m_y}{\partial y} - \frac{\partial m_{xy}}{x} \quad (\text{A.10})$$

The two expressions are then differentiated with respect to x and y and is inserted in equation A.6, which then yields the equation of equilibrium of a plate from which the calculations of lower bound values are results of and is given in equation A.11:

$$\frac{\partial^2 m_x}{\partial x^2} + \frac{\partial^2 m_y}{\partial y^2} - 2 \frac{\partial^2 m_{xy}}{\partial x \partial y} = -p \quad (\text{A.11})$$

In practice, usually the simple so called *Strip method* is used. Using this method the plate is split up into beams which is possible through the assumption of the torsional moment, m_{xy} , being equal to 0, and thereby the equation of equilibrium being split as well. The separate resulting equations are then solved individually.

The strip method is suitable for reinforced concrete plates where the separate reinforcement in both directions is of interest. However, a more complex variation exists which includes the effects of torsional moments. Experience shows, that inclusion of the torsional moments will lead to an increase of the lower bound value of around 50 % in comparison to the strip method.[21]

Upper bound value

According to the upper bound statement a geometrically possible yielding mechanism must be defined. Usually multiple possible yielding mechanisms exist and the most critical represents the optimal upper bound value. As a possible mechanism is defined, the corresponding upper bound value is determined by evaluating the equation of work:

$$A_i = A_o \quad (\text{A.12})$$

Where A_i is the inner work performed in the yield lines, and A_o is the outer work performed on the plate by an outer exposure.

The inner work is a result of the yielding criterion which a given plate follows. For an isotropic material or an isotropically reinforced concrete plate the inner work is determined from the moment capacity and the angle of rotation as stated in equation A.13:

$$A_i = \sum m_{yield} d \varphi \quad (\text{A.13})$$

Where l is the length of the yield line, and φ is the angle of rotation for the plate part being delimited by a one or more yield lines. Equation A.13 is valid under the assumption of Tresca yielding criterion which is a linearisation of the von Mises criterion. In order to convert to von Mises yield criterion a factor of $\frac{2}{\sqrt{3}}$ must be multiplied on the equation.[21]

The outer work is a result of the outer exposure from a load and is equal to the force multiplied by the displacement and is found from equation A.14:

$$A_o = \int_0^{l_x} \int_0^{l_y} p \delta dy dx + \sum_n P_i \delta_i \quad (\text{A.14})$$

Where p is a distributed load, P is a point load and δ is the displacement of the load.

A.7.2 Analytical Validation of Yield Line Calculations

The analytical calculations regarding the validation of the yield lines has been performed for a rectangular plate being simply supported by its four sides. The plate consist of steel, meaning it has isotropic properties. This has been performed in order to compare the numerical results with analytical calculations.

The plate used in the comparison is given in figure A.19.

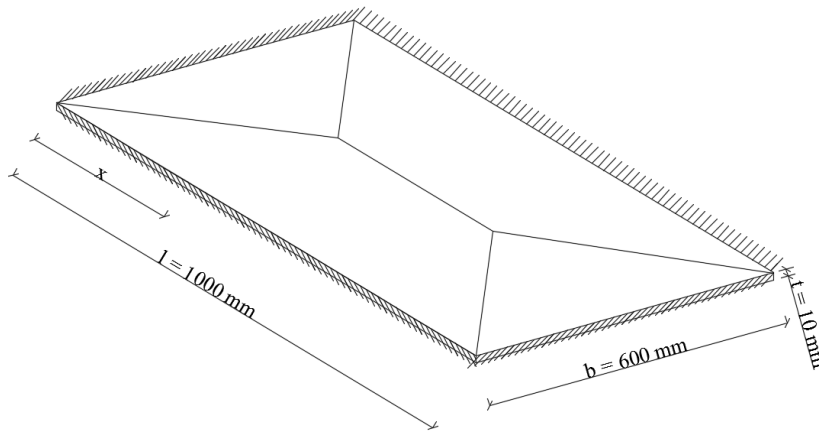


Figure A.19: Design of plate used for the validation of the numerical setup.

The yield lines are found in the optimal locations numerically by FE model which means that the lines may not be completely straight which is also illustrated in figure A.24b. This is in contrast to the analytical approach which states straight lines.

In order to execute the calculations analytically the moment capacity per unit of length, m_{yield} , has to be determined. This parameter is defined in figure A.20, where T and C are the tension and compression forces respectively that are found for a cross section by:

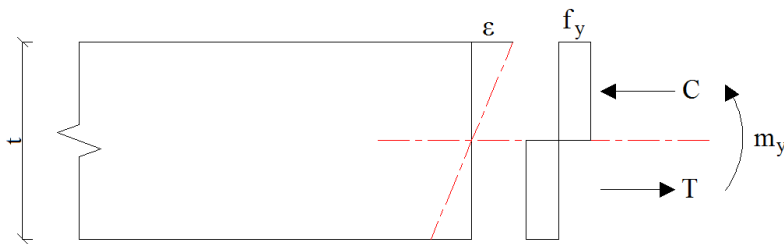


Figure A.20: Definition of m_{yield} .

$$C = T = \frac{1}{2} t f_y \quad (\text{A.15})$$

Where t is the thickness of the plate, and f_y is the yielding strength of the material, given it is isotropic. m_{yield} can then be found from equation A.16:

$$m_{yield} = \frac{1}{4} f_y t^2 \quad (\text{A.16})$$

Calculations

A plate which cross section varies throughout the beam has been produced, and the plastic model in figure 5.14 has been applied in order to validate the useability. The properties of the plate are given in figure A.21. In figure A.21b the expected generation of yield lines is illustrated. Here yielding hinges are developed at the fixity and at the changes in the cross section given that the thickening of the center segment of the plate has the necessary moment capacity.

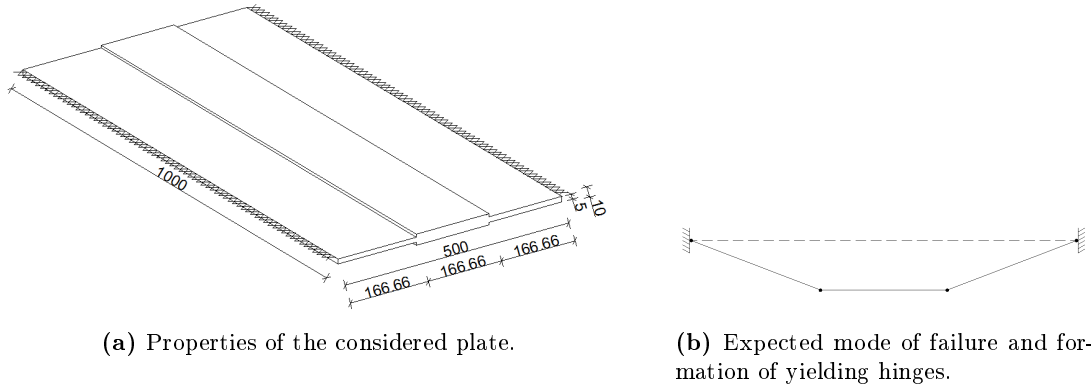


Figure A.21: Plate used for validation of the plastic model.

Figure A.22 illustrates the results obtained using ANSYS Workbench for the given example. It is noticed from the results that the failure mode corresponds to the expectations.

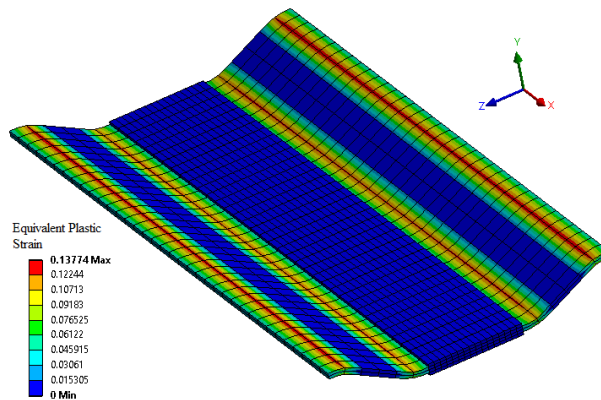


Figure A.22: Results for the plate. Plastic strains are plotted.

In addition a study of a plate being simply supported by all its four sides has been carried out. The aim of this analysis is to determine the failure mechanism of the plate both numerically and analytically and to compare the results. It will be determined whether the yield lines as well as the deviations between the yielding forces matches. The study is performed in the following.

Validation

The plate used in the validation is illustrated in figure A.19, and the properties are as follows:

- Length = 1000 mm
- Width = 600 mm
- Thickness = 10 mm
- $x_{guess} = \frac{b}{2}$
- $f_y = 400 MPa$
- $E = 200000 MPa$
- Boundary conditions - simple supported

The moment capacity is determined by:

$$m_{yield} = \frac{1}{4} f_y t^2 = \frac{1}{4} \cdot 400 \cdot 10^2 = 10000 \frac{Nmm}{mm} \quad (A.17)$$

As the moment capacity is found an upper bound value for the allowable yielding force, p , can be determined evaluating the equation of work for the plate (See equation A.12). By insertion and rewriting of the equation it is shortened to equation A.18:[21]

$$p = 12m_{yield} \frac{b^2 + 2lx}{b^2(3lx - 2x^2)} = 12 \cdot 10000 \frac{600^2 + 2 \cdot 1000 \cdot 300}{600^2(3 \cdot 1000 \cdot 300 - 2 \cdot 300^2)} = 0.444 \frac{N}{mm^2} \quad (A.18)$$

Where x is the distance from the shorter side to the yielding line in the middle of the plate. By minimisation regarding to x in equation A.18 the optimal upper bound value is determined by:

$$p = \frac{24m_{yield}}{b^2 \left(\sqrt{3 + \left(\frac{b}{l}\right)^2} - \frac{b}{l} \right)^2} = \frac{24 \cdot 10000}{600^2 \left(\sqrt{3 + \left(\frac{600}{1000}\right)^2} - \frac{600}{1000} \right)^2} = 0.438 \frac{N}{mm^2} \quad (A.19)$$

The optimal magnitude of x is:

$$x = -\frac{1}{2} \frac{b^2}{l} + \frac{1}{2} b \sqrt{3 + \left(\frac{b}{l}\right)^2} = -\frac{1}{2} \frac{600^2}{1000} + \frac{1}{2} 600 \sqrt{3 + \left(\frac{600}{1000}\right)^2} = 370mm \quad (A.20)$$

For a rectangular plate a lower bound value is found from equation A.21 where the effects from the torsional moments are included:[21]

$$p = 8 \left(\frac{1}{l^2} + \frac{1}{b^2} + \frac{1}{bl} \right) m_{yield} = 8 \left(\frac{1}{1000^2} + \frac{1}{600^2} + \frac{1}{600 \cdot 1000} \right) 10000 = 0.436 \frac{N}{mm^2} \quad (\text{A.21})$$

Figure A.23 illustrates the results of the analytical approach. Blue dots represent upper bound values for various lengths of x . The red dot marks the critical value of x found by optimisation.

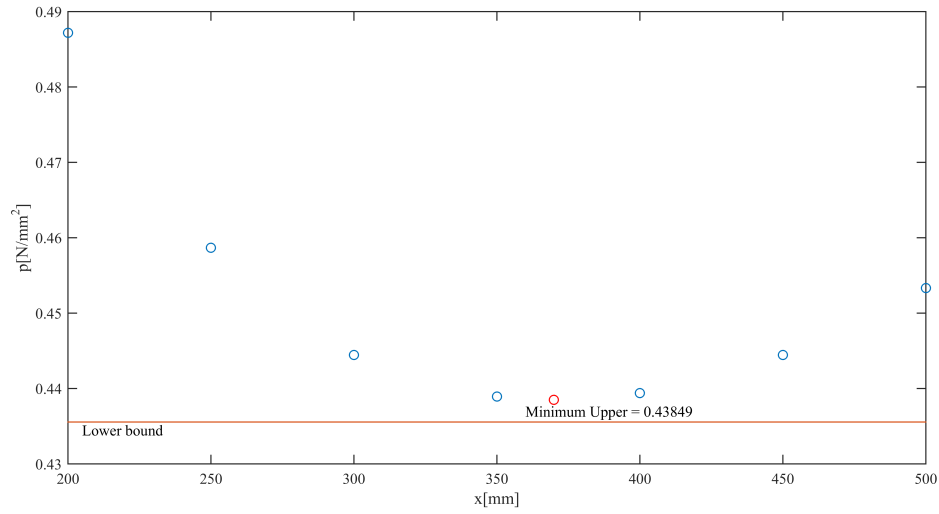


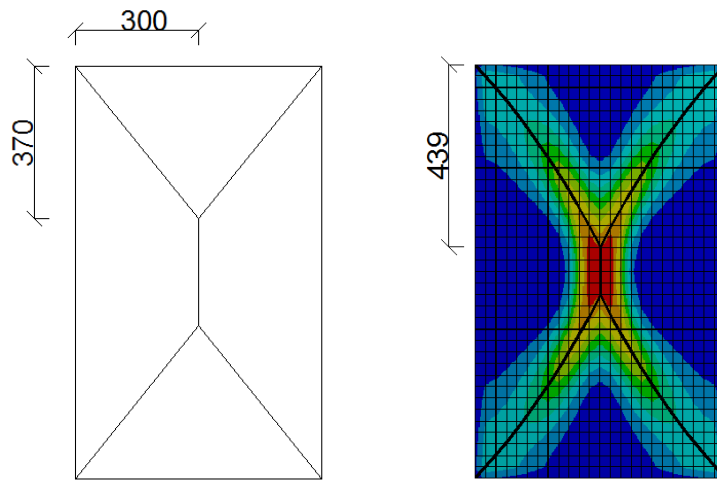
Figure A.23: Optimisation study for varying lengths of x .

The results from the analytical and numerical analyses are given in table A.7 and illustrated in figure A.24 showing the differences between the yield line contours.

Table A.7: Comparison of analytical and numerical approaches for yield line calculations.

| | Distance, x | Dev. | Yielding Force, p | Dev. |
|-------------------|---------------|-------|----------------------|------|
| | [mm] | [%] | [N/mm ²] | [%] |
| Numerical | 439 | - | 0.460 | - |
| Analytical | 370 | -15.7 | 0.436 (Lower Bound) | -4.7 |
| | | | 0.438 (Upper Bound) | -4.0 |

Evaluating table A.7 and figure A.24 it is seen, that the contours of the optimal yield lines more or less has been captured by the plastic model constructed. The deviations in the contours may be as result of the FE approach. However, as it is given from the results, a relatively great change in the precision only leads to insignificant changes in the calculated yielding force which is also stated in the theory in section 3.4.1. This means, that the deviations in the contours is considered insignificant, as far as the critical mechanism type is determined.



(a) Optimal yield line contours by the analytical approach.

(b) Yield line contours by the numerical approach.

Figure A.24: Yield line contours for the analytical and numerical analyses.

A.7.3 Yield Line Calculation by Inclusion of Corner Effect

As stated in section 3.4.1 the corner effect occurs for inappropriate or insufficient anchoring of a plate causing a corner lever to form. In figure A.25 only the underside of the boundary of the plate is anchored which leads to the a negative yield line and the formation of a corner lever. By adding topside anchoring to the boundary this may be avoided.

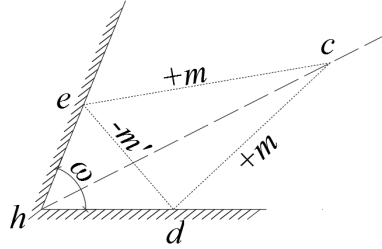


Figure A.25: Formation of corner levers. de forms a negative yield line.[42]

Equation A.22 gives the relationship between topside and underside anchoring. Corner levers may form as $m \neq m'$. For $m = m'$ it can be shown that the line de given in figure A.25 will disappear in the point h :[42]

$$\text{Relationship} = \frac{m}{m'} \tag{A.22}$$

Only symmetrically corner levers will be considered in the following calculations as this is a common assumption having an evenly distributed load. In figure A.26 the geometry of the corner lever represented by cde is given. By moment equilibrium about the center of gravity of cde , g , and some manipulations, the angle, α , is found by equation A.23:[42]

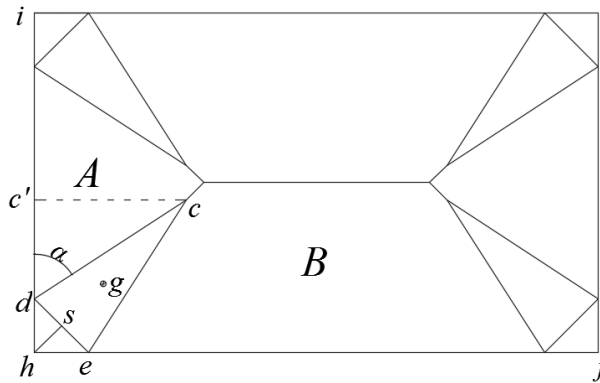


Figure A.26: Geometry of the corner lever cde with relevant notations. Point g is the center of gravity.[22]

$$\cot(\alpha) = \left(\sqrt{\left(1 + \frac{m'}{m}\right) \left(4 + \frac{m'}{m} + 3\cot^2\left(\frac{\omega}{2}\right)\right)} - 2 - \frac{m'}{m} \right) \cdot \tan\left(\frac{\omega}{2}\right) \tag{A.23}$$

As α is known, the distance, hs , is found by projection in equation A.24:

$$|hs| = \sqrt{\frac{2m}{3p}} \left(\sqrt{4 + \frac{m'}{m} + 3\cot^2\left(\frac{\omega}{2}\right)} - 2\sqrt{1 + \frac{m'}{m}} \right) \quad (\text{A.24})$$

Where p is the distributed yielding force. By moment about the line de , the distance, cs , is obtained in equation A.25:

$$|cs| = \sqrt{\frac{6(m + m')}{p}} \quad (\text{A.25})$$

For a plate with no upperside anchoring $m' = 0$. The yield capacity m is given in equation A.26 for a square plate having corner levers which will be used as an approximation of the capacity of the rectangular plate. It is known that this yields deviations, which however are neglected:

$$m = \frac{pa^2}{22} \quad (\text{A.26})$$

m is substituted with $\frac{1}{4}f_y t^2$, thus the yielding load:[22]

$$p = \frac{22 \cdot \frac{1}{4}f_y t^2}{a^2} \quad (\text{A.27})$$

Calculations

In this section the plate illustrated in figure A.27 is evaluated which is equal to the plate used in the calculations in appendix A.7.2.

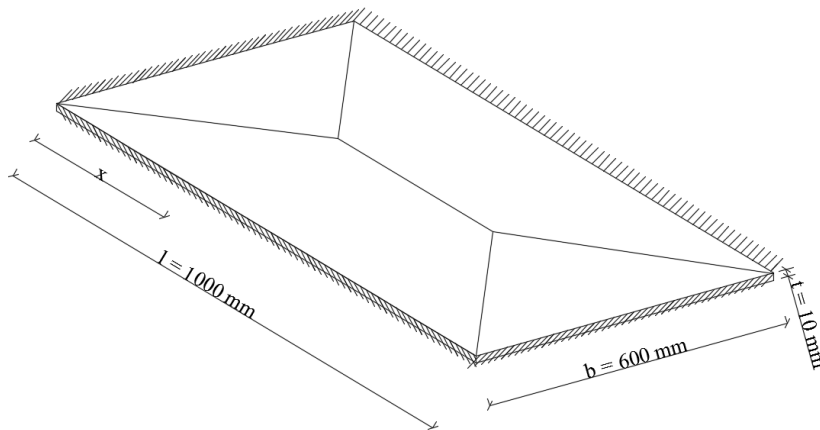


Figure A.27: Design of plate used for calculation of corner effect.

The properties are as follows:

- Length = $l = 1000 \text{ mm}$
- Width = $b = 600 \text{ mm}$
- Thickness = $t = 10 \text{ mm}$
- $f_y = 400 \text{ MPa}$
- $\omega = 90^\circ$

In the calculations no upperside anchoring is assumed, thus $m' = 0$. As only the symmetrical corner lever is considered α is calculated:

$$\begin{aligned} \cot(\alpha) &= \left(\sqrt{4 + 3\cot^2\left(\frac{90^\circ}{2}\right)} - 2 \right) \cdot \tan\left(\frac{90^\circ}{2}\right) = 0.646 \rightarrow \\ \alpha &= 57.15^\circ \end{aligned} \quad (\text{A.28})$$

As α is known, the distance, hs , is found by equation A.29:

$$|hs| = \sqrt{\frac{2 \frac{p \cdot 600^2}{22}}{3p}} \left(\sqrt{4 + 3\cot^2\left(\frac{90^\circ}{2}\right)} - 2 \right) = 67.45 \text{ mm} \quad (\text{A.29})$$

cs is now obtained:

$$|cs| = \sqrt{\frac{6 \left(\frac{p \cdot 600^2}{22} \right)}{p}} = 313.34 \text{ mm} \quad (\text{A.30})$$

As distances, hs and cs , are determined it is possible to calculate, hd and cc' , which are used for obtaining the yielding load, by trigonometry. The distances are given in figure A.26:

$$|hd| = \sqrt{2 \cdot |hs|^2} = 95.38 \text{ mm} \quad (\text{A.31})$$

$$|cc'| = \frac{|hc|\sqrt{2}}{2} = 269.26 \text{ mm} \quad (\text{A.32})$$

The moment equilibrium about hi for the plate part denoted A in figure A.28 is given in equation A.33.

$$m(b - 2|hd|) = \frac{1}{6}pb \cdot \frac{b \cdot l}{4} - 2 \cdot \frac{1}{6}p \cot |hd| \cdot |cc'| \quad (\text{A.33})$$

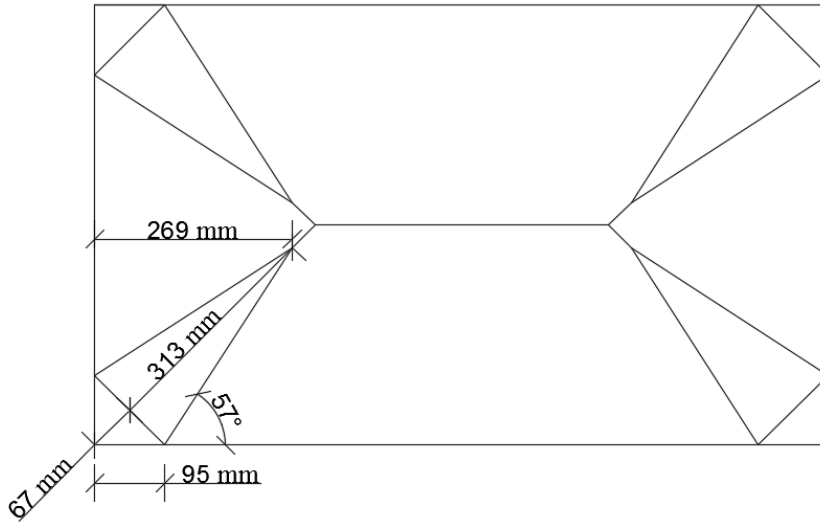


Figure A.28: Design values for geometrical distances.

Where m is substituted, thus:

$$p = \frac{6(b - 2|hd|) \cdot f_y \cdot t^2}{b^2l - 8|cc'|^2 \cdot |hd|} = \frac{6(600 - 2 \cdot 95.38) \cdot 400 \cdot 10^2}{600^2 \cdot 1000 - 8 \cdot 269.26^2 \cdot 95.38} = 0.322 \frac{N}{mm^2} \quad (\text{A.34})$$

A is considered the fatal plate part. Evaluating plate part B yields a yielding force of $p = 0.637 \frac{N}{mm^2}$. The effects of corner levers greatly reduces the yielding capacity of the plate. Having a rectangular plate, the effects reduce the capacity of up to 26.6 % considering the plate part separately compared to the optimised upper bound solution.

It is possible to achieve a yielding mechanism having corner levers using a numerical software which figure A.29 illustrates.

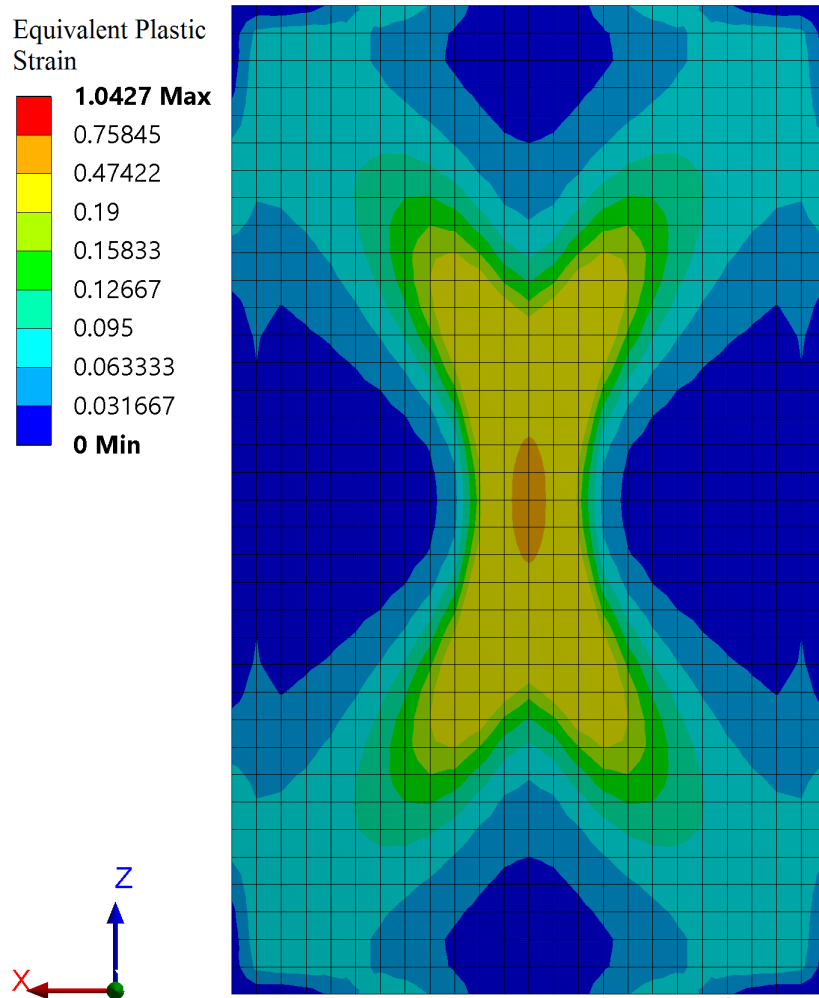


Figure A.29: Numerical yielding mechanism including corner levers.

A.8 Calculation of the Load Bearing Plate, DS/EN 1993-5

The design of the load bearing plate is performed according to DS/EN 1993-5 concerning piling. The chosen design of the plate must ensure stability of the sheet pile which has to be able to transfer the anchor force. The Eurocode prescribes that the shear resistance of the flange beneath the load bearing plate must exceed the shear force acting in the flange as a result of the anchor force. Furthermore the tensile resistance of the webs must exceed the forces acting as a result of the anchor force.

The calculations include a number of variables which appear in appendix A.9:

- h - Overall height of the profiles in mm
- t_f - Thickness of the flange in mm
- t_w - Thickness of the webs in mm
- b - Width of the flange. The distance between the centers of the radii of the circle sections in mm
- b_a - Width of the load bearing plate in mm . Must be greater than $0.8b$
- h_a - Length of the load bearing plate in mm . Must be equal to b_a or less than $1.5b_a$
- t_{lbp} - Thickness of the load bearing plate mm . Must be greater than $2t_f$
- f_y - Yield strength of the sheet pile in MPa

The shear resistance of the flange is calculated by equation A.35:

$$R_v = 2(b_a + h_a)t_f \left(\frac{f_y}{\sqrt{3}\gamma_{M0}} \right) \quad (A.35)$$

Where γ_{M0} is a partial safety factor. A value of 1.0 is recommended for piling in the National Annex. Inserting:

$$R_v = 2 \cdot (292 + 292) \cdot 10.5 \cdot \left(\frac{355}{\sqrt{3} \cdot 1.0} \right) = 2520.5kN \quad (A.36)$$

The tensile resistance of the webs is calculated by equation A.37:

$$R_t = \frac{2h_a t_w f_y}{\gamma_{M0}} \quad (A.37)$$

Inserting:

$$R_t = \frac{2 \cdot 292 \cdot 9.1 \cdot 235}{1.0} = 1891.8kN \quad (A.38)$$

A.9 Arcelor Sheet Pile Catalogue

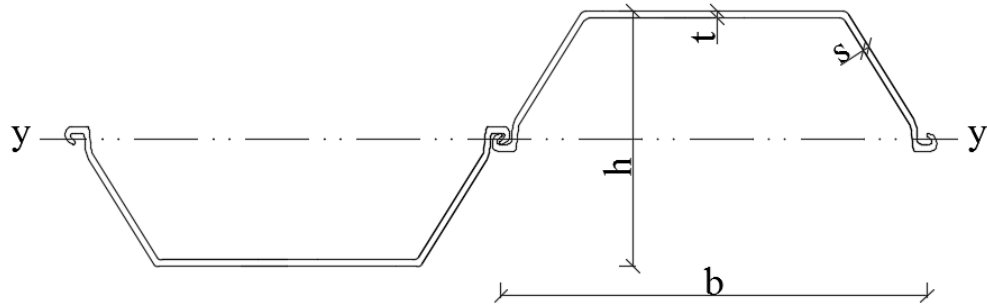


Figure A.30: Product information for ArcelorMittal AU18 sheet pile sections.

Table A.8: Product information for ArcelorMittal AU18.[27]

| Section | Dimensions | | | | A | G_{sp} | G_w | I_y | $W_{el,y}$ | S_y | $W_{pl,y}$ |
|---------|------------|------|------|------|-------|----------|-------|--------|------------|-------|------------|
| | b | h | t | s | | | | | | | |
| | [mm] | [mm] | [mm] | [mm] | | | | | | | |
| AU18 | 750 | 441 | 10.5 | 9.1 | 150.3 | 88.5 | 118.0 | 39,300 | 1,780 | 1,030 | 2,082 |

A.10 Validation of Model

A.10.1 Study of Convergence

A study of convergence has been carried out for the sheet pile wall analyses described in chapter 5.

A total of three studies have been executed:

- Deformations
- Equivalent von Mises stresses
- Eigenfrequencies

The convergence studies are performed for the area of interest highlighted in figure A.31.

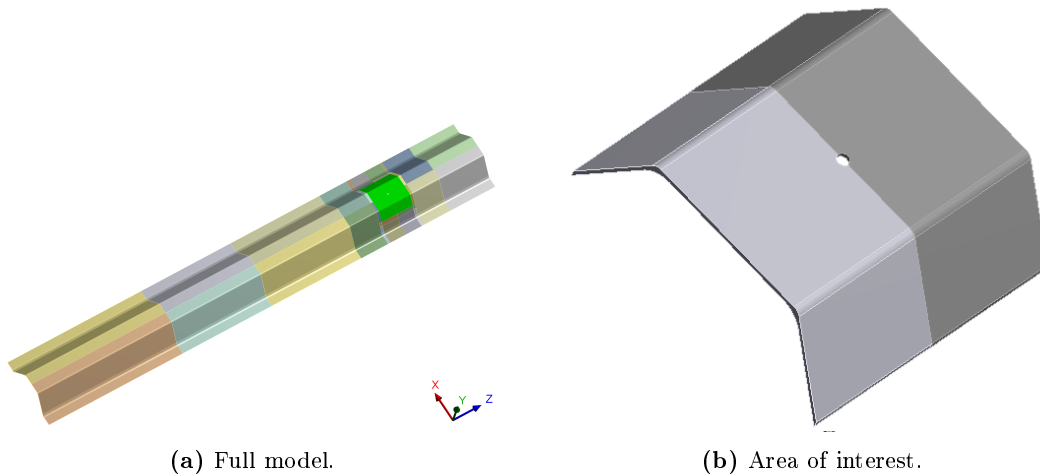


Figure A.31: Area of interest used in the studies of interest.

An anchor force of 1000 N has been applied to the anchor tendon. In order to simplify the calculations no earth pressure actions are applied on the sheet pile. The static boundary conditions are as described in section 5.1.1.

The mesh in the highlighted area has a maximum size of 50 mm and is then refined gradually to a minimum of 5 mm . Figures A.32, A.33 and A.34 illustrate the development of the deformations, equivalent von Mises stresses and eigenfrequencies as the mesh is refined. The deformations and stresses have been read in a fixed point in the sheet pile near the load bearing plate.

Figure A.32 reveals that the variation of the deformations are minimal as the mesh is refined. At a element sizing of around 40 mm the change is considered insignificant.

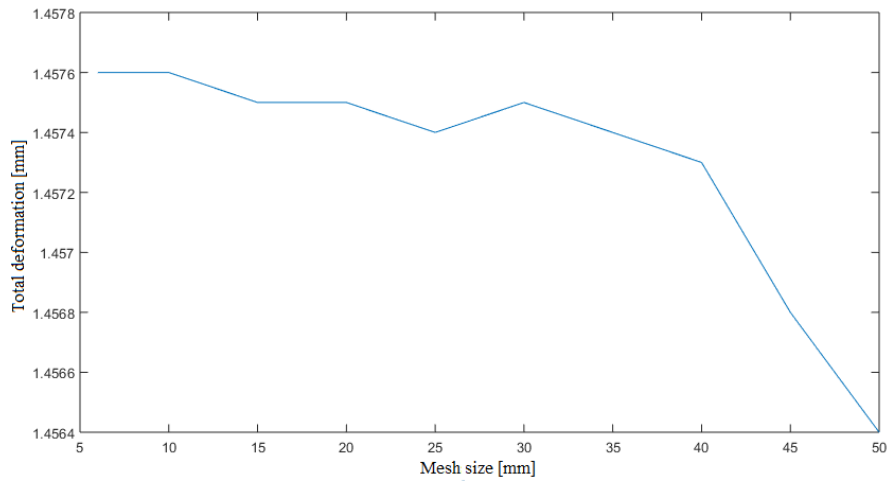


Figure A.32: Variation of total deformations as the mesh is refined.

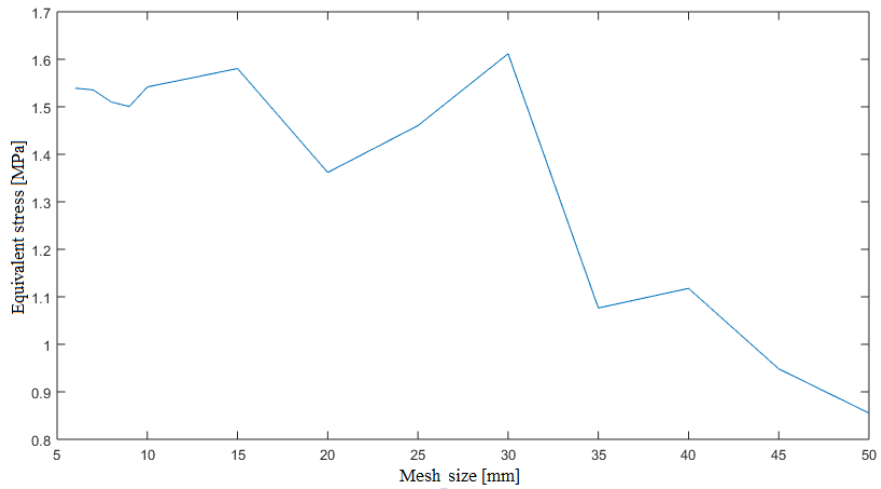


Figure A.33: Variation of equivalent von Mises stresses as the mesh is refined.

In contrary the variation of the von Mises stresses in the assigned point is relatively more changing. As seen in figure A.33 the stresses rise significantly. At a refinement of around 10 *mm* the stresses seem to have converged.

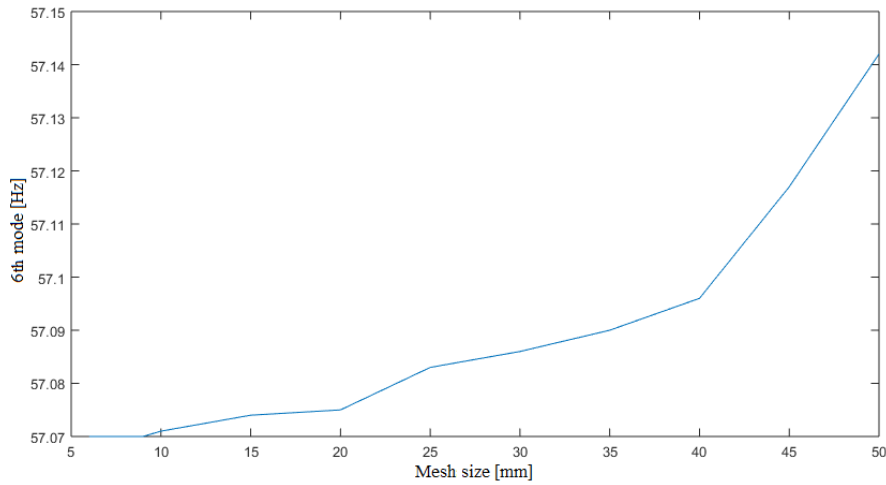


Figure A.34: Variation of eigenfrequencies as the mesh is refined.

An eigenfrequency analysis has been carried out as well as singularities appear beneath the load bearing plate. Investigating the eigenfrequencies may overcome the singularity issue. Figure A.34 show that the eigenfrequency of the 6th eigenmode converges at a mesh of around 15 *mm* and at 9 *mm* the values does not change at all.

Based on this study of convergence a mesh sizing of the area of interest of 10 *mm* is assumed appropriate as satisfying accuracy is obtained while unnecessarily high computational time is avoided. For solid FE structures a minimum of two elements in the thickness must be computed in order to capture the stress field sufficiently. Therefore a mesh size in the considered area of interest of 5 *mm* has been chosen (which is within the range of convergency), as this yields two elements in the thickness.

A.10.2 Validation of Symmetry of Model

In this study a rectangular plate with a cylindrical block welded on is modeled. The dimensions are illustrated in figure A.35 and the boundary conditions appear in figure A.36. A force acting on the surface of the cylindrical block of 1000 N is applied. The resulting equivalent von Mises stress distribution is pictured in figure A.37 for the whole model and likewise in figure A.38 for the half model.

The stresses have been probed in two points placed equal to the symmetry line of the plate. This is done in order to validate the symmetry. Afterwards it is validated that results are equal in the whole and half model.

By evaluating table A.9 it is clear that both symmetry is maintained and that it is possible to construct a half model and still obtain the same results as the conditions are equal.

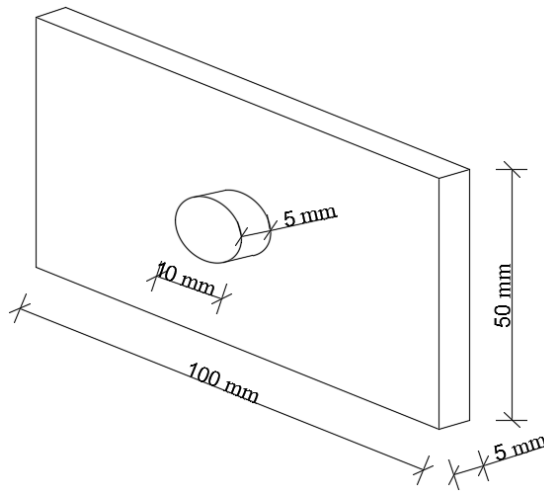


Figure A.35: Dimensions.

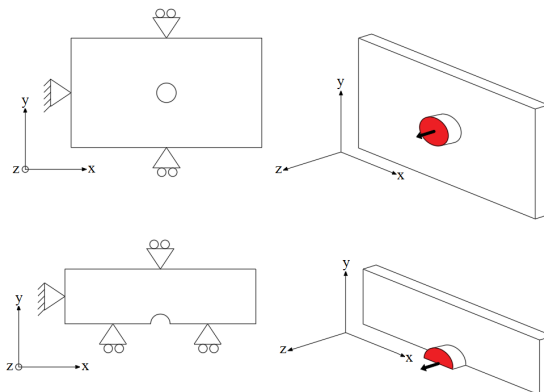


Figure A.36: The static model.

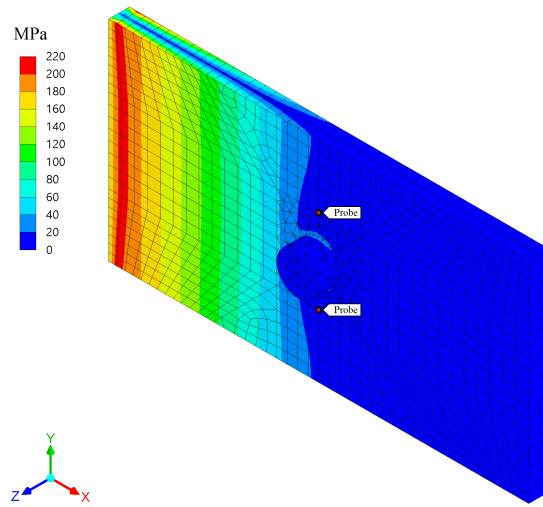


Figure A.37: Stress model in ANSYS workbench.

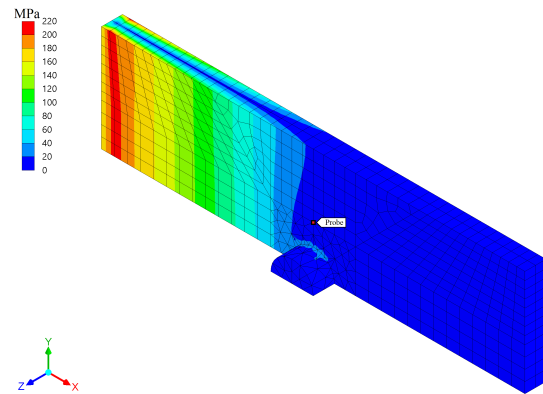


Figure A.38: Half of the stress model in ANSYS workbench.

Table A.9: Stress probes comparison.

| | Stress Probe |
|---------------------|--------------|
| | [MPa] |
| Full Model, Probe 1 | 5.53 |
| Full Model, Probe 2 | 5.53 |
| Half model | 5.53 |

A.10.3 Validation of Submodel

In this study a rectangular plate having a cylindrical hole is modeled. The dimensions are illustrated in figure A.39 and the boundary conditions appear in figure A.40. The resulting equivalent von Mises stress distribution is pictured in figure A.41 for the whole model and likewise in figure A.42 for the submodel.

The stresses have been probed in three points placed in a line from the hole. This is done in order to validate the implementation of a submodel.

By evaluating table A.10 it is clear that the implementation is valid as the stresses in all three probes are equal.

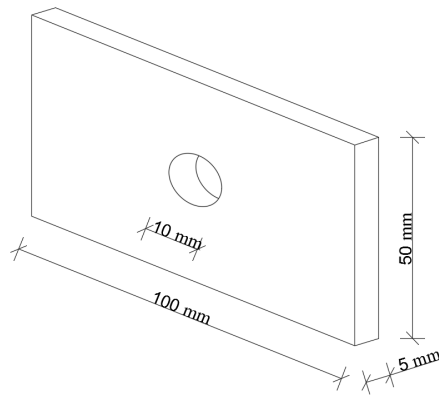


Figure A.39: Dimensions.

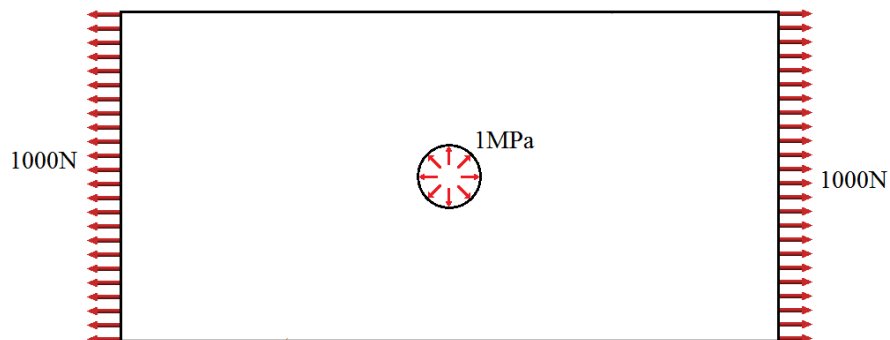


Figure A.40: Static model.

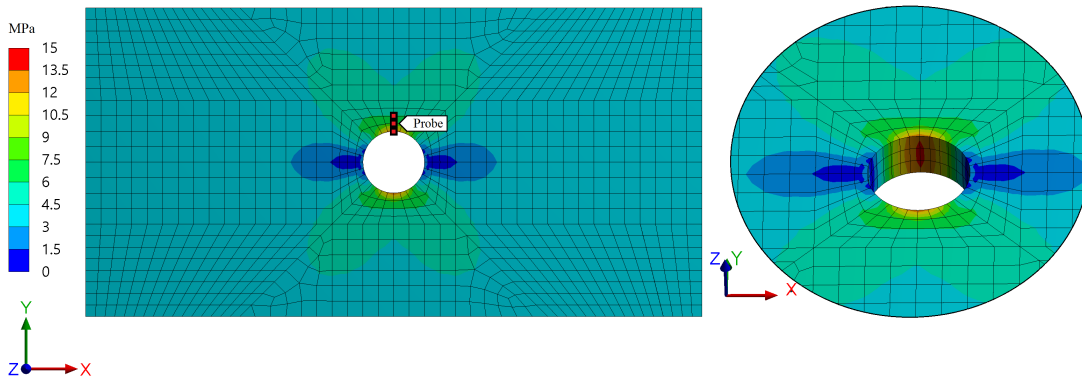


Figure A.41: Model in ANSYS Workbench.

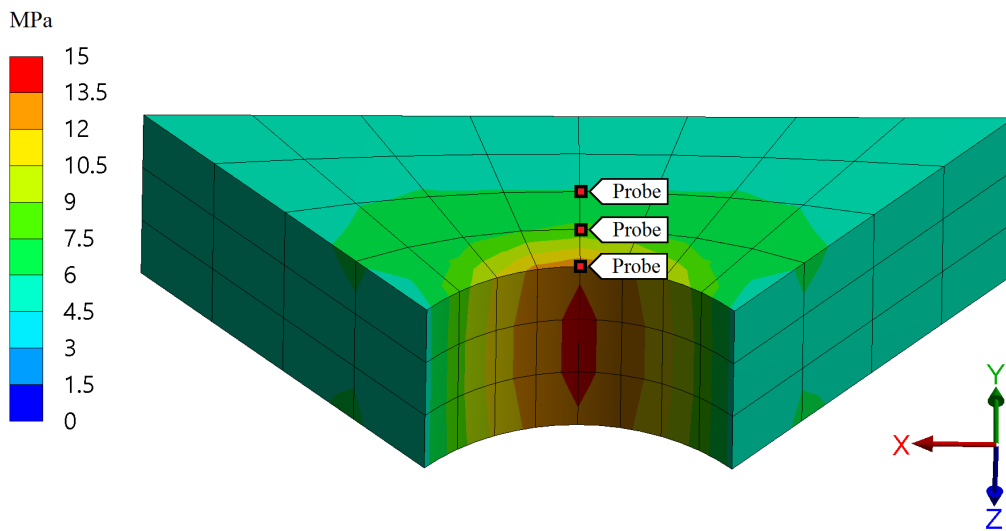


Figure A.42: Submodel in ANSYS Workbench.

Table A.10: Stress comparison of full model and submodel.

| | Probe 1 | Probe 2 | Probe 3 |
|------------|---------|---------|---------|
| | [MPa] | [MPa] | [MPa] |
| Full model | 13.30 | 7.82 | 6.03 |
| Submodel | 13.30 | 7.82 | 6.03 |

A.10.4 Validation of Load Step Application

In this study a rectangular plate with a cylindrical block welded on is modeled. The dimensions are equal to the model in figure A.39 and the boundary conditions appear in figure A.43. A varying force acting normal to the surface of the right side of the plate is applied. The force gradually increases from 0 to 1000 N in increments of 100 N per time step. A varying pressure is applied to the inner surface of the hole which gradually increases from 0 to 1 MPa in increments of 0.1 MPa . The resulting equivalent von Mises stress distribution is pictured in figure A.44 for the whole model and likewise in figure A.45 for the submodel. This study is performed using an bilinear Elastoplastic model.

As the maximum equivalent von Mises stress appear in the part representing the submodel, the maximum is used for comparison in table A.11. Evaluating the results it is evident that the implementation of load steps is validated, as the stresses are equal.

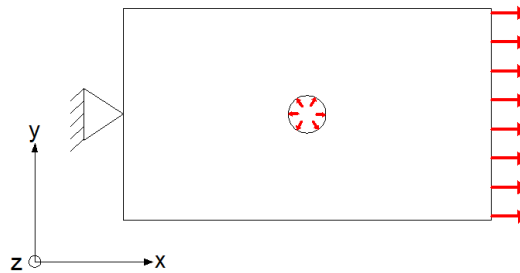


Figure A.43: The static model.

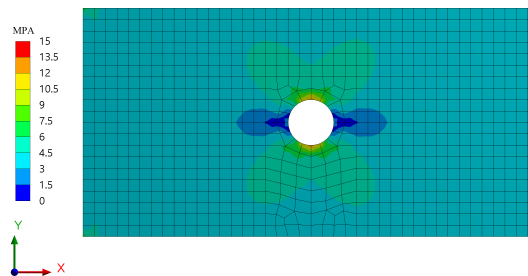


Figure A.44: Stress model in ANSYS Workbench for the whole model representing the final load step.

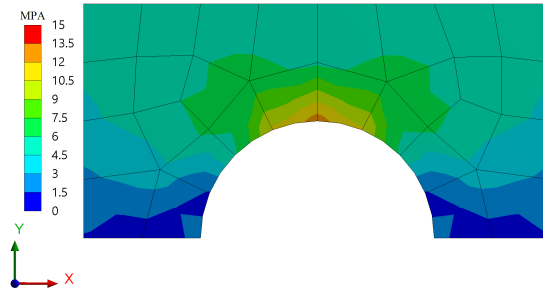


Figure A.45: Stress model in ANSYS Workbench for the submodel representing the final load step.

Table A.11: Stress comparison.

| Time step | Full model | Submodel |
|-----------|------------|----------|
| | [MPa] | [MPa] |
| 1 | 1.38 | 1.38 |
| 2 | 2.75 | 2.75 |
| 3 | 4.13 | 4.13 |
| 4 | 5.50 | 5.50 |
| 5 | 6.89 | 6.89 |
| 6 | 8.26 | 8.26 |
| 7 | 9.63 | 9.63 |
| 8 | 11.01 | 11.01 |
| 9 | 12.39 | 12.39 |
| 10 | 13.76 | 13.76 |

A.10.5 Validation of Multilinear Model

In this study a rectangular plate is modeled. The dimensions are illustrated in figure A.46 and the boundary conditions appear in figure A.47. A varying load is applied to the surface of the end of the plate gradually increasing from 0 N to 3500 N . The resulting stresses in the point marked in figure A.46 are measured and plotted in figure A.48.

Figure A.48 reveals a clear picture of the desired multilinear development of the stresses. It is therefore assumed that the multilinear model is applicable. As no experimental results are available in order to determine the hardening, the model is assumed valid.

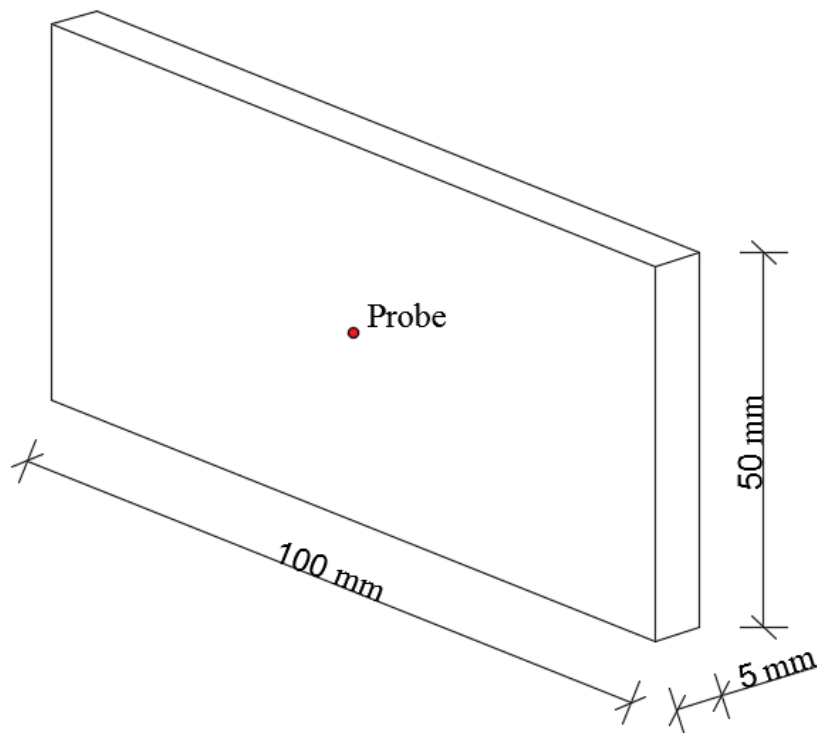


Figure A.46: Dimensions.

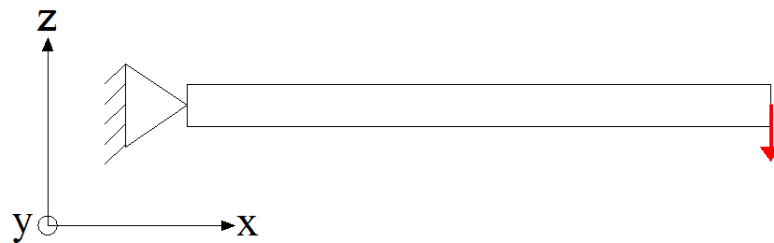


Figure A.47: The static system.

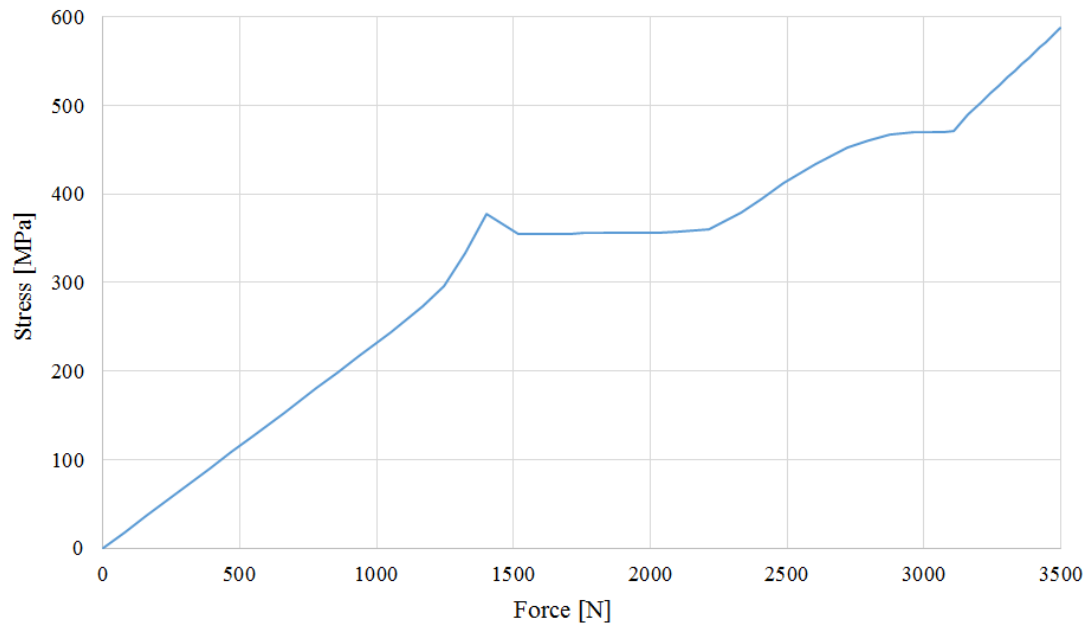


Figure A.48: Force/stress diagram, which clearly reveals the multilinear model created in section 5.1.3.

A.10.6 Implementation of Shell Elements

The implementation of shell elements is desirable, as this type of element is less computational demanding considering the amount of calculations compared to solid elements. A complex structure requires a heavily refined mesh which yields immense computational time using solids. The computational time can therefore advantageously be reduced, and the implementation of shell elements are an accessible tool that can be used to achieve this.

Shell elements are applicable for plane stress cases, where one dimension is far smaller than the two remaining. For thin members, shells have the advantage that the stress field is described through the thickness of the element. Correspondingly at least two solid elements must be used in order to create an acceptable representation of the stress field through the cross section, which yields an increase in calculation time due to a increased number of elements and equations.

Using ANSYS Workbench there are multiple possibilities of creating a mesh consisting of shell elements from a solid structure. A relatively easy possibility is to create a surface on top of a face of the structure that is to be converted to shells. A thickness of the surface is then defined. It is also possible to create the surface representing the structure by mid-surfacing. This require a pair of parallel surfaces or a set of curving faces. Both procedures are illustrated in figure A.49.

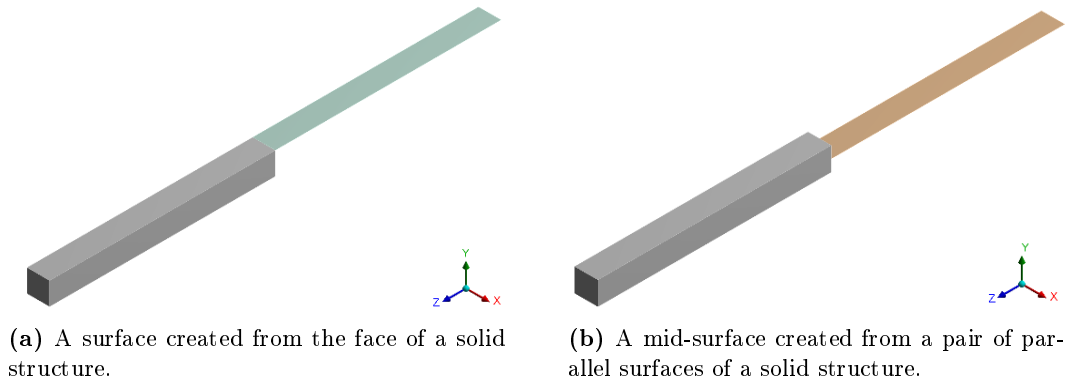


Figure A.49: Different possibilities of creating a surface representing a solid structure.

Implementing shell elements in the sheet pile configuration, it is necessary to create a contact between solids and shells due to the complexity of the sheet pile. Without precaution this will lead to false results. False results may arise due to the DOF's in the two types of elements, as shells do include all rotational DOF's except for rotation about the direction normal to the element, which is not the case for solids that entirely contain translational DOF's in the nodes. This means that a moment can not be transferred between the solid and shell elements, and rotation of the shells are therefore not prevented. In other words a hinge is created in the connection between the two types of elements. This is illustrated in figure A.50a.[43]

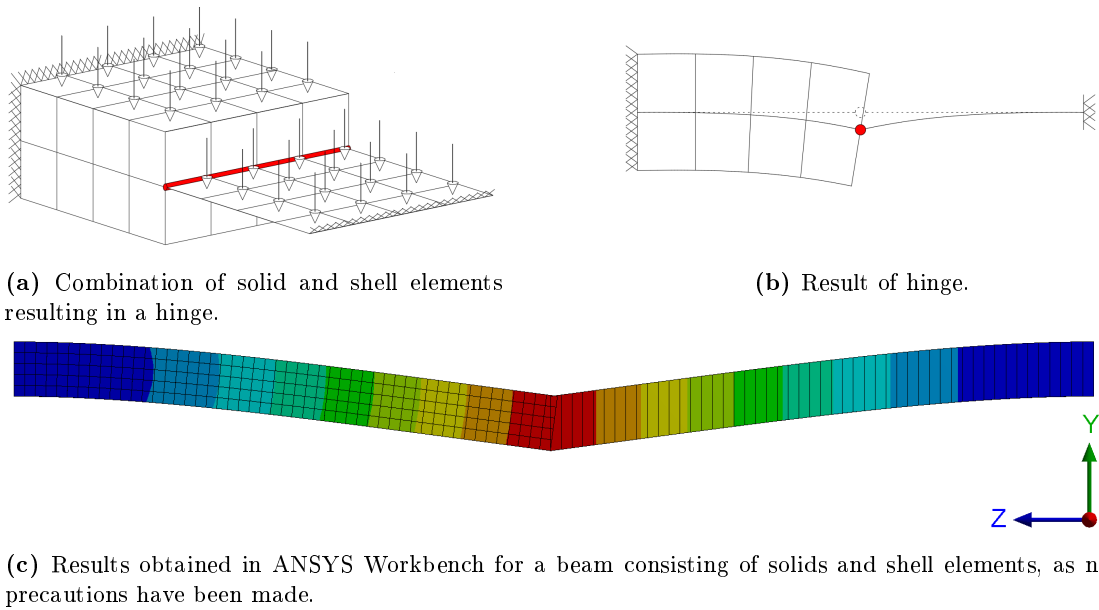


Figure A.50: Hinge development issue combining solid and shell elements.

Several solutions solve this issue either by modeling extensions to the shell elements or by application of a contact surface, which is possible in ANSYS Workbench. An extension of the shells is created in order to create shared surfaces between the two types of elements. This is possible by embedding the shells into the solid body of the structure or by creating a lip or extrusion of the shell part located on the surface of the solid body. The second solution is the simplest as an embedment require a split of the solid body, as the mesh generator will not connect the shells to the solid elements automatically. Both solutions are shown in figure A.51.

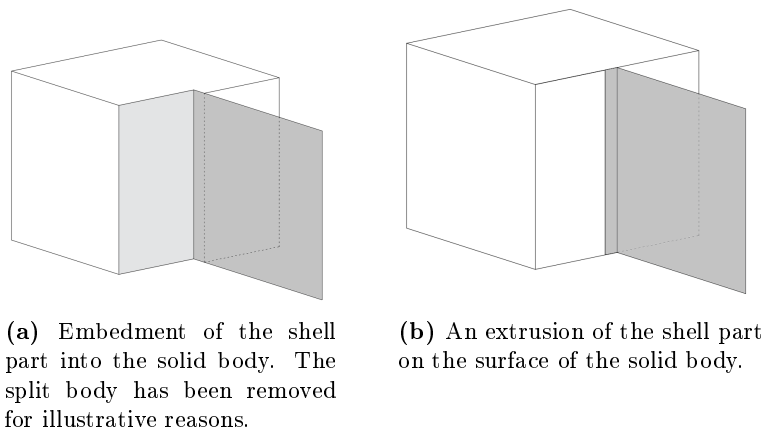


Figure A.51: Possible solutions by modeling.

A third option is possible, which does not include further modeling. This solution relies on the creation of a contact region between the two types of elements. Here Multi-Point Contact (MPC) is used, which is suitable for bonded or non-separated contacts. MPC is used in order to couple the rotational DOF's to the solid elements, as the solid elements only have translational DOF's. The rotations of the edge of the shells are transformed to the attached nodes of the solid elements. This is done by using rigid constraint equations between the solid and shell part for a bonded connection.[44]

Connecting the two types of elements, MPC has several advantages. This method eliminates the DOF's at the nodes on the contact faces by constraint equations, which is appropriate as the numbers of DOF do not correspond. For nonlinear analyses the constraint equations will be updated for MPC, which is desirable for the nonlinear analyses of the sheet pile. As the rigid connection between the parts are defined by constraint equations, calculation of the contact stiffness is not required, which reduces the problem.

In ANSYS Workbench the definition of a contact region is the simplest of the three and by little effort creates the most precise results compared to a full solid structure, and will therefore be applied.

A test of the beam pictured in figure A.50c has been carried out in the following, in order to validate that the implementation of shell elements is possible. In figure A.52 three configurations has been analysed:

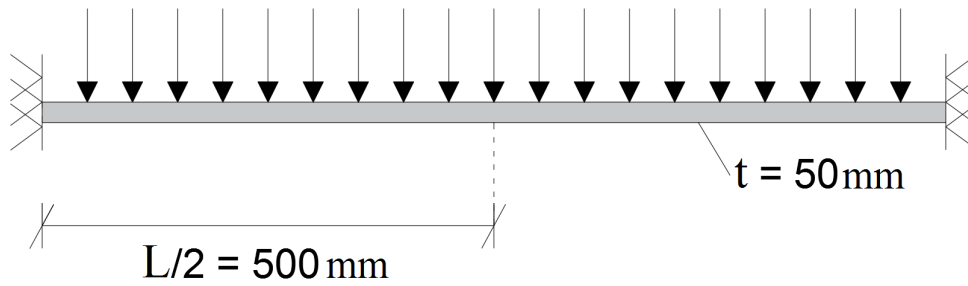
- Beam consisting of full solid mesh
- Beam consisting of part solid and part shell mesh. The shell elements are created using face-surfacing which can be seen in figure A.49a
- Beam consisting of part solid and part shell mesh. The shell elements are created using mid-surfacing which can be seen in figure A.49b

Deformation results for the three configurations are given in table A.12. The force is gradually increased to 10 *kN*.

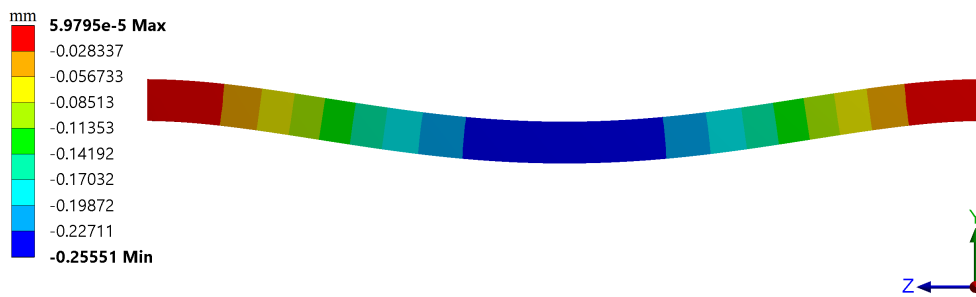
Table A.12: Results obtained for the three configurations of the beam.

| Configuration | Deformation | Deviation |
|------------------------------------|---------------|-----------|
| | [<i>mm</i>] | [%] |
| Solid beam | 0.2555 | - |
| Solid/shell beam mid-surfacing | 0.2571 | 0.62 |
| Solid/shell beam surface from face | 0.2863 | 10.76 |

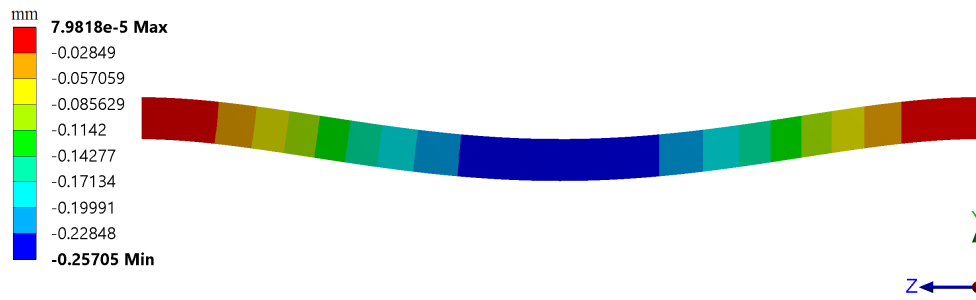
The results reveal that the contact between the two types of elements is appropriate using mid-surfacing. The minor deviation may be caused by the difference in application of an evenly distributed load on solid and shell elements. The difference is illustrated in figure A.53.



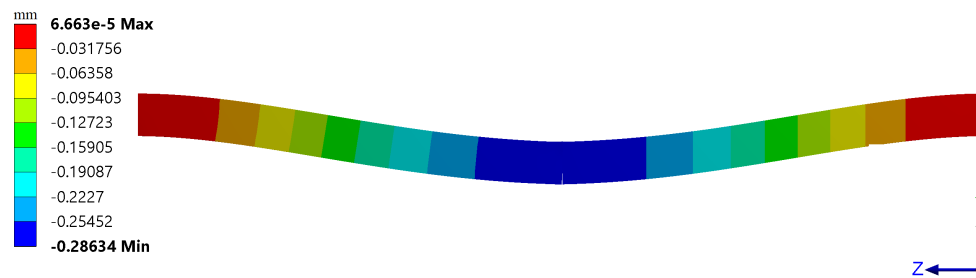
(a) Static system of the considered beam.



(b) Results for full solid beam model.



(c) Results for combination of solids and shells using mid-surfacing.

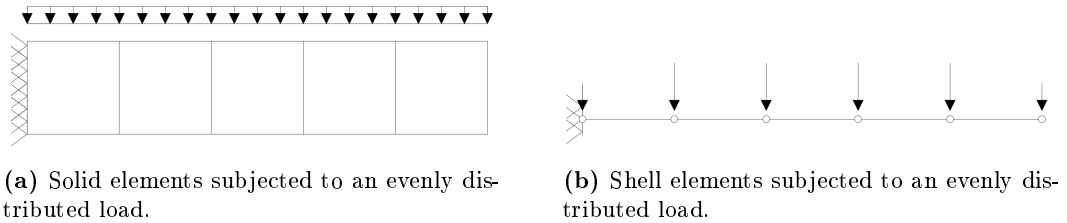


(d) Results for combination of solids and shells using surface from face.

Figure A.52: Results for different mesh configurations of the considered beam.

A. APPENDIX

The relatively great deviation occurring, as surface from face is used creating shell elements may be a result of the elements not being able to couple properly. Observing closely, figure A.52d reveal a minor gap in the connection between the solids and shells. The method for creation of shell element does seem to affect the coupling of shells and solids, as the two types of elements are continuing.

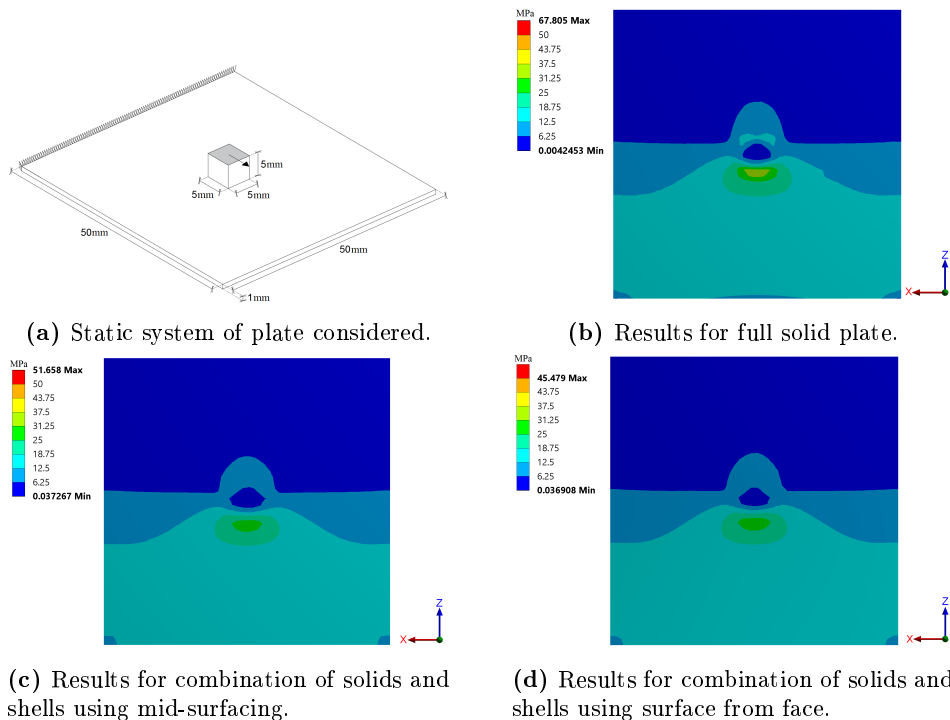


(a) Solid elements subjected to an evenly distributed load.

(b) Shell elements subjected to an evenly distributed load.

Figure A.53: Difference in application of an evenly distributed load on solid and shell elements.

Additionally the same study has been carried out for a plate having an attached block on the top face as pictured in figure A.54a. This has been performed to investigate, if the observations are true, when the shell and solid elements are coupled face to face. A load gradually increasing to 25 N affect the top surface of the block horizontally. The resulting deformations are given in figure A.54 for the three mesh configurations. The contact of interest is connection between the plate and the block. The plate will be meshed as solids and as shells by the two approaches respectively.



(a) Static system of plate considered.

(b) Results for full solid plate.

(c) Results for combination of solids and shells using mid-surfacing.

(d) Results for combination of solids and shells using surface from face.

Figure A.54: Results for different mesh configurations of the considered plate.

Figure A.54 reveals no immediate difference. In table A.13 deviations in deformations and stresses are given.

Table A.13: Results obtained for the three configurations of the plate.

| Configuration | Deformation | Deviation | Stress probe | Deviation |
|------------------------------------|---------------|-----------|----------------|-----------|
| | [<i>mm</i>] | [%] | [<i>MPa</i>] | [%] |
| Solid beam | 0.1470 | - | 16.625 | - |
| Solid/Shell beam mid-surfacing | 0.1462 | 0.55 | 16.827 | 1.20 |
| Solid/Shell beam surface from face | 0.1466 | 0.27 | 16.801 | 1.05 |

Using MPC bonded contact between shells and solids this analysis does not reveal any significant deviations between the two methods of shell element creation. It is therefore concluded that by using MPC contact shell elements can be combined properly, as precautions are taken.

Implementation of shell elements in the sheet pile configuration

In the following shell elements have been implemented in the sheet pile. The goal is to achieve the same precision as for solid element, but with a reduction in the calculation time.

As stated above the choice of method for creation of shell elements does not have significant influence on the results when solids are connected to shells on the face. Mid-surfacing has therefore been used, as this method has proven to be the most manageable of the two for the complexity of the sheet pile. The thickness varies across the cross section, and this fact has been accounted for. The MPC contact, explained in the foregoing has been used for the contact region, as high precision using this contact setting has been found.

Creation of the shell model has proven to be a time consuming process, as the thickness varies in every segment of the model, and the application of earth pressure and the mesh configuration requires a vast amount of segments. The possibility of making mistakes is high, as the thickness of any segment has to be manually inputted.

Comparison to solids

The sheet pile has been modeled using both solids and shells. A load of 325 *kN* has been applied gradually and the resulting stresses and total deformations in a probe is then given in table A.14.

Table A.14: Relative precision of the two types of elements.

| Configuration | Deformation | Deviation | Stress probe | Deviation |
|----------------|---------------|-----------|----------------|-----------|
| | [<i>mm</i>] | [%] | [<i>MPa</i>] | [%] |
| Solid elements | 134.05 | - | 275.88 | - |
| Shell elements | 141.59 | 5.62 | 246.68 | 10.58 |

Table A.14 reveals that the stresses and deformations captured have some deviations. The deformations deviates more than 5 % and the stresses more than 10 %. The deviations may be explained from the differences in the cross section considering the bends of the sheet pile, as

these have been modeled having a constant thickness in the shell model, which is not the case using solids.

Table A.15: Computational time consumption of the two types of elements for a specific load.

| Configuration | Computational Time | Reduction |
|-----------------------------|---------------------------|------------------|
| | [s] | [%] |
| Full model - solid elements | 77760 | - |
| Full model - shell elements | 3840 | 95.06 |
| Solid model with submodel | 7457 | 90.41 |

Evaluating table A.15 it is clear that the configuration containing shell elements has been computed faster than for solid elements. A reduction of 95 % is considered a useful result revealing that shell elements can be implemented advantageously. Compared to the inclusion of a submodel the shell model is about 50 % more time efficient. What this table does not reveal is the time consumed setting up the model. Due to the complexity of the sheet pile the creation of shell elements is a lengthy process full of potential mistakes. Thus, the time saved using shells during calculation does not make up for the time consumed, while creating the elements. It has been chosen not to implement this type of element to the structure in the analyses of chapter 5.

A.11 Eurocode Study

A.11.1 Dimension Study

A rectangular load bearing plate has been created. By altering both of the sides the resulting stress distribution are given in figures A.55 to A.59.

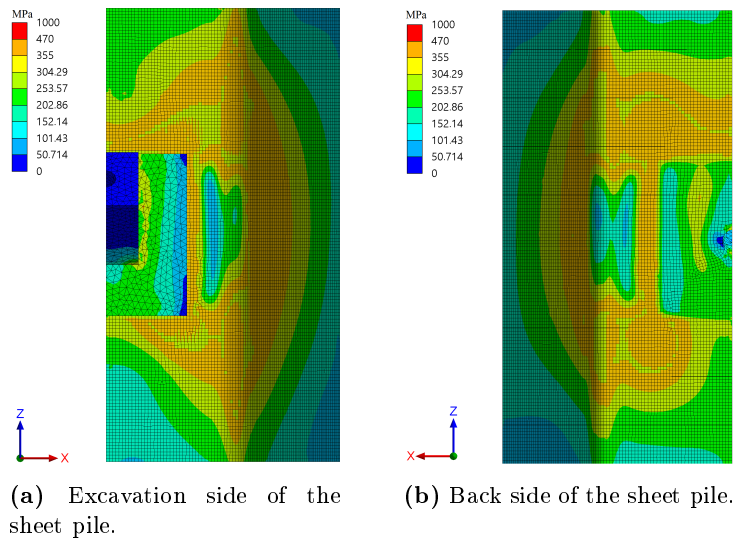


Figure A.55: Distribution of equivalent von Mises for a load bearing plate with the dimension of $250 \times 250 \text{ mm}$ and a horizontal anchor force of 350 kN .

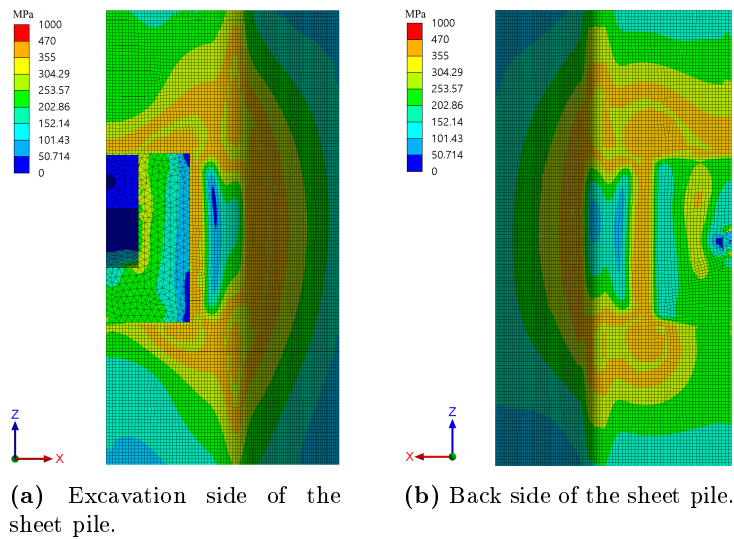


Figure A.56: Distribution of equivalent von Mises for a load bearing plate with the dimension of $260 \times 260 \text{ mm}$ and a horizontal anchor force of 350 kN .

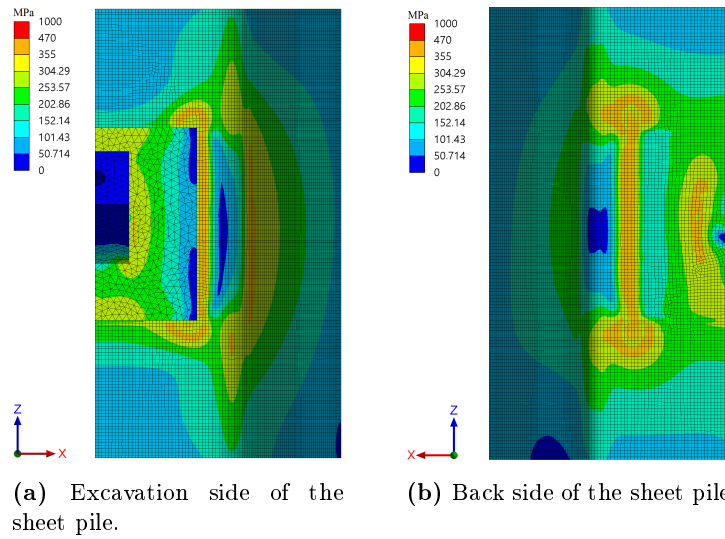


Figure A.57: Distribution of equivalent von Mises for a load bearing plate with the dimension of $300 \times 300 \text{ mm}$ and a horizontal anchor force of 350 kN .

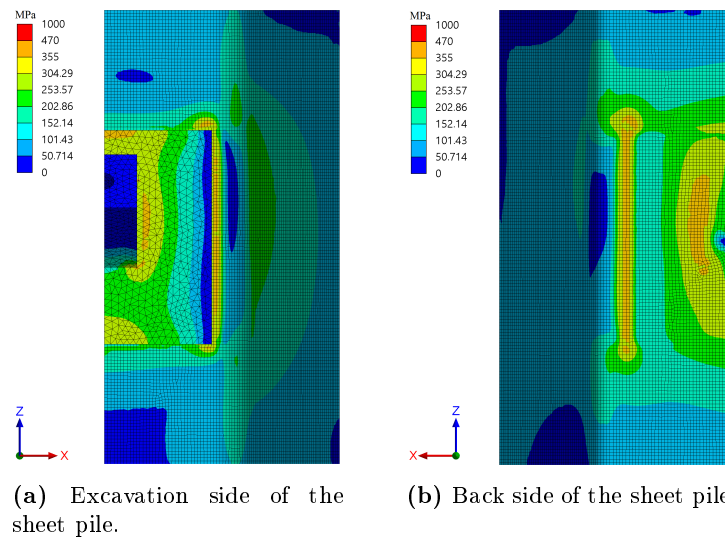


Figure A.58: Distribution of equivalent von Mises for a load bearing plate with the dimension of $330 \times 330 \text{ mm}$ and a horizontal anchor force of 350 kN .

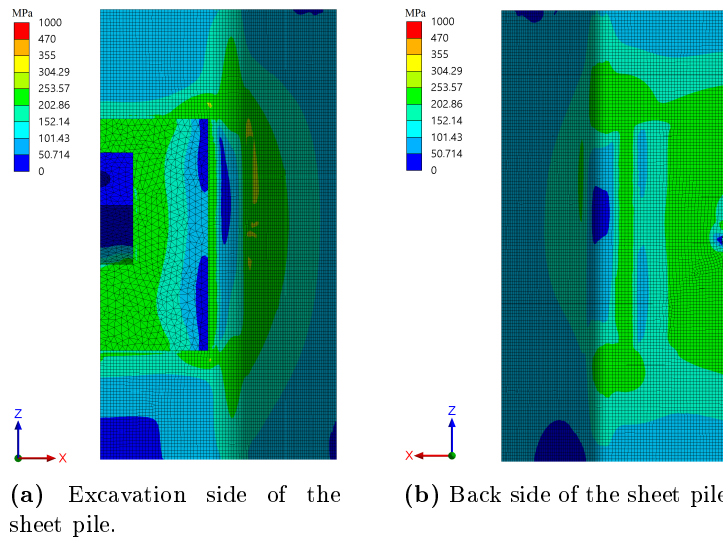


Figure A.59: Distribution of equivalent von Mises for a load bearing plate with the dimension of $330 \times 360 \text{ mm}$ and a horizontal anchor force of 350 kN .

A.11.2 Force Study

By altering the anchor force, the stress contour on the sheet piles changes which are shown in the following.

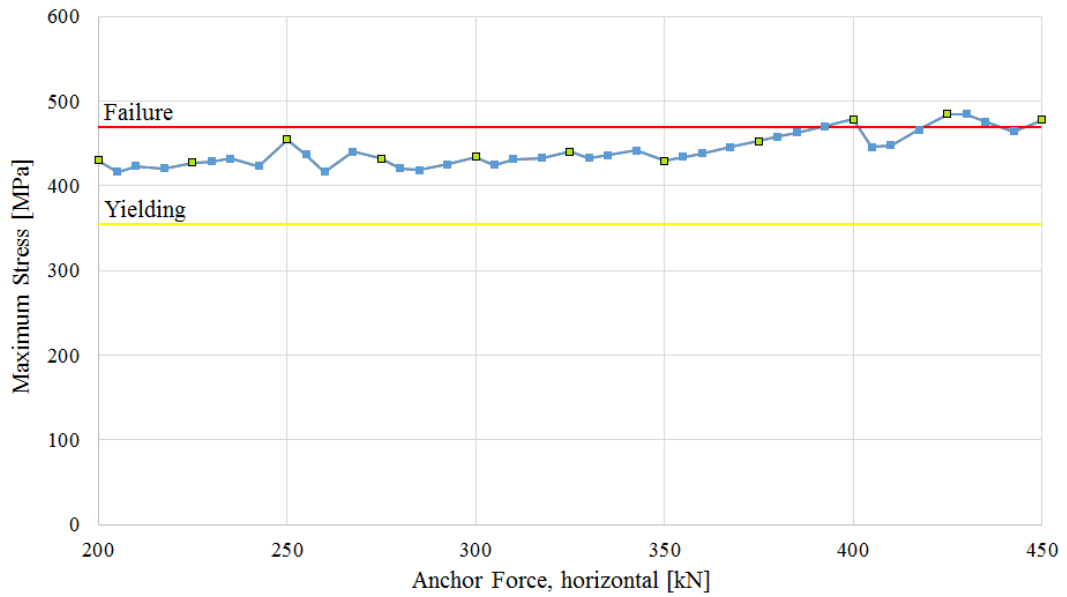


Figure A.60: Development of the maximum equivalent von Mises stress in sheet pile according to the respective anchor force. A stress plot can be found in the following related to the square green dots.

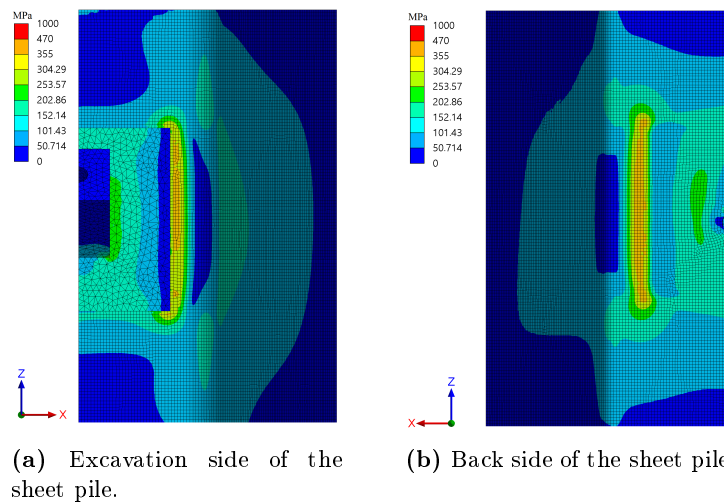


Figure A.61: Distribution of equivalent von Mises stress for a horizontal anchor force of 200 kN.

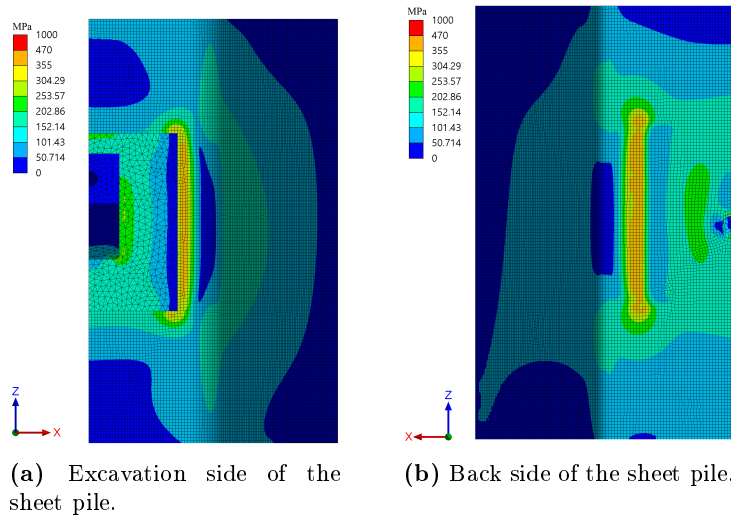


Figure A.62: Distribution of equivalent von Mises stress for a horizontal anchor force of 225 *kN*.

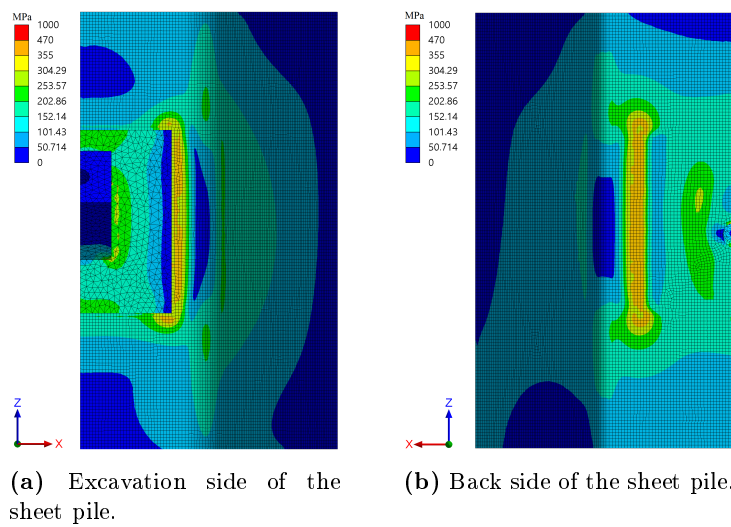
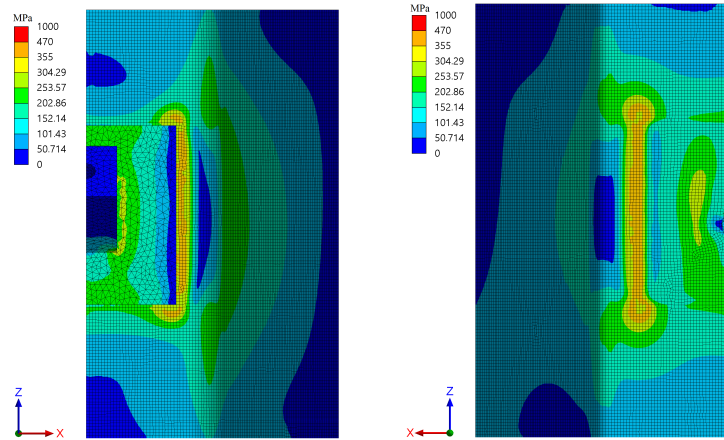
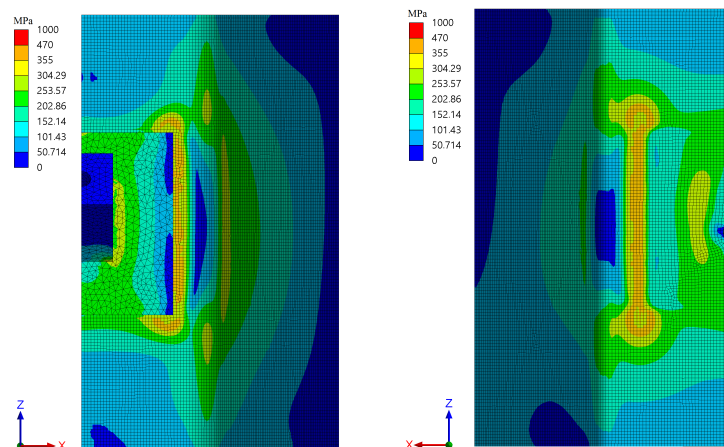


Figure A.63: Distribution of equivalent von Mises stress for a horizontal anchor force of 250 *kN*.



(a) Excavation side of the sheet pile. (b) Back side of the sheet pile.

Figure A.64: Distribution of equivalent von Mises stress for a horizontal anchor force of 275 *kN*.



(a) Excavation side of the sheet pile. (b) Back side of the sheet pile.

Figure A.65: Distribution of equivalent von Mises stress for a horizontal anchor force of 300 *kN*.

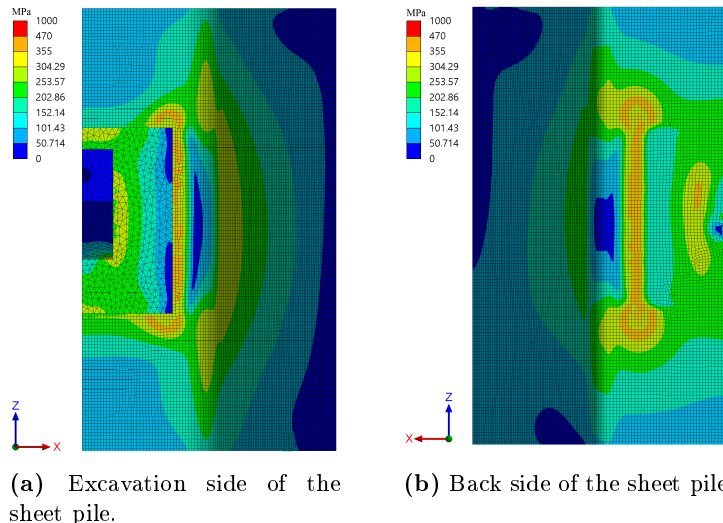


Figure A.66: Distribution of equivalent von Mises stress for a horizontal anchor force of 325 *kN*.

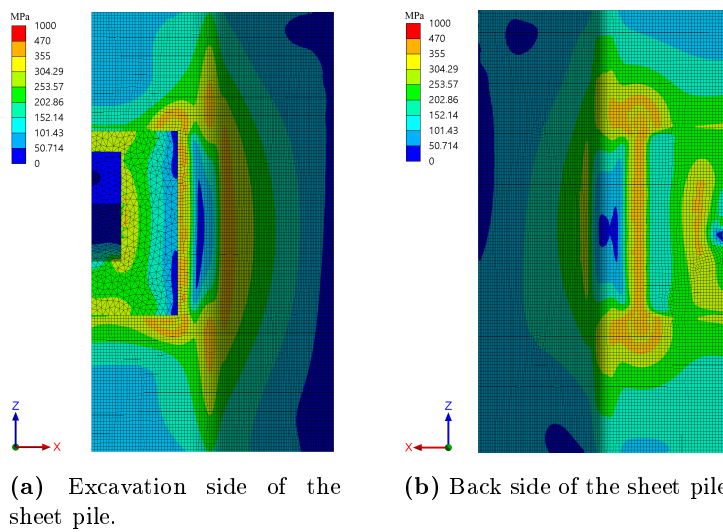


Figure A.67: Distribution of equivalent von Mises stress for a horizontal anchor force of 350 *kN*.

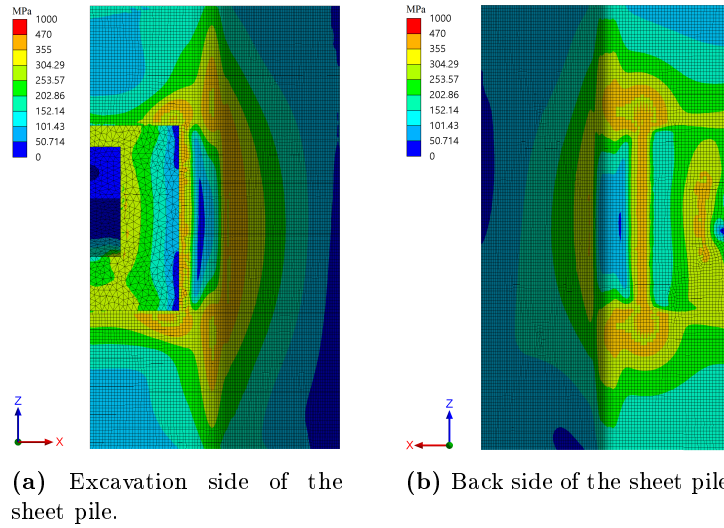


Figure A.68: Distribution of equivalent von Mises stress for a horizontal anchor force of 375 *kN*.

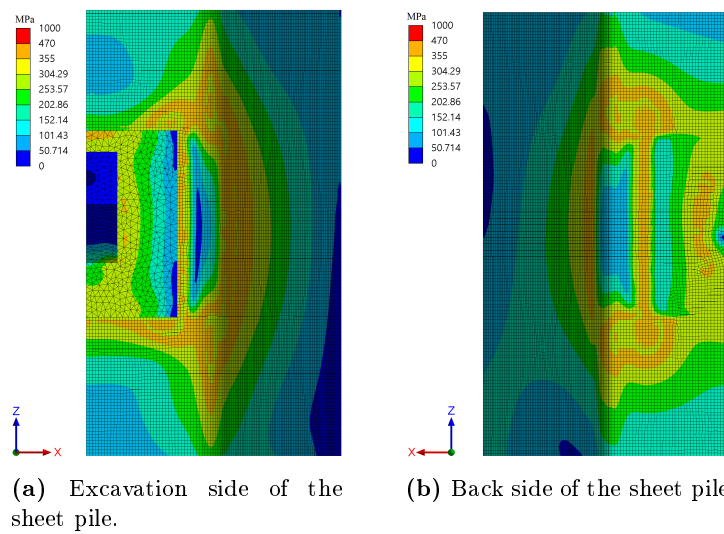
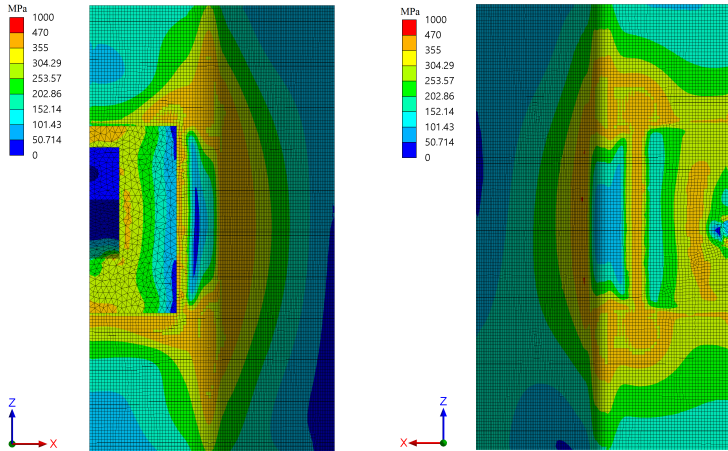
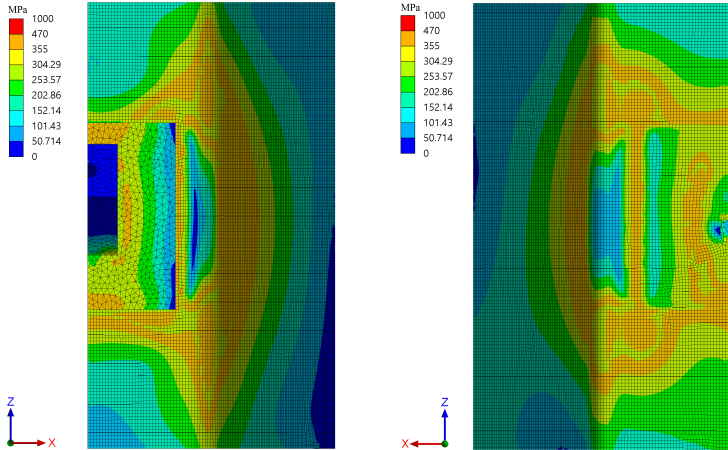


Figure A.69: Distribution of equivalent von Mises stress for a horizontal anchor force of 400 *kN*.



(a) Excavation side of the sheet pile. (b) Back side of the sheet pile.

Figure A.70: Distribution of equivalent von Mises stress for a horizontal anchor force of 425 kN.



(a) Excavation side of the sheet pile. (b) Back side of the sheet pile.

Figure A.71: Distribution of equivalent von Mises stress for a horizontal anchor force of 450 kN.

A.12 Parameter Study of Sheet Pile and Load Bearing Plate

A.12.1 Appendix - Thickness Study of the Load Bearing Plate

A quadratic load bearing plate has been created. The lengths of the plate has been fixed to 292 mm. The thickness, t , is then altered, and the resulting stress distributions are given.

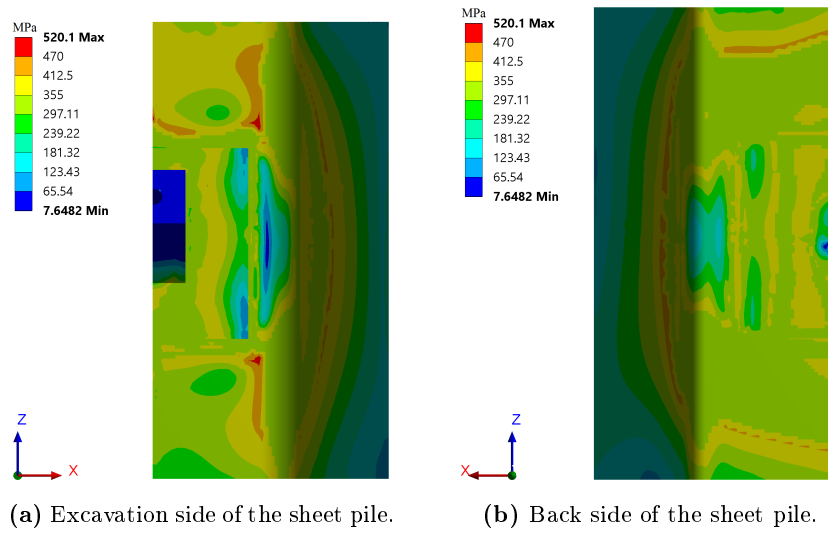


Figure A.72: Distribution of equivalent von Mises stresses having $t = 15mm$.

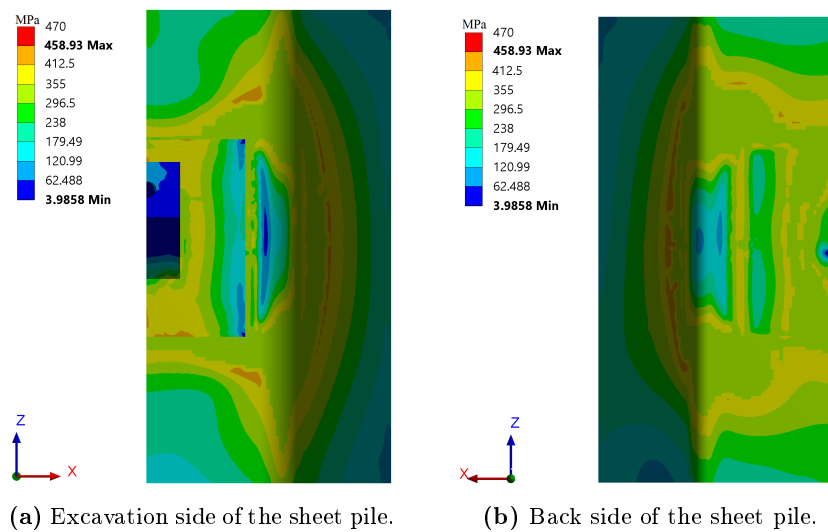


Figure A.73: Distribution of equivalent von Mises stresses having $t = 18mm$.

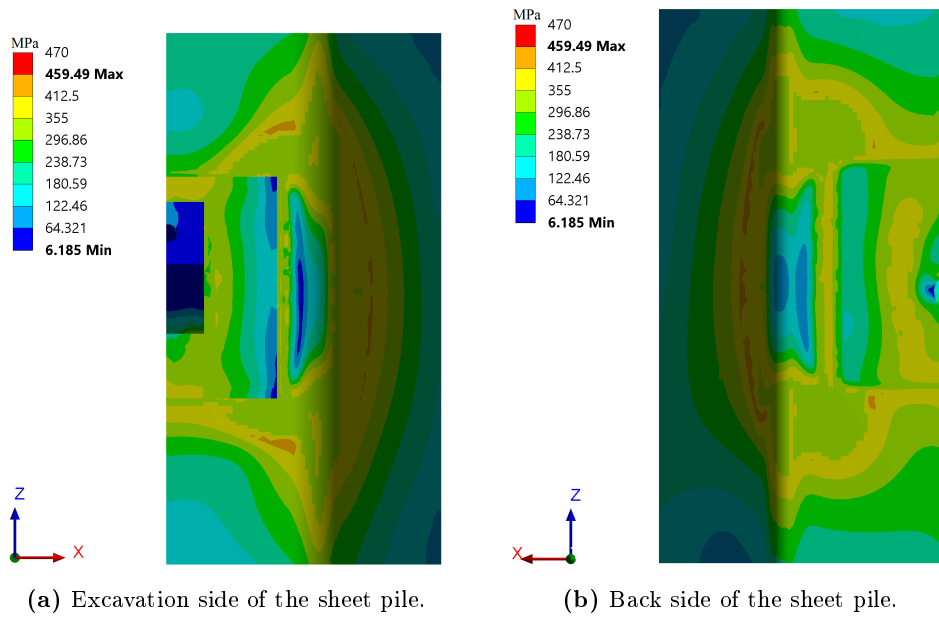


Figure A.74: Distribution of equivalent von Mises stresses having $t = 21mm$.

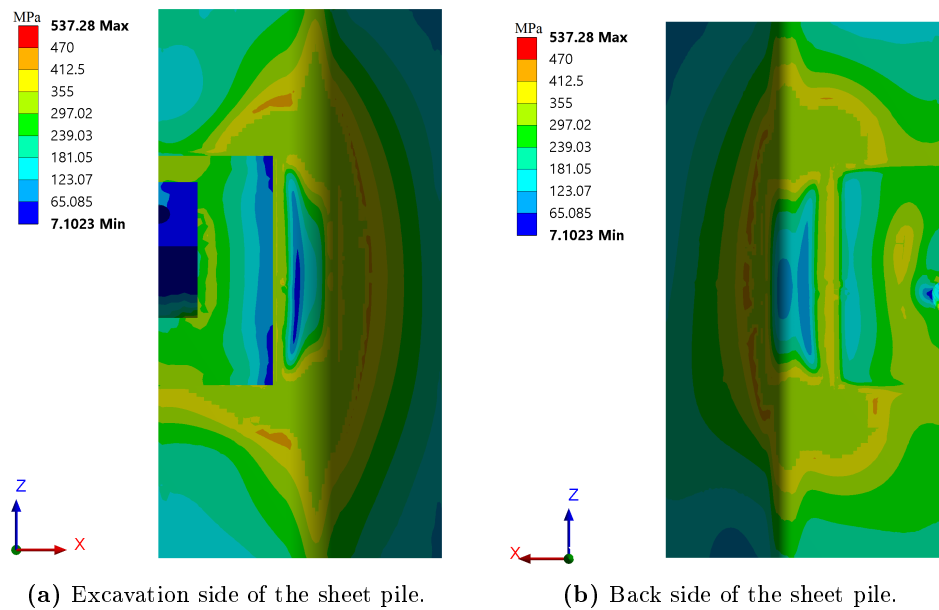
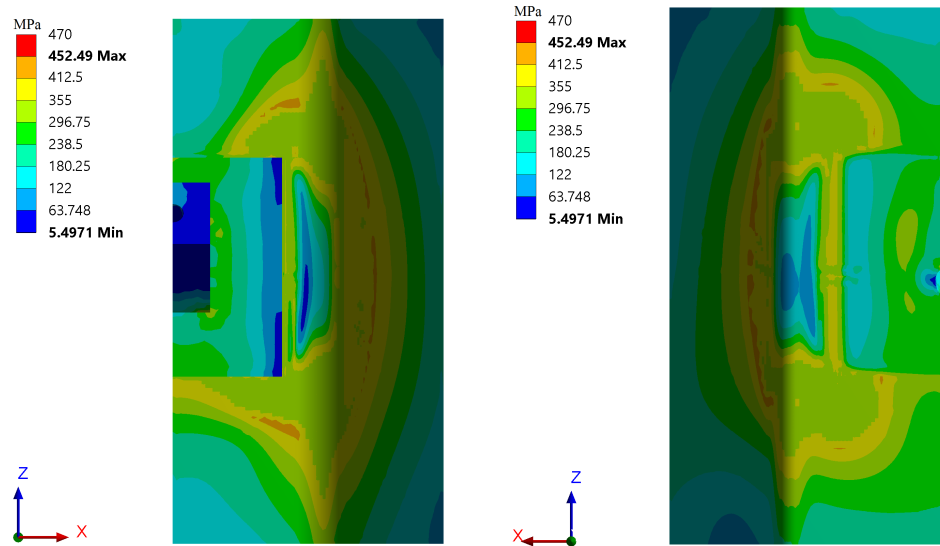


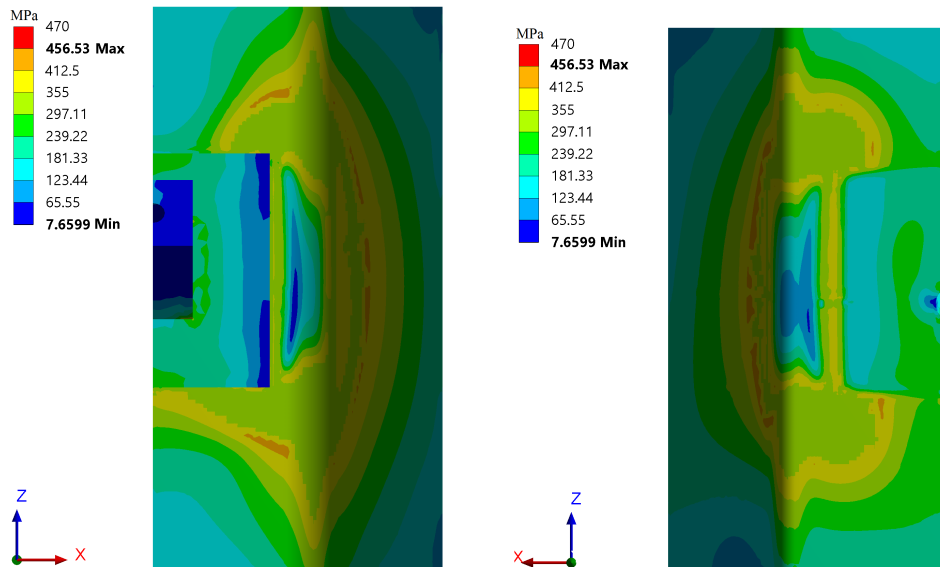
Figure A.75: Distribution of equivalent von Mises stresses having $t = 24mm$.



(a) Excavation side of the sheet pile.

(b) Back side of the sheet pile.

Figure A.76: Distribution of equivalent von Mises stresses having $t = 27\text{mm}$.



(a) Excavation side of the sheet pile.

(b) Back side of the sheet pile.

Figure A.77: Distribution of equivalent von Mises stresses having $t = 30\text{mm}$.

The maximum stresses has been captured in the flange and web in both the excavation side and the back side respectively resulting in four sets of data which are given in figures A.78 to A.83. Stress peaks related to singularities have been neglected.

- *P1* refers to the back side of the flange
- *P2* refers to the excavation side of the flange
- *P3* refers to the back side of the web
- *P4* refers to the excavation side of the web

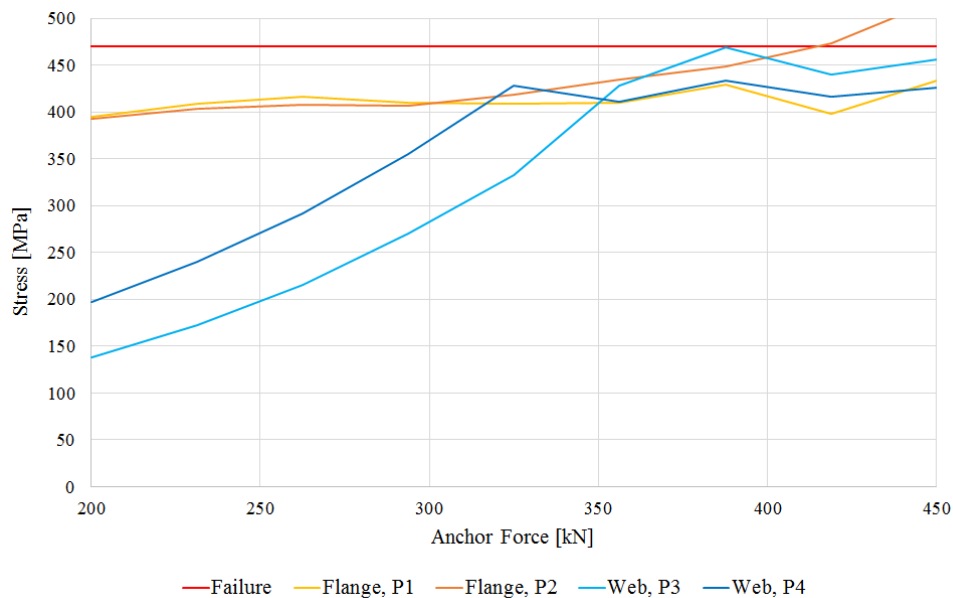


Figure A.78: Development of the maximum equivalent von Mises stresses in the two sides of the flange and web respectively having $t = 15mm$.

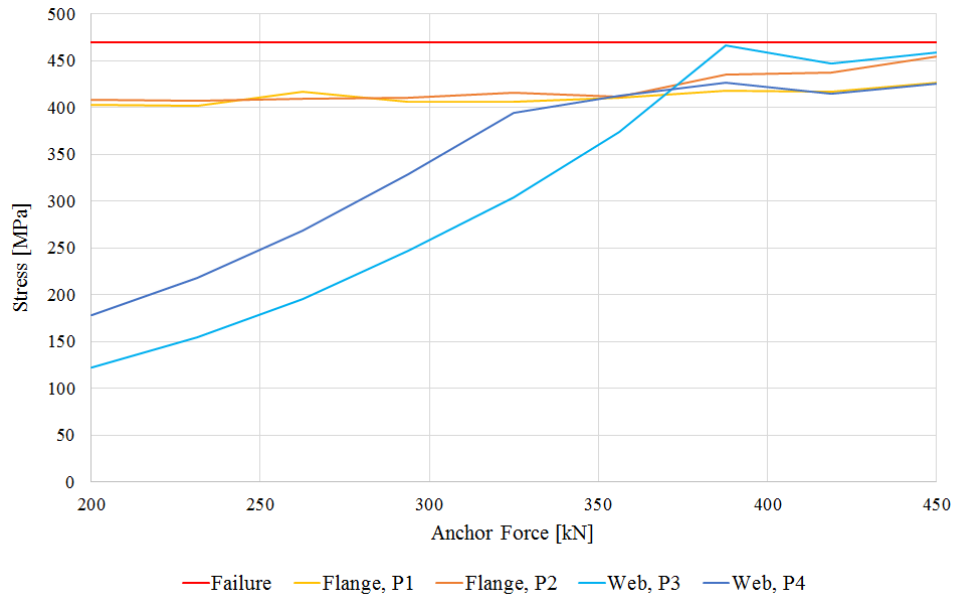


Figure A.79: Development of the maximum equivalent von Mises stresses in the two sides of the flange and web respectively having $t = 18mm$.

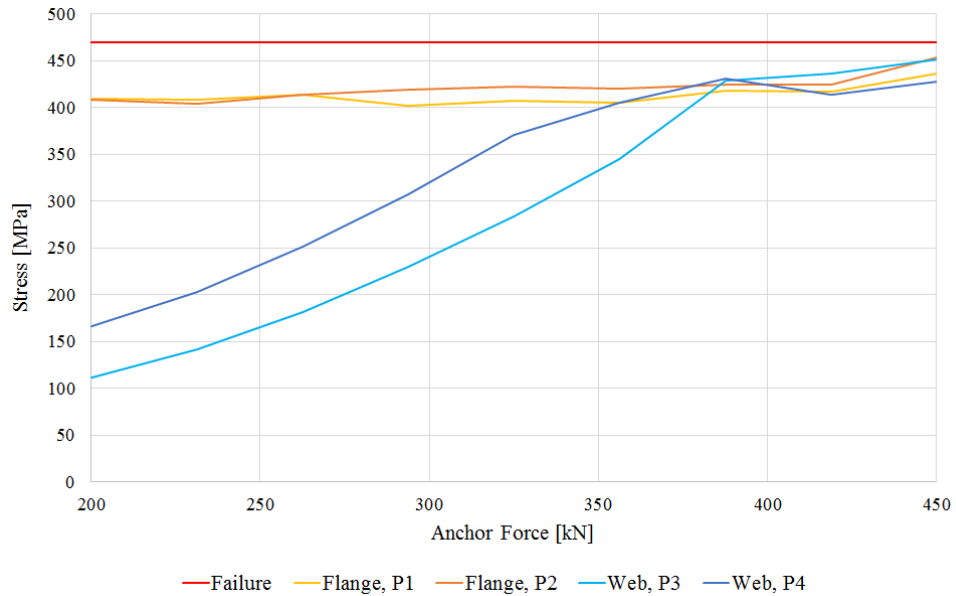


Figure A.80: Development of the maximum equivalent von Mises stresses in the two sides of the flange and web respectively having $t = 21mm$.

A.12. Parameter Study of Sheet Pile and Load Bearing Plate

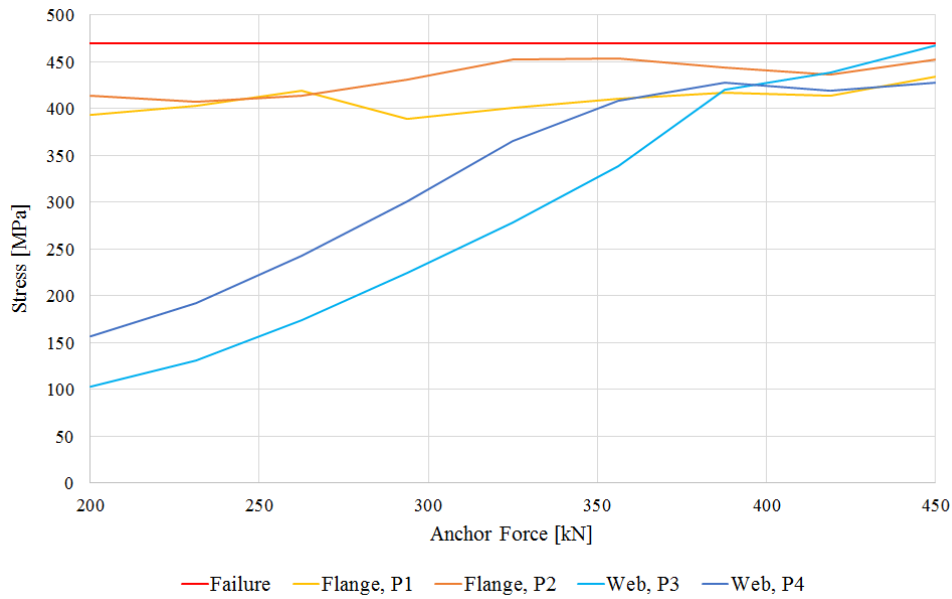


Figure A.81: Development of the maximum equivalent von Mises stresses in the two sides of the flange and web respectively having $t = 24mm$.

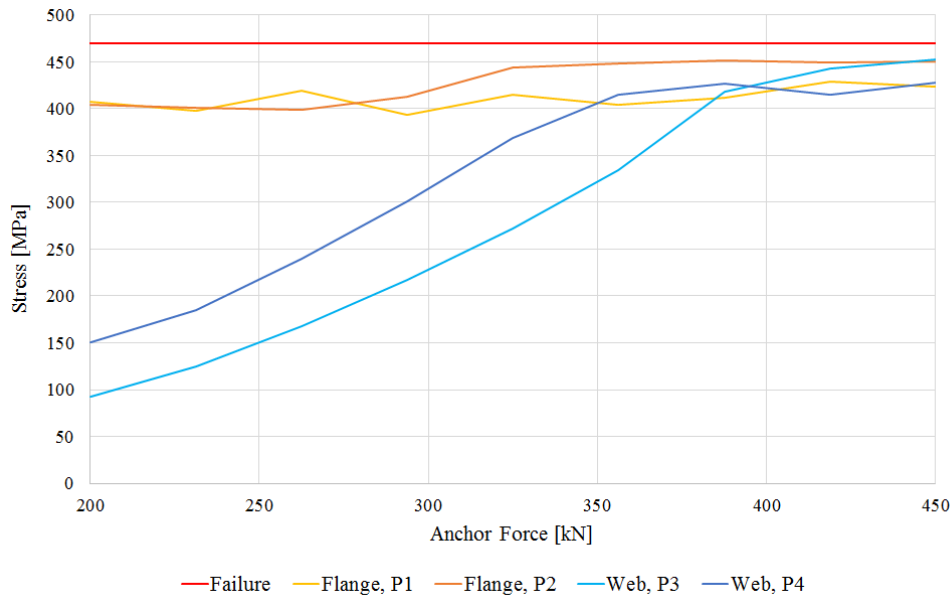


Figure A.82: Development of the maximum equivalent von Mises stresses in the two sides of the flange and web respectively having $t = 27mm$.

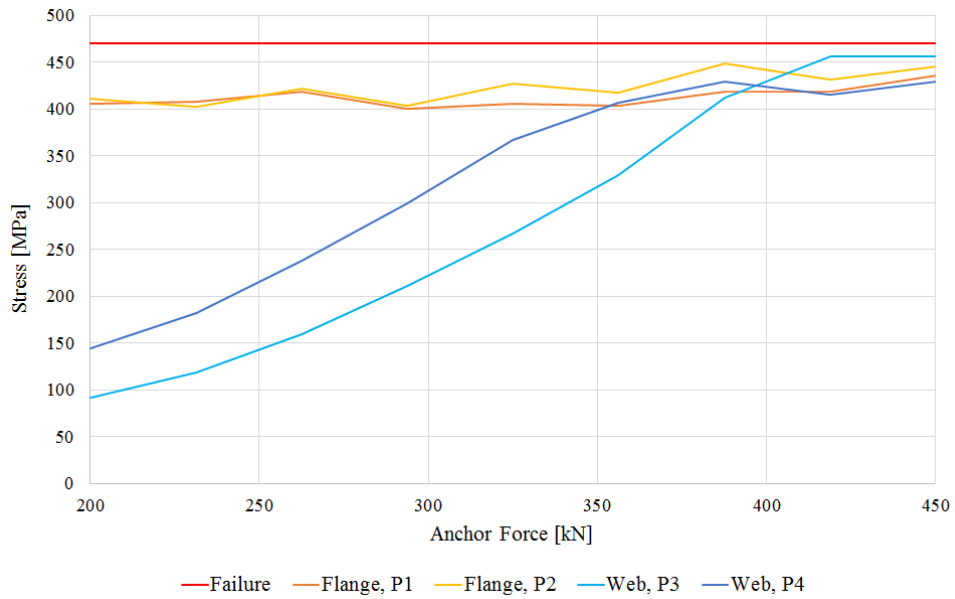


Figure A.83: Development of the maximum equivalent von Mises stresses in the two sides of the flange and web respectively having $t = 30mm$.

The maximum plastic strains for any of the size configurations are shown in figure A.84, which shows the development in the strains as the size is altered.

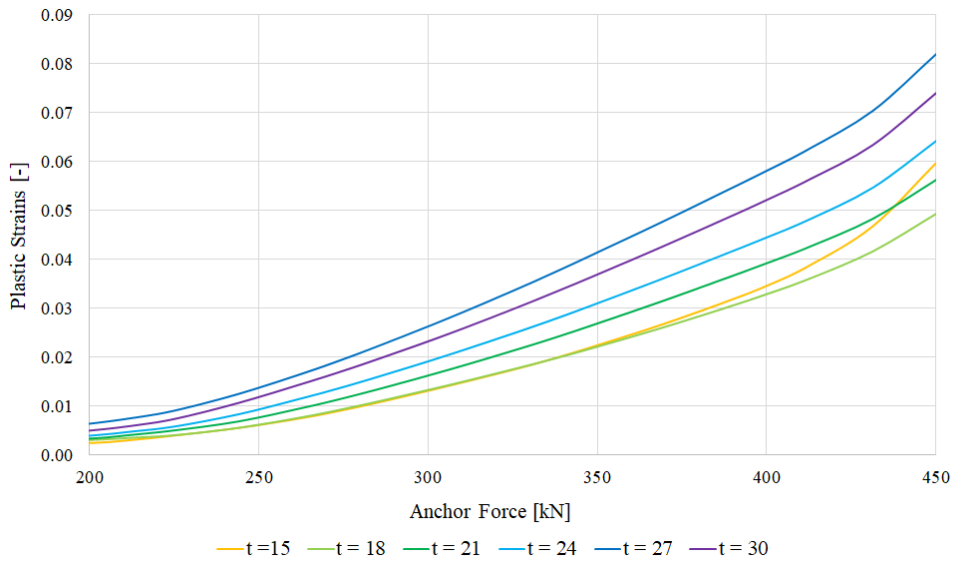


Figure A.84: Development of the maximum plastic strains in the sheet pile for different thickness configurations of the load bearing plate.

A.12.2 Width Study

A rectangular load bearing plate has been created. The length of the plate has been fixed to 292 mm. The width, w , is then altered, and the resulting stress distributions are given.

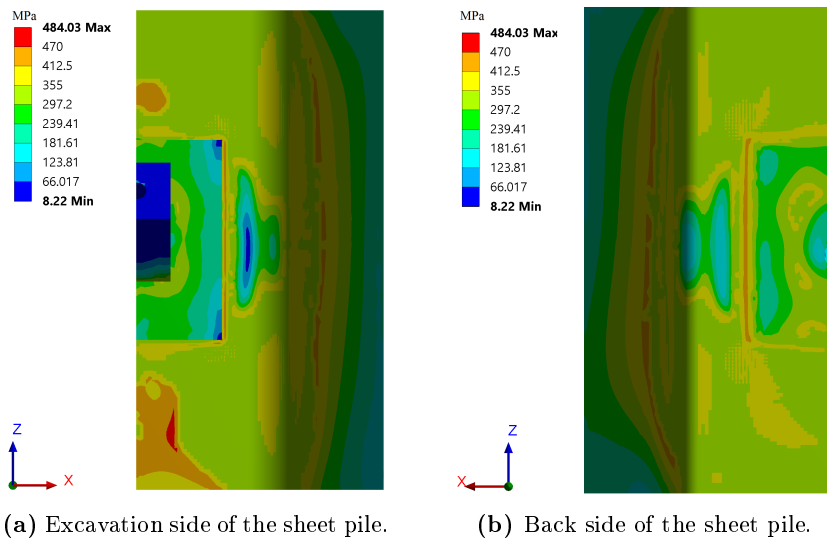


Figure A.85: Distribution of equivalent von Mises stresses having $w = 250mm$.

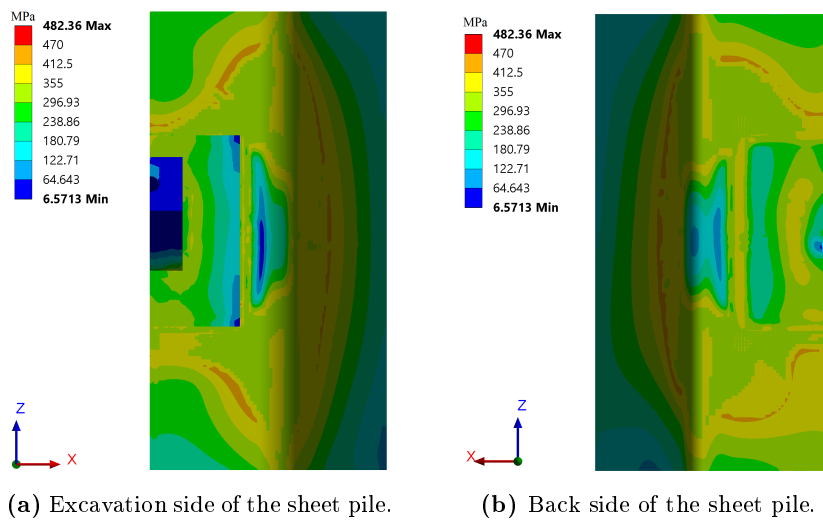
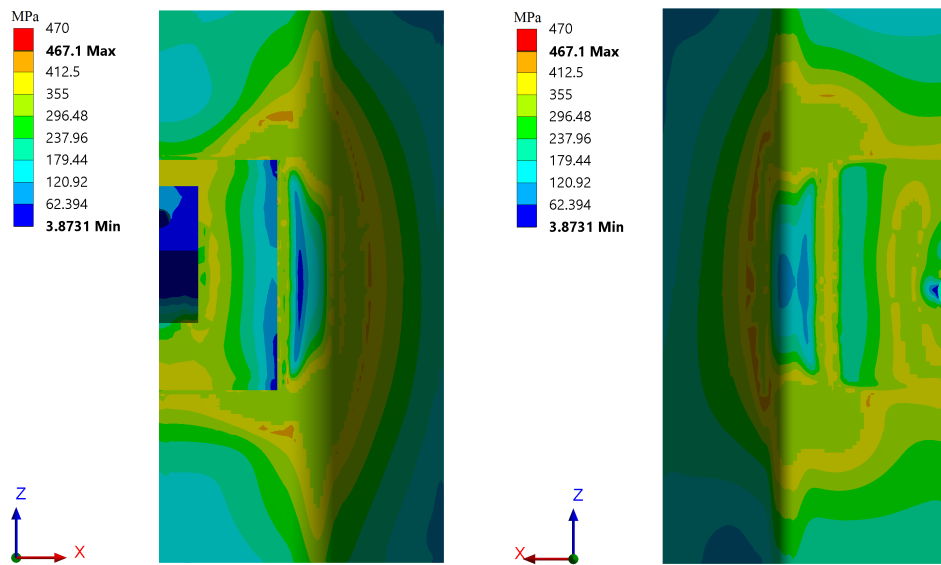


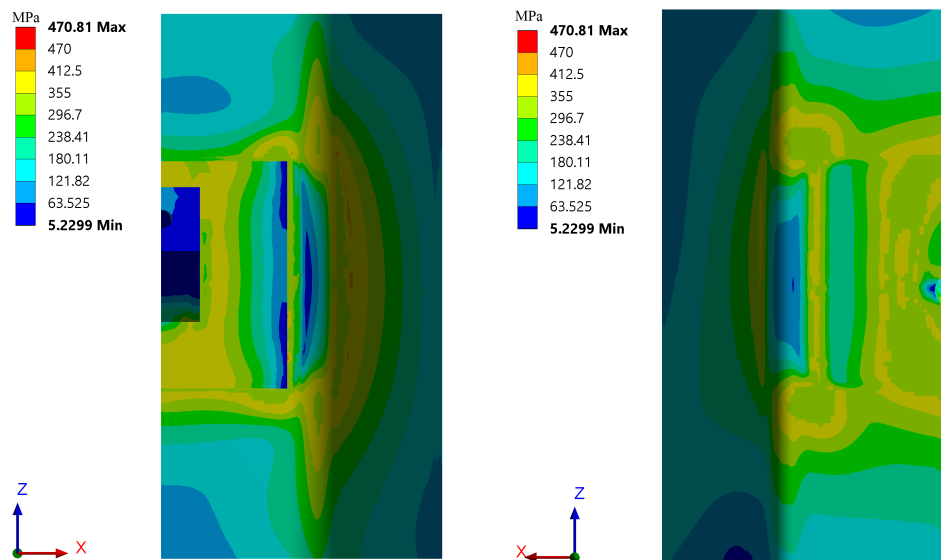
Figure A.86: Distribution of equivalent von Mises stresses having $w = 275mm$.



(a) Excavation side of the sheet pile.

(b) Back side of the sheet pile.

Figure A.87: Distribution of equivalent von Mises stresses having $w = 300mm$.



(a) Excavation side of the sheet pile.

(b) Back side of the sheet pile.

Figure A.88: Distribution of equivalent von Mises stresses having $w = 325mm$.

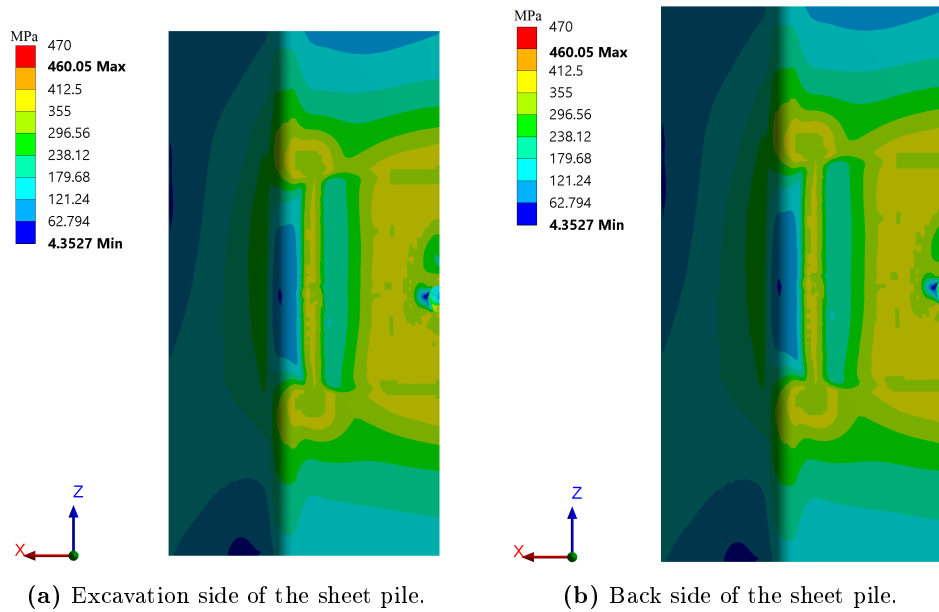


Figure A.89: Distribution of equivalent von Mises stresses having $w = 335mm$.

The maximum stresses has been captured in the flange and web in both the excavation side and the back side respectively resulting in four sets of data which are given in figures A.90 to A.94. Stress peaks related to singularities have been neglected.

- $P1$ refers to the back side of the flange

- $P2$ refers to the excavation side of the flange

- $P3$ refers to the back side of the web

- $P4$ refers to the excavation side of the web

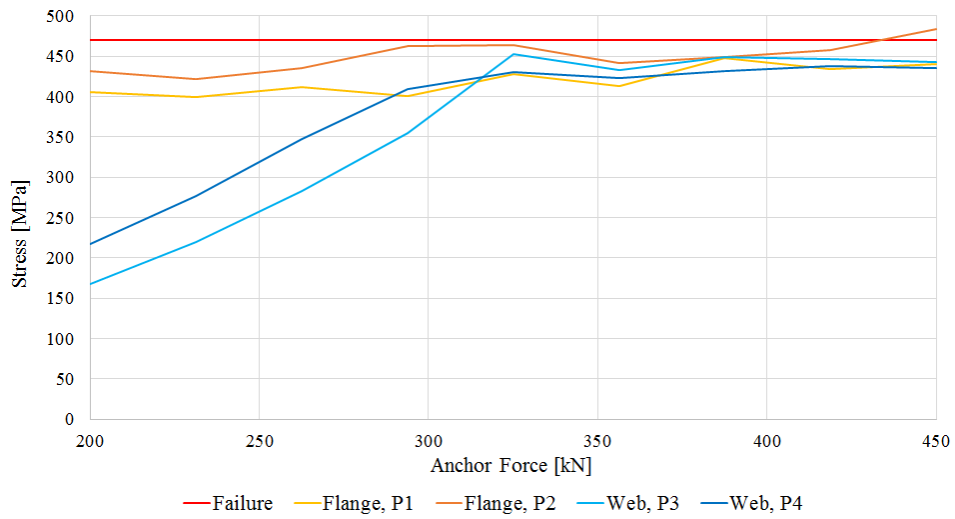


Figure A.90: Development of the maximum equivalent von Mises stresses in the two sides of the flange and web respectively having $w = 250mm$.

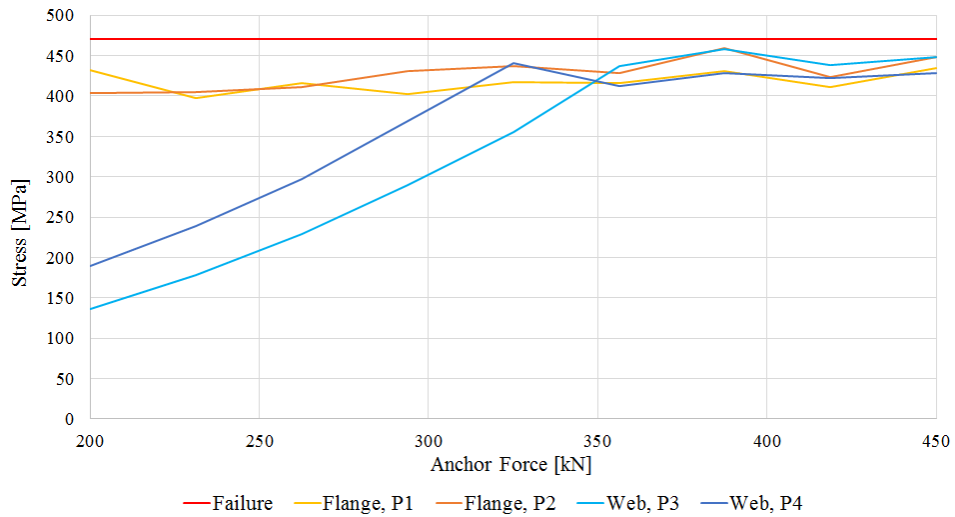


Figure A.91: Development of the maximum equivalent von Mises stresses in the two sides of the flange and web respectively having $w = 275mm$.

A.12. Parameter Study of Sheet Pile and Load Bearing Plate

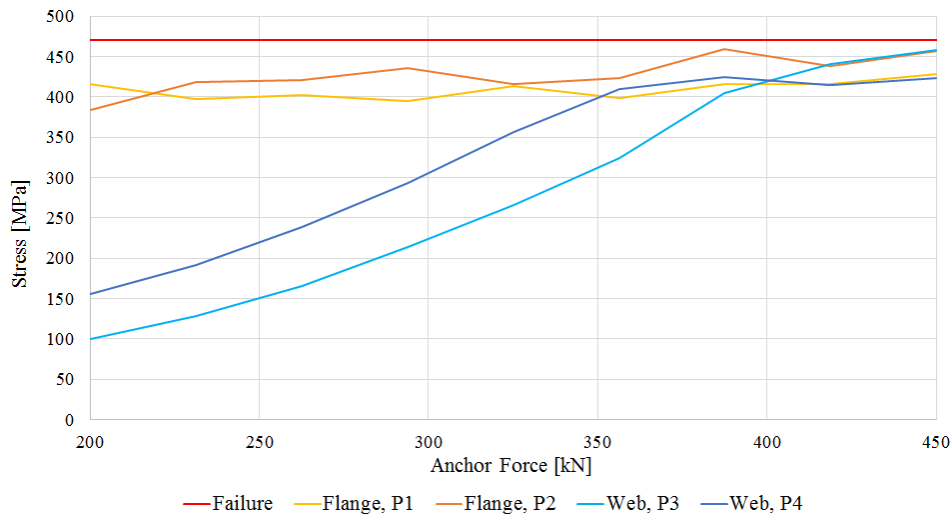


Figure A.92: Development of the maximum equivalent von Mises stresses in the two sides of the flange and web respectively having $w = 300mm$.

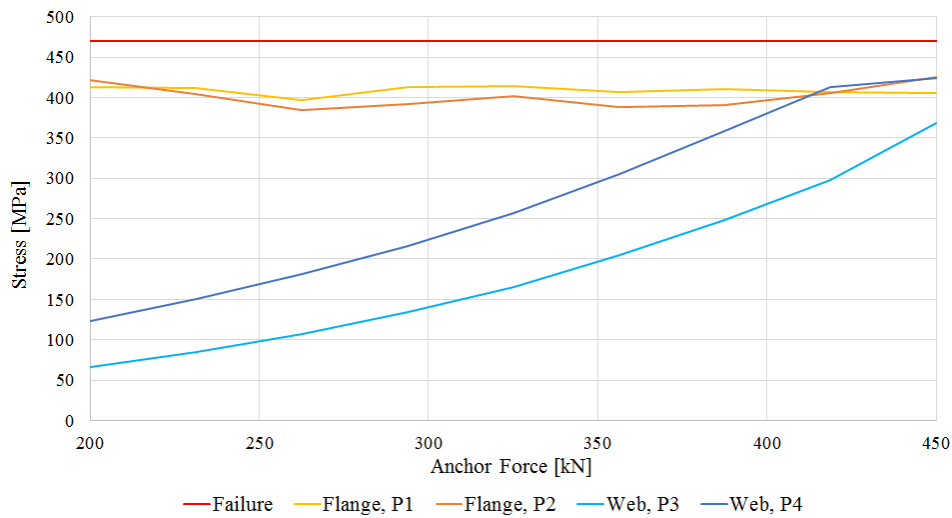


Figure A.93: Development of the maximum equivalent von Mises stresses in the two sides of the flange and web respectively having $w = 325mm$.

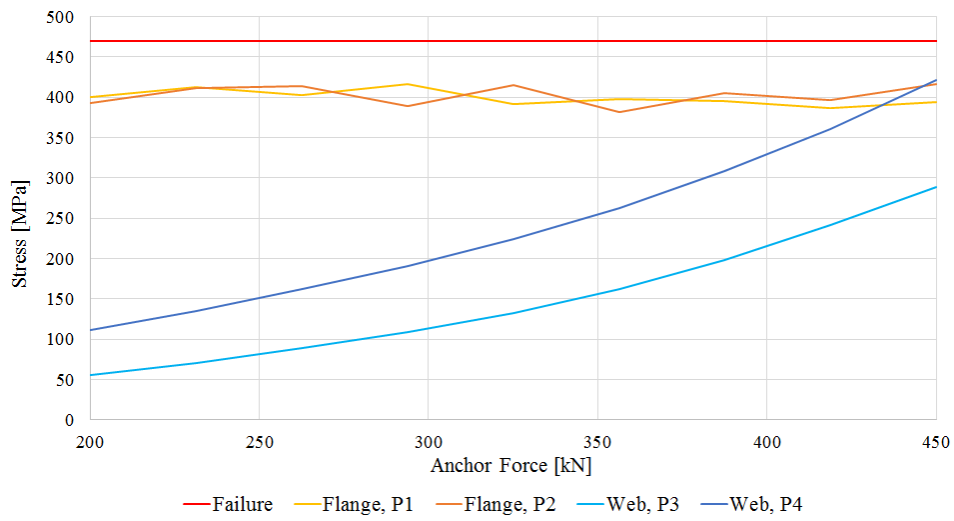


Figure A.94: Development of the maximum equivalent von Mises stresses in the two sides of the flange and web respectively having $w = 335mm$.

The maximum plastic strains for any of the size configurations are shown in figure A.95, which shows the development in the strains as the size is altered.

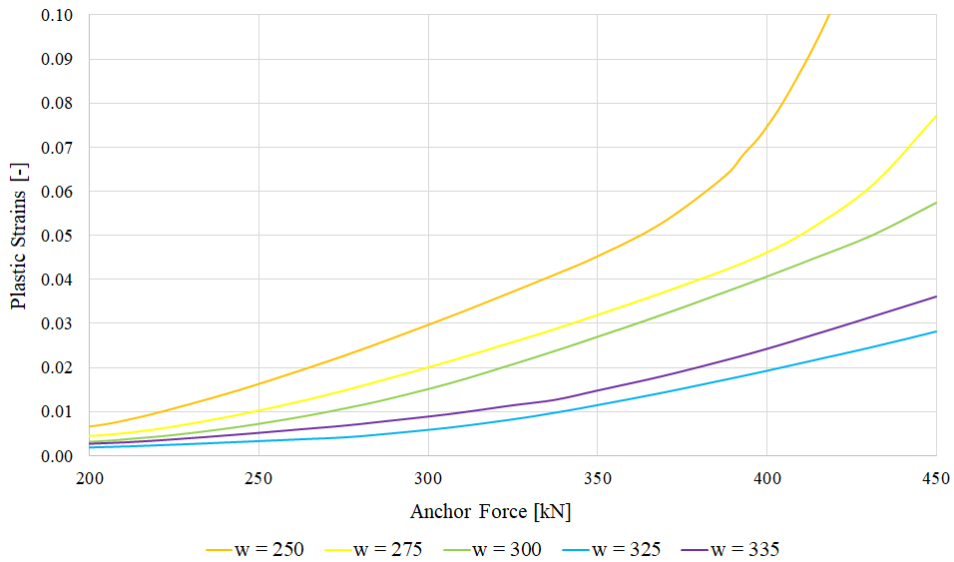
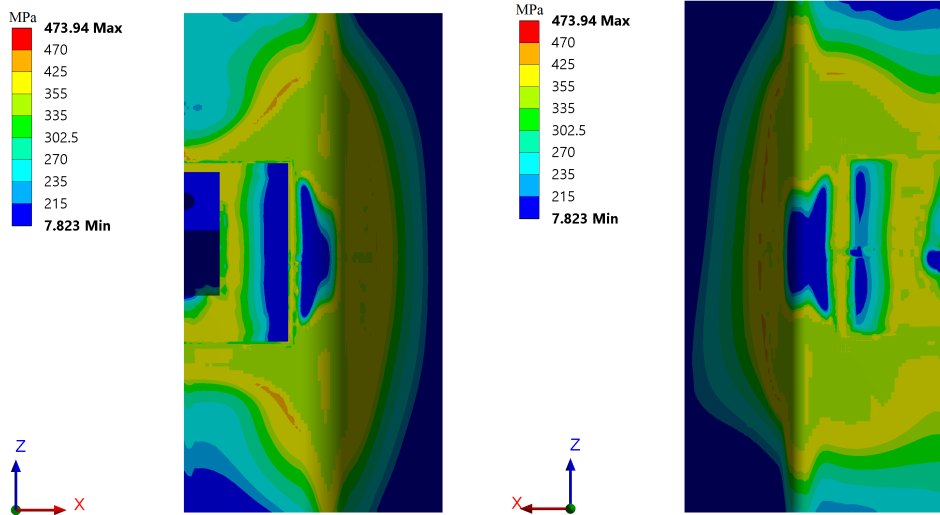


Figure A.95: Development of the maximum plastic strains in the sheet pile for different width configurations of the load bearing plate.

A.12.3 Length Study

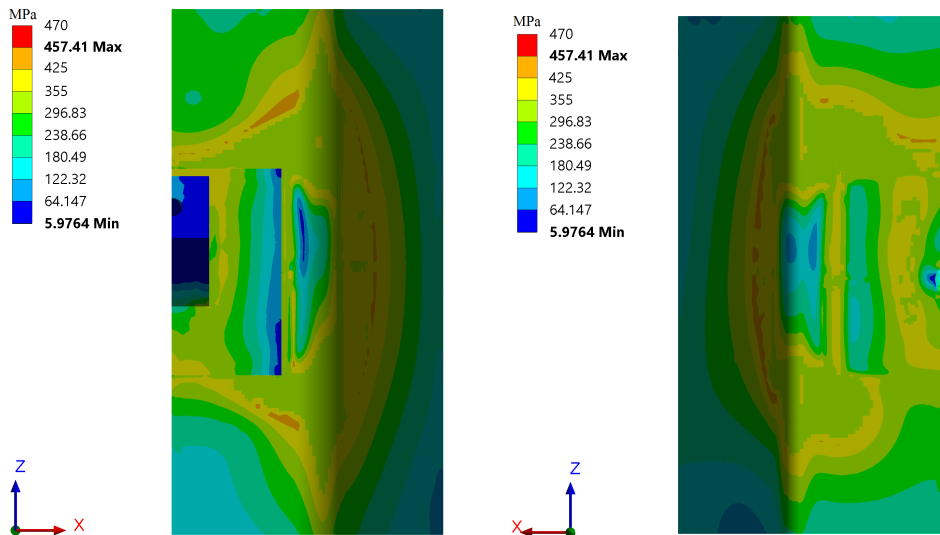
A rectangular load bearing plate has been created. The width of the plate has been fixed to 292 mm. The length, l , is then altered, and the resulting stress distributions are given.



(a) Excavation side of the sheet pile.

(b) Back side of the sheet pile.

Figure A.96: Distribution of equivalent von Mises stresses having $l = 250mm$.



(a) Excavation side of the sheet pile.

(b) Backside of the sheet pile.

Figure A.97: Distribution of equivalent von Mises stresses having $l = 275mm$.

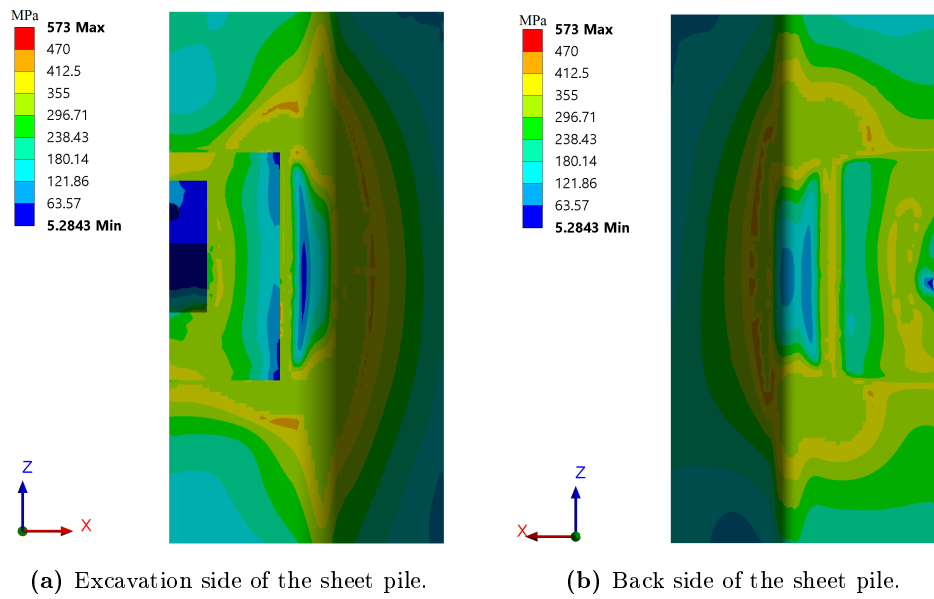


Figure A.98: Distribution of equivalent von Mises stresses having $l = 300mm$.

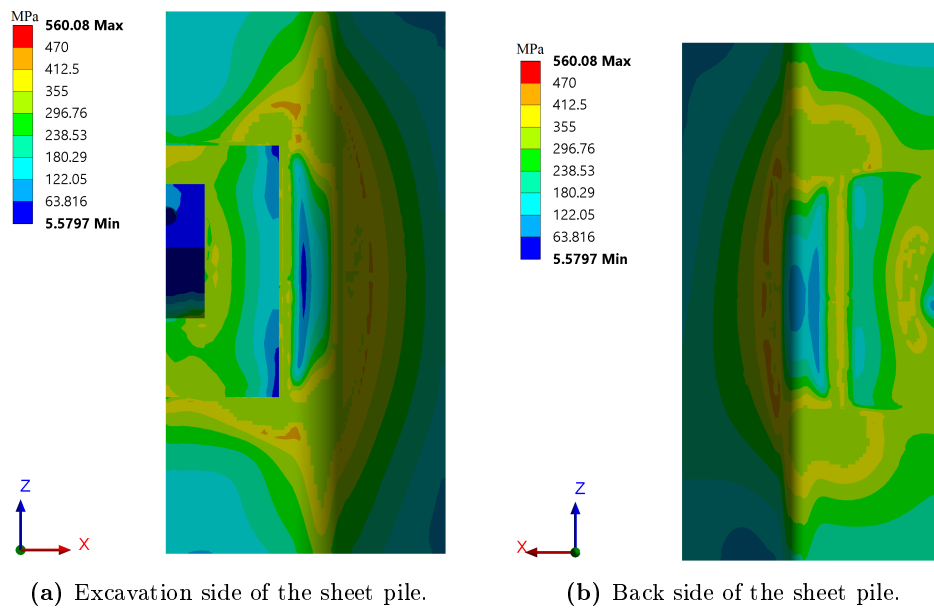
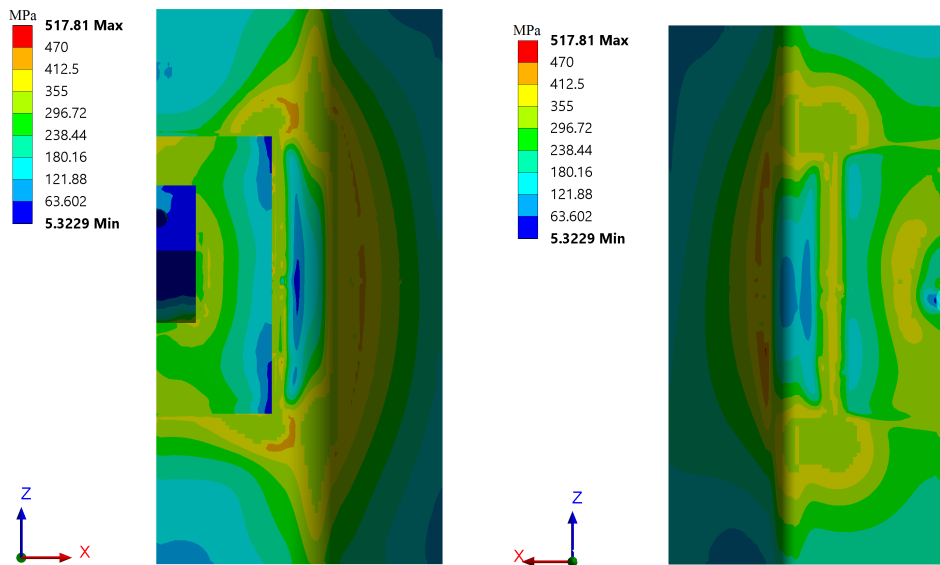


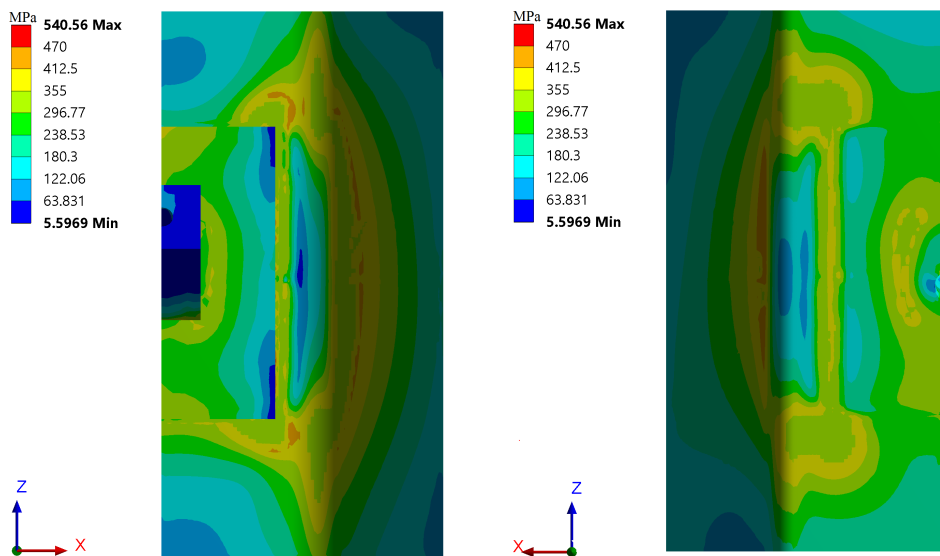
Figure A.99: Distribution of equivalent von Mises stresses having $l = 325mm$.



(a) Excavation side of the sheet pile.

(b) Back side of the sheet pile.

Figure A.100: Distribution of equivalent von Mises stresses having $l = 350mm$.



(a) Excavation side of the sheet pile.

(b) Back side of the sheet pile.

Figure A.101: Distribution of equivalent von Mises stresses having $l = 375mm$.

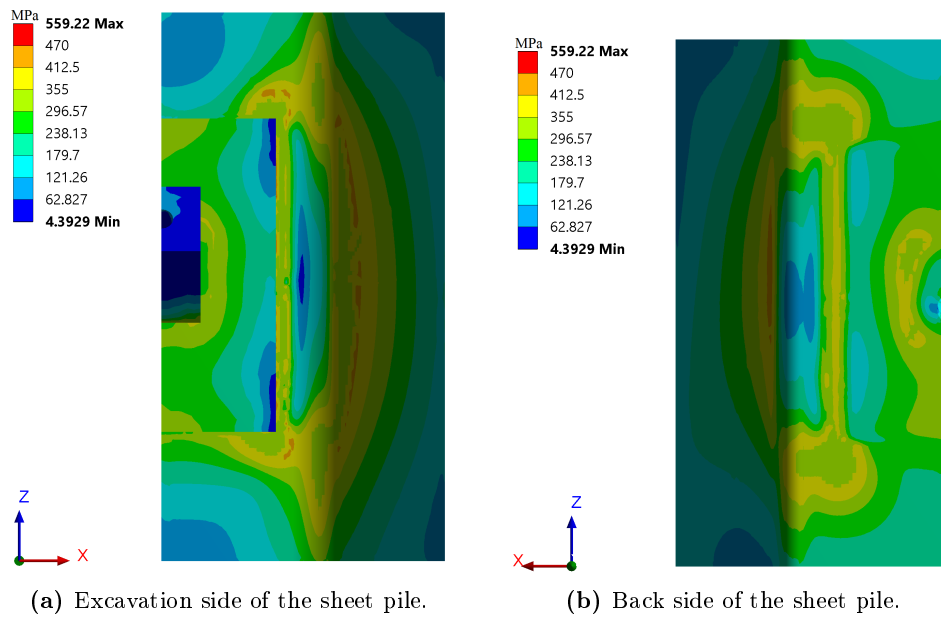


Figure A.102: Distribution of equivalent von Mises stresses having $l = 400\text{mm}$.

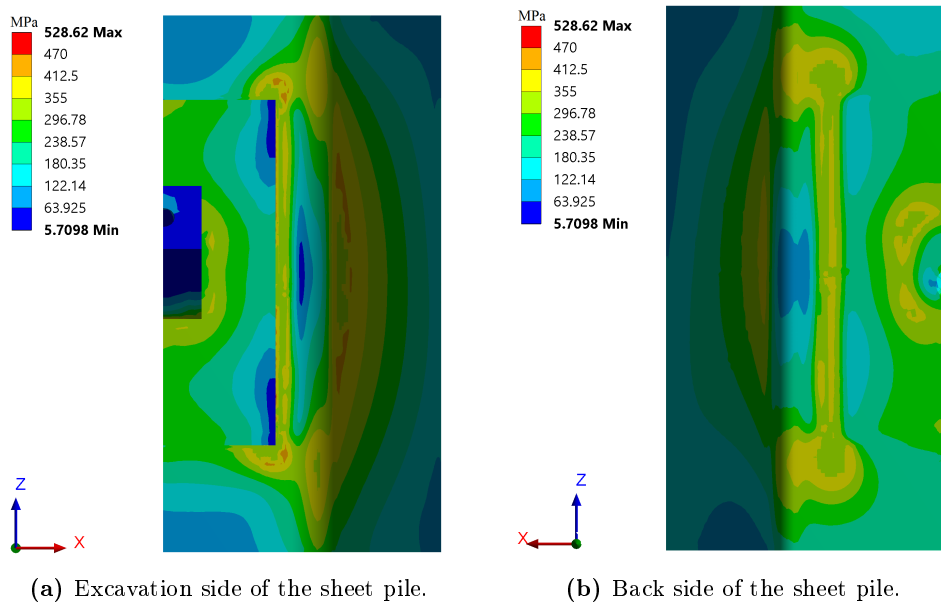


Figure A.103: Distribution of equivalent von Mises stresses having $l = 450\text{mm}$.

The maximum stresses has been captured in the flange and web in both the excavation side and the back side respectively resulting in four sets of data which are given in figures A.104 to A.111. Stress peaks related to singularities have been neglected.

- *P1* refers to the back side of the flange
- *P2* refers to the excavation side of the flange
- *P3* refers to the back side of the web
- *P4* refers to the excavation side of the web

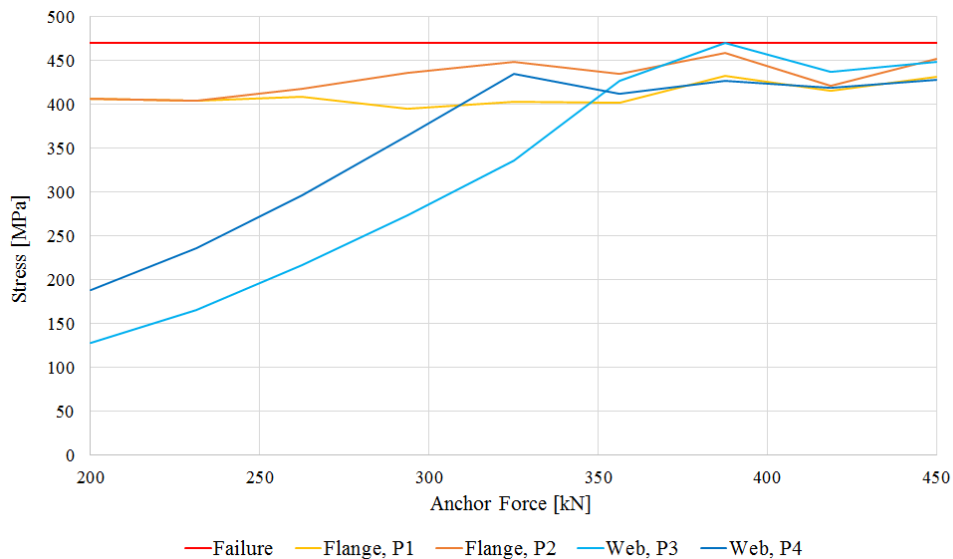


Figure A.104: Development of the maximum equivalent von Mises stresses in the two sides of the flange and web respectively having $l = 250mm$.

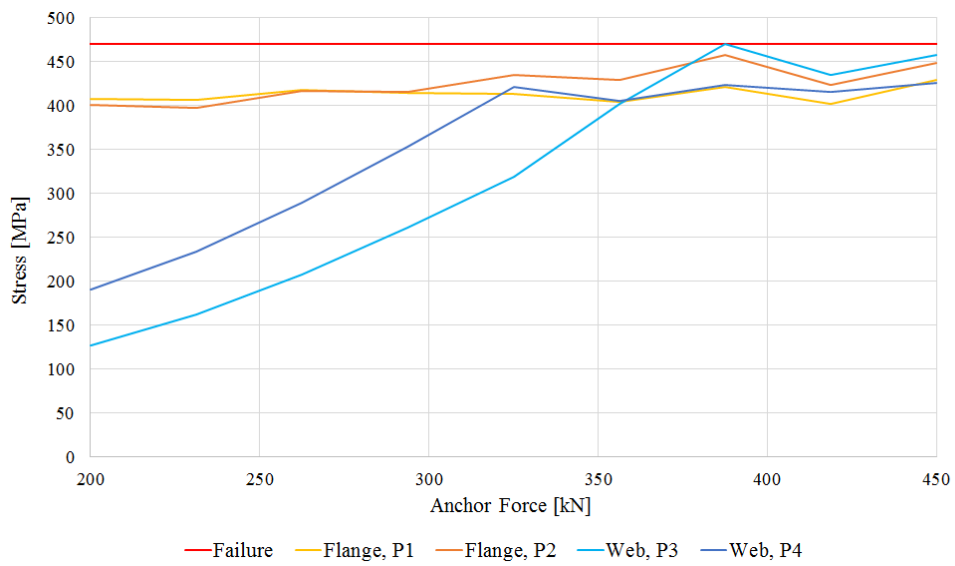


Figure A.105: Development of the maximum equivalent von Mises stresses in the two sides of the flange and web respectively having $l = 275mm$.

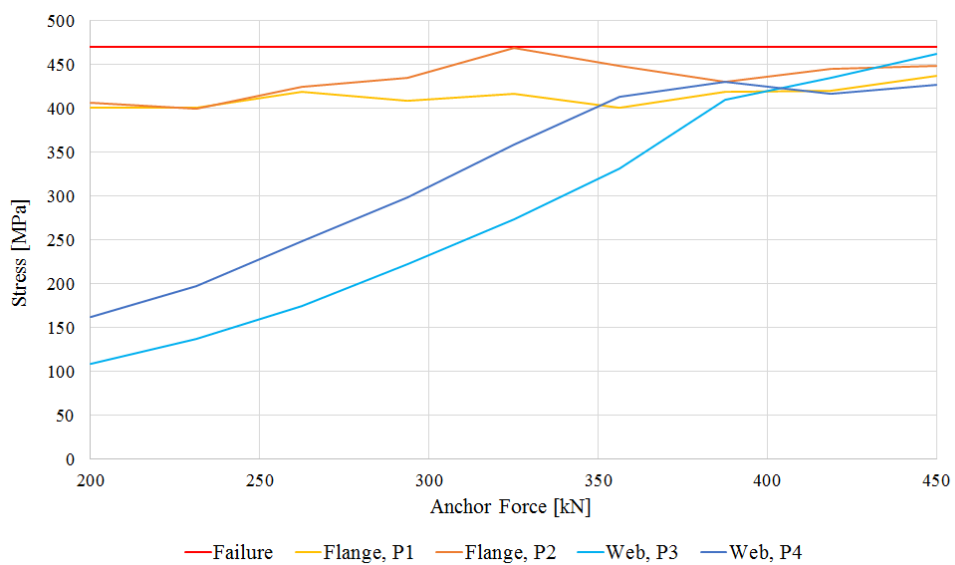


Figure A.106: Development of the maximum equivalent von Mises stresses in the two sides of the flange and web respectively having $l = 300mm$.

A.12. Parameter Study of Sheet Pile and Load Bearing Plate

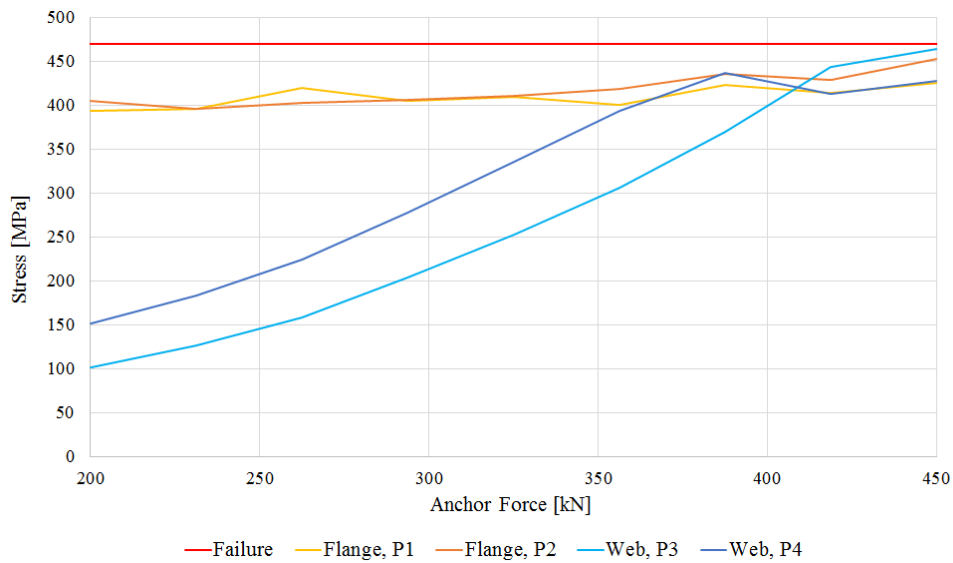


Figure A.107: Development of the maximum equivalent von Mises stresses in the two sides of the flange and web respectively having $l = 325mm$.

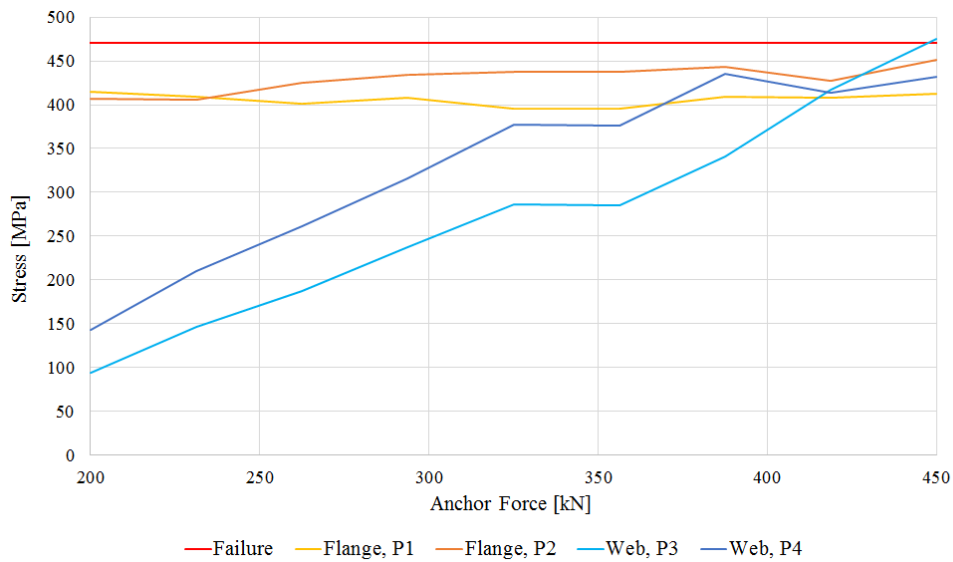


Figure A.108: Development of the maximum equivalent von Mises stresses in the two sides of the flange and web respectively having $l = 350mm$.

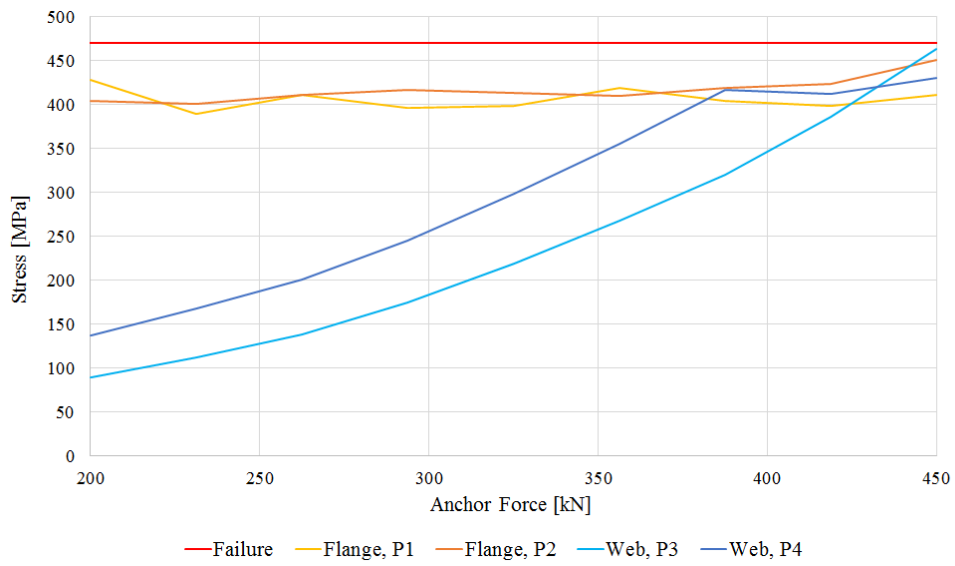


Figure A.109: Development of the maximum equivalent von Mises stresses in the two sides of the flange and web respectively having $l = 375mm$.

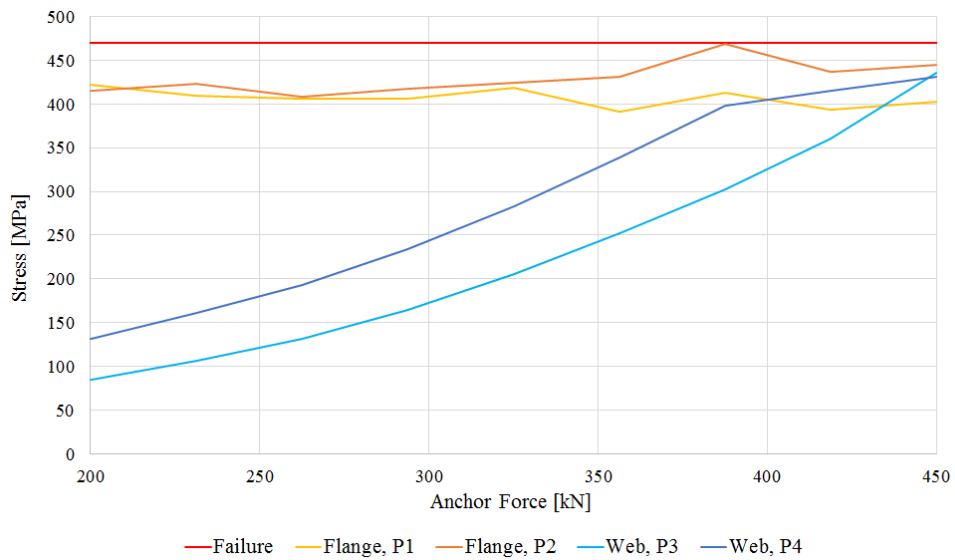


Figure A.110: Development of the maximum equivalent von Mises stresses in the two sides of the flange and web respectively having $l = 400mm$.

A.12. Parameter Study of Sheet Pile and Load Bearing Plate

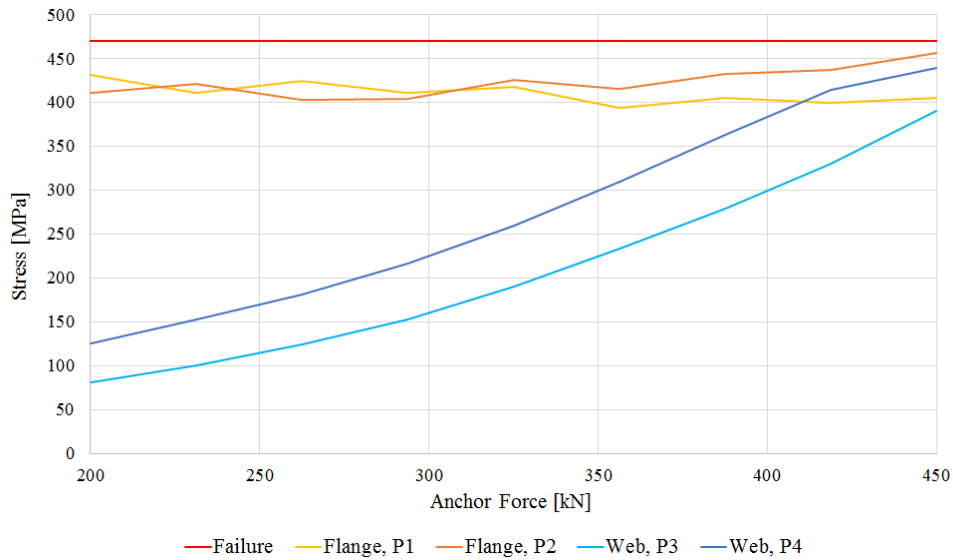


Figure A.111: Development of the maximum equivalent von Mises stresses in the two sides of the flange and web respectively having $l = 450mm$.

The maximum plastic strains for any of the size configurations are shown in figure A.112, which shows the development in the strains as the size is altered.

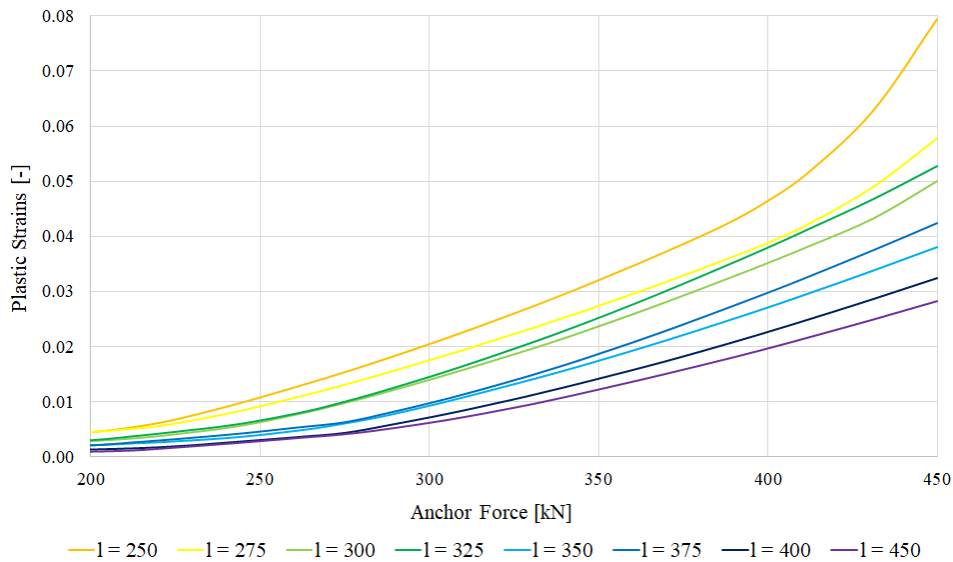


Figure A.112: Development of the maximum plastic strains in the sheet pile for different length configurations of the load bearing plate.

A.12.4 Angle Study

A rectangular load bearing plate has been created. The width of the plate has been fixed to 292 mm, and the thickness is fixed to 21 mm. The angle of the tendon, α , is then altered.

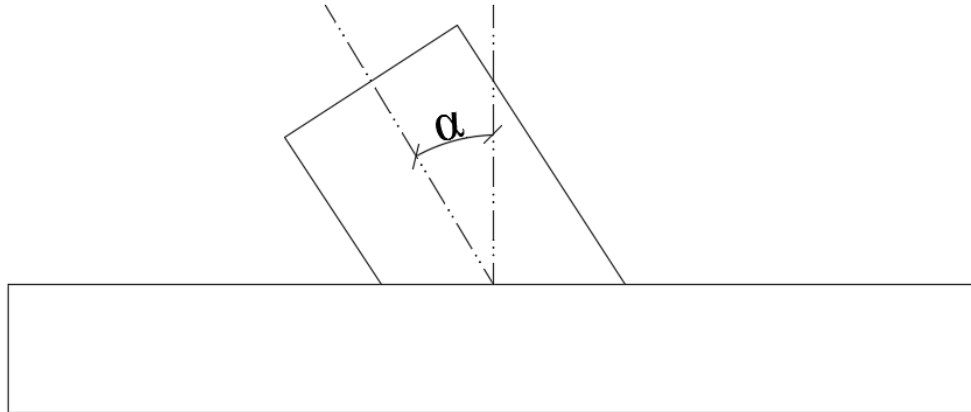
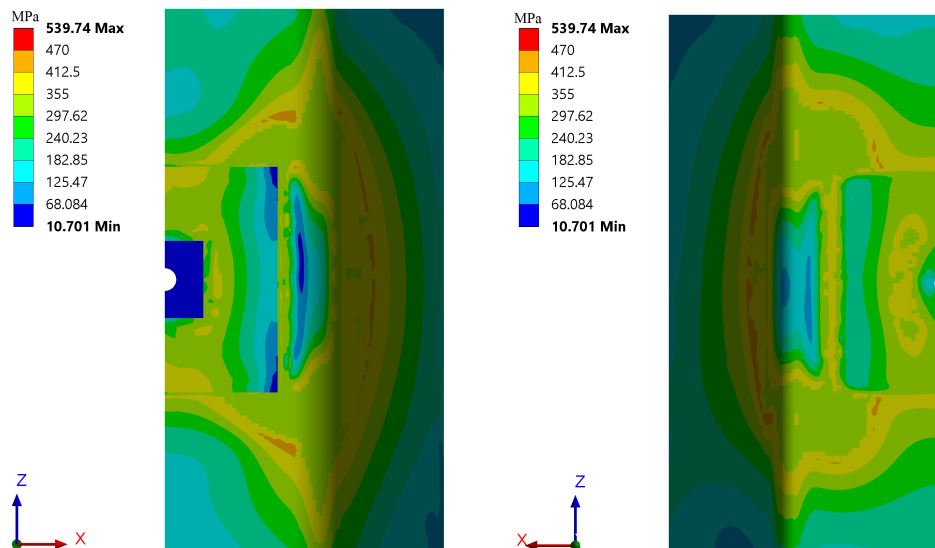


Figure A.113: α .

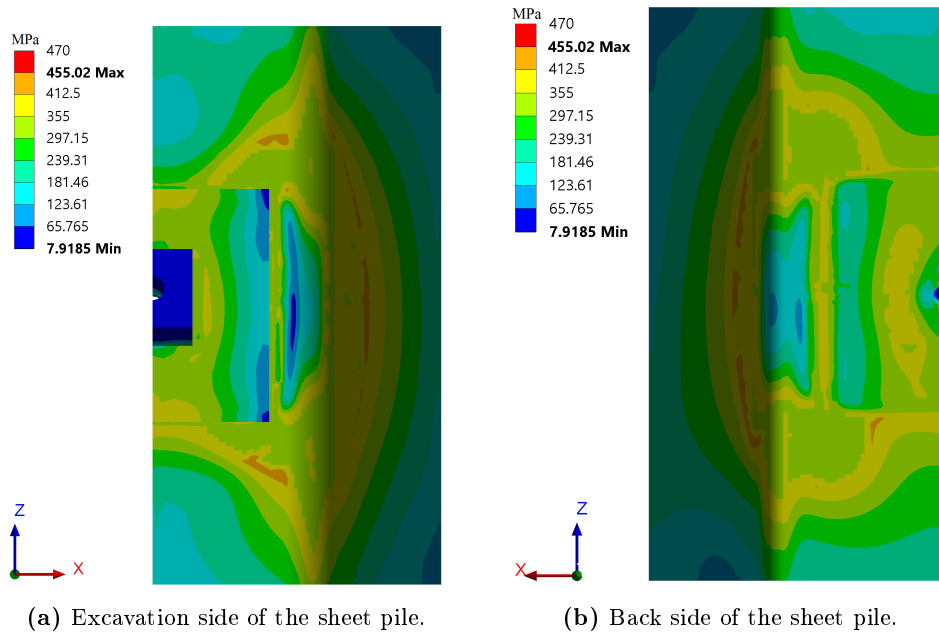
The resulting stress distributions are given.



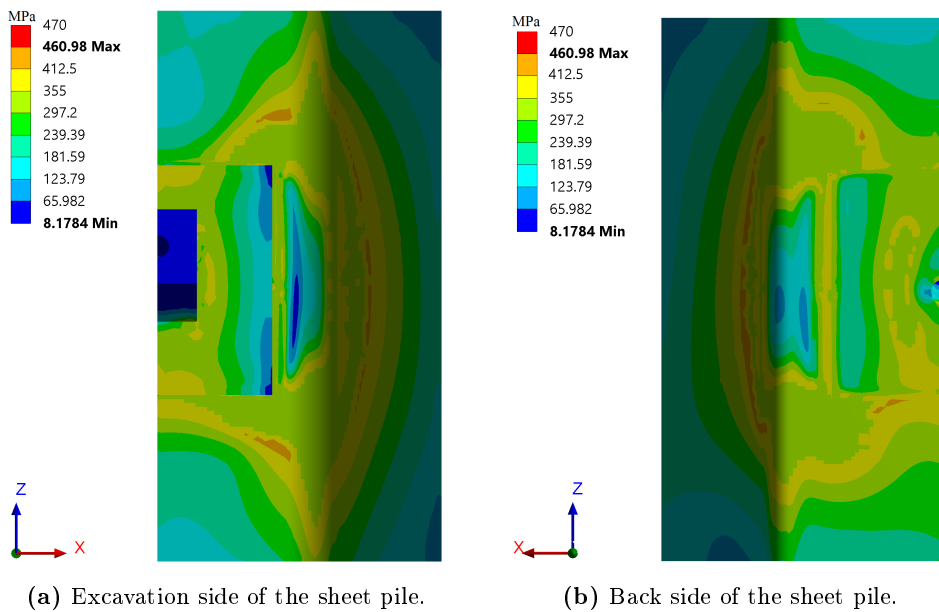
(a) Excavation side of the sheet pile.

(b) Back side of the sheet pile.

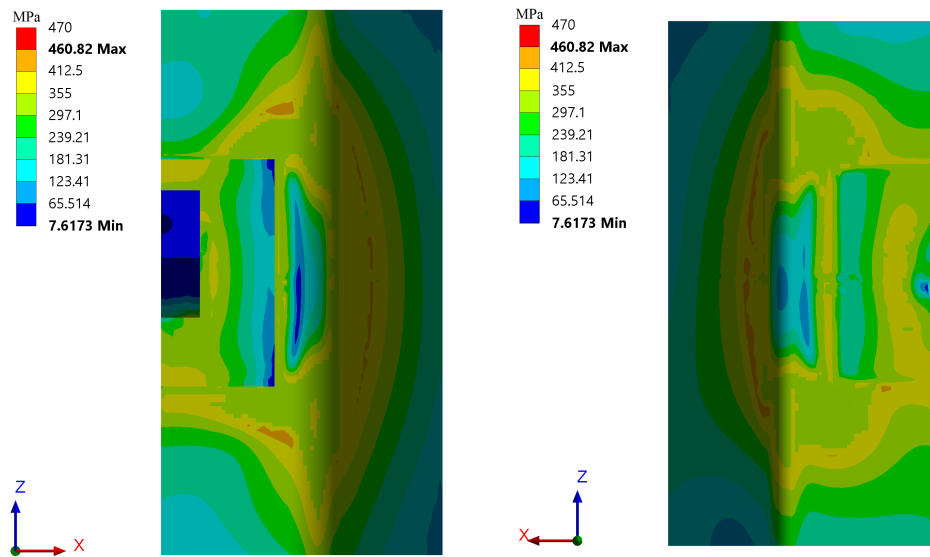
Figure A.114: Distribution of equivalent von Mises stresses having $\alpha = 0^\circ$.



(a) Excavation side of the sheet pile. (b) Back side of the sheet pile.
Figure A.115: Distribution of equivalent von Mises stresses having $\alpha = 10^\circ$.



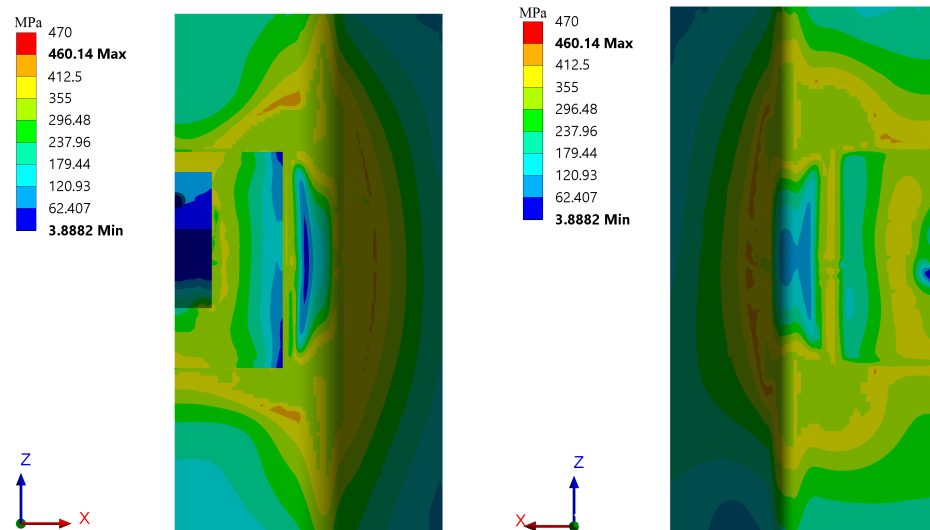
(a) Excavation side of the sheet pile. (b) Back side of the sheet pile.
Figure A.116: Distribution of equivalent von Mises stresses having $\alpha = 20^\circ$.



(a) Excavation side of the sheet pile.

(b) Back side of the sheet pile.

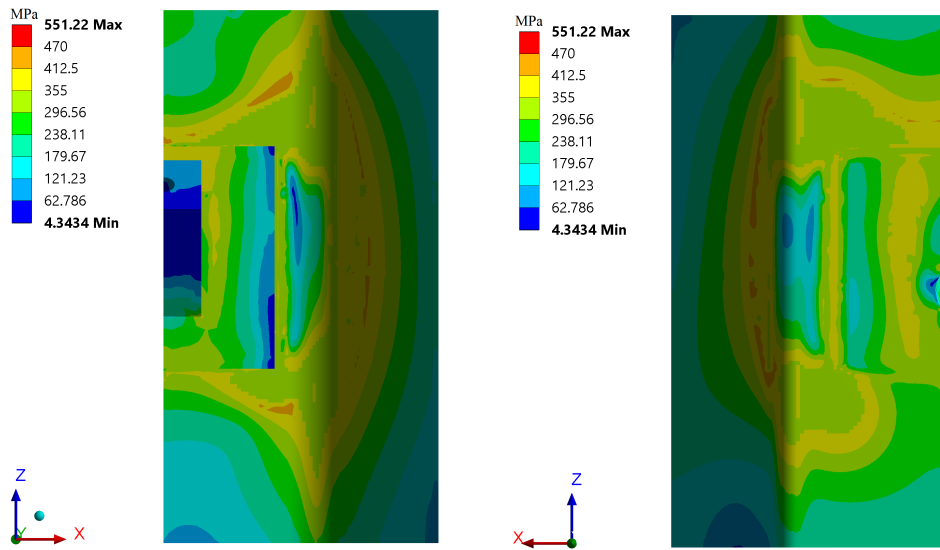
Figure A.117: Distribution of equivalent von Mises stresses having $\alpha = 30^\circ$.



(a) Excavation side of the sheet pile.

(b) Back side of the sheet pile.

Figure A.118: Distribution of equivalent von Mises stresses having $\alpha = 40^\circ$.



(a) Excavation side of the sheet pile.

(b) Back side of the sheet pile.

Figure A.119: Distribution of equivalent von Mises stresses having $\alpha = 50^\circ$.

The maximum stresses has been captured in the flange and web in both the excavation side and the back side respectively resulting in four sets of data which are given in figures A.120 to A.125. Stress peaks related to singularities have been neglected.

- *P1* refers to the bak side of the flange
- *P2* refers to the excavation side of the flange
- *P3* refers to the back side of the web
- *P4* refers to the excavation side of the web

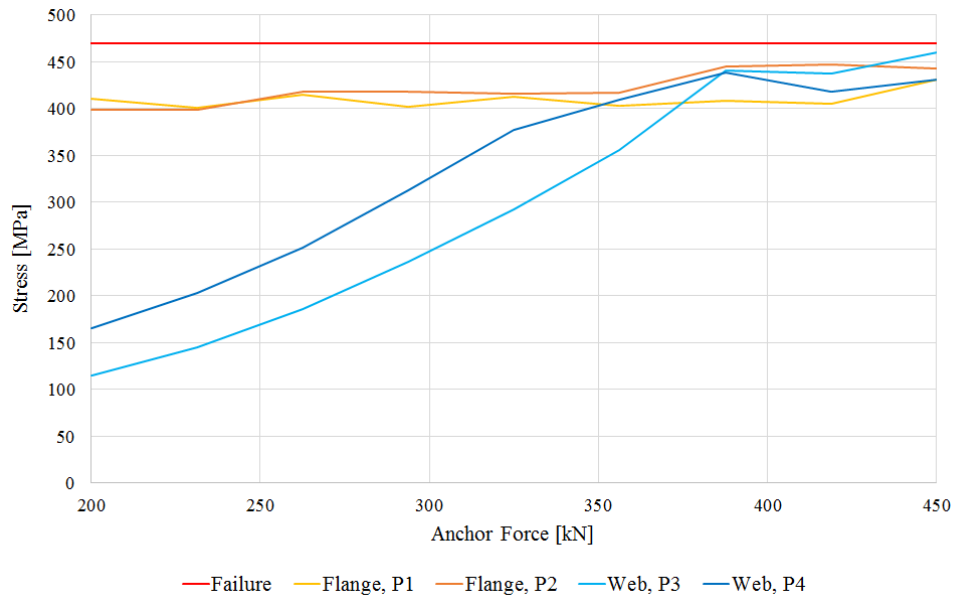


Figure A.120: Development of the maximum equivalent von Mises stresses in the two sides of the flange and web respectively having $\alpha = 0^\circ$.

A.12. Parameter Study of Sheet Pile and Load Bearing Plate

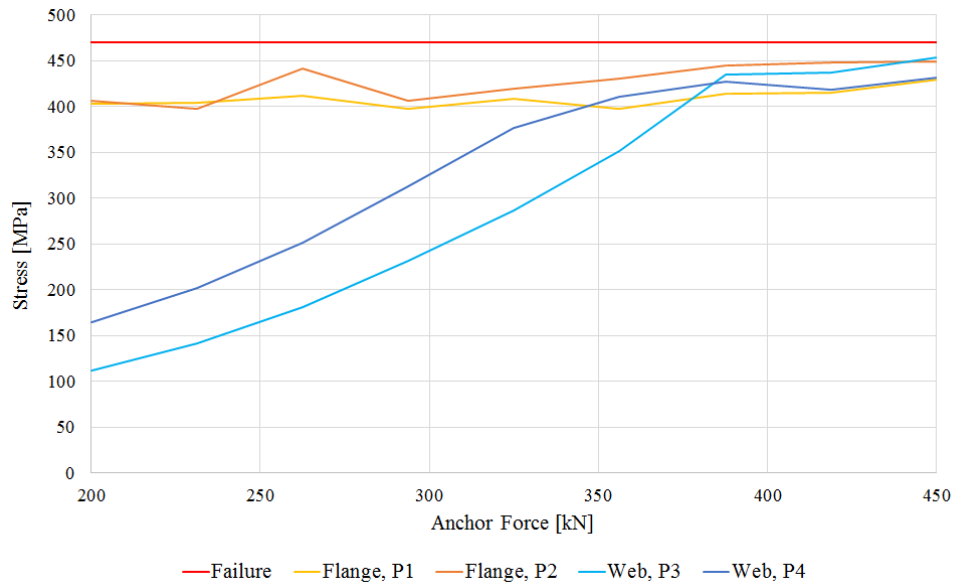


Figure A.121: Development of the maximum equivalent von Mises stresses in the two sides of the flange and web respectively having $\alpha = 10^\circ$.

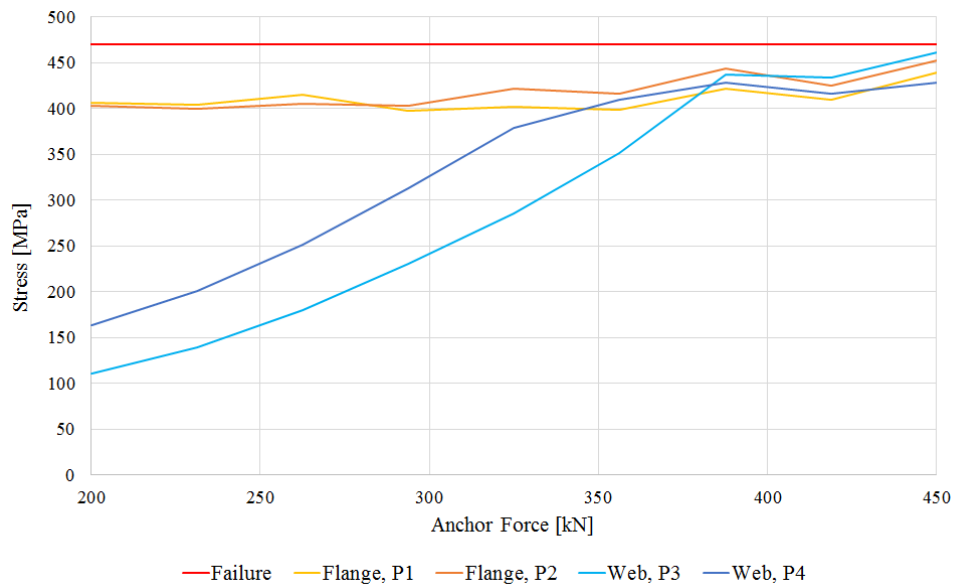


Figure A.122: Development of the maximum equivalent von Mises stresses in the two sides of the flange and web respectively having $\alpha = 20^\circ$.

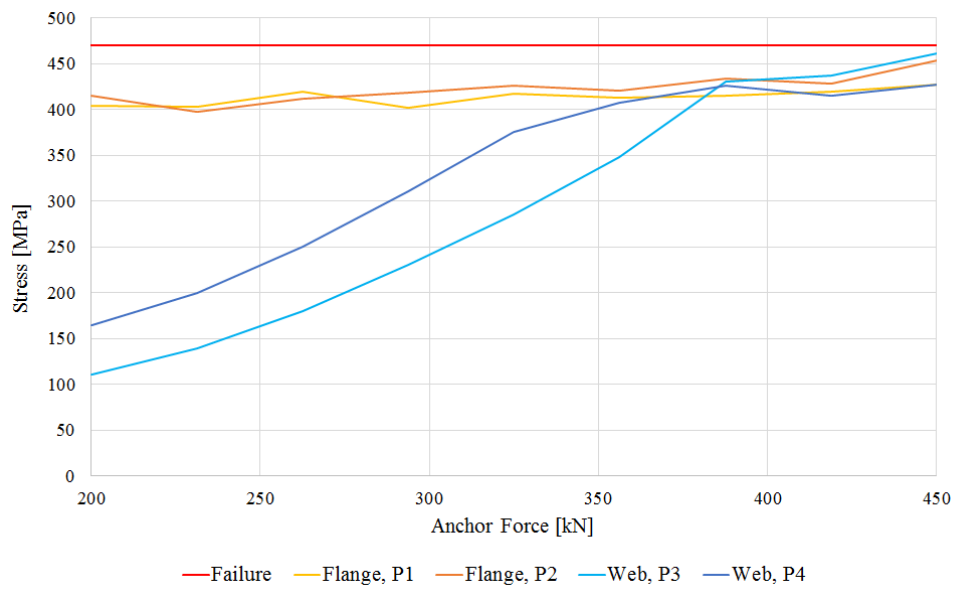


Figure A.123: Development of the maximum equivalent von Mises stresses in the two sides of the flange and web respectively having $\alpha = 30^\circ$.

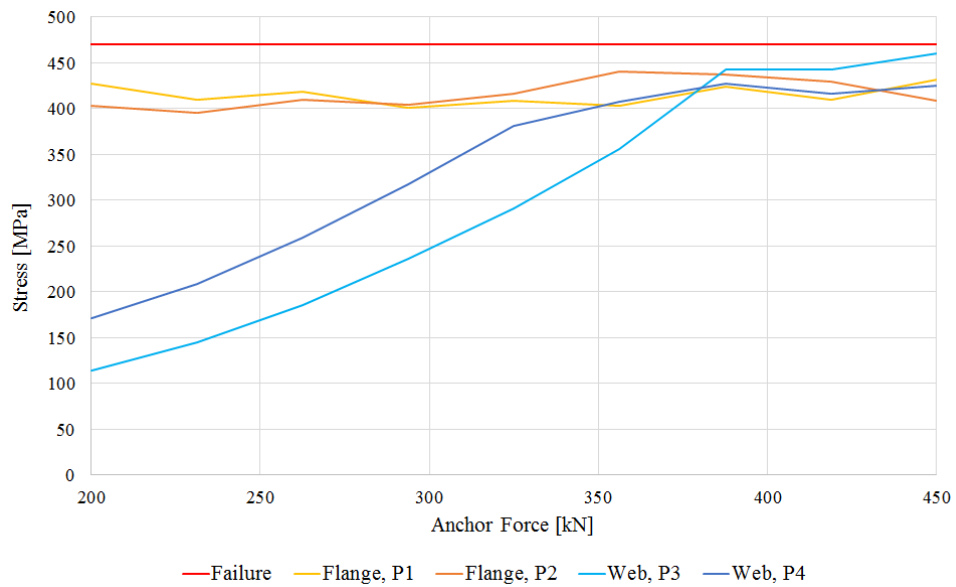


Figure A.124: Development of the maximum equivalent von Mises stresses in the two sides of the flange and web respectively having $\alpha = 40^\circ$.

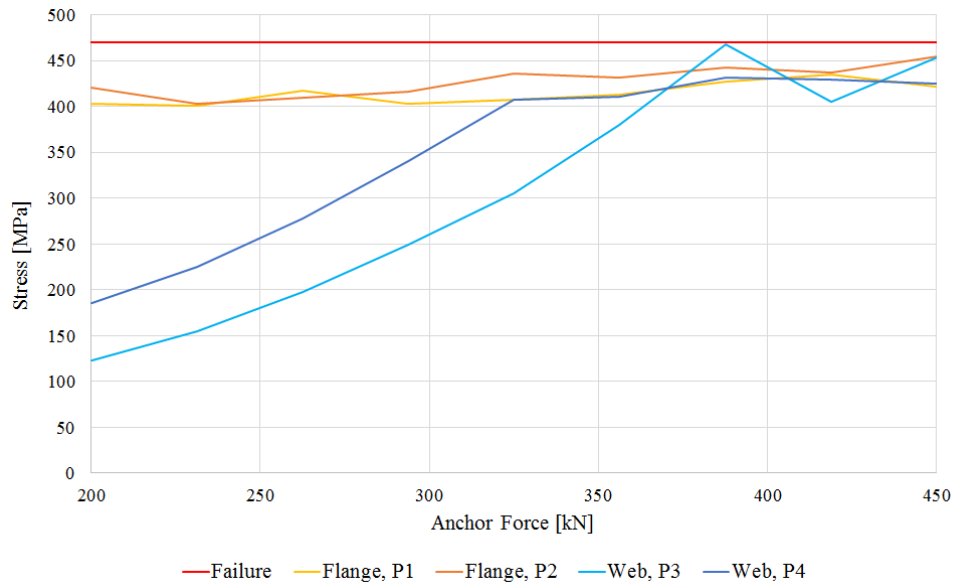


Figure A.125: Development of the maximum equivalent von Mises stresses in the two sides of the flange and web respectively having $\alpha = 50^\circ$.

The maximum plastic strains for any of the size configurations are shown in figure A.126, which shows the development in the strains as the size is altered.

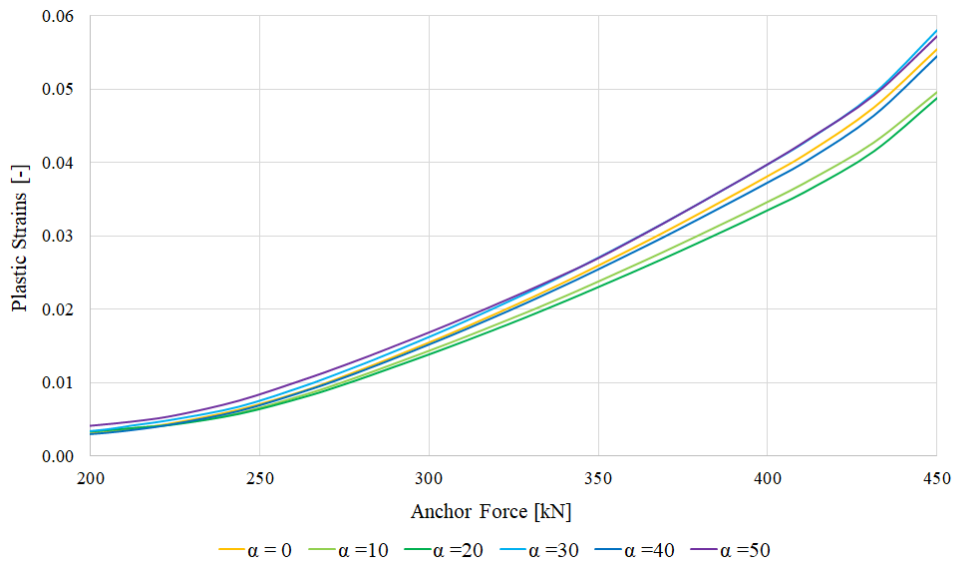
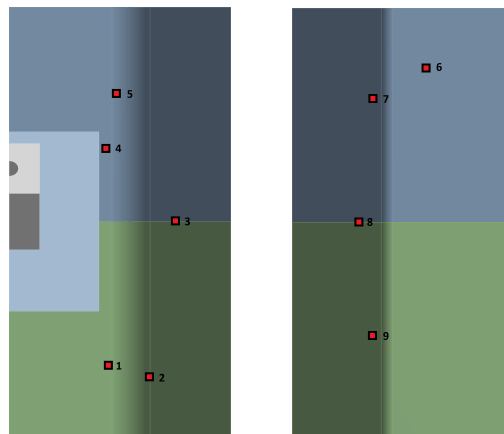


Figure A.126: Development of the maximum plastic strains in the sheet pile for different angle configurations of the load bearing plate.

A.12.5 Thickness Study of Sheet Pile

A sheet pile with a varying thickness of the cross section has been created. By altering the cross section related to the growth of the corrosion, the resulting stress distributions are given. First presented for each case is a illustration of the probe locations, next a force and stress graph and last stress plot of the sheet pile.

First is presented the results for a sheet pile after 6.25 years.



(a) Excavation side of the sheet pile.

(b) Back side of the sheet pile.

Figure A.127: Probe location on the sheet pile for 6.25 years.

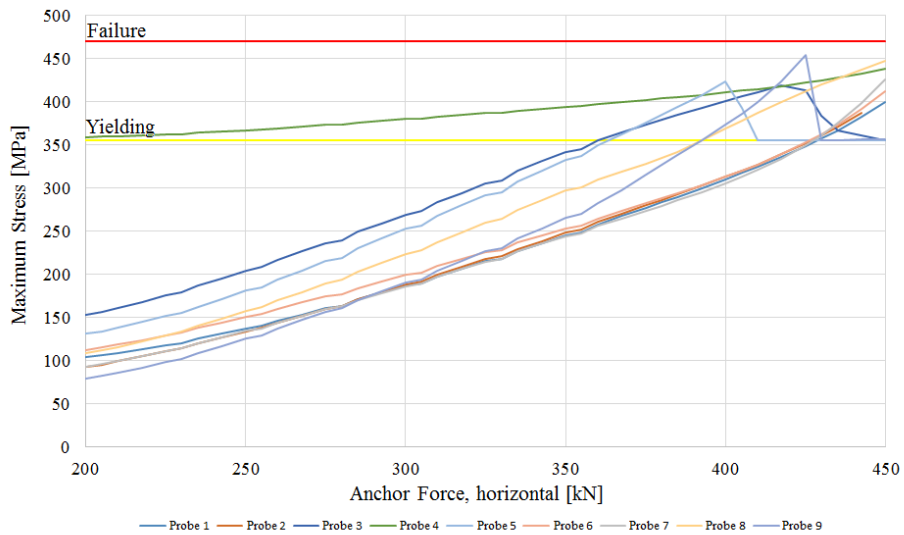


Figure A.128: Development of the maximum equivalent von Mises stresses for the sheet pile after 6.25 years.

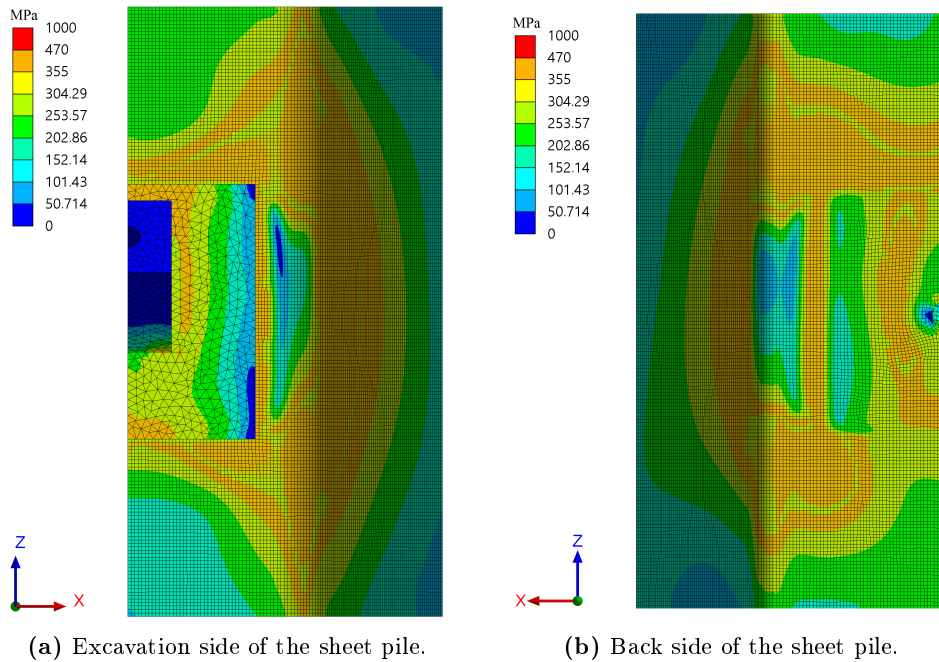


Figure A.129: Distribution of equivalent von Mises stresses after 6.25 years for the sheet pile.

Sheet pile results after 12.5 years.

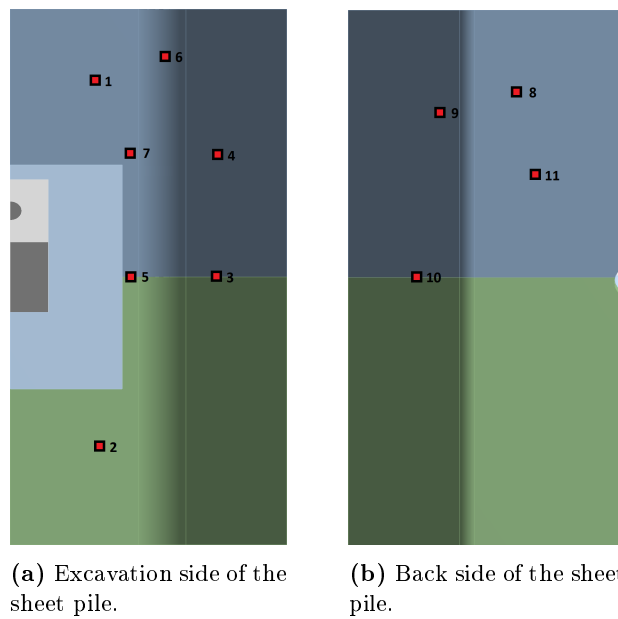


Figure A.130: Probe location on the sheet pile for 12.5 years.

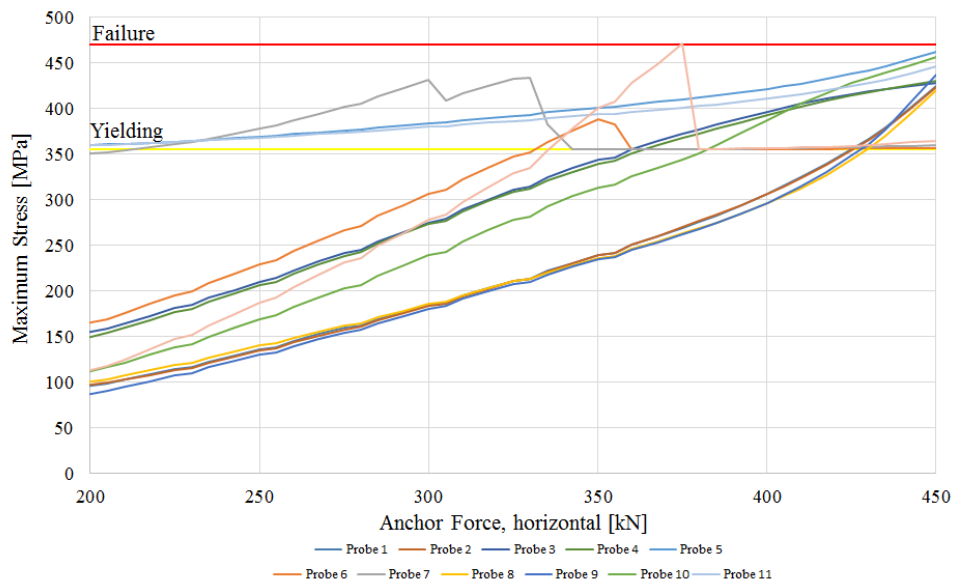


Figure A.131: Development of the maximum equivalent von Mises stresses for the sheet pile after 12.5 years.

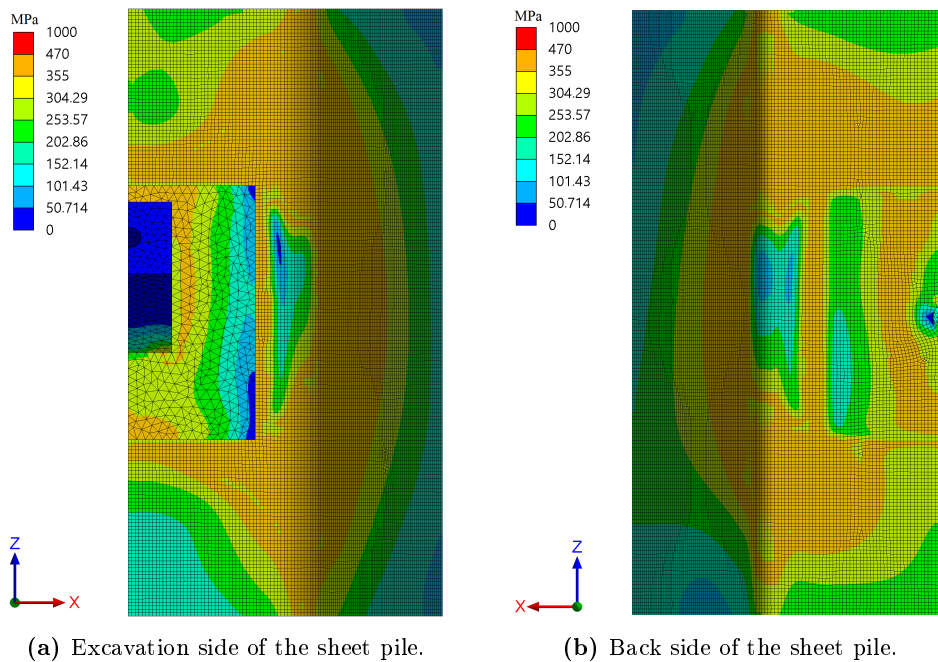
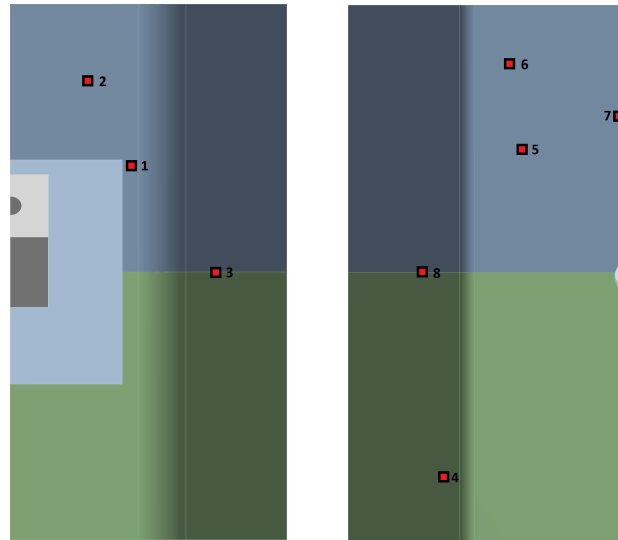


Figure A.132: Distribution of equivalent von Mises stresses after 12.5 years for the sheet pile.

Sheet pile results after 25 years.



(a) Excavation side of the sheet pile. (b) Back side of the sheet pile.

Figure A.133: Probe location on the sheet pile for 25 years.

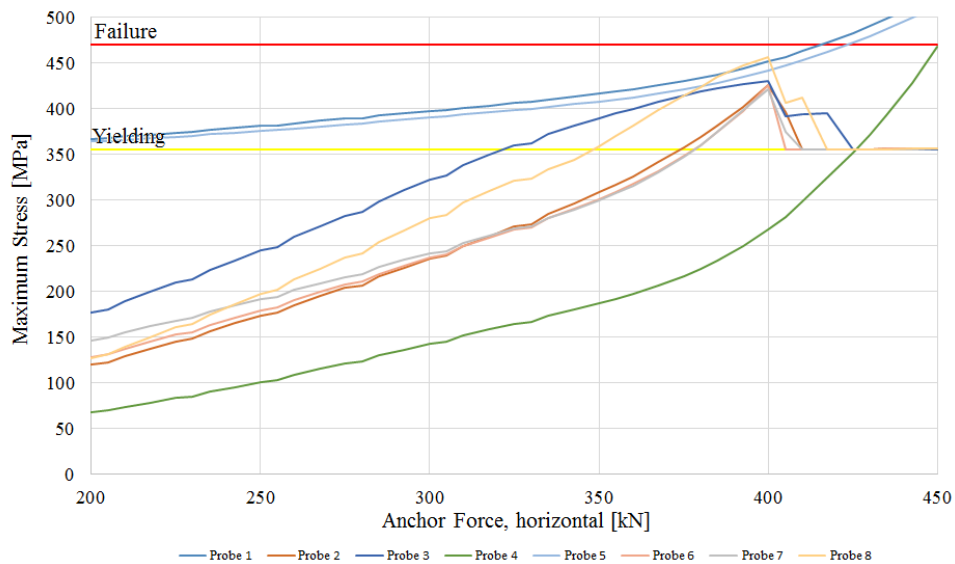


Figure A.134: Development of the maximum equivalent von Mises stresses for the sheet pile after 25 years.

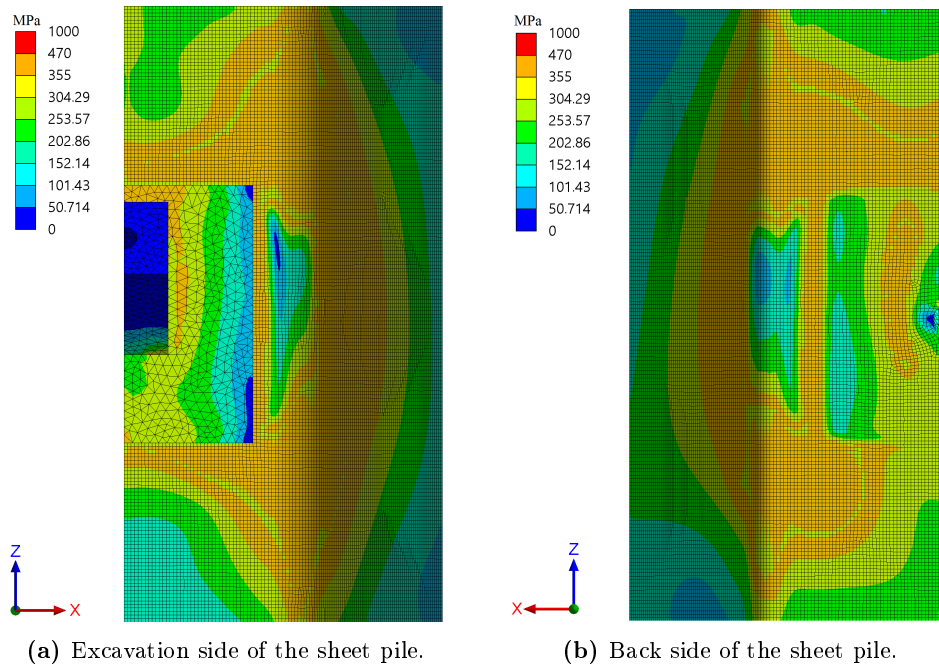


Figure A.135: Distribution of equivalent von Mises stresses after 25 years for the sheet pile.

Sheet pile results after 50 years.

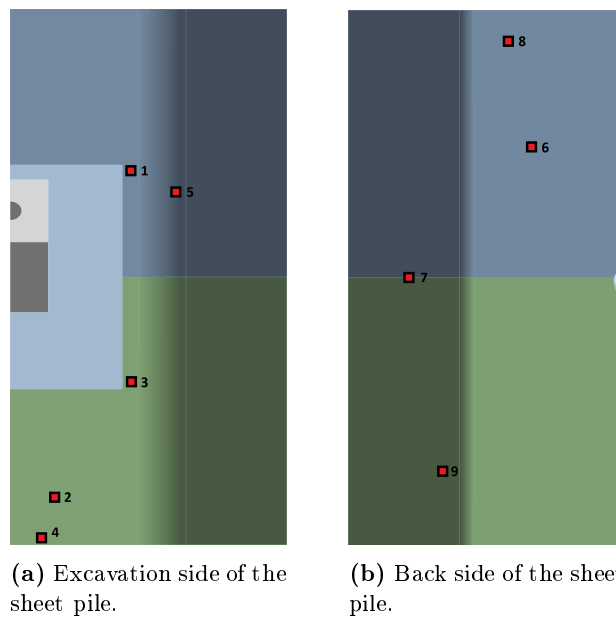


Figure A.136: Probe location on the sheet pile for 50 years.

A.12. Parameter Study of Sheet Pile and Load Bearing Plate

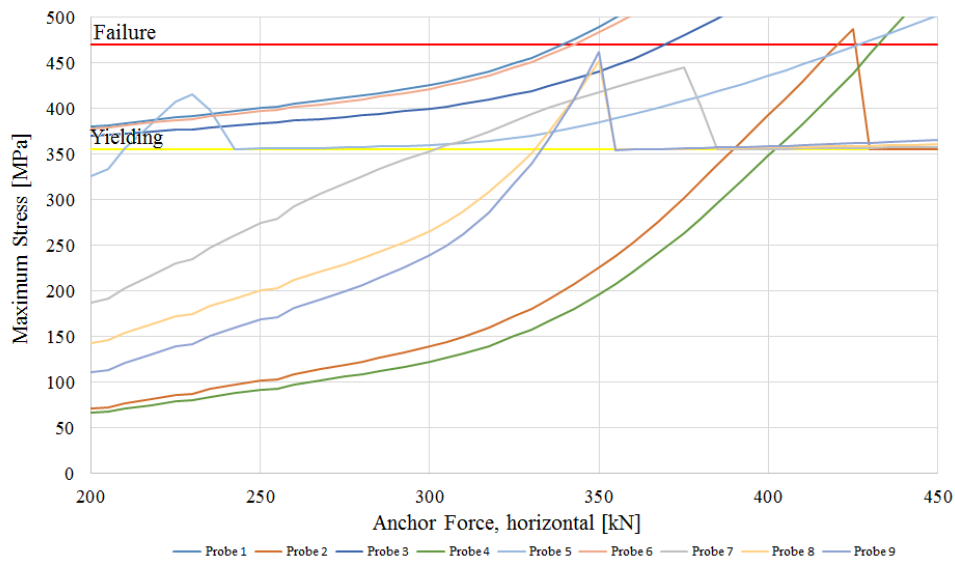


Figure A.137: Development of the maximum equivalent von Mises stresses for the sheet pile after 50 years.

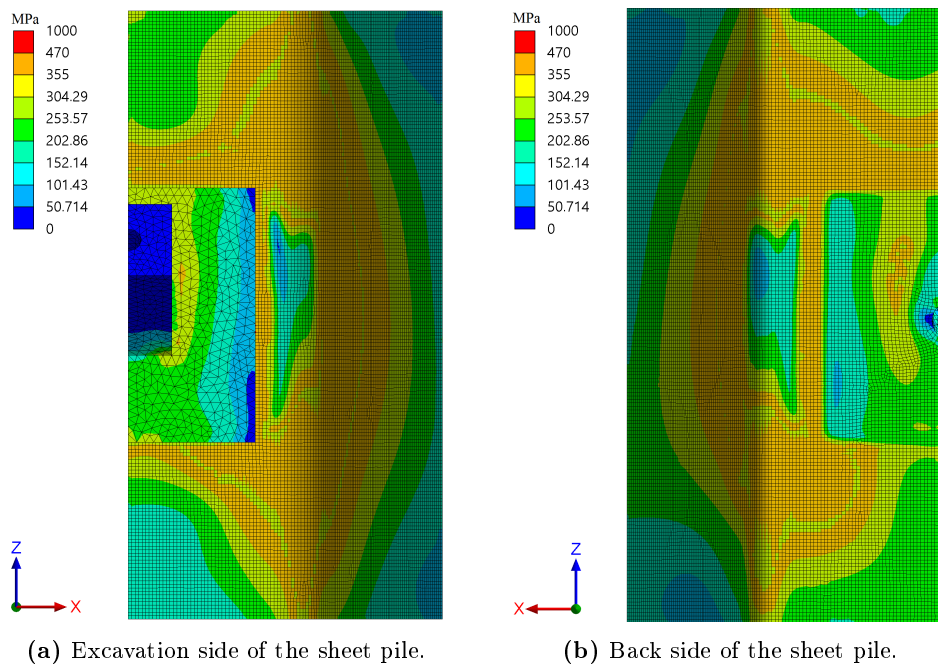


Figure A.138: Distribution of equivalent von Mises stresses after 50 years for the sheet pile.

A.12.6 Ellipse Study

An elliptical shaped load bearing plate has been created. The length of the minor axis, b , is then altered, and the resulting stress distributions are given.

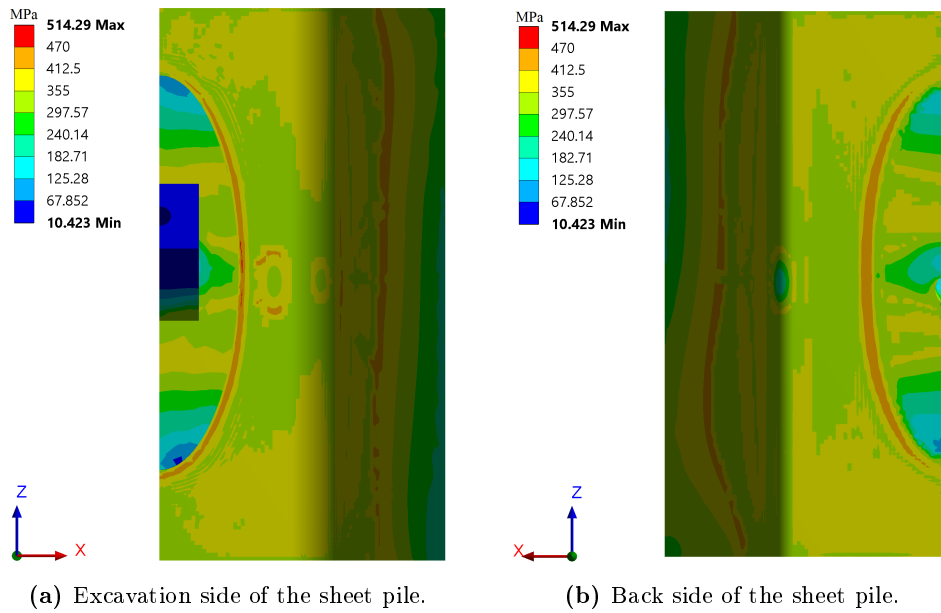


Figure A.139: Distribution of equivalent von Mises stresses having $b = 200mm$.

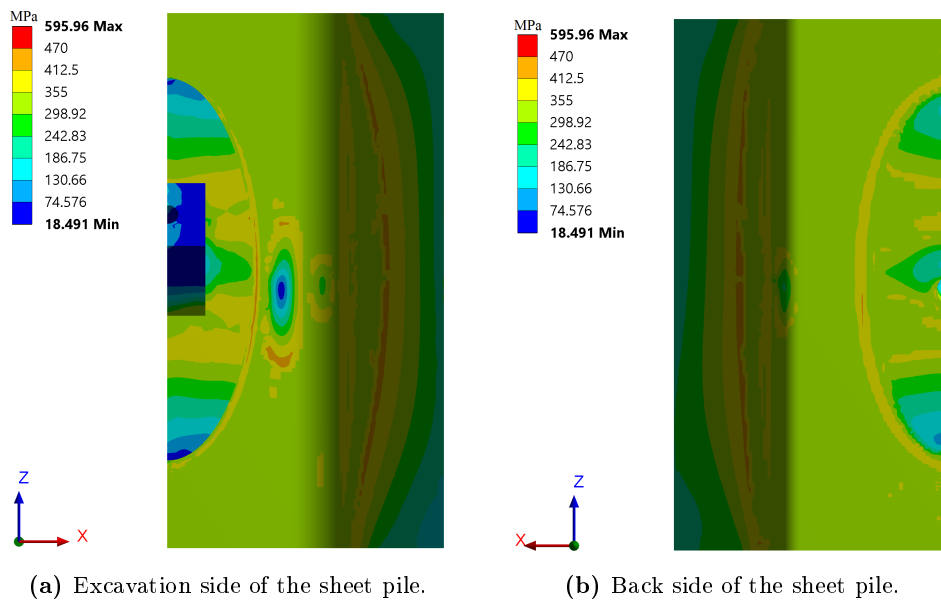
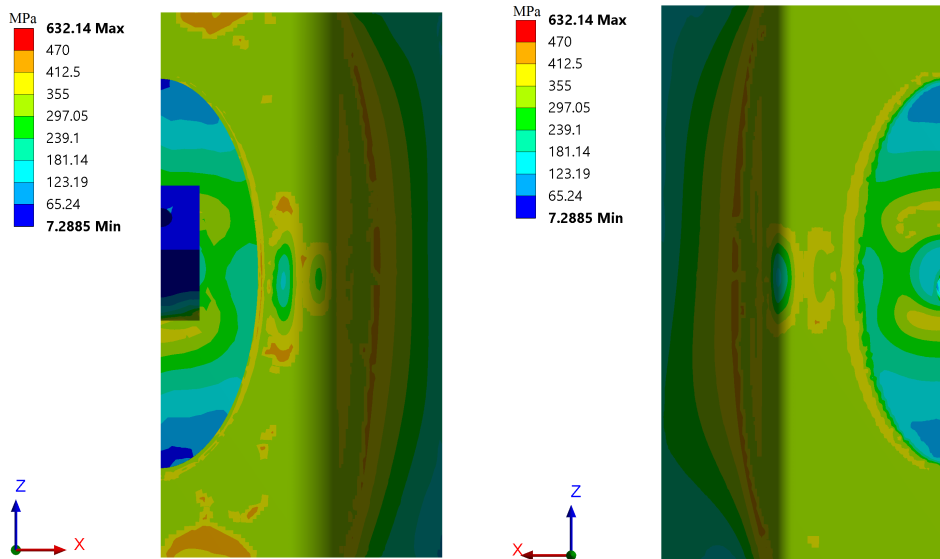


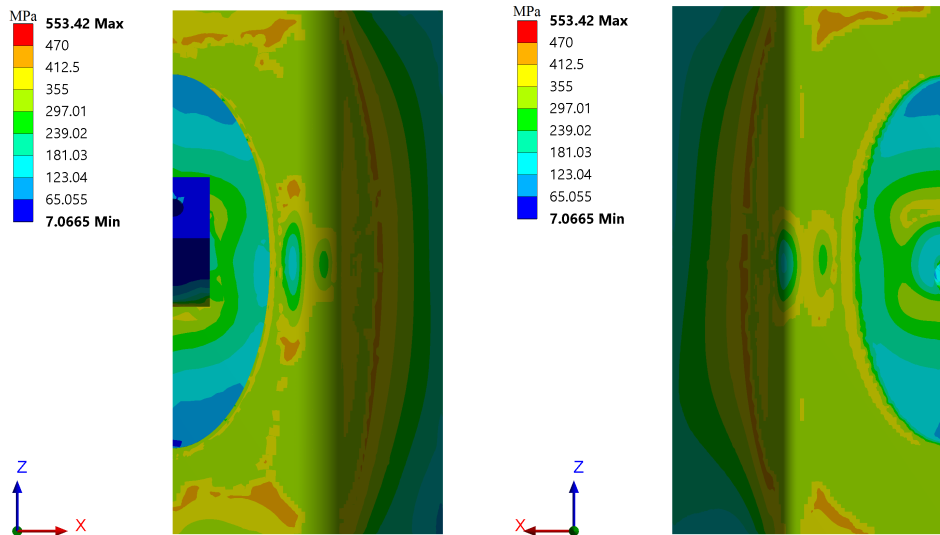
Figure A.140: Distribution of equivalent von Mises stresses having $b = 225mm$.



(a) Excavation side of the sheet pile.

(b) Back side of the sheet pile.

Figure A.141: Distribution of equivalent von Mises stresses having $b = 250\text{mm}$.



(a) Excavation side of the sheet pile.

(b) Back side of the sheet pile.

Figure A.142: Distribution of equivalent von Mises stresses having $b = 260\text{mm}$.

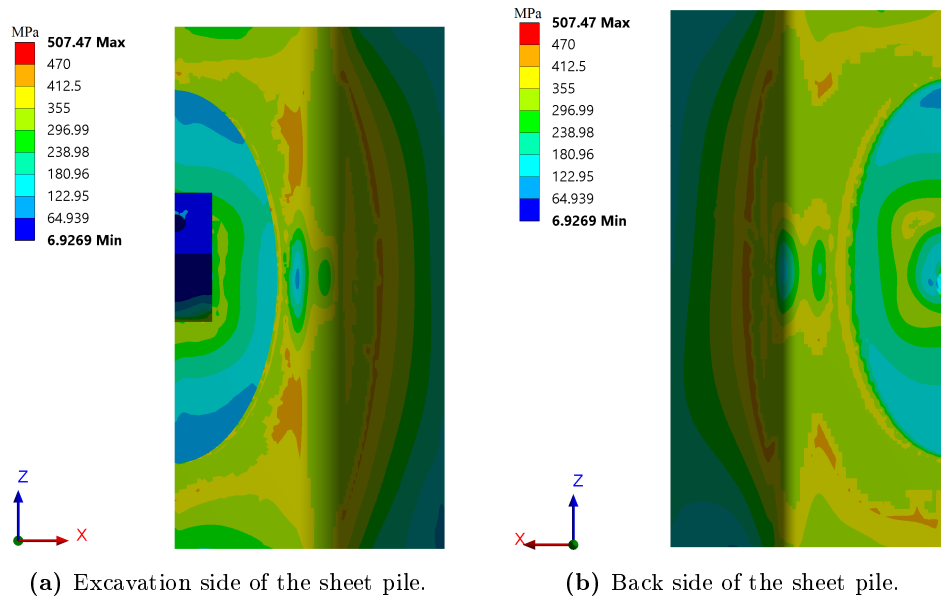


Figure A.143: Distribution of equivalent von Mises stresses having $b = 275mm$.

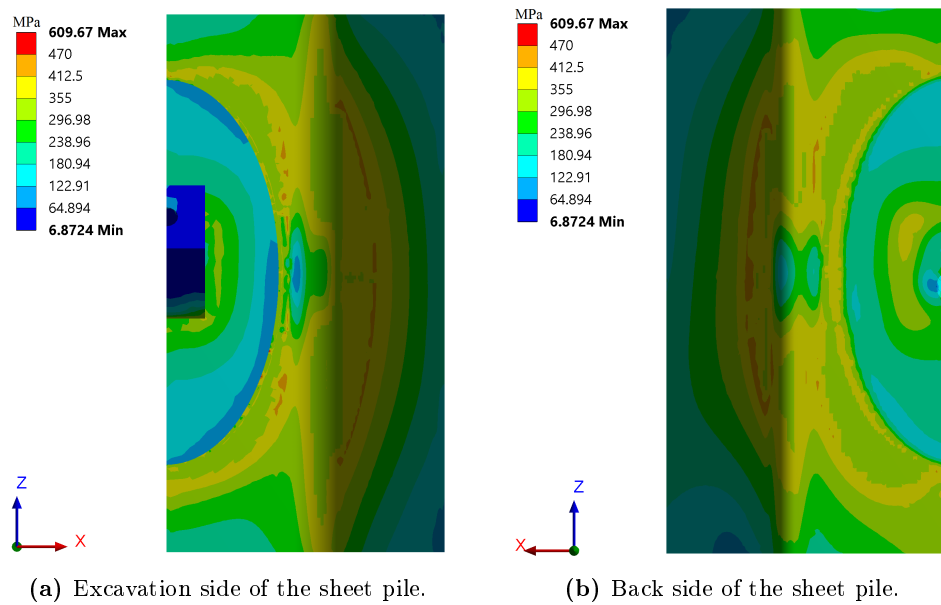


Figure A.144: Distribution of equivalent von Mises stresses $b = 292mm$.

The maximum stresses has been captured in the flange and web in both the excavation side and the back side respectively resulting in four sets of data which are given in figures A.145 to A.150. Stress peaks related to singularities have been neglected.

- *P1* refers to the back side of the flange
- *P2* refers to the excavation side of the flange
- *P3* refers to the back side of the web
- *P4* refers to the excavation side of the web

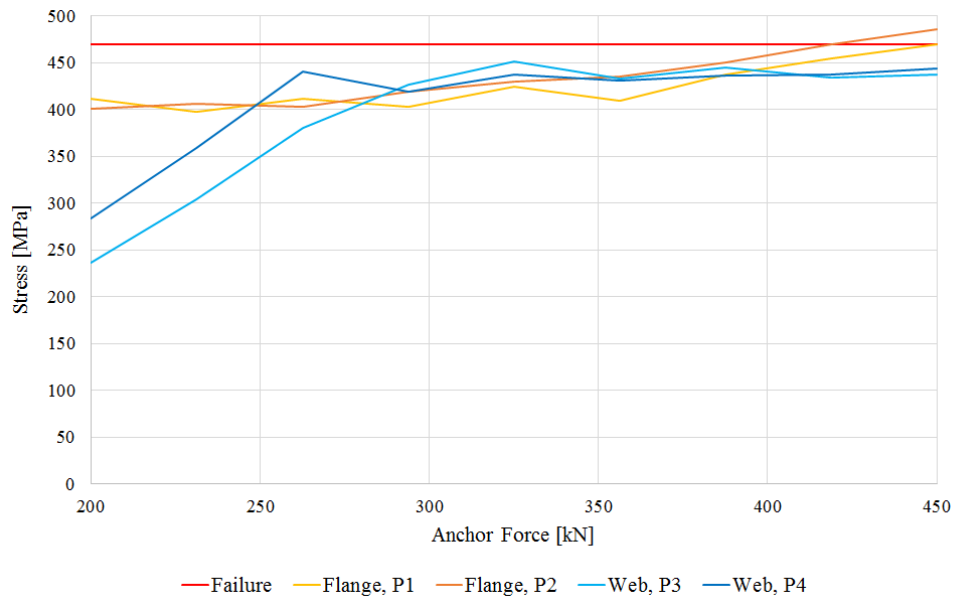


Figure A.145: Development of the maximum equivalent von Mises stresses in the two sides of the flange and web respectively having $b = 200mm$.

A. APPENDIX

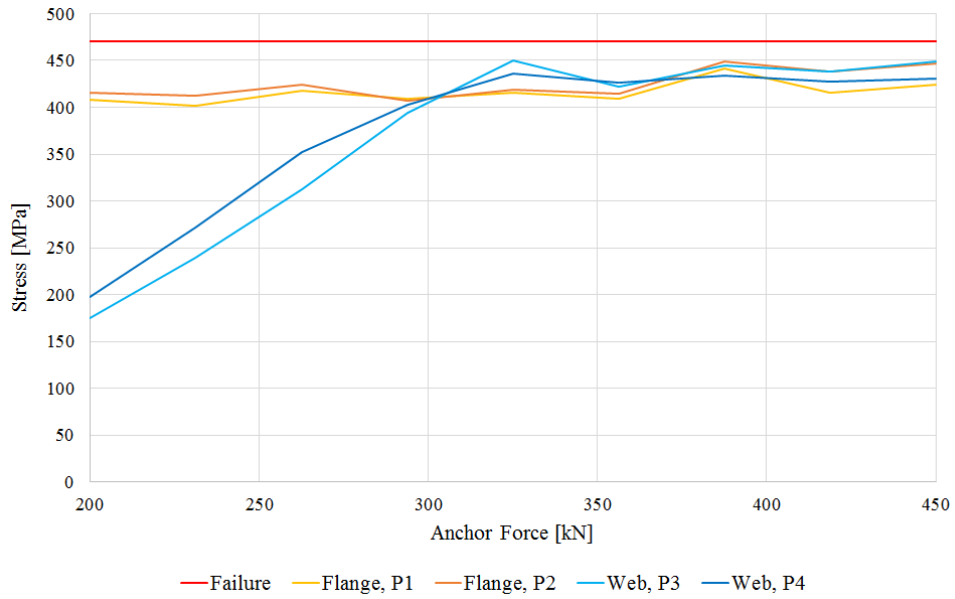


Figure A.146: Development of the maximum equivalent von Mises stresses in the two sides of the flange and web respectively having $b = 225mm$.

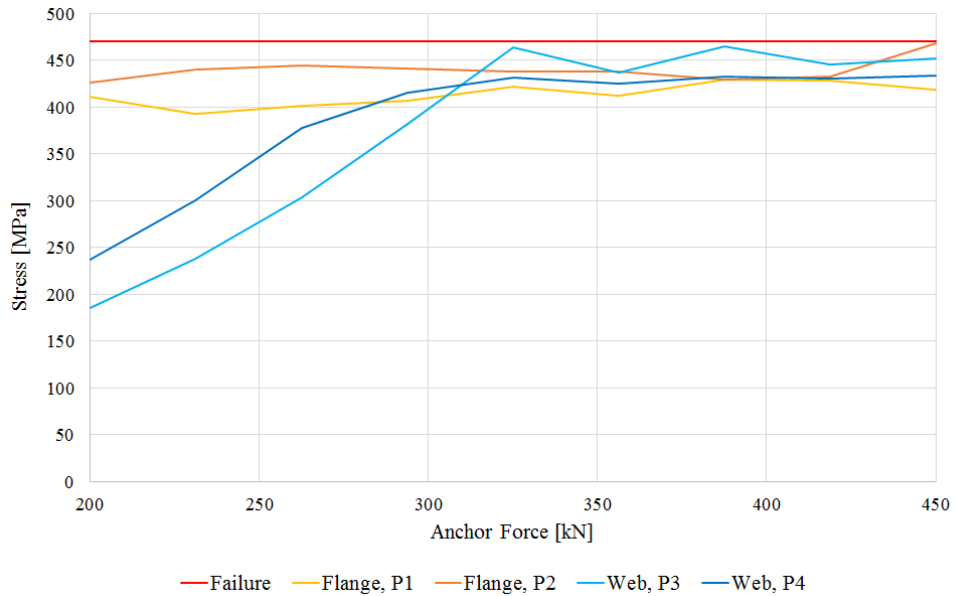


Figure A.147: Development of the maximum equivalent von Mises stresses in the two sides of the flange and web respectively having $b = 250mm$.

A.12. Parameter Study of Sheet Pile and Load Bearing Plate

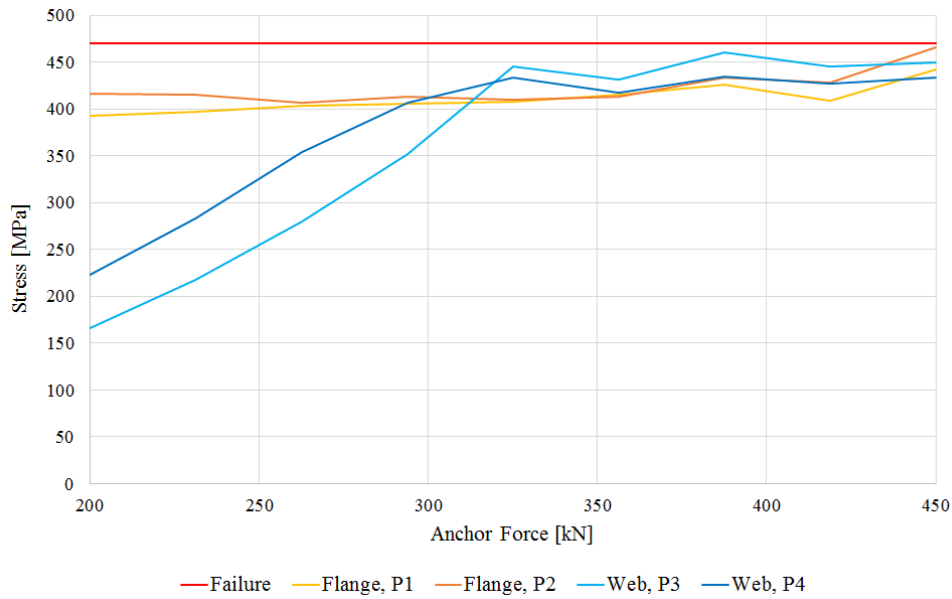


Figure A.148: Development of the maximum equivalent von Mises stresses in the two sides of the flange and web respectively having $b = 260mm$.

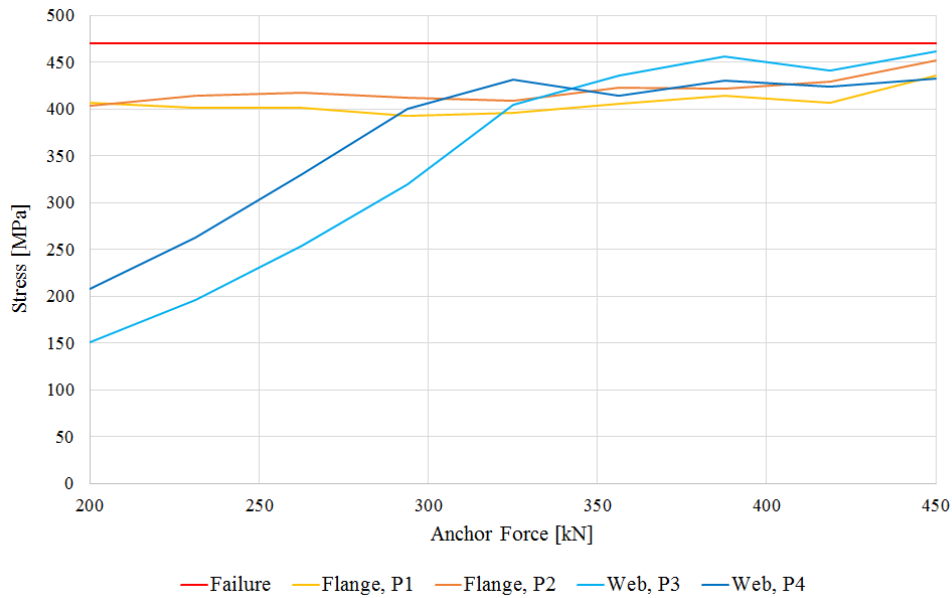


Figure A.149: Development of the maximum equivalent von Mises stresses in the two sides of the flange and web respectively having $b = 275mm$.

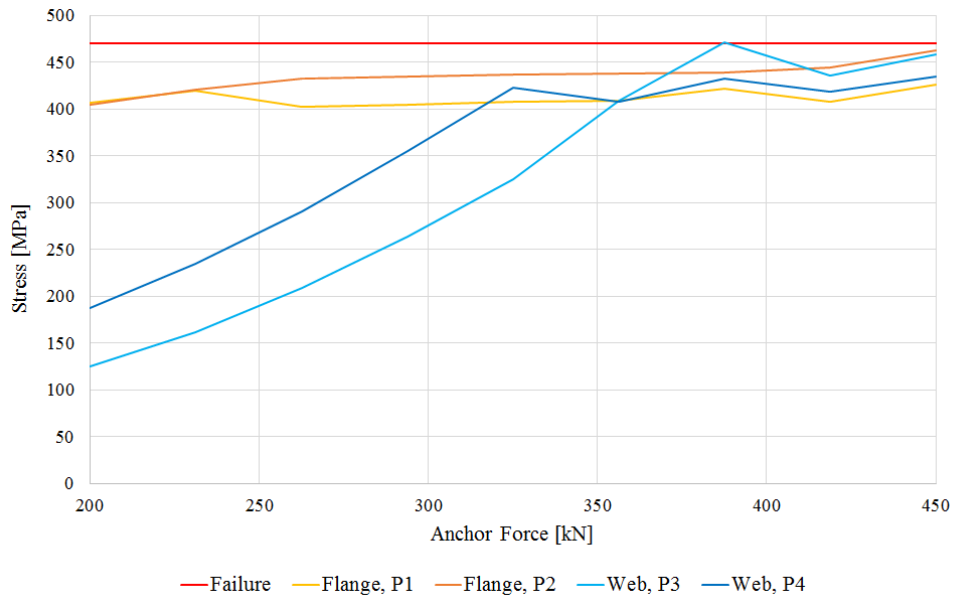


Figure A.150: Development of the maximum equivalent von Mises stresses in the two sides of the flange and web respectively having $b = 292mm$.

The maximum plastic strains for any of the size configurations are shown in figure A.151, which shows the development in the strains as the size is altered.

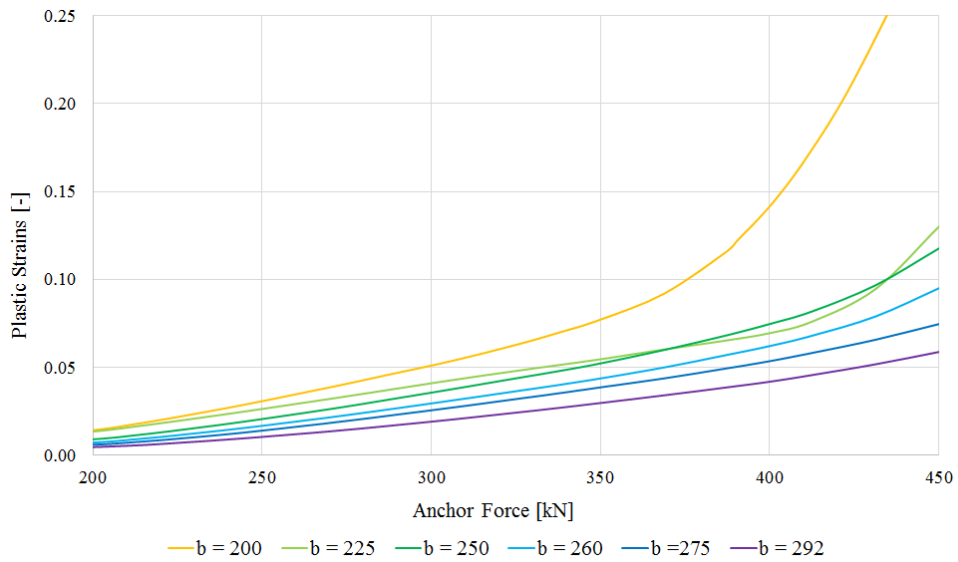


Figure A.151: Development of the maximum plastic strains in the sheet pile for different configurations of the load bearing plate.

A.12.7 'Foot' Study

An unconventional shaped load bearing plate has been created. The dimensions have been given in figure A.152.

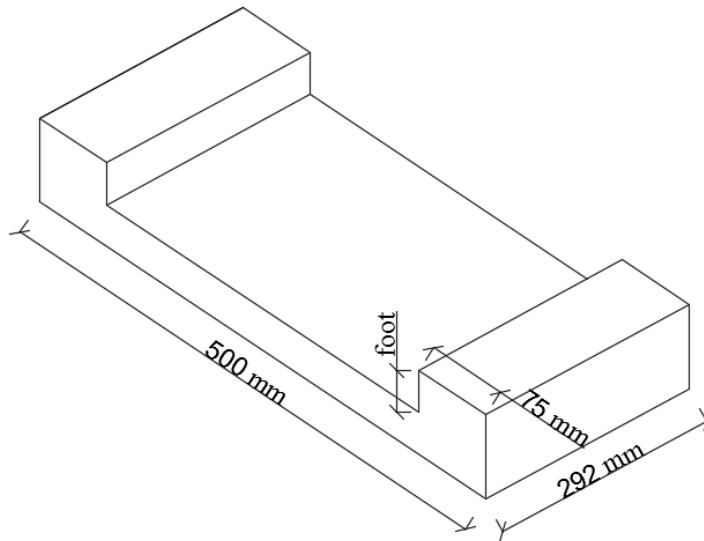
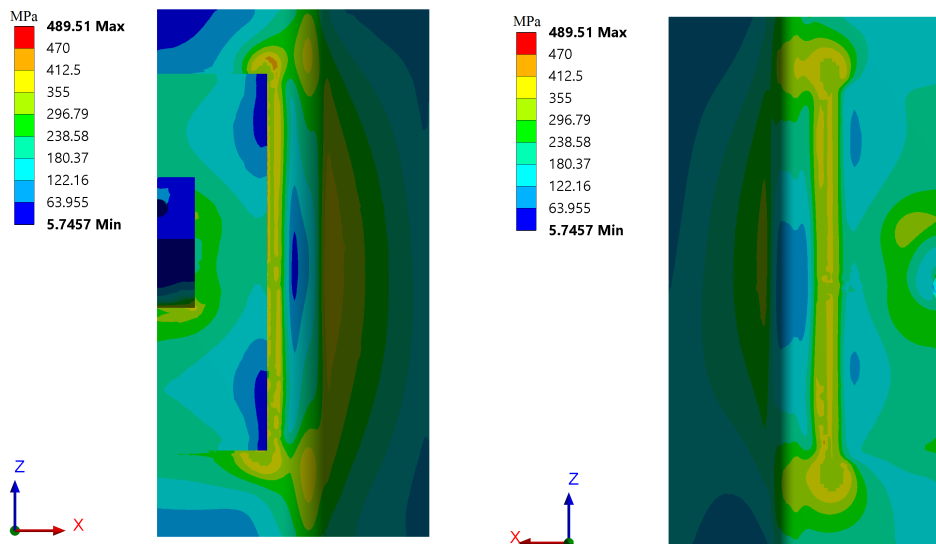


Figure A.152: Dimensions of the unconventional shaped plate.

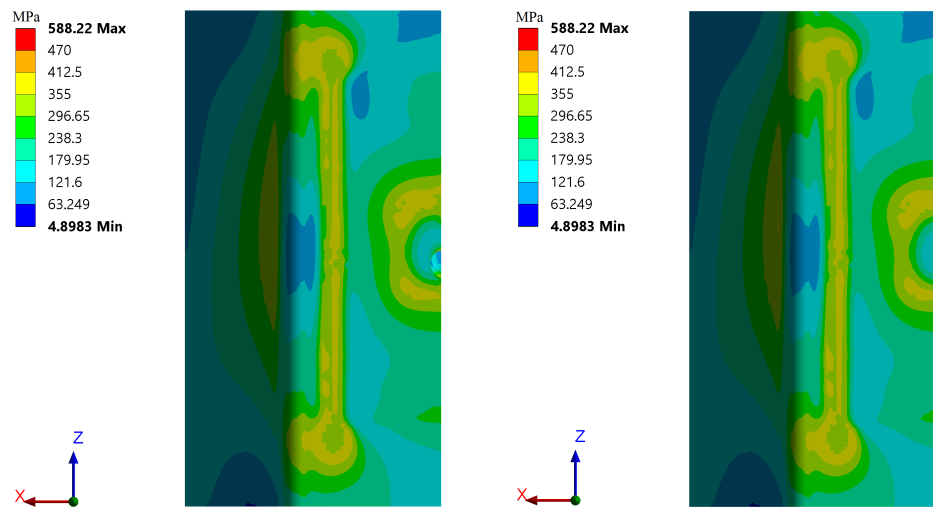
The size of the 'feet' is altered, and the resulting stress distributions are given.



(a) Excavation side of the sheet pile.

(b) Back side of the sheet pile.

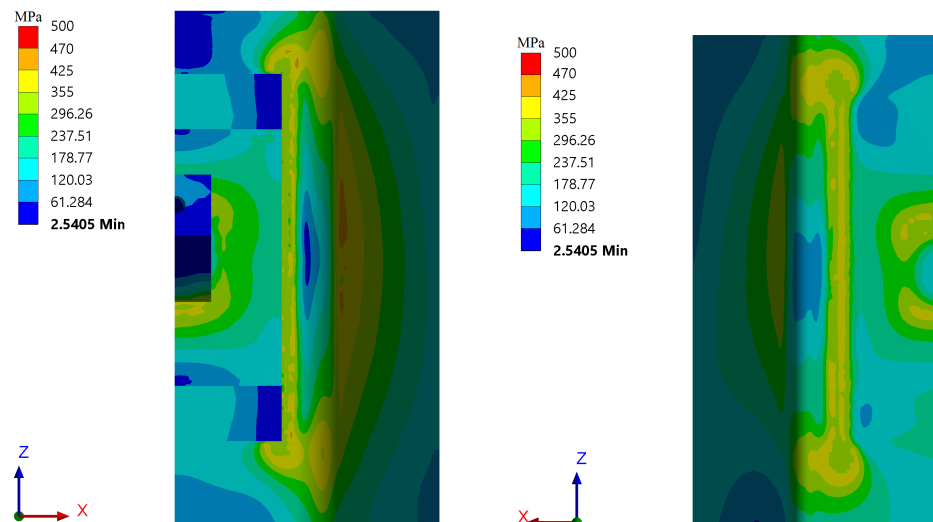
Figure A.153: Distribution of equivalent von Mises stresses having no feet.



(a) Excavation side of the sheet pile.

(b) Back side of the sheet pile.

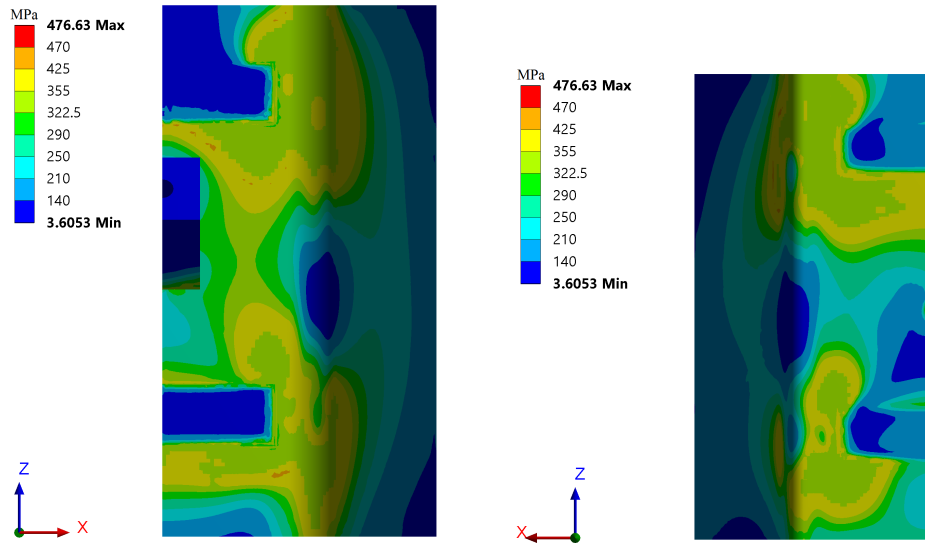
Figure A.154: Distribution of equivalent von Mises stresses having 14 mm feet pointing upwards.



(a) Excavation side of the sheet pile.

(b) Back side of the sheet pile.

Figure A.155: Distribution of equivalent von Mises stresses having 29 mm feet pointing upwards.



(a) Excavation side of the sheet pile.

(b) Back side of the sheet pile.

Figure A.156: Distribution of equivalent von Mises stresses having 29 mm feet pointing downwards.

A. APPENDIX

The maximum stresses has been captured in the flange and web in both the excavation side and the back side respectively resulting in four sets of data which are given in figures A.157 to A.160. Stress peaks related to singularities have been neglected.

- *P1* refers to the back side of the flange
- *P2* refers to the excavation side of the flange
- *P3* refers to the back side of the web
- *P4* refers to the excavation side of the web

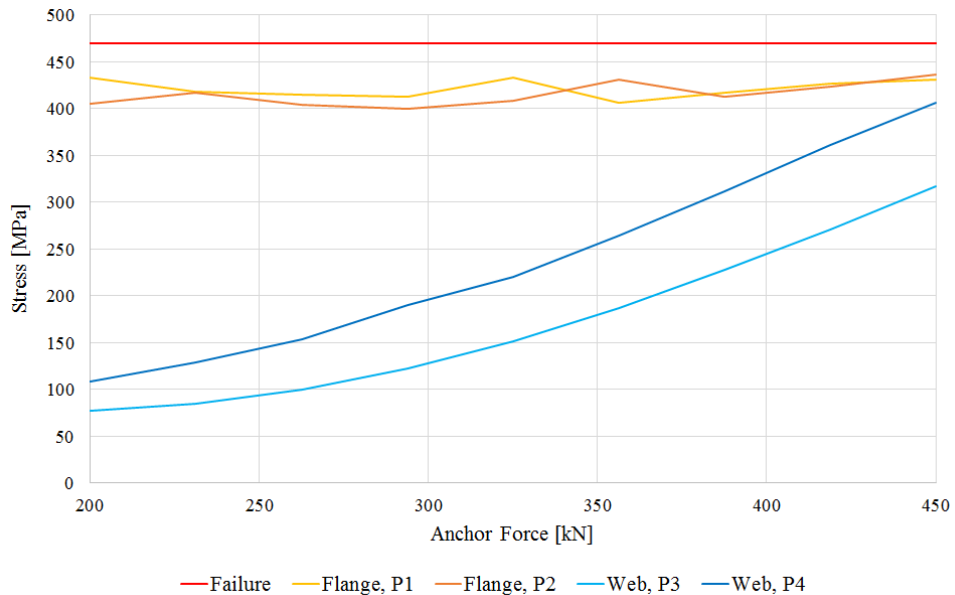


Figure A.157: Development of the maximum equivalent von Mises stresses in the two sides of the flange and web respectively having no feet.

A.12. Parameter Study of Sheet Pile and Load Bearing Plate

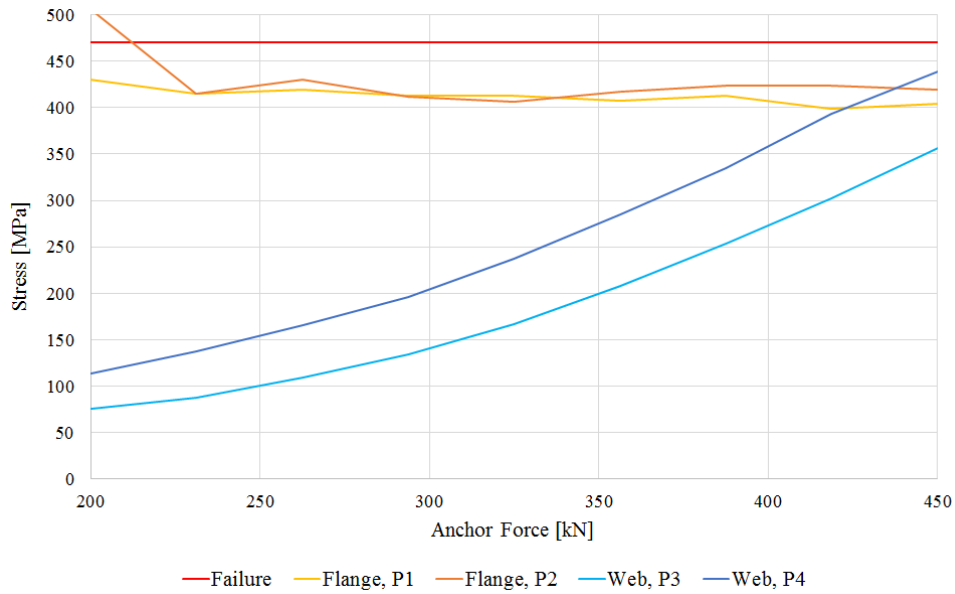


Figure A.158: Development of the maximum equivalent von Mises stresses in the two sides of the flange and web respectively having 14 mm feet pointing upwards.

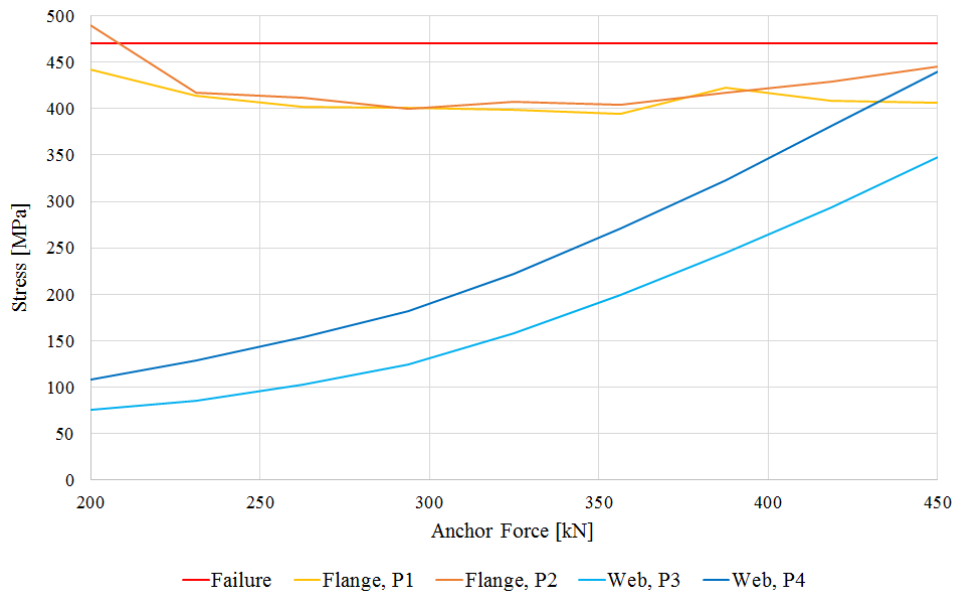


Figure A.159: Development of the maximum equivalent von Mises stresses in the two sides of the flange and web respectively having 29 mm feet pointing upwards.

A. APPENDIX

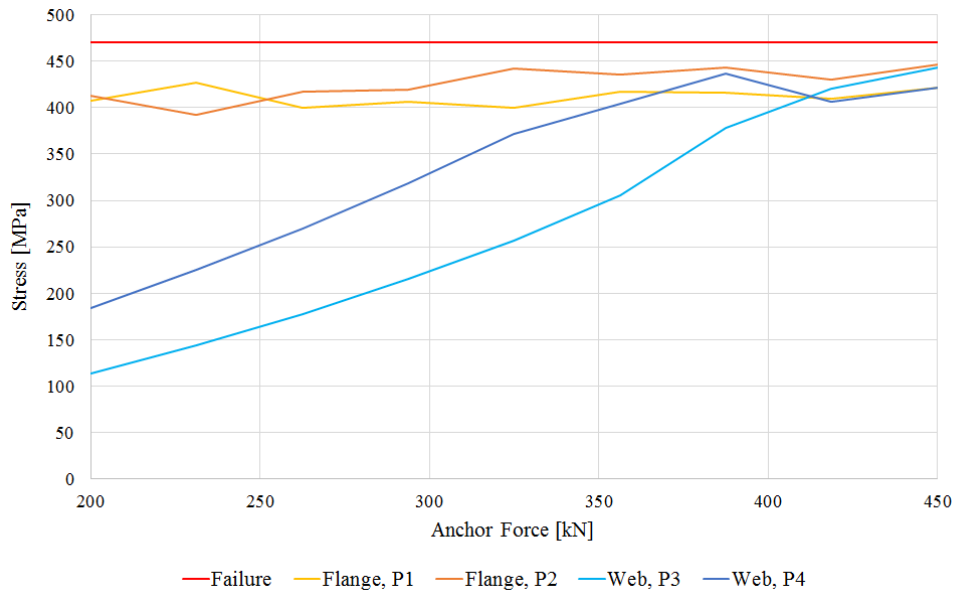


Figure A.160: Development of the maximum equivalent von Mises stresses in the two sides of the flange and web respectively having 29 mm feet pointing downwards.

The maximum plastic strains for any of the size configurations are shown in figure A.161, which shows the development in the strains as the size is altered.

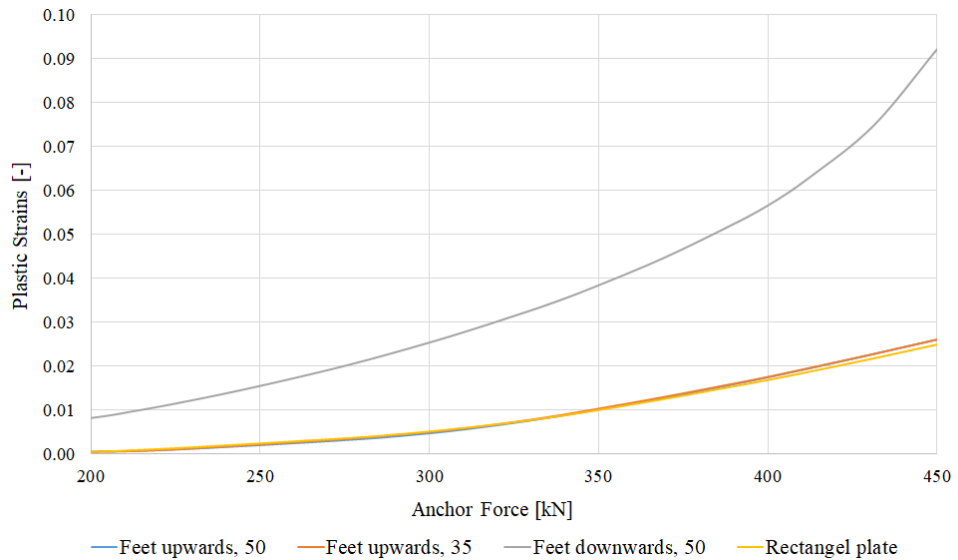


Figure A.161: Development of the maximum plastic strains in the sheet pile for different configurations of the load bearing plate.

A.13 Membrane Actions

A study of the influence of the membrane actions in a plate is carried out. In order to investigate the effects a single clamped plate is modeled exposed to a evenly distributed load, thus the plate will act as a beam. The plate is analysed being constrained from longitudinal movements and being able to move longitudinal in one end. The static models are given figure A.162.

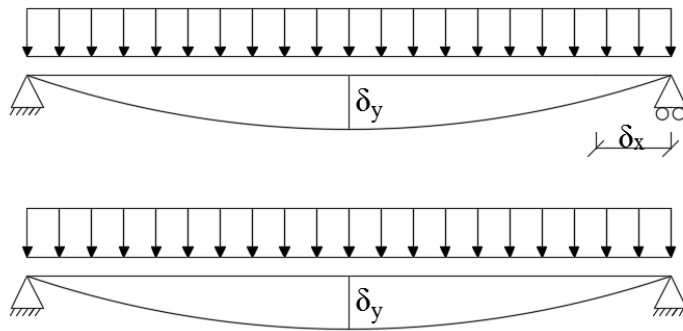
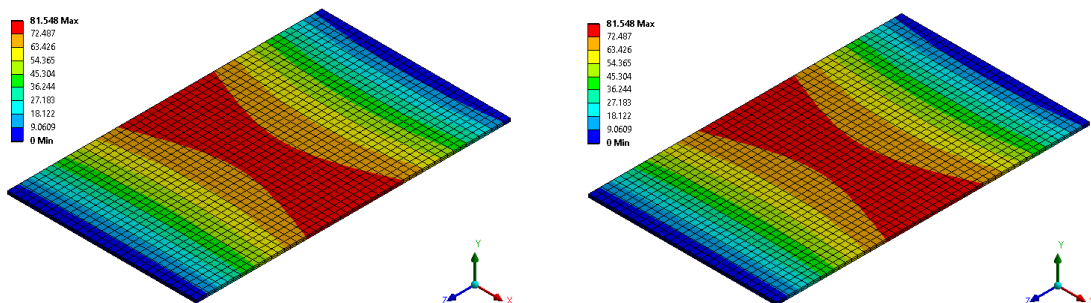


Figure A.162: Static model of analyses. Simple supported and simple supported having longitudinal movement constrains are used.

The purpose is to illustrate the differences between linear and nonlinear analyses considering the membrane actions. No deviations should be captured performing linear analyses by the setups given in figure A.162. However as nonlinear analyses using the same configurations as for the linear are performed, deviations are expected to appear which is a result of large deformations. The deviations between the two configuration are expected to increase as the deformations grow.

Linear Analysis

Total deformations are pictured in figure A.163.



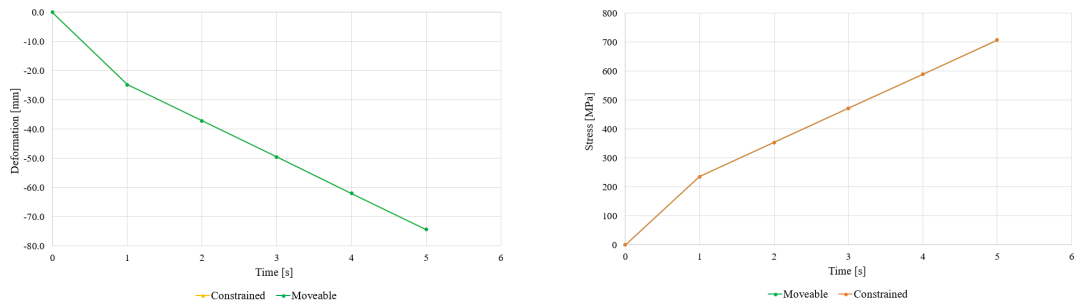
(a) Simple supported with one side being supported by a remote displacement.

(b) Simple supported with longitudinal movement constrains.

Figure A.163: Total deformations obtained by linear analyses.

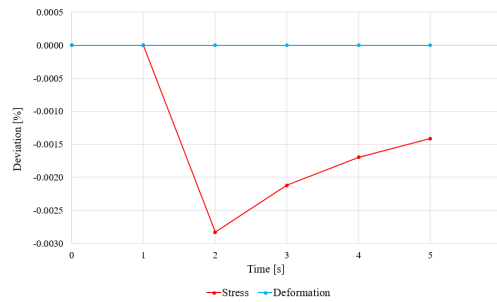
A. APPENDIX

Figures A.163a and A.163b reveal no apparent differences. Deviations in the development of the deformations in the z direction and equivalent von Mises stresses in the middle of the plate are given in figure A.164.



(a) Deformations in the z direction.

(b) Equivalent von Mises stresses in the middle of the plate.



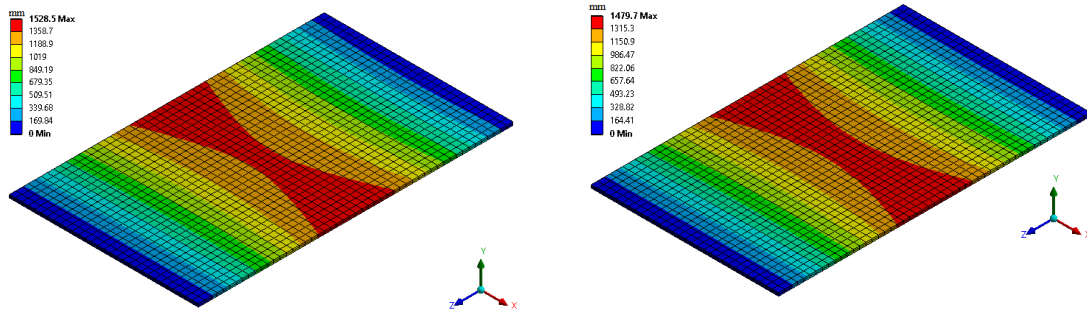
(c) Deviations.

Figure A.164: Deviations between the two linear analyses.

It is seen that the deviations are insignificant considering the linear analyses.

Bilinear Analysis

Total deformations are pictured in figure A.165.

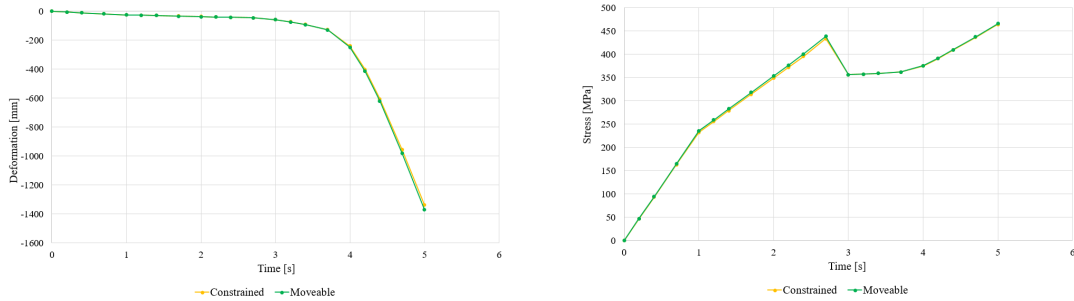


(a) Simple supported with one side being supported by a remote displacement.

(b) Simple supported with longitudinal movement constrains.

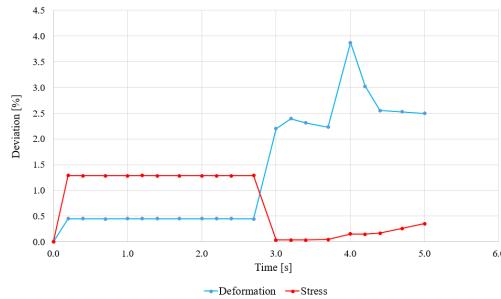
Figure A.165: Total deformations obtained by bilinear analyses.

Figures A.165a and A.165b have differences and are not identical. Deviations in the development of the deformations in the z direction and equivalent von Mises stresses in the middle of the plate are given in figure A.166.



(a) Deformations in the z direction.

(b) Equivalent von Mises stresses in the middle of the plate.



(c) Deviations.

Figure A.166: Deviations between the two bilinear analyses.

It is seen that the deviations grow for the bilinear model in comparison to the linear analyses as the deformations increase. The deviations in stresses however decrease as the stresses reach the plastic region and will then grow.

Realistic Plastic Model

Additionally a study applying a realistic plastic model is carried out. Total deformations are pictured in figure A.167.

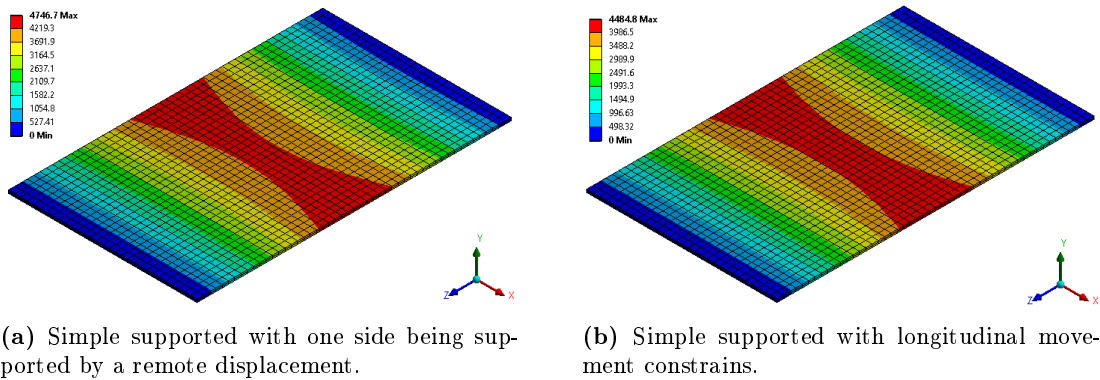
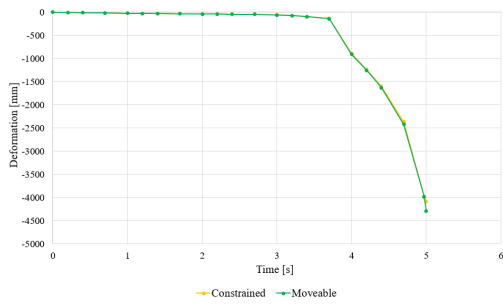


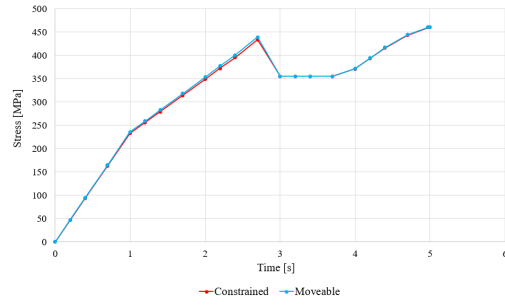
Figure A.167: Total deformations obtained by realistic plastic model analyses.

Deviations in the development of the deformations in the z direction and equivalent von Mises stresses in the middle of the plate are given in figure A.168.

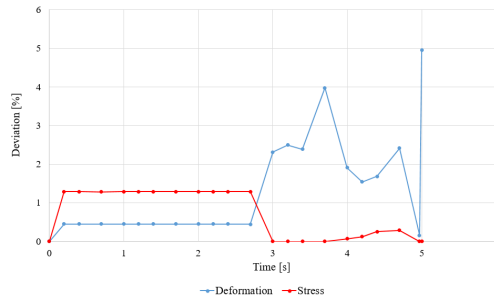
Evaluating figure A.168 the same tendency appears as captured for the bilinear model.



(a) Deformations in the z direction.



(b) Equivalent von Mises stresses in the middle of the plate.



(c) Deviations.

Figure A.168: Deviations between the two analyses using a realistic plastic model.

A.14 Validation of Elastoplastic Analysis in OptumG2

A.14.1 Mesh Influence Study

A study of convergence is performed to determine the appropriated number of elements required to obtain accurate results using OptumG2. The number of elements is gradually increased, and the development is shown in figure A.169.

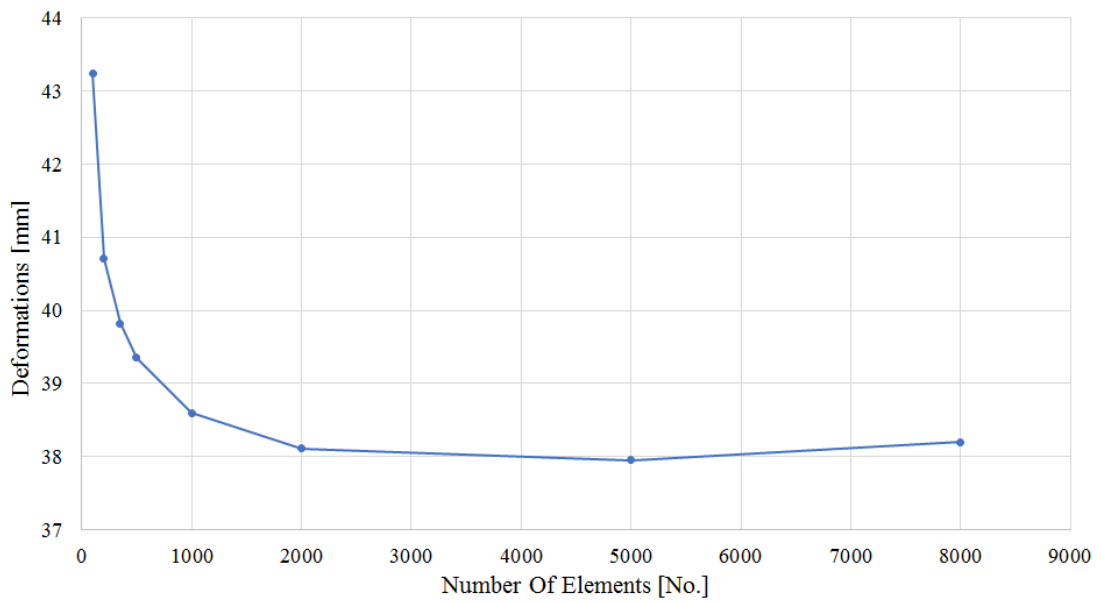


Figure A.169: Convergence study determining the appropriate number of elements in OptumG2.

At approximately 2000 elements the curve starts to converge. Theoretically, any greater number of elements is wasted considering computational time spend, thus a number of 2000 elements is considered appropriate in the analyses.

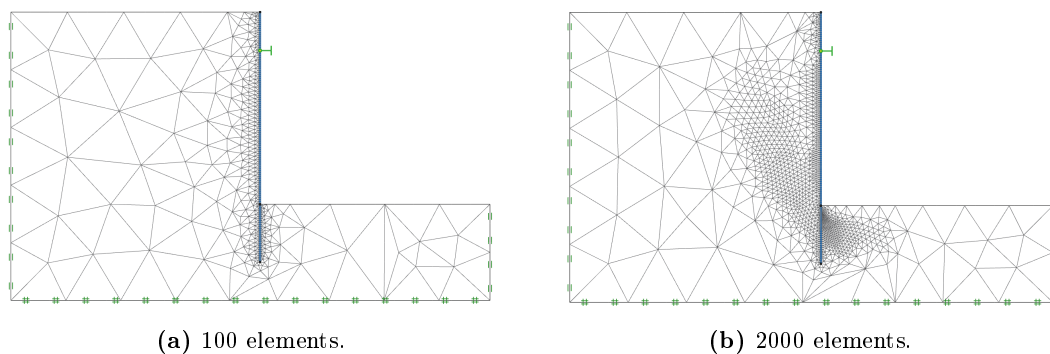


Figure A.170: Mesh given for different amounts of elements.

A.14.2 Influence of Repeatable Identical Analyses

The mesh is generated randomly for each analysis. This means the mesh is different each time a new analysis is computed in the software which influences the results with an unknown magnitude. In this study, identical analyses are computed multiple time to investigate the variation in the deformation results. All configurations are kept and the only difference is the mesh generation. In figure A.171 a mesh is generated twice for the same analysis with identical configurations. The generated meshes appear identical, however at a closer comparison small variations near the sheet pile wall are apparent.

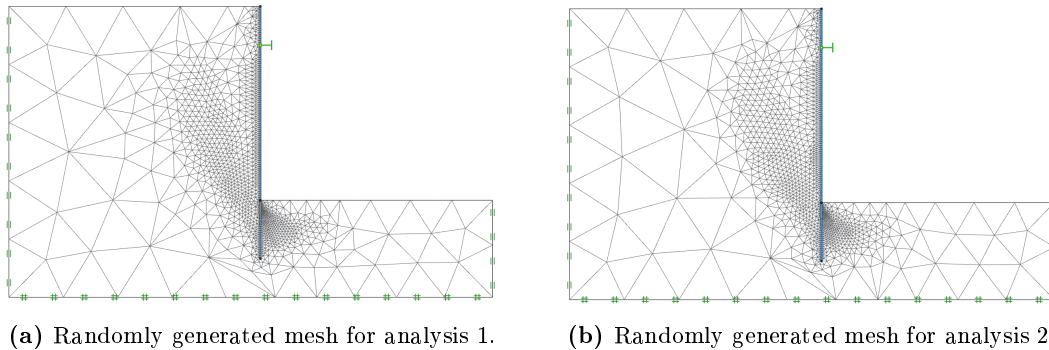


Figure A.171: Randomly generated mesh for two identical analysis. 2000 elements are used.

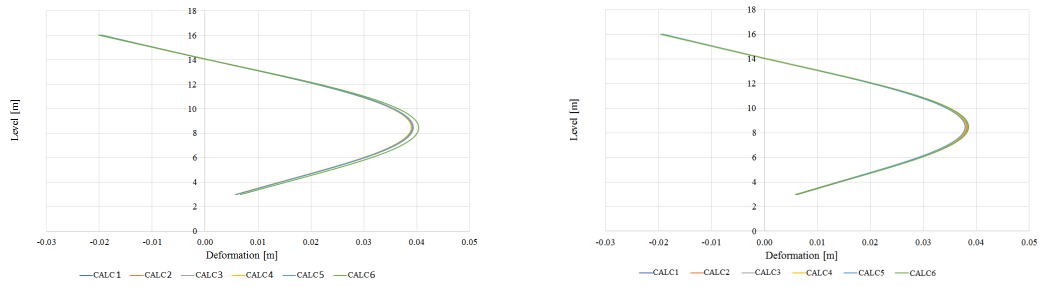
In table A.16 the deformations are calculated for several identical analyses. Two investigations have been carried out using 500 and 2000 elements respectively in order to determine the influence of the refinement of the mesh considering deformations for a sheet pile wall. The mean of all the calculations has been determined, which marks a threshold from which the listed deviations are results of.

Table A.16: Deviation for identical analyses.

| | Minimum Deformation | | Maximum Deformation | |
|-----------------------|---------------------|----------|---------------------|----------|
| | [m] | Dev. [%] | [m] | Dev. [%] |
| Elements: 500 | 0.039 | -1.02 | 0.0403 | 2.45 |
| Elements: 2000 | 0.0379 | -0.84 | 0.0386 | 0.88 |

Having 500 elements the results are varying with approximately 3 % which is lowered to around 2 % for 2000 elements. This variation is rather small and has no significant influence on the deformation results. However, the variation might be caused by the randomly generated mesh or how the iteration process is performed. Figure A.172 reveals the deformations for each calculation.

A. APPENDIX



(a) Deformation results using 500 no. of elements.

(b) Deformation results using 2000 no. of elements.

Figure A.172: Deformations results with 4 identical analyses having different amounts of elements.

A.14.3 Soil Domain Influence Study

In OptumG2 the size of the soil domain is not prespecified, but is defined by the user. The size must be appropriate to not interfere with the failure zone which is a results of the mesh generated by shear dissipation adaptivity. Initially a mesh must be generated in order to capture the failure zone of the soil which is an area consisting of small elements compared to the undisturbed areas of the soil domain. In figure A.171 a soil domain capturing the full failure zone is generated, thus no further expansions are needed. In contrary an unnecessary large soil domain must be avoided in order to reduce computational time.

In the following a study is carried out to investigate any effect obtained by increasing the size of the soil domain, and the influence of the respective dimensions on the deformations. In figure A.173 a template for the soil domain is given. The lengths of the distances used in the study are presented in table A.17.

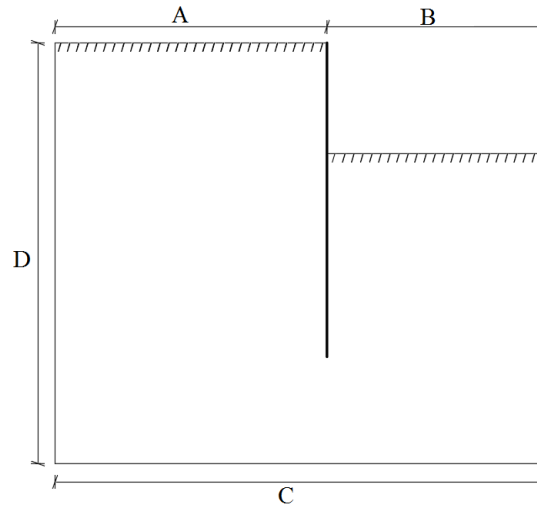


Figure A.173: Soil domain lengths.

Table A.17: Soil domain lengths related to figure A.173 with related calculated deviations for the maximum deformation of the sheet pile wall.

| | <i>A</i> | <i>B</i> | <i>C</i> | <i>D</i> | Deformation | Deviation |
|-----------------|--------------|--------------|--------------|--------------|---------------|-----------|
| | [<i>m</i>] | [<i>m</i>] | [<i>m</i>] | [<i>m</i>] | [<i>mm</i>] | [%] |
| Domain 1 | 13 | 12 | 25 | 15 | 38.23 | 0.00 |
| Domain 2 | 19 | 15 | 35 | 19 | 39.74 | 3.94 |
| Domain 3 | 24 | 19 | 43 | 22 | 40.20 | 5.16 |
| Domain 4 | 19 | 12 | 31 | 15 | 37.93 | -0.78 |
| Domain 5 | 25 | 12 | 37 | 15 | 37.86 | -0.96 |
| Domain 6 | 13 | 12 | 25 | 20 | 40.24 | 5.27 |
| Domain 7 | 13 | 12 | 25 | 25 | 39.51 | 3.35 |
| Domain 8 | 13 | 17 | 30 | 15 | 38.18 | -0.11 |
| Domain 9 | 13 | 18 | 34 | 15 | 38.03 | -0.51 |

Domain 1 is used as the reference example. The domain of analyses 2 and 3 are increased by 77 % and 150 % respectively. It appears in table A.17 that the deviation for Domain 3 is 5 %, but the soil domain is greater by a factor of 2.5. This means, that the size of the soil domain is interfering with the deformation results and the reason might be the mesh generation in the model. To investigate this, figure A.174 reveals both the mesh for the standard example, Domain 1, and the greater soil domain, Domain 3.

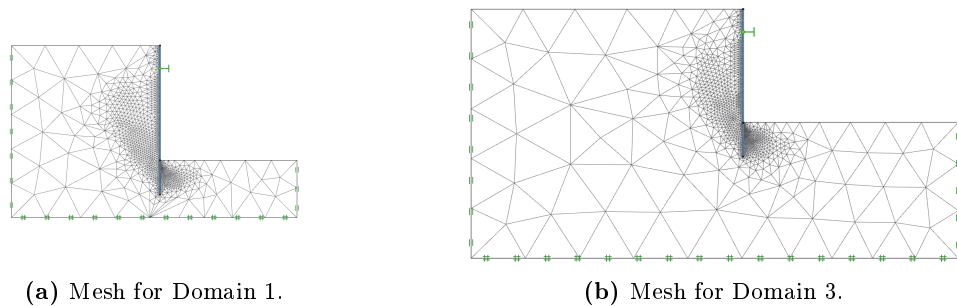
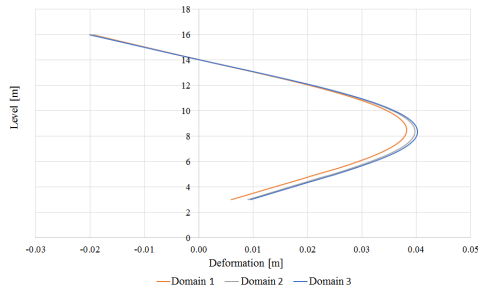


Figure A.174: Soil domain influence.

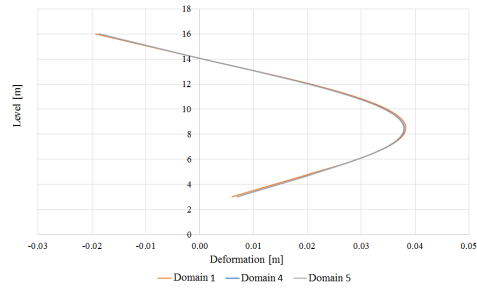
Figure A.174 indicates only minor changes in the mesh near the sheet pile wall. A further investigation of the effect on the deformations is then performed. By increasing one length separately keeping the other unchanged, it is possible to determine the influence of each dimension.

For Domain 4 and 5 the back side area of the sheet pile wall has been expanded. Increasing the length A with 50 % and 100 % a deviation of 1 % is obtained which is considered neglectable. The area beneath the sheet pile wall has been increased for Domain 6 and 7 by approximate 30 % and 65 % respectively. It appears that by increasing the area by 30 % the deformation has increased by 2 mm which equals approximately 5 %. The scale of this deviation cannot be neglected due to the impact on the results. For Domain 8 and 9 the excavation side of the sheet pile wall has been expanded by 40 % and 75 % respectively. However, only a deviation of 1 % is captured which is considered neglectable.

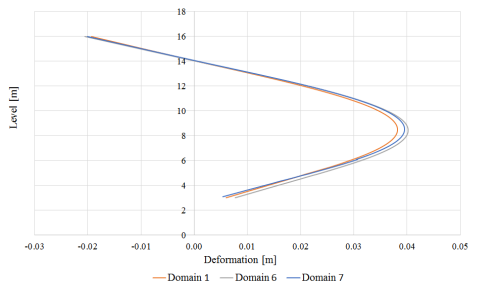
The deviations obtained as the depth of the domain is enlarged may as well be explained by the mesh generation, and as this domain parameter seems to have the greatest impact it is recommended that unnecessary depth of the domain is avoided, as the deformations grows perceptible. The results are pictured in figure A.175.



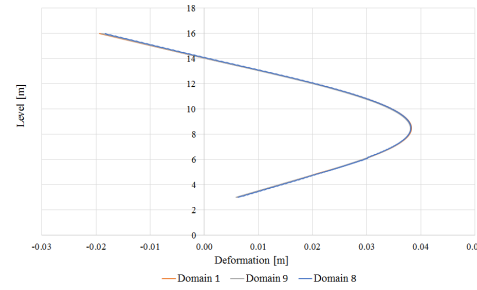
(a) Soil domain 1, 2 and 3. All lengths are increased to investigate the effect on the deformation results.



(b) Soil domain 1, 4 and 5. The back side of the sheet pile wall is increased to investigate the effect on the deformation results.



(c) Soil domain 1, 6 and 7. The soil domain beneath the sheet pile is increased to investigate the effect on the deformation results.



(d) Soil domain 1, 8 and 9. The excavation side of the sheet pile wall is increased to investigate the effect on the deformation results.

Figure A.175: Soil domain influence

A.14.4 Stage Influence Study

Constructing an Elastoplastic analysis in OptumG2, multiple stages have to be created, gradually lowering the excavation level. In order to investigate the influence of the number of stages applied including the influence of the application of the anchor, different calculation altering the amount of stages are performed. Initially the standard case using 5 stages is computed which is also used in the validations investigated in appendixes A.14.1, A.14.2 and A.14.3. Afterward the number of stages is altered. The results are illustrated in figure A.176.

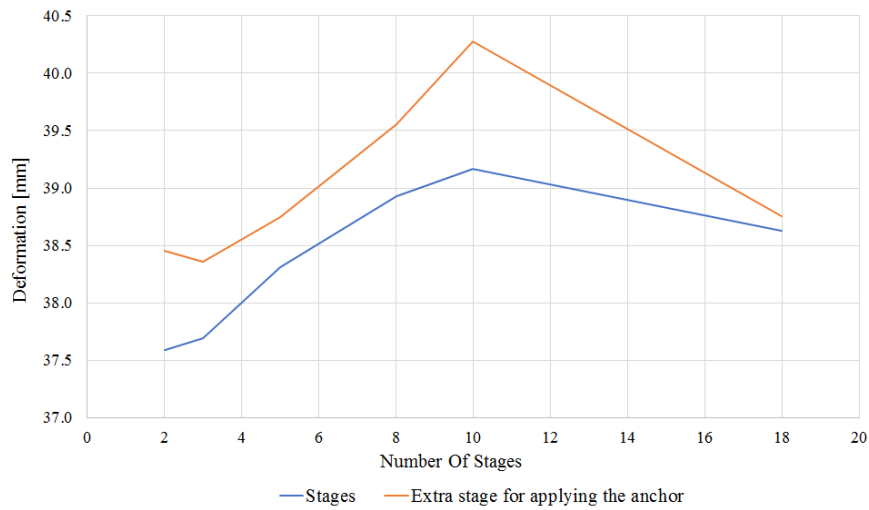


Figure A.176: Deformation results obtained altering the number of stages with an without an extra stage for application of the anchor.

Modeling an extra stage for application of the anchor yields a minor difference, thus it should be implemented in the further analyses, as this replicates the reality best possible. 10 stages gives an increase in the result but declines again with 18 stages and levels out with a number of 5 stages. It is concluded that 5 stages are sufficient in order to achieve accurate results.

In table A.18 the results are given with the corresponding deviations.

Table A.18: Deviations by altering the number of stages.

| Maximum Deformation | Stages | Stages and Anchor | Deviation |
|---------------------|--------|-------------------|-----------|
| | [mm] | [mm] | [%] |
| 2 Stages | 37.59 | 38.46 | 2.25 |
| 3 Stages | 37.69 | 38.36 | 1.75 |
| 5 Stages | 38.31 | 38.74 | 1.11 |
| 8 Stages | 38.93 | 39.55 | 1.57 |
| 10 Stages | 39.16 | 40.27 | 2.76 |
| 18 Stages | 38.63 | 38.75 | 0.32 |

A.15 Inclinometer Measurements

Inclinometers are used for tilt measurements in a soil domain that can be transformed into a variety of soil related entities, primarily deformations. The inclinometer is typically inserted in a quadratic RHS-profile used as a casing. The casing is welded to the web of the sheet pile, which ensures that the movements of the wall are captured. A typical inclinometer is pictured in figure A.177. The inclinometer is lowered to the bottom of the casing and measurements are performed, while gradually raising the instrument in intervals of 500 *mm*.



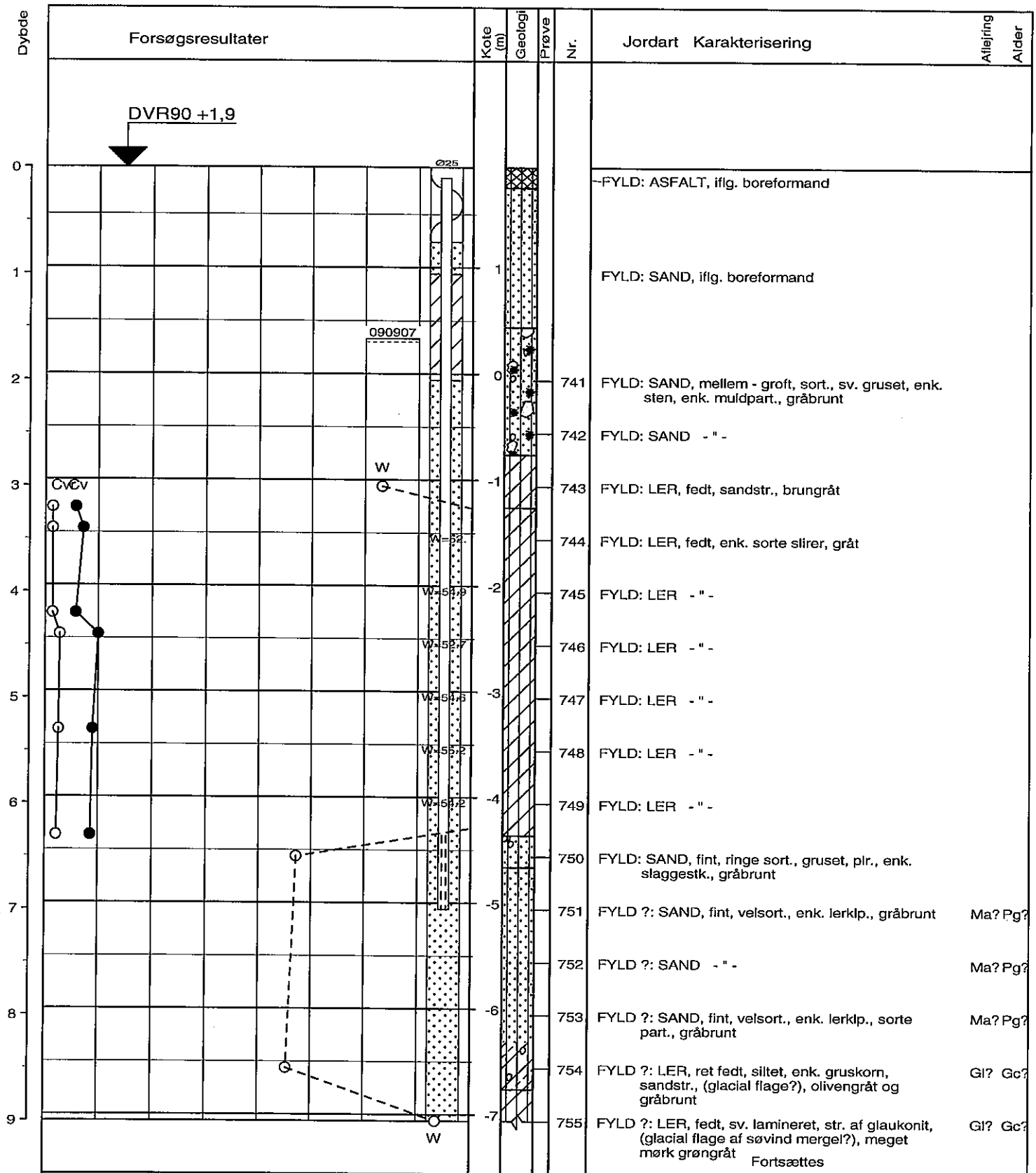
Figure A.177: A typical portable inclinometer.[45]

The gravity change introduced by tilting affects the accelerometers located in the inclinometer. This results in a change in the resistance, and the output is measured, which is proportional to the sine of the angle of inclination, thus the resistance is proportional to the horizontal deviation of an initial state. The angle can then be converted to a deformation or deflection of the sheet pile wall by integration. It is possible to determine the bending moment, as the curvature is calculated by further integration.

The instrument has the capability of measuring the angle of inclination in both axes, which reduces the possible errors. After the initial measurement has been performed, the inclinometer is rotated 180°, inserted in the casing once again and a re-reading is performed equalising measurement uncertainties related to imperfections.

The anticipated direction of movement may differ from the actual direction, which may cause errors in the readings. Another source of error related to the inclinometer measurements is the placement of the casing. If the reference inclination is not completely vertical or is misread, the resulting deformations will not be representative.

A.16 Core Boring Sample



| W (%) | Cv, Cvr (kN/m²) |
|-------|-----------------|
| ○ 10 | ○ 100 |
| ○ 20 | ○ 200 |
| ○ 30 | ○ 300 |

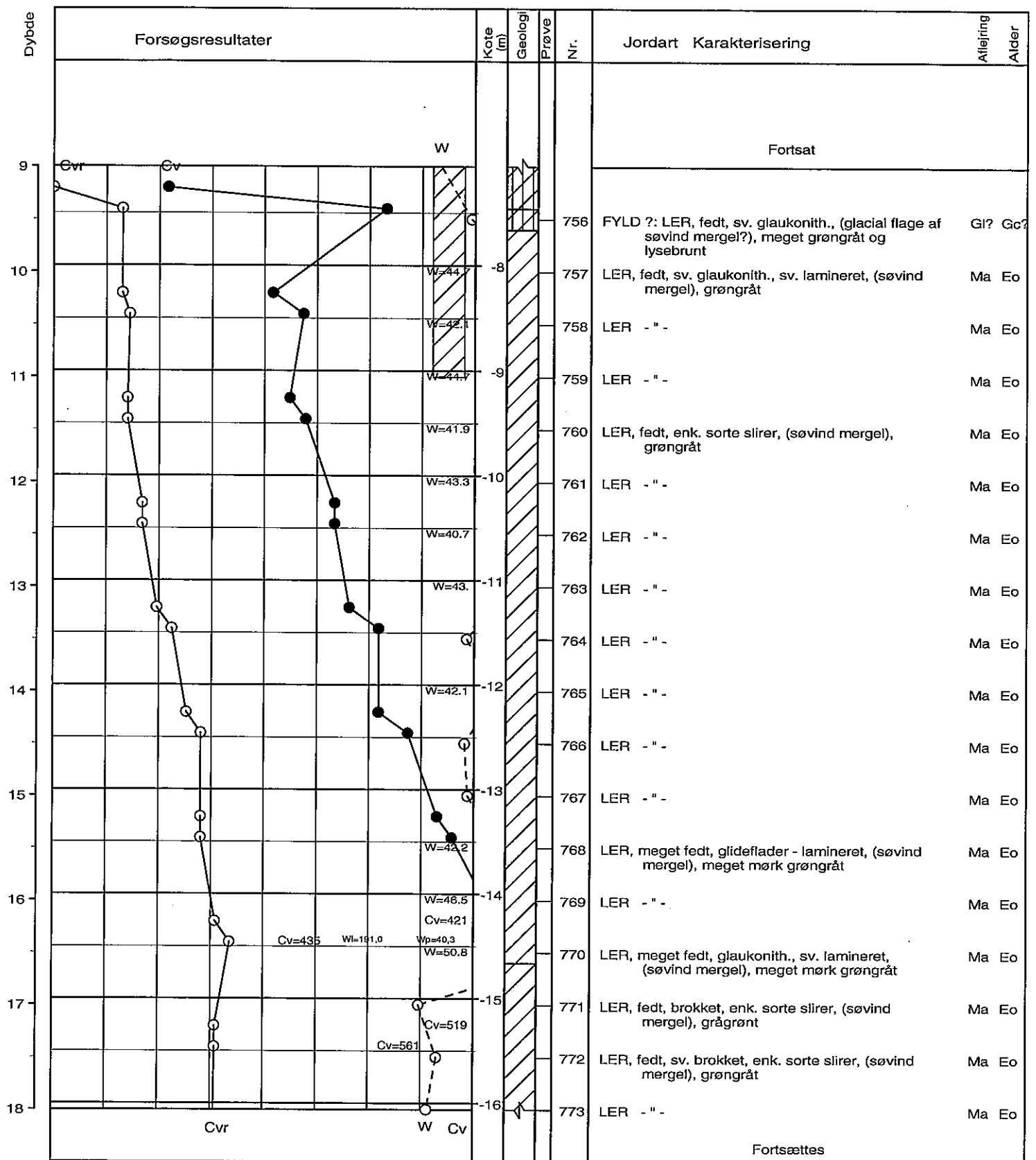
Boremethode : 6 " med foring
 X : 220053 (m) Y : 191498 (m) Plan :

Sag : 0749401F MULTIMEDIEHUSET, ÅRHUS HAVN
 Strækning : Boret af : GEO Dato : 20090803 DGU-nr.: Boring : 18
 Udarb. af : IH Kontrol : RUC Godkendt : *H28* Dato : *30/11-09* Bilag : 2.2018 s. 1 / 4

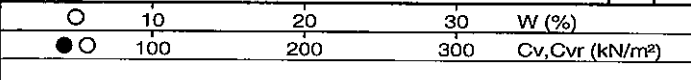


Boreprofil

BRegister - PSTGD&K 2.0 - 12/11/2009 10:10:05



Fortsættes



Boremethode : 6 " med foring

X : 220053 (m) Y : 191498 (m) Plan :

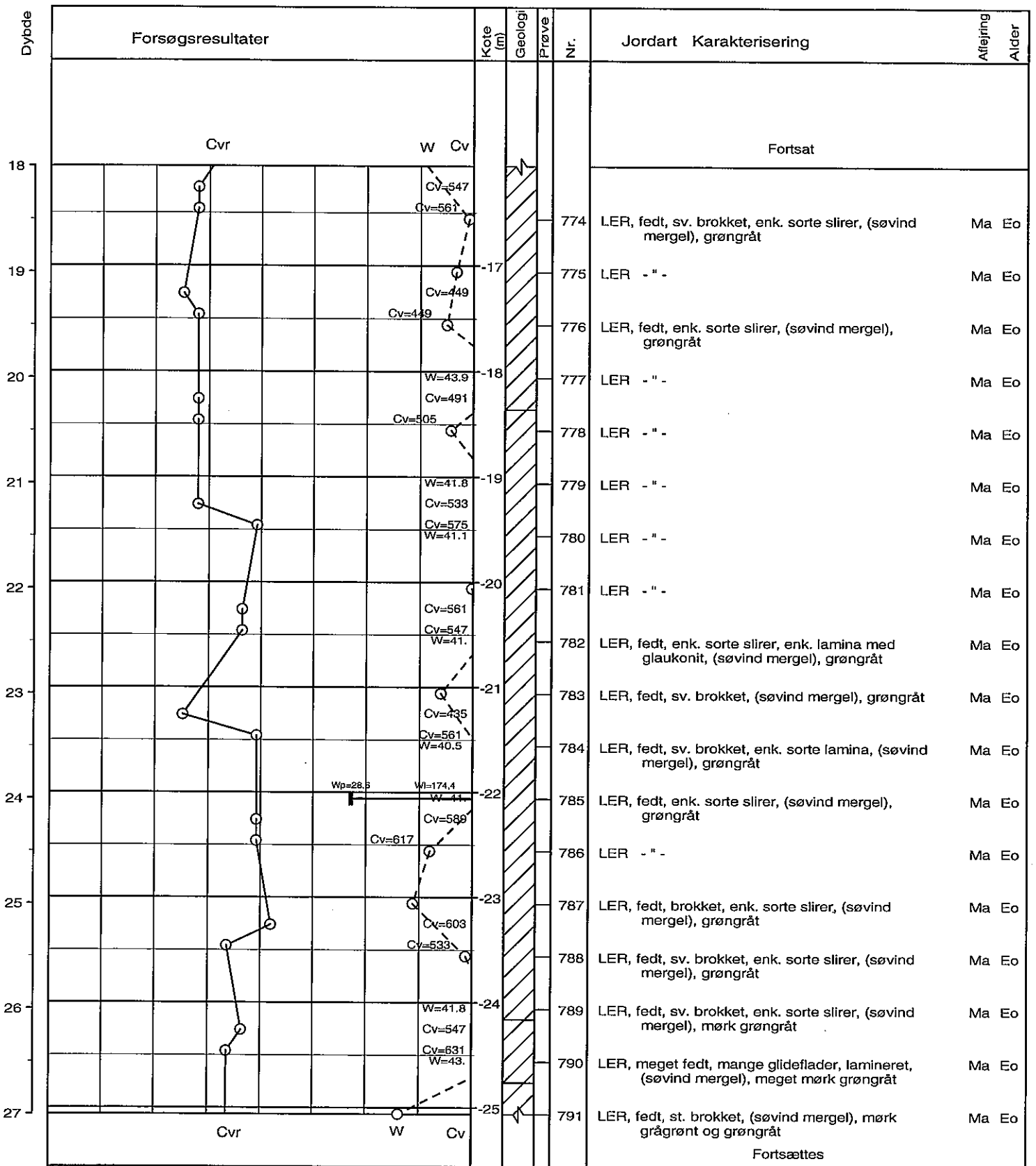
Sag : 0749401F MULTIMEDIEHUSET, ÅRHUS HAVN

Strækning : Boret af : GEO Dato : 20090803 DGU-nr.: Boring : 18
 Udarb. af : IH Kontrol : RUC Godkendt : *HRP* Dato : *30/11-09* Bilag : 2.2018 s.2/4



Boreprofil

BRegister - PSTGDK 2.0 - 12/11/2009 10:10:05



| | | | | |
|---|-----|-----|-----|-----------------|
| ○ | 10 | 20 | 30 | W (%) |
| ● | 100 | 200 | 300 | Cv, Cvr (kN/m²) |
| | | | | |
| | | | | |
| | | | | |
| | | | | |
| | | | | |

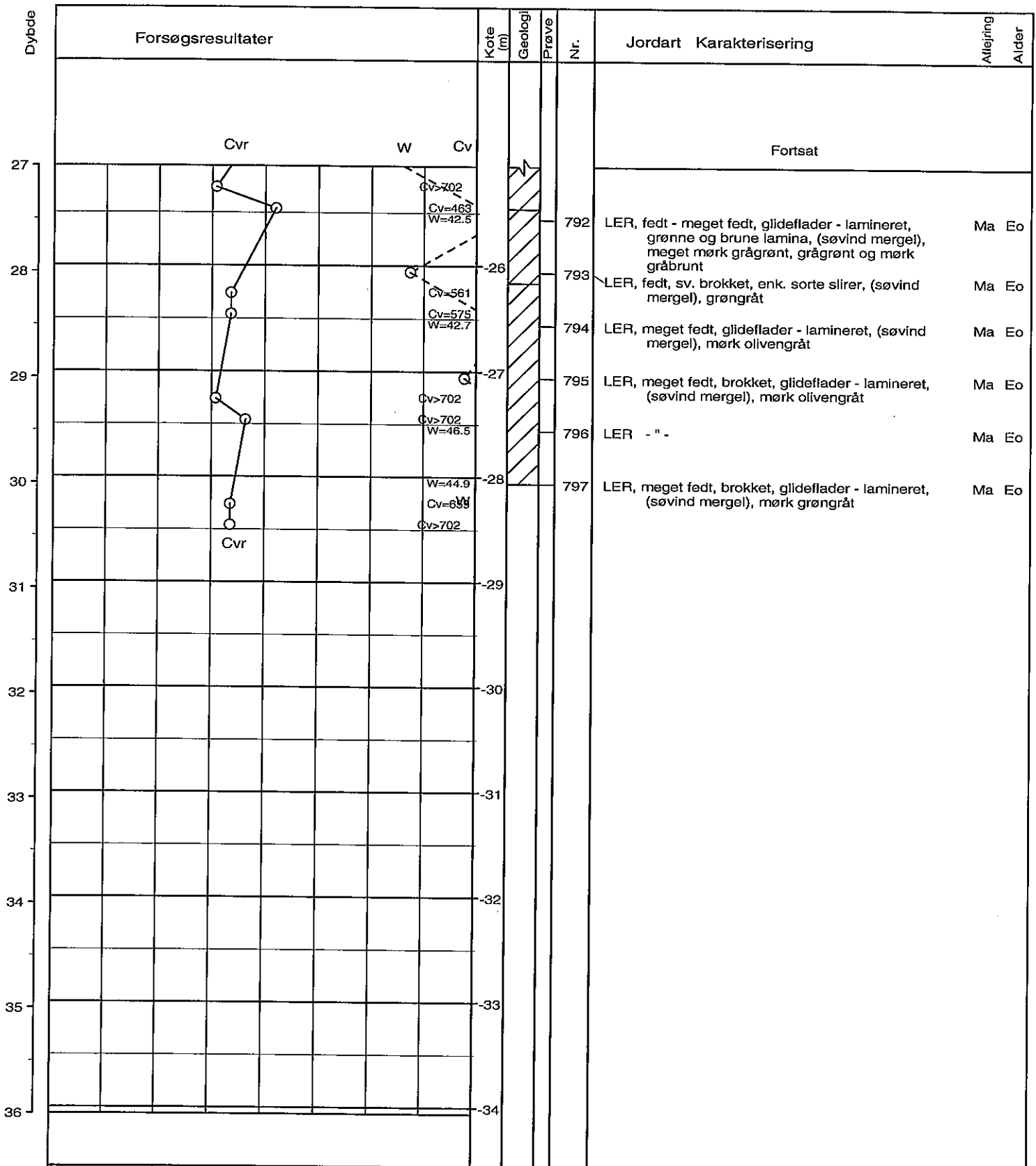
Boremethode : 6 " med foring
 X : 220053 (m) Y : 191498 (m) Plan :

Sag : 0749401F MULTIMEDIEHUSET, ÅRHUS HAVN
 Strækning : Boret af : GEO Dato : 20090803 DGU-nr.: Boring : 18
 Udarb. af : IH Kontrol : RUC Godkendt : *HAP* Dato : *30/11-09* Bilag : 2.2018 s. 3/4



Boreprofil

BRegistrier - PSTGDK 2.0 - 12/11/2009 10:10:05



| | | | | |
|---|-----|-----|-----|-----------------|
| ○ | 10 | 20 | 30 | W (%) |
| ● | 100 | 200 | 300 | Cv, Cvr (kN/m²) |

Boremethode : 6 " med foring
 X : 220053 (m) Y : 191498 (m) Plan :

Sag : 0749401F MULTIMEDIEHUSET, ÅRHUS HAVN

Strækning : Boret af : GEO Dato : 20090803 DGU-nr.: Boring : 18
 Udarb. af : IH Kontrol : RUC Godkendt : *HSP* Dato : *30/11-09* Bilag : 2.2018 s.4/4



Boreprofil

BRegister - PSTGDK 2.0 - 12/11/2009 10:10:05

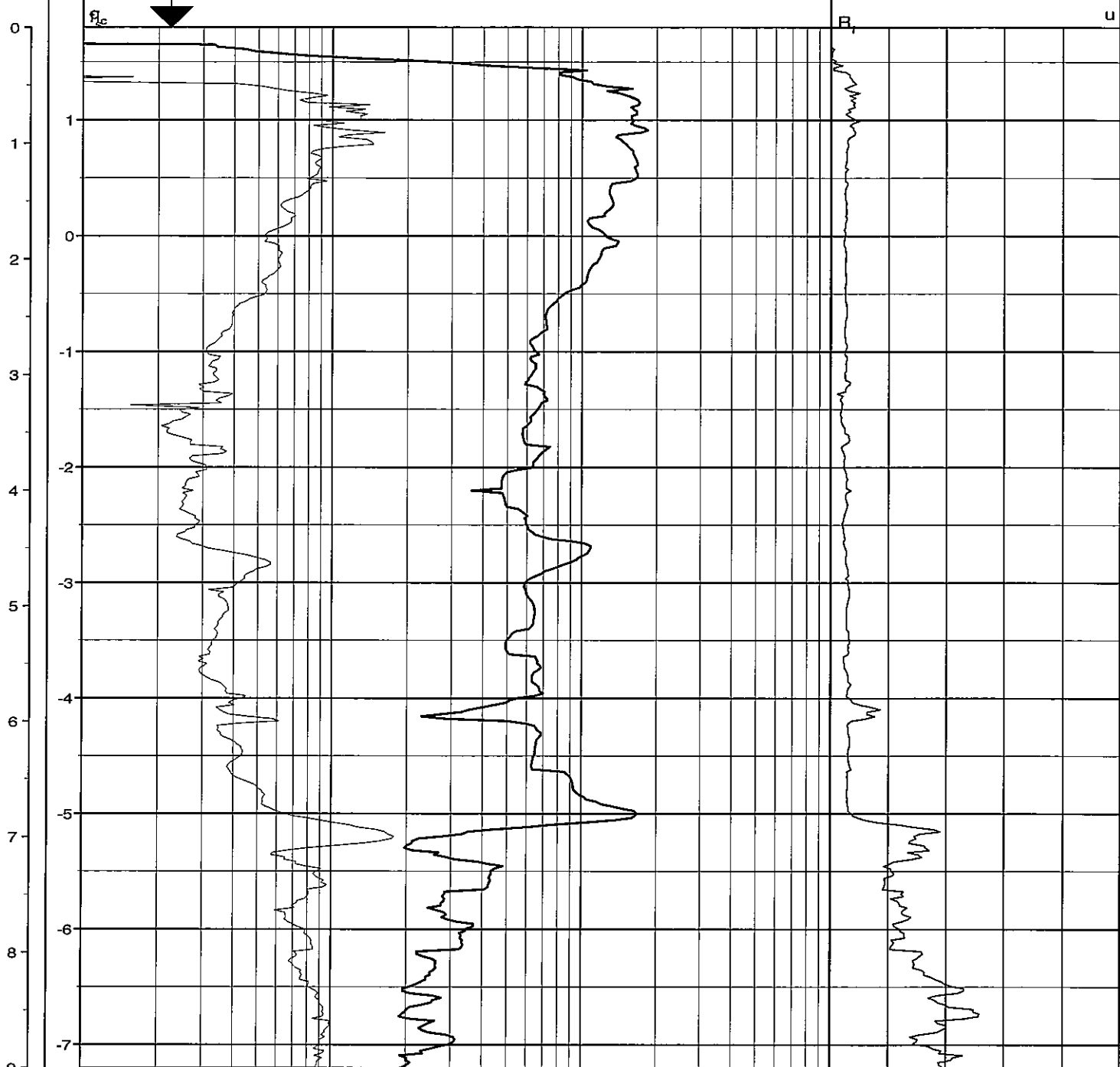
A.17 CPT Sample

Dybde

Kote (m)

Forsøgsresultater

DVR90 +1,8



f_s q_c
Fortsættes

| | | | | | | |
|---------------|-----|----|-------------|-----|-----|-------------|
| q_c (MPa) → | 1 | 10 | R_f (%) → | 4 | 6 | 8 |
| f_s (MPa) → | 0.1 | 1 | 0.3 | 0.2 | 0.1 | ← 0 u (MPa) |

Sonde nr. :
Sonde type : TSP

X: X: 220049 (m)
Y: Y: 191538 (m)
Plan :

Sag : 0749401F MULTIMEDIEHUSET, ÅRHUS HAVN

Strækning : Boret af : GEO JEJ/HRE Dato : 20090622 Rig : Landrig CPT nr. : 44
Udarb. af : Kontrol : Godkendt : *WSP* Dato : *30/11-09* Bilag : 2.4014 s. 1/2



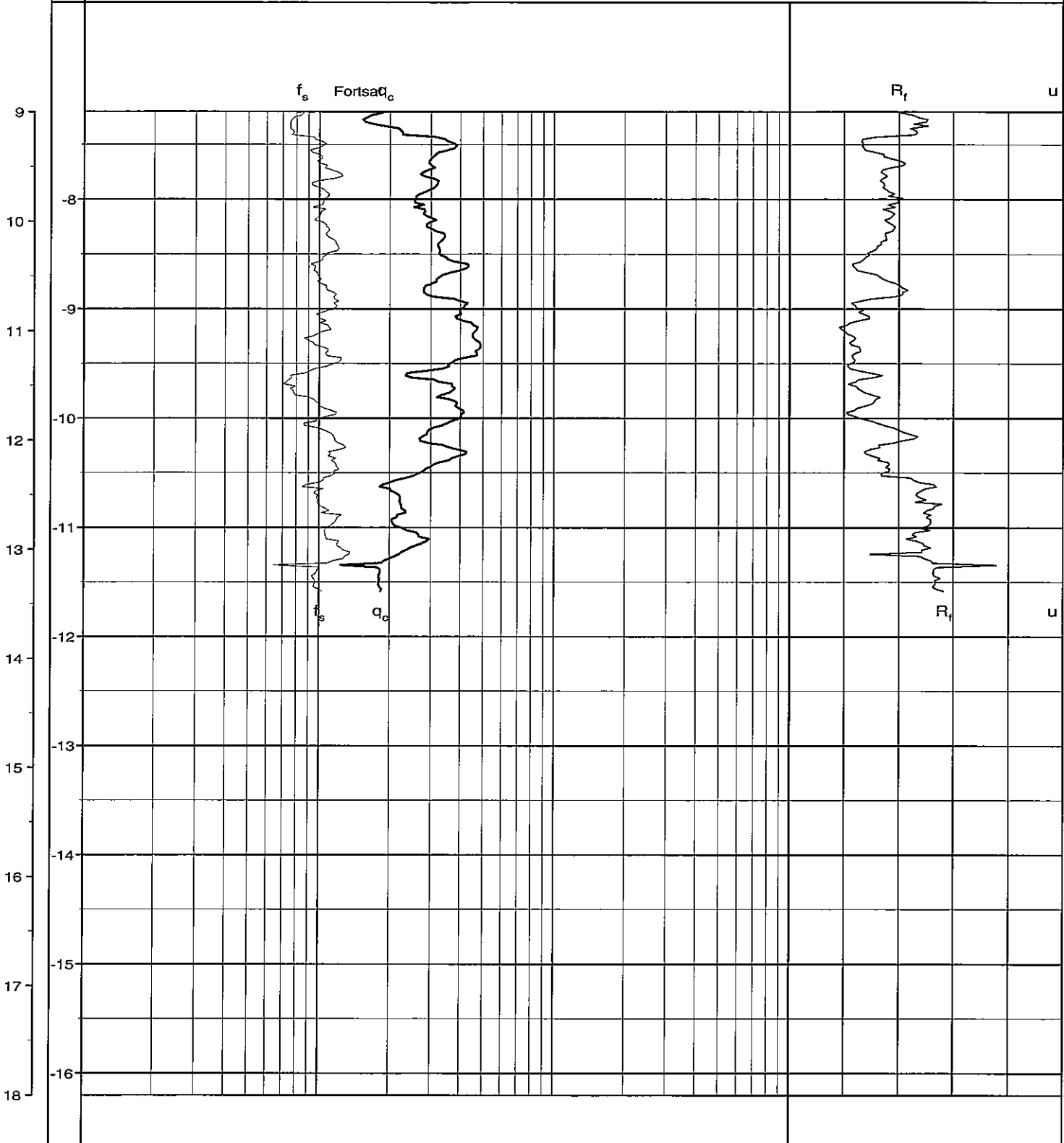
CPT profil

BRRegister - PSTGLDK 2.0 - 2009/11/20 11:25:39

Dybde

Kote (m)

Forsøgsresultater



| | | | | | | | |
|---------------|-----|----|-------------|-----|-----|-----|-------------|
| q_c (MPa) → | 1 | 10 | R_f (%) → | 2 | 4 | 6 | 8 |
| f_s (MPa) → | 0.1 | 1 | | 0.3 | 0.2 | 0.1 | ← 0 u (MPa) |

Sonde nr. : X: X: 220049 (m)
 Sonde type : TSP Y: Y: 191538 (m)
 Plan :

Sag : 0749401F MULTIMEDIEHUSET, ÅRHUS HAVN
 Strækning : Boret af : GEO JEJ/HRE Dato : 20090622 Rig : Landrig CPT nr. : 44
 Udarb. af : Kontrol : Godkendt : *HTP* Dato : *30/11-09* Bilag : 2.4014 s.2/2



CPT profil

BRregulater - PSTCLDK 2.0 - 2009/11/30 11:23:39

A.17.1 Parameter Influence Results

A study of the influence of the soil parameters has been carried out. Figures A.178 to A.185 reveals the results obtained.

The parameters count:

- Friction angle
- Cohesion
- Soil density
- Modulus of elasticity
- Poisson's ratio
- Wall friction angle
- Initial earth pressure coefficient
- Dilation angle

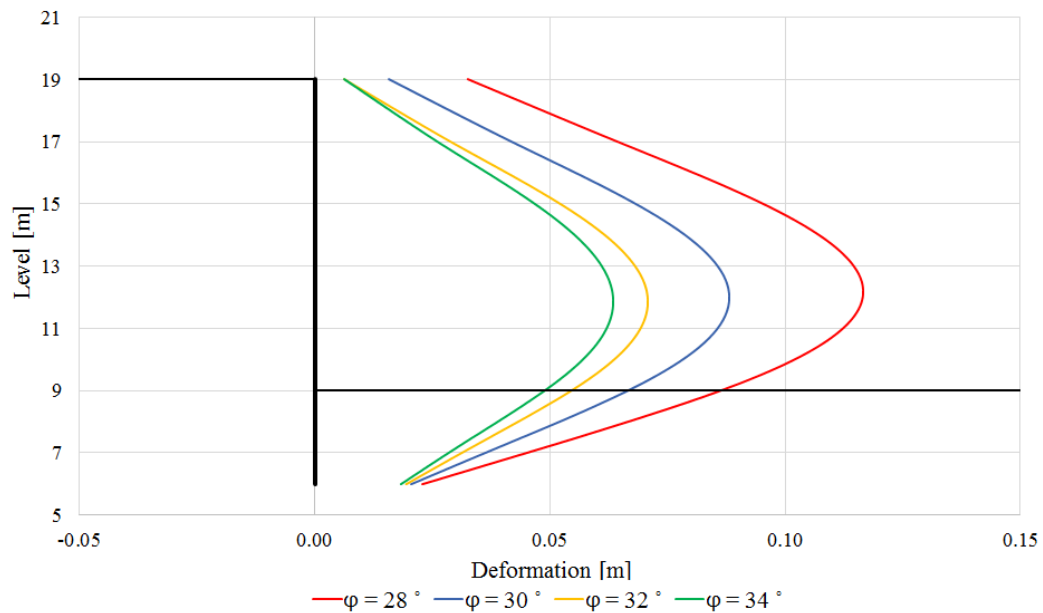


Figure A.178: Deformations altering the friction angle value.

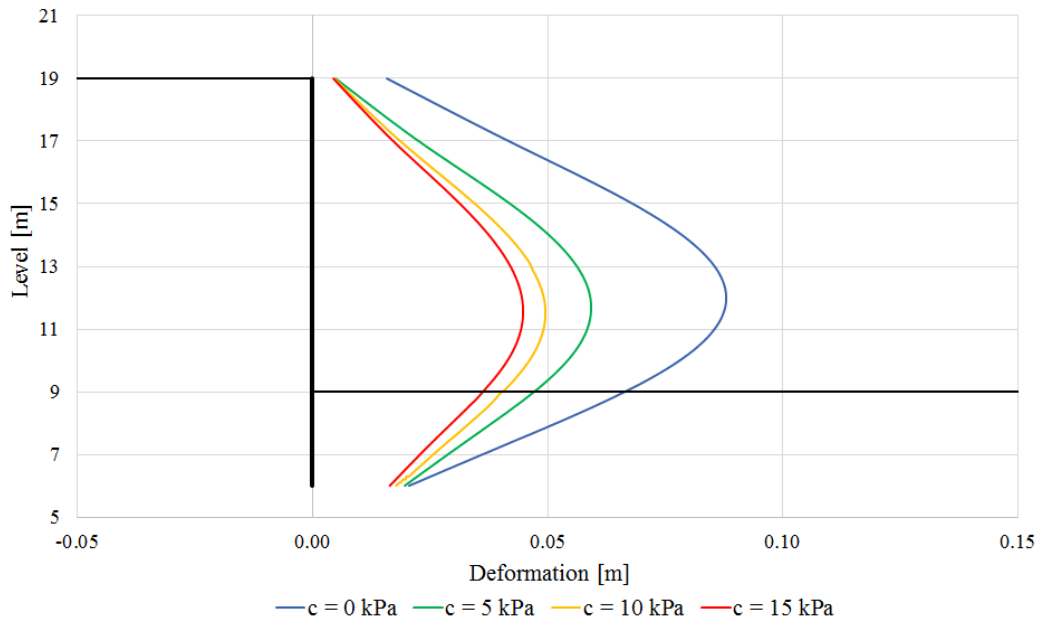


Figure A.179: Deformations altering the shear strength value.

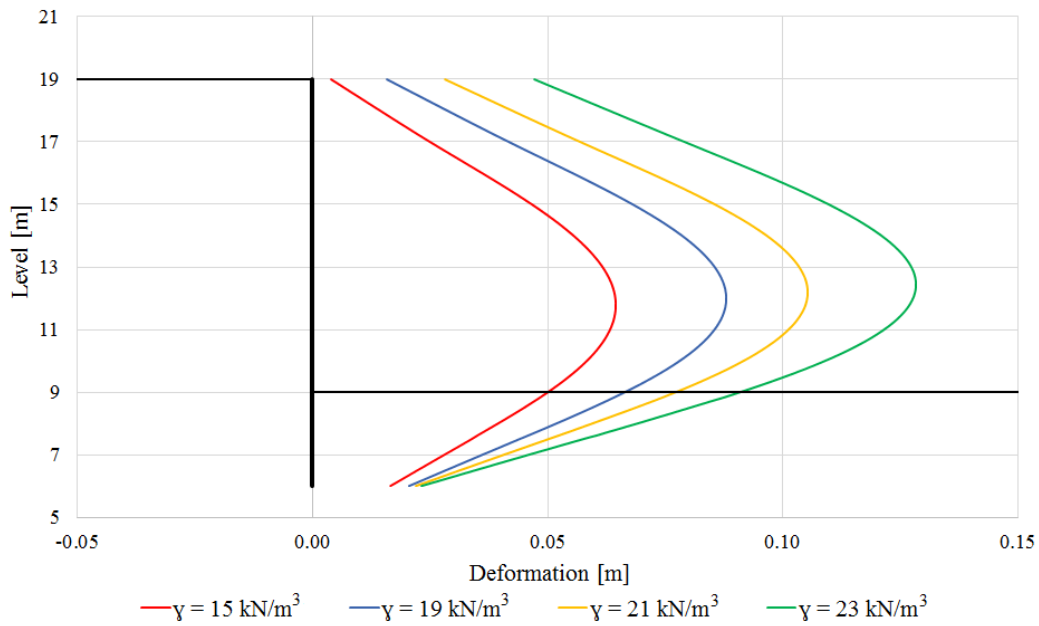


Figure A.180: Deformations altering the soil density value.

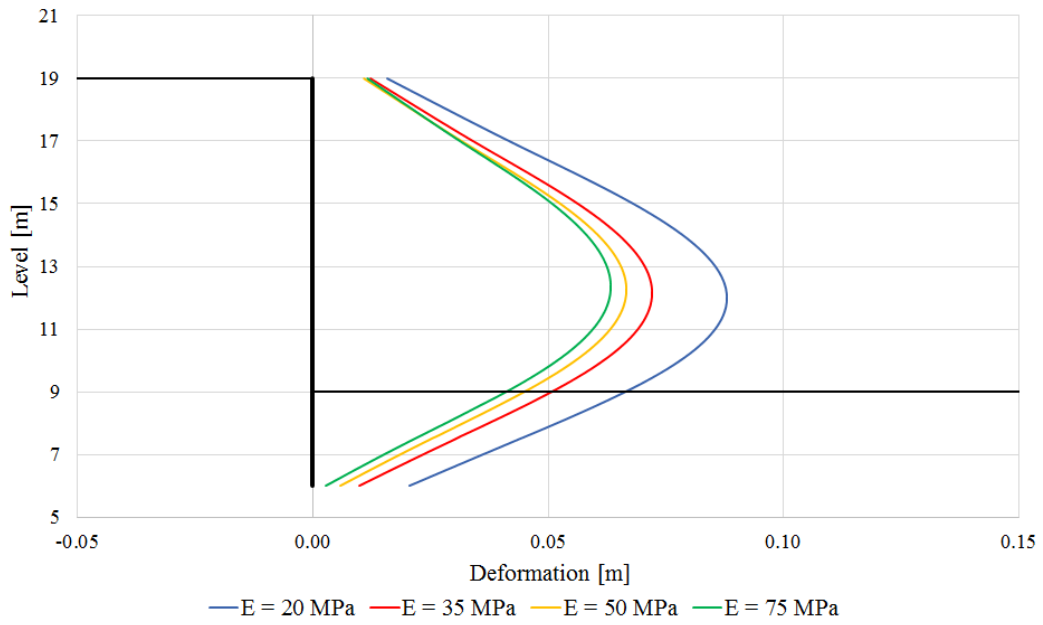


Figure A.181: Deformations altering the modulus of elasticity.

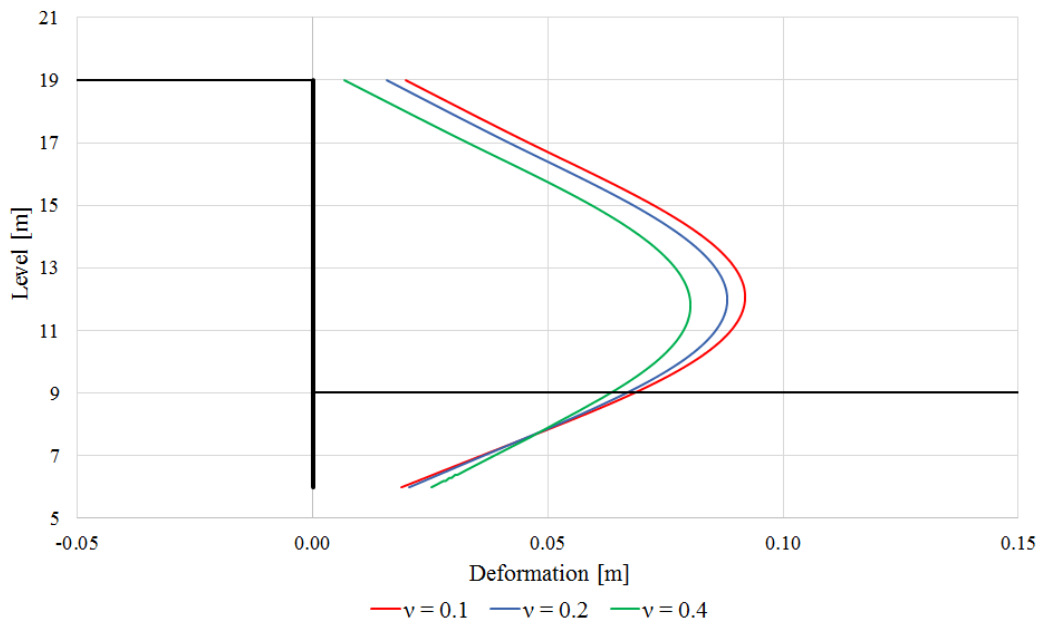


Figure A.182: Deformations altering the Poisson's ratio.

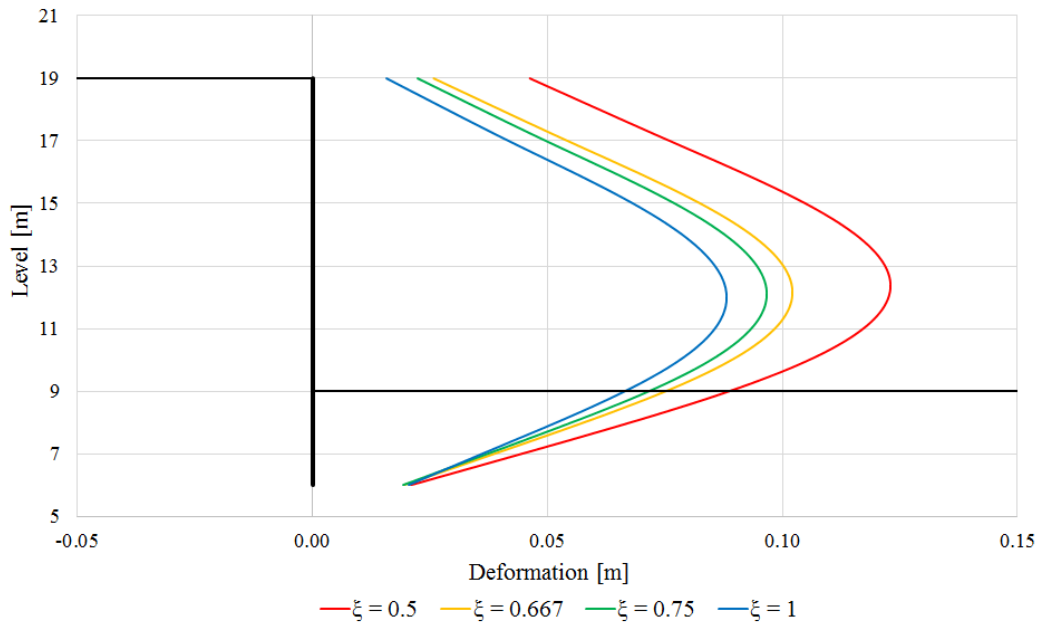


Figure A.183: Deformations altering the wall friction coefficient.

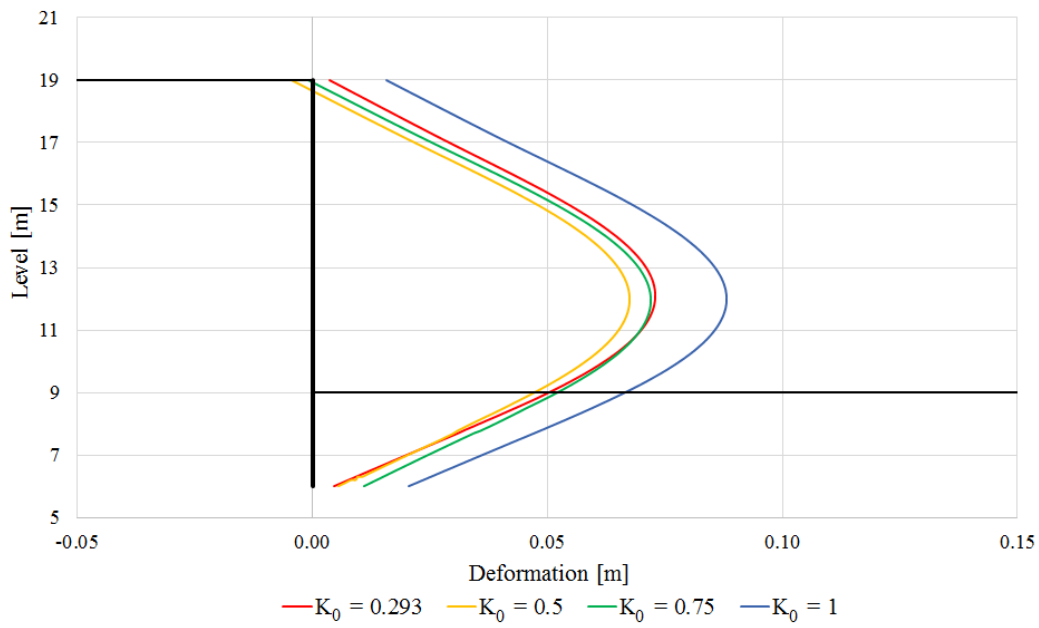


Figure A.184: Deformations altering the initial earth pressure coefficient.

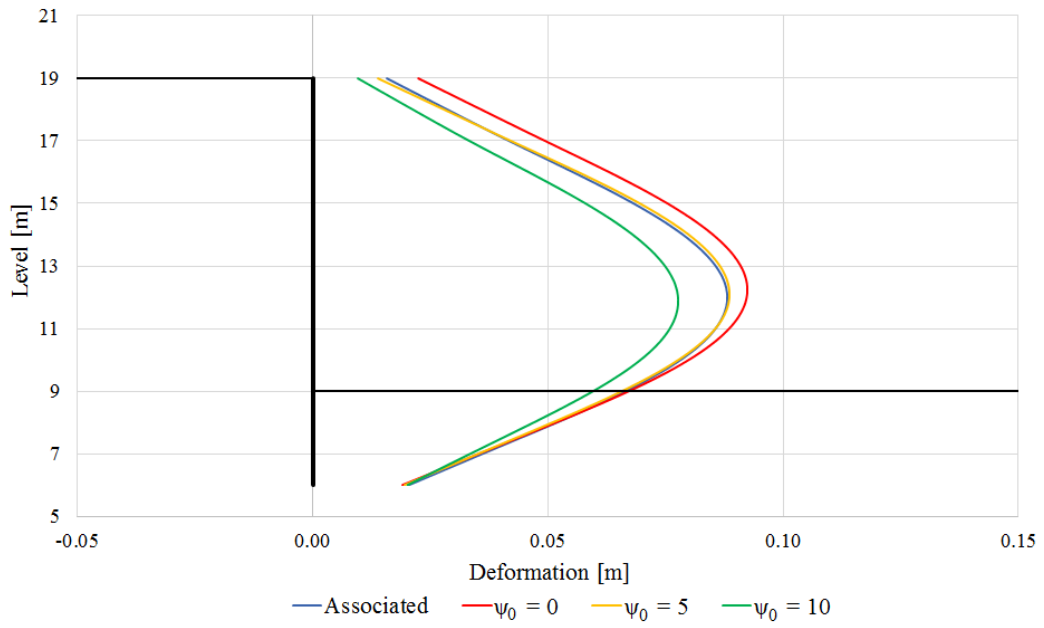


Figure A.185: Deformations altering the flow rule and the associated dilation angle.

A.17.2 Anchor Parameter Influence Results

A study of the influence of the anchor parameters has been carried out. Figures A.186 to A.190 reveals the results obtained.

The parameters count:

- Length of anchor tendon
- Anchor inclination
- Installation level of anchor
- Scale of pretension
- Stage of pretension application

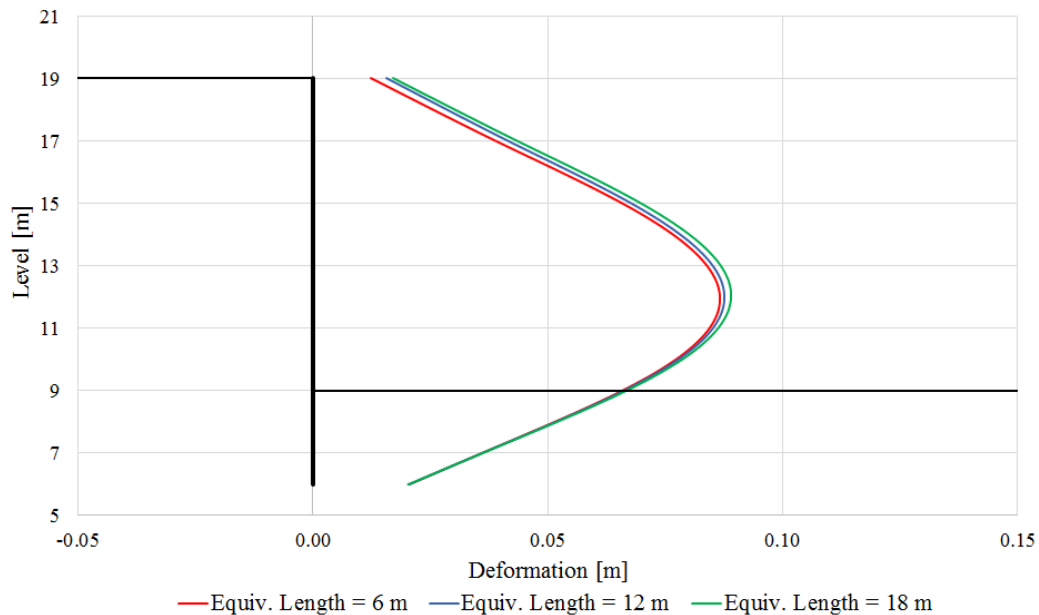


Figure A.186: Deformations altering the equivalent length of the anchor tendon.

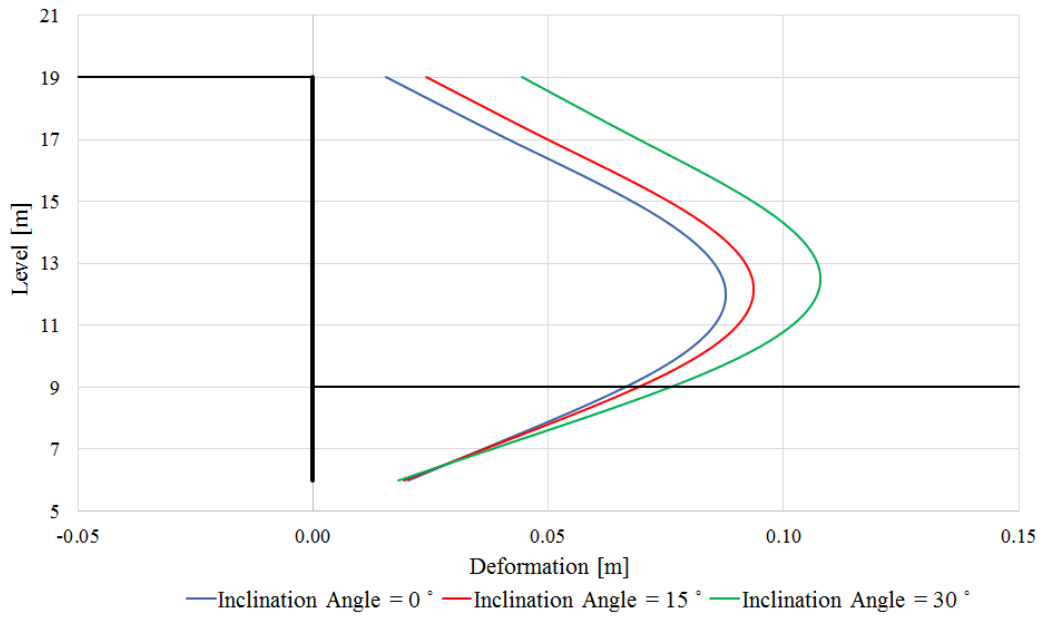


Figure A.187: Deformations altering the inclination angle of the anchor.

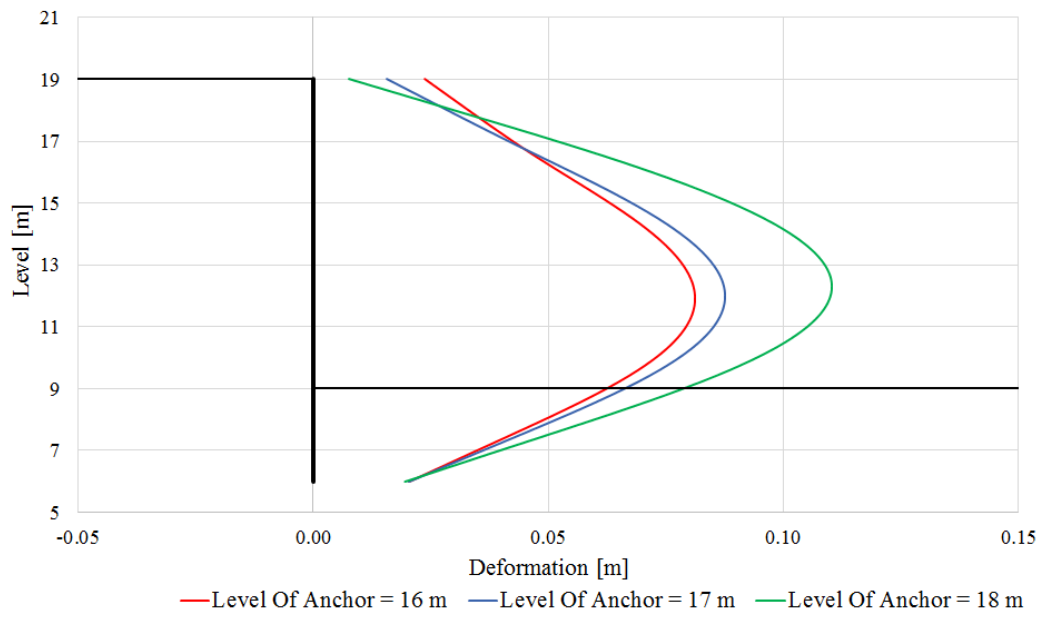


Figure A.188: Deformations altering the installed level of the anchor.

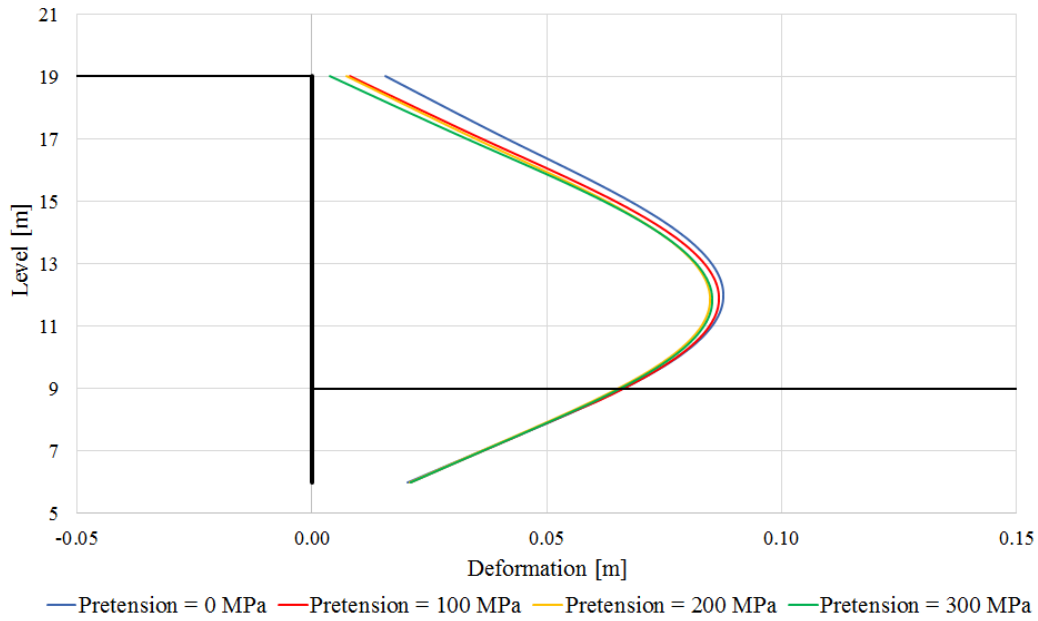


Figure A.189: Deformations altering the pretension of the anchor.

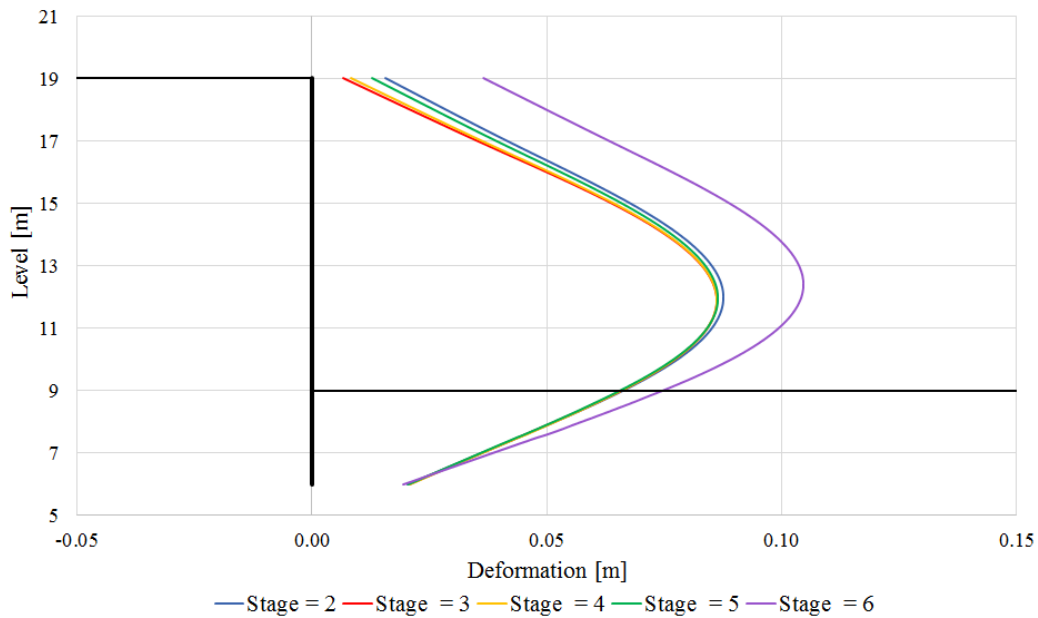
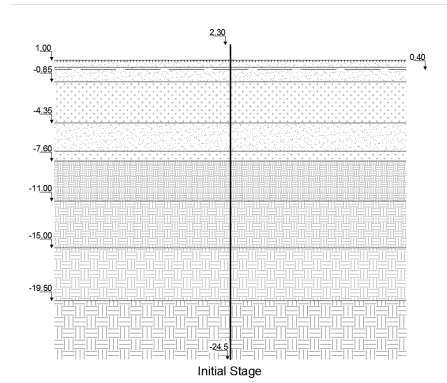
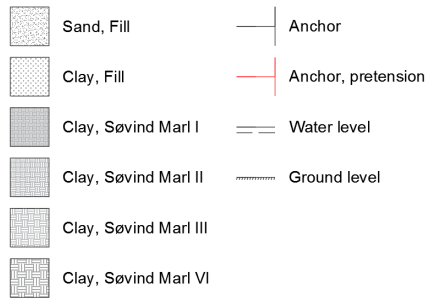


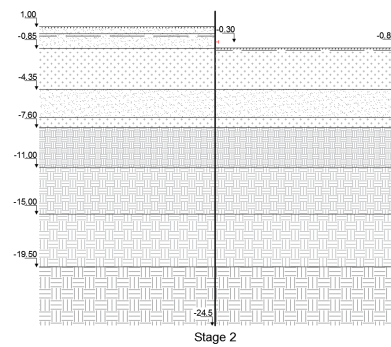
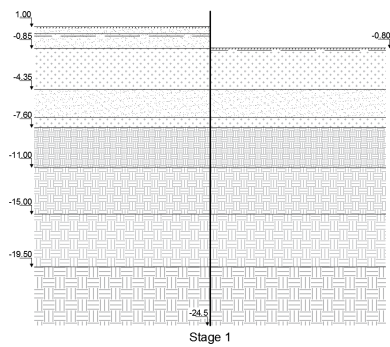
Figure A.190: Deformations altering which stage the pretension is implemented. At stage 2 the anchor is installed in the analysis.

A.18 Stages in the Deformation Analysis



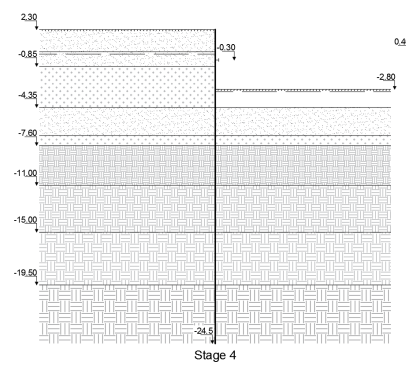
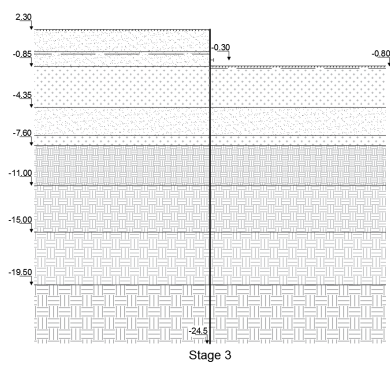
(a) Signatures.

(b) Initial stage.



(c) Stage 1.

(d) Stage 2.

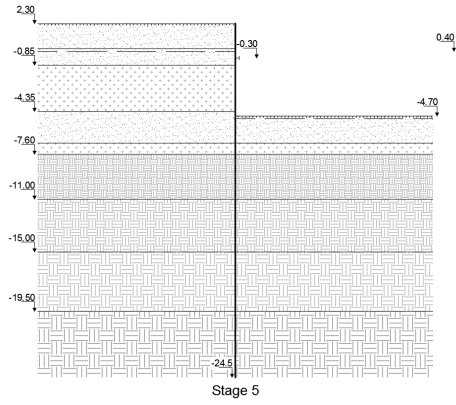


(e) Stage 3.

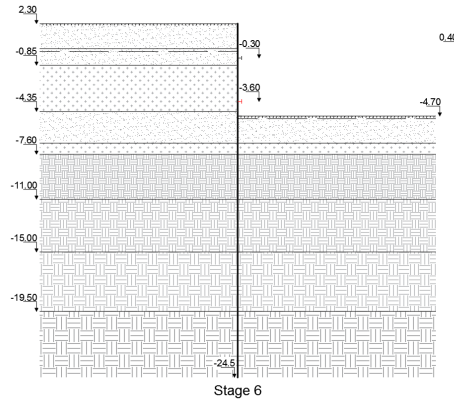
(f) Stage 4.

Figure A.191: Stages used in the numerical model.

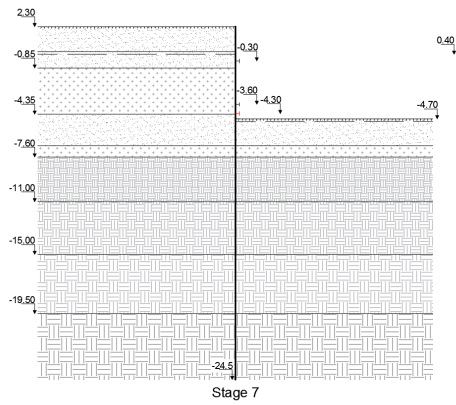
A.18. Stages in the Deformation Analysis



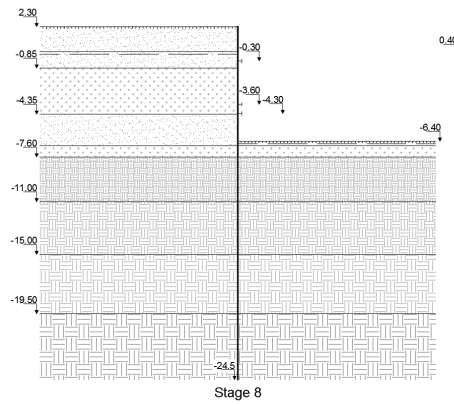
(a) Stage 5.



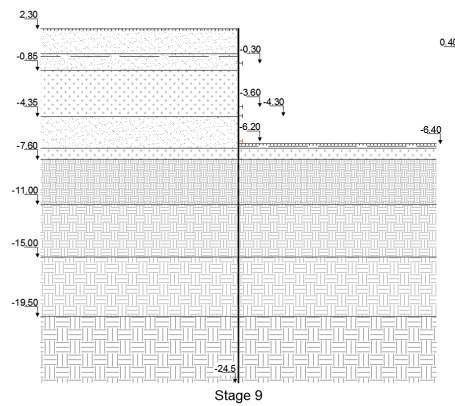
(b) Stage 6.



(c) Stage 7.



(d) Stage 8.



(e) Stage 9.

Figure A.192: Stages used in the numerical model.

A.19 Enhanced Numerical Model Study

Results obtained from the enhanced model. Figure A.193 reveals the effects of the inclusion of staggered wall, and figure A.194 shows the deviation between using Tresca and Mohr-coulomb clay.

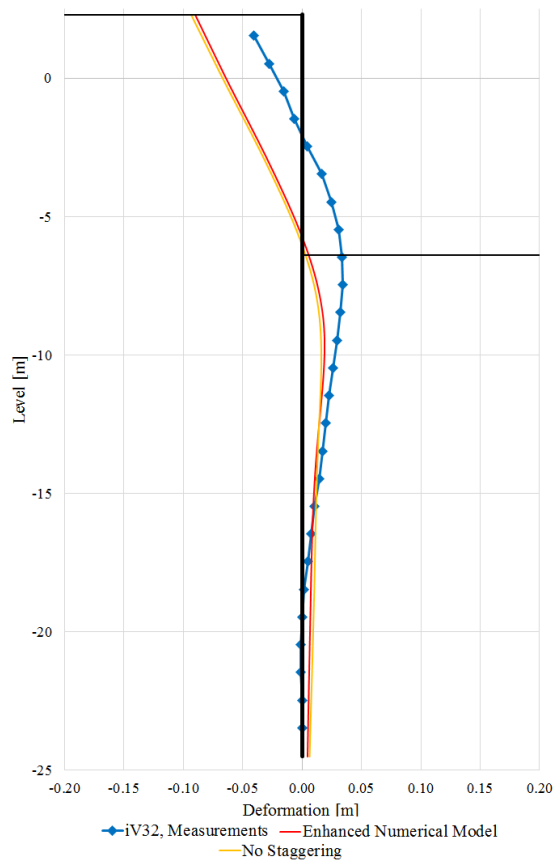


Figure A.193: Deformation results for the enhanced numerical model with and without the staggering installation.

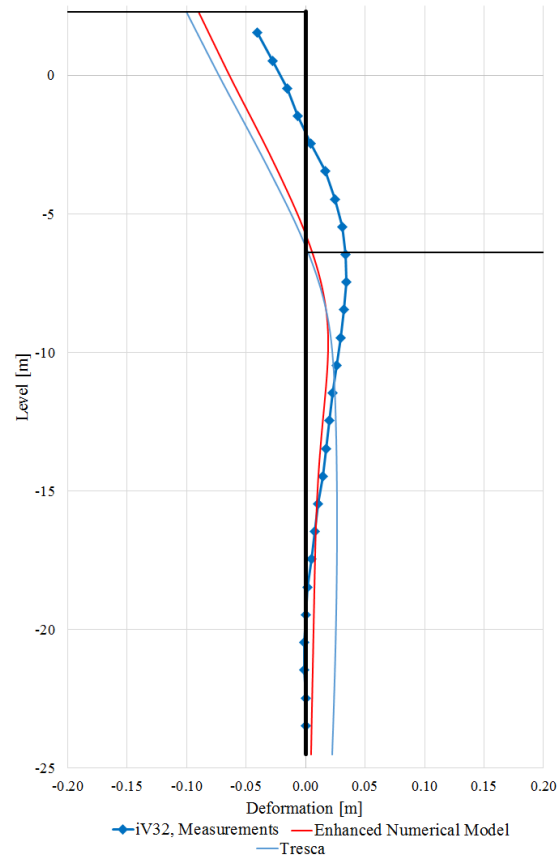


Figure A.194: Deformation results for the enhanced numerical model with Tresca clay and Mohr-Coulomb clay.

A.20 Deformations in Anchor Tendon

The investigations mentioned in section 6.5 have been carried out. As the transfer of the anchor force in the sheet pile wall is investigated, a study of how the load disseminates into the soil is considered and how it affects the system. The deformations the sheet pile wall will experience are revealed in section 6.5. These deformations will be used in order to investigate the strength of the anchor tendon and to determine whether the size of rod used complies with the requirements.

In section 1.1.3 two types of anchors are presented. For both configurations an anchor tendon connects the sheet pile to the plate or injected concrete block in the soil. As the earth pressure on the back side tries to push the wall over, great tension appears in the tendon and possible issues regarding deformations must be considered, as this will affect the scale of deformations the sheet pile wall will experience.

In general the tendon is made of high quality steel and thus the elongation may be great before reaching yielding and further plastic elongation, which is usually not allowed. As the anchor is installed, it gets pretensioned in order to prevent slacking of the tendon. However, there are no specific design rules regarding the magnitude of the pretension and often a qualified guess is used.[11]

As the retaining wall is installed and the excavation is happening, the earth pressure gets established and the anchor becomes activated. Steel has the same Young's Modulus, thus high quality steel allows for larger elongations within the elastic zone. This yields a great load will also mean a large elongation of the tendon and this effect is important to consider.

Pretension

Pretension must be between 0 and 100 % of the ULS design anchor load. 100 % is not recommended as the sheet pile wall will probably never experience a load of this scale resulting in unwanted movements of the wall towards the soil and 0 % may lead to slacking. Usually the anchor tendon is pretensioned to 70 % of the ULS anchor force, however because of the increasing interest in strain compatibility in the tendon, the pretension is often reduced in order to lower the loads in the system.

Tendon design

As specified in the anchor table received matching the deformations of the wall, the anchor of the deformation analyses must withstand a test load of 685 kN. The diameter of the tendon is 36 mm using a strength of 950 MPa, which has been found suitable by the entrepreneur. The design of the tendon is given in figure A.195.

The free length of the anchor is fixed to 19.7 m to ensure that the anchoring reaches beneath the upper boundary of the Søvind Marl surface. The rod is restricted from movements in the longitudinal axis and in the XY-plan along the full course of the anchor rod. In order to

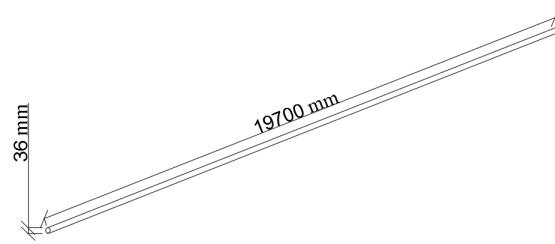


Figure A.195: Design of anchor tendon used in the analyses.

simulate the boundary conditions, lines have been drawn 90° apart. Movement constrains are then applied to the lines such that narrowing or enlargement of the cross section is allowed but not deformations caused by bending or instability of the model in order to simulate reality as much as possible. The constrains are pictured in figure A.196.

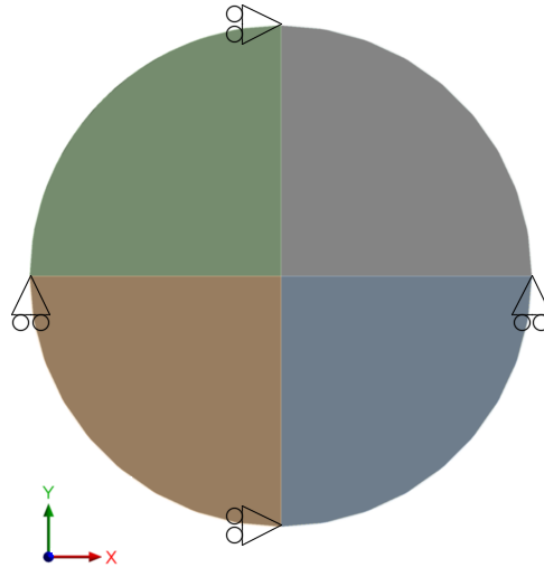


Figure A.196: Movements in the x - and y -directions respectively are constrained.

The material properties of the the anchor tendon are summed up as follows:

- $E = 210000 \text{ MPa}$
- $E_t = 1450 \text{ MPa}$ (bilinear model)
- $\nu = 0.3$
- $f_y = 950 \text{ MPa}$
- $f_u = 1050 \text{ MPa}$

Strain Compatibility

As mentioned strain compatibility of the tendon is of increasing interest. If the anchor head is fully fixed in the soil the tendon must be capable of obtaining the deformations introduced to the wall. As the tendon deforms due to increasing forces, issues rise, and if plasticity is reached, high strains will concentrate in one specific weak area caused by an imperfection leading to abnormalities in the cross section. If the deformations are too great, failure will occur.

A perfect modeled rod will not show the desired effect, as the normal strains will be evenly distributed throughout the full course of the rod. In the analyses an imperfection has been modeled over a span of 50 mm . The imperfection is represented by a reduction of the diameter of 5% which is pictured in figure A.197. This will ensure that the strains are concentrated, which is a realistic consideration.

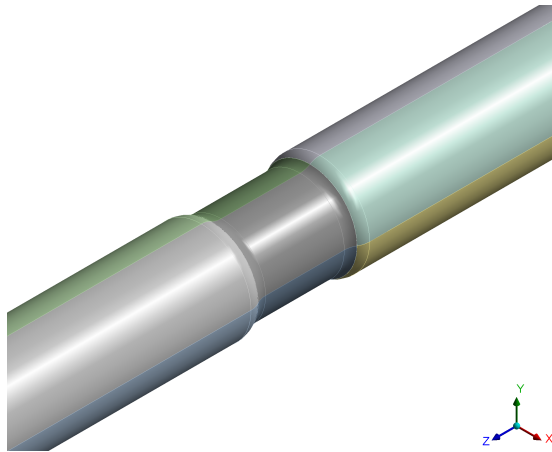


Figure A.197: Minor imperfection created by decreased diameter of the rod.

The studies of the anchor tendon include a deformation analysis altering the scale of the anchor force, and a displacement based analysis forcing a displacement by the use of remote displacements. In both cases the plastic strains are of interest, which must be in a region below the failing strains. According to the *Macalloy* product catalogue the failing strains of a high strength anchor rod are 12% . Strains below this threshold are considered allowable.[11]

The results of the analyses are given in table A.19, which reveals that a anchor force of 685 kN will lead to elongations of 63 mm which is in the elastic region of the tendon. Using forced displacements, yielding will occur at elongations of 74 mm and failing strains reaching 600 mm . In this perspective the strain compatibility has been proved as the test load does not lead to yielding by the inclusion of an imperfection reducing the diameter by 5% .

The results are plotted in figure A.198. Both the deformations and the total equivalent strains for the test load have been given.

Figure A.199 illustrates the results of the forced displacement analysis. Both the deformations and the total equivalent strains for collapse have been given.

Table A.19: Results of strain compatibility studies investigated in appendix A.20. The strains given in the results are total equivalent strains.

| Analysis Load step | Application of anchor force | | | Forced displacement | |
|-----------------------|-----------------------------|---------------------|----------------------|----------------------|----------------------|
| | Force [kN] | Deformation [mm] | Total strains [%] | Displacement [mm] | Total strains [%] |
| 1 | 100.00 | 9.22 | 0.0006 | 20.00 | 0.0014 |
| 2 | 246.25 | 22.70 | 0.0016 | 40.00 | 0.0028 |
| 3 | 392.50 | 36.19 | 0.0025 | 60.00 | 0.0041 |
| 4 | 538.75 | 49.67 | 0.0034 | 80.00 | 0.0054 |
| 5 | 685.00 | 63.17 | 0.0044 | 100.00 | 0.0091 |
| 6 | 1000.00 | 533.88 | 0.1131 | 300.00 | 0.1016 |

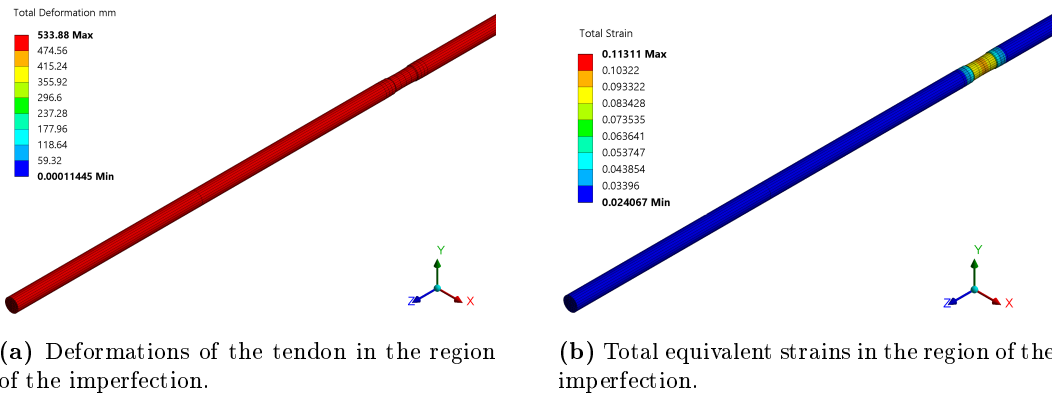


Figure A.198: Results of the force study.

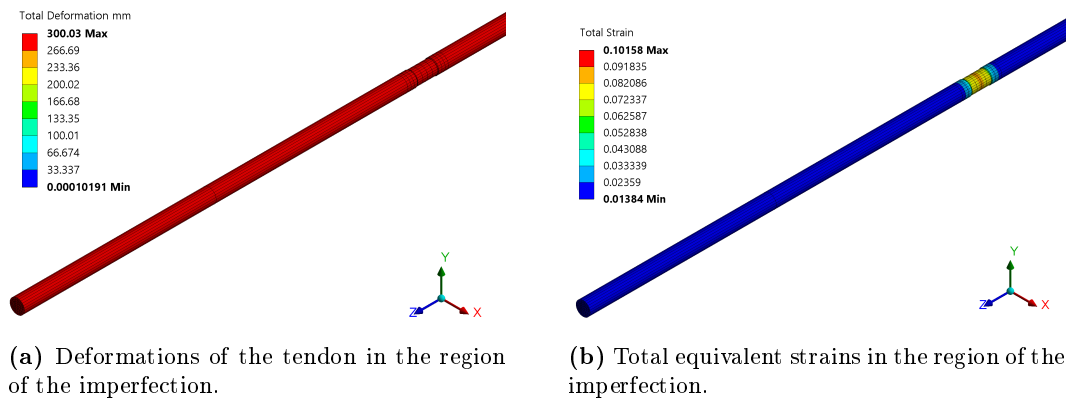


Figure A.199: Results of the forced displacement study.

A.21 Dropbox Link

Link to Dropbox files:

https://www.dropbox.com/sh/n27gk5u1gamei73/AAAdiuFqhez_9VKnGQSBB_Qpa?dl=0

This link contain folders named after the respective chapters in the report. In each folder the relevant files are located. The type of files are as following:

- ANSYS Workbench files
- OptumG2 files
- SPOOKS files
- MATLAB scripts
- Design report for the Dokk1 project
- Copy of report and appendix